UNIVERSITY POITEHNICA OF TIMISOARA
FACULTY OF ELECTRICAL ENGINEERING

DIRECT TORQUE CONTROL OF SENSORLESS INDUCTION MACHINE DRIVES

Ph.D. Thesis

Ing. Cristian Lascu

Timisoara
2002

PREFACE

The present thesis is devoted to high performance direct torque and flux control of sensorless induction machine drives. It approaches the most important features of sensorless direct torque controlled drives: the state estimation and the torque and flux control. The most important existing solutions in terms of direct torque control and induction machine state estimation are analyzed and several novel or entirely new solutions are proposed.

The most important part of the work for the present thesis was carried out in the Laboratory of Intelligent Motion Control, at Faculty of Electrical Engineering, University Politehnica of Timişoara, Romania. Another important part was carried out in the Laboratory of Power Electronics and Drives, at Institute of Energy Technology, Allborg University, Denmark and in the Laboratory of Power Electronics and Drives at Department of Electrical Engineering, University of Nevada, Reno, NV, USA.

I wish to thank to my family for the great support and understanding provided in all these years of hard work.

I would like to express my gratitude to my supervisor, Prof. Ion Boldea, from University Politehnica of Timişoara, Faculty of Electrical Engineering, whose support and guidance made possible the fulfillment of this work.

I wish to thank to Prof. Frede Blaabjerg from Allborg University, Institute of Energy Technology, Denmark and to Prof. Andrzej M. Trzynadlowski from University of Nevada, Reno, NV, USA. They hosted my experiments in their laboratories.

I wish to thank to all my colleagues and friends from University Politehnica of Timişoara who helped me with their advices.

Timişoara — Cristian Lascu

September, 2002

CONTENTS

ABBREVIATIOS

AC	Alternating Current
ASD	Adjustable Speed Drive
BJT	Bipolar Junction Transistor
BPF	Band Pass Filter
CSI	Current Source Inverter
DC	Direct Current
DSP	Digital Signal Processor
DTC	Direct Torque (and Flux) Control
EMF	Electromagnetic Force
GTO	Gate turn Off Thyristor
IGBT	Insulated Gate Bipolar Transistor
LPF	Low Pass Filter
MCT	MOS Controlled Thyristor
MRAS	Model Reference Adaptive System
MOSFET	Metal Oxide Semiconductor Field Effect Transistor
OVM	Overmodulation
PLL	Phase-Locked Loop
PWM	Pulse Width Modulation
RMS	Root Mean Square value
SMO	Sliding Mode Observer (Variable Structure Observer)
SVM	Space Vector (Pulse Width) Modulation
THD	Total Harmonic Distortion factor
WTHD	Weighted Total Harmonic Distortion factor
VSC	Variable Structure Control (Sliding Mode Control)
VSI	Voltage Source Inverter

LIST OF SYMBOLS

$\boldsymbol{A}$, $\boldsymbol{B}$, $\boldsymbol{C}$	generic state space model matrices, $\boldsymbol{A}(n\times n)$, $\boldsymbol{B}(n\times r)$, $\boldsymbol{C}(m\times n)$
D_a, D_b, D_c	SVM modulation functions (duty cycle ratios)
D_k	VSI voltage vector duty cycle ratio, k=1, …, 6
$\boldsymbol{E}$	state observer matrix, $\boldsymbol{E}(n\times n)$, $\boldsymbol{E}=\boldsymbol{A}-\boldsymbol{KC}$
$\underline{i}_s$	stator current space vector
$\underline{i}_r$	rotor current (stator referred) space vector
j	imaginary operator
J	rotor inertia
$\boldsymbol{K}$, $\boldsymbol{L}$	state observer gains, $\boldsymbol{K}(n\times m)$, $\boldsymbol{L}(n-m\times m)$
L_m	magnetizing inductance
L_s	stator inductance
L_r	rotor inductance (stator referred)
$L_{s\sigma}$	stator leakage inductance
$L_{r\sigma}$	rotor leakage inductance (stator referred)
p	number of pole pairs,
R_s	stator resistance
R_r	rotor resistance (stator referred)
S	sliding surface in VSC or SMO
S_a, S_b, S_c	VSI switching signals
sgn(x)	sign function: sgn(x)=1 if x>0 and sgn(x)=-1 if x<0.
T_k	on time for VSI voltage vectors, k=1, …, 6
T_e	electromagnetic torque
T_L	load torque
T_s	stator time constant
T_r	rotor time constant
u	generic input of a dynamic system, $u(r\times 1)$
u_a, u_b, u_c	three phase voltage system

$\underline{u}_{comp}$	compensation voltage vector for flux estimation
$\underline{u}_s$	stator voltage space vector
$\underline{u}_r$	rotor voltage space vector
V_{dc}	VSI DC link voltage
$\underline{V}_k$	VSI basic voltage vector
$\underline{V}^*$	reference voltage vector
x	generic state of a dynamic system, $x(n\times 1)$
$\underline{x}$	generic complex space vector
x_0	zero sequence component of a three phase system
x_a, x_b, x_c	generic three phase system
y	generic output of a dynamic system $y(m\times 1)$
ν, ν_{eq}	sliding mode control (innovation term) and equivalent control
θ_e	arbitrary reference frame position
θ_r	rotor position
$\theta_{\psi r}$	rotor flux vector position
$\theta_{\psi s}$	stator flux vector position
σ	induction machine leakage coefficient
ω_e	arbitrary reference frame speed
ω_r	rotor speed (electrical rad/s)
ω_s	rotor slip speed (electrical rad/s)
$\omega_{\psi r}$	rotor flux vector angular speed
$\omega_{\psi s}$	stator flux vector angular speed
$\underline{\Psi}_s$,	stator flux linkage space vector
$\underline{\Psi}_r$	rotor flux linkage (stator referred) space vector

1 INTRODUCTION

1.1 Review of AC Variable Speed Drives

Energy is the life-blood of the human civilization progress. Our dependence on energy, in general, and on electrical energy, in particular, is absolute. Today, the most developed countries produce and consume the highest amount of energy. The ability to efficiently use the available energy is of capital importance. About 50% of total electrical energy produced is used in electric drives today [1].

An *electric drive* is an industrial system which performs the conversion of electrical energy into mechanical energy, in motoring operation, or from mechanical energy to electrical energy, in generating operation. Such systems are employed to run various processes as: production plants, machine tools, spindles, transportation of goods and people, ship propulsion, rolling mills, ventilation and air-conditioning, home appliances, automation equipments, robotics, cranes and elevators, CD-ROM players, and so on [1]-[6].

An *Adjustable Speed Drive* (ASD) is a drive that runs at variable speed. A typical ASD contains a power electronic converter, an electric motor, a mechanical coupling and the mechanical load. Such a drive must achieve precise, fast, efficient and reliable mechanical motion control, as required by the application.

ASD is an emerging technology pushed by the spectacular evolution in power electronics components and microprocessors. The significant increase in power density and the high integration level in modern microprocessors helped ASD-s to become a very competitive technology. The growth in motor drives has exceeded 25% over the

past 10 years and the world market for ASD-s is still growing rapidly. By far, AC drives dominate the marketplace with 4.85 billion USD sales in 1998, [7]-[9].

Adjustable speed induction motor drives have reached the status of a mature technology in a broad range of applications ranging from low-cost solutions to high-performance drive systems. Modern industrial ASD-s with induction machines have to fulfill many demands related to: accuracy of speed control, wide speed range, torque-speed characteristic, sensor or sensorless operation, dynamic response, control methods, braking, efficiency optimization, self-commissioning, fault detection and handling, electromagnetic interference, harmonic generation, interfacing to other ASD, application software, etc, [8], [9].

Today, the induction machine is recognized as the workhorse of the electromechanical conversion systems. The preference for induction machines is due to their low cost, constructive simplicity, reliability and ruggedness. The cage rotor induction motor covers a wide power range, from 0.5 kW to 10 MW, while wound rotor machines may handle even higher powers. Induction machines have two limitations that are important issues at high powers: rather poor power factor and lower efficiency than the synchronous machine, at powers above 1 MW, [1]-[6].

Motion control systems have traditionally been developed using permanent magnet DC servomotors with high-bandwidth current regulators and has made the high-bandwidth electromagnetic torque control a de facto standard for servo drives. Similar dynamic capability is also possible with induction machines, since, like DC machine, the induction machine poses very small transient inductance. There are three basic measures of motion control performance: command tracking accuracy, response quickness and disturbance rejection or dynamic stiffness, [5], [6].

Motion control with induction motors is a challenging theoretical problem, since its dynamic model is nonlinear, time-variable, the rotor quantities are most often non measurable and the physical parameters are sometimes imprecisely known. In this context, *motion control* means torque, speed and/or position control. In induction machines, torque control requires also flux control and very fast torque control is the key for high performance motion control.

There are two basic techniques for induction motor control:

- The scalar control, known as voltage/frequency (V/f) control or current-slip frequency control. The scalar control is an open loop speed control system and provides variable speed with low precision and modest dynamic performance. This method is based on a simple, steady state model of the machine and sometimes includes slip frequency and load torque compensation.
- The Vector Control, also known as Field Oriented Control. It is based on a dynamic machine model and includes the indirect vector control, the direct vector control and the direct torque and flux control. The vector control was developed as a closed loop speed/torque control system and provides fast and precise motion control.

From the point of view of how the mechanical quantities are sensed and how the motion control is achieved, there are two research trends:

- Motion control with motion sensors that employ different motion sensors to detect the rotor speed or position. These sensors are expensive and unreliable. Wide speed ranges, typically above 1:1000, can be achieved using motion sensors.
- Motion control without motion sensors, known as *sensorless control*. In this case, the mechanical quantities are estimated rather than measured. Currently, speed ranges of above 1:100 can be obtained in this way.

Research efforts in this area are devoted toward developing high performance vector controlled sensorless ASD-s. The very low speed range operation is still a challenging problem and various solutions are proposed to overcome the difficulties that occur at very low speeds and to provide fast, robust and accurate motion control in a wide speed range.

1.2 Vector Control of Induction Machine Drives

Vector control or *Field Oriented Control* (FOC) implies independent control (decoupled control) of flux and torque, or of flux current component and torque current component trough a coordinated change of the supply voltage amplitude, phase and frequency. This is achieved by orienting the stator current with respect to the rotor flux, so that to realize the decoupled torque and flux control, [2]-[5].

There are three requirements for vector control [5]:

- An independently controlled current that accounts for the torque production.
- An independently controlled, or constant value of the field flux.
- An independently controlled spatial angle between the flux axis and the magneto motive force (MMF) axis.

If these requirements are met at every moment, the torque will follow the torque component of the stator current and instantaneous torque control will result. If these conditions are only met for steady state conditions, only steady state torque control will result.

The stator current vector is controlled such that its component along the rotor flux vector (the flux component) controls the rotor flux magnitude, while its component orthogonal to rotor flux vector (the torque component) controls the electromagnetic torque. In voltage source inverters, the desired current is impressed by means of current regulated pulse width modulation techniques (CRPWM).

The vector control of stator currents and voltages results in control of the spatial orientation of the electromagnetic field in the machine and has lead to the term *Field Orientation Control* (FOC), [1]-[6].

Since the induction machine is a high order, cross-coupled dynamic system, the torque and flux control is realized by adequate decoupling between the torque controller and the flux controller. The most important sub-variants of vector control are: indirect vector control, direct vector control and direct torque and flux control [1]-[5]. These are shortly described next.

1.2.1 Indirect Vector Control

The indirect vector control block diagram for induction machine drives is presented in Figure 1.1. It is based on the slip speed ω_s equation, using estimated or measured rotor speed ω_r: $\omega_s = \omega_e - \omega_r$. The reference torque and rotor flux, T_e^* and ψ_r^* that enter as primary references are translated into reference currents in rotor flux reference frame by a current decoupling network. The reference currents are converted to stator frame by a coordinate transformation that uses the field position and are realized by current regulation and PWM.

The field position θ_e is obtained by summing the rotor position signal θ_r and the slip position signal θ_s. The slip speed is derived from the reference currents and its position is obtained by integration. The rotor position is measured or estimated.

Basically, the indirect vector control is a feedforward type scheme. The stator current only is controlled in closed loop, while the torque and flux control is indirectly achieved by means of the decoupling network and current control. This scheme achieves high performance control at low speeds, but is rather sensitive to parameter detuning. There are two types of indirect vector control: uncompensated flux response indirect controller and compensated flux response indirect controller [5].

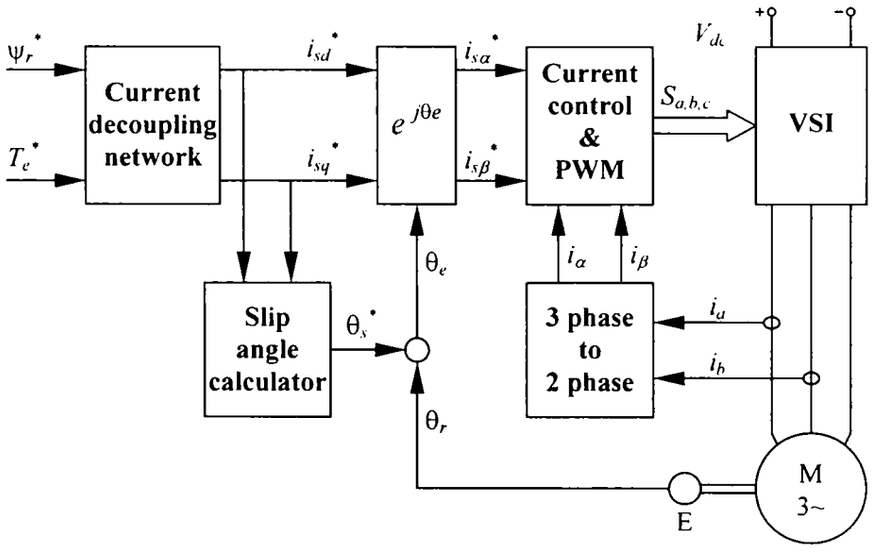

Figure 1.1 Indirect Vector Control for induction machine drives

1.2.2 Direct Vector Control

The direct vector control block diagram for induction machine drives is presented in Figure 1.2. This scheme employs closed loop control of torque, flux and stator current. The measurement of rotor position is eliminated by making other measurements directly on machine electrical quantities. The slip relation is no longer used and the field angle is directly determined by calculation from measured electrical quantities. The advantage of this approach is elimination of the position sensor, that is, sensorless implementation. This leads to increased complexity of the control and estimation system.

Basically, the direct vector control is a feedback type scheme. It employs torque and flux controllers. These controllers replace the decoupling network and produce the reference current vector. The current control is achieved in the same way as for indirect vector control, by means of CRPWM.

Current controllers may be implemented in stator frame, as shown in Figure 1.2, or in rotor flux frame. In both cases, PI controllers with decoupling are recommended, [5]. For sensorless implementation, a state observer, that uses the measured currents and voltages, is implemented. In general, the direct vector control is less sensitive to parameter detuning than indirect vector control.

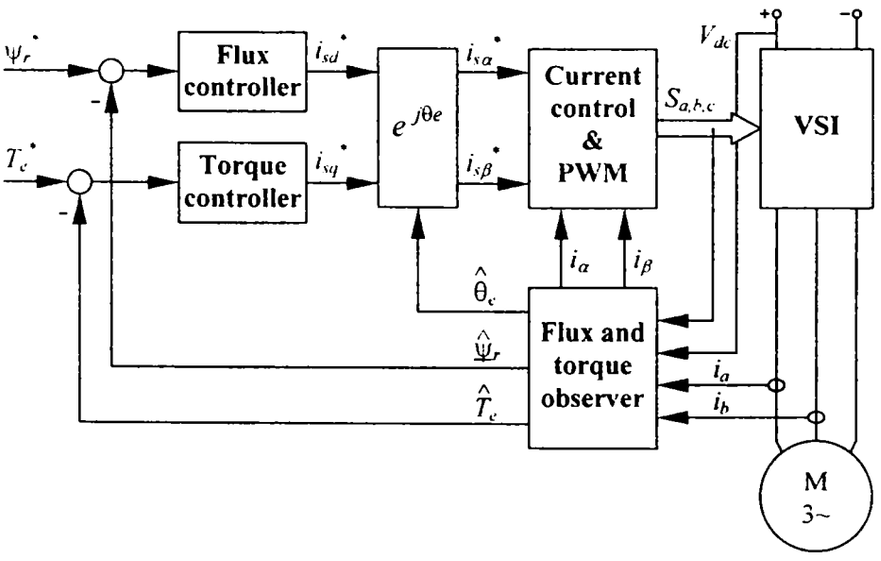

Figure 1.2 Direct Vector Control for induction machine drives

1.2.3 Direct Torque and Flux Control

The *Direct Torque and flux Control* (DTC) realizes the control directly, without intermediate current controllers. Its block diagram is shown in figure 1.3. Like the direct vector control, DTC employs a state estimator to calculate the actual torque and stator flux. The torque and flux control is achieved by means of nonlinear bang-bang controllers, while the current control is replaced by an adequate switching strategy that directly generates the inverter switching signals.

This scheme provides extremely fast and robust torque and flux control. It is simple and does not employ coordinate transformations and pulse width modulation. However it exhibits large torque ripple and annoying acoustical noise if operated at low sampling frequencies. Comparative results between DTC and direct vector control demonstrated that both strategies are viable and exhibit comparable performance, each with its own advantages and limitations [10].

The DTC strategy makes the subject of the present thesis. The objective is to develop alternative DTC schemes that offer superior performance and operate in sensorless drives. In particular, the problem of maintaining the DTC advantages (fast dynamic response and robustness) and reducing the torque, flux and current ripple is addressed.

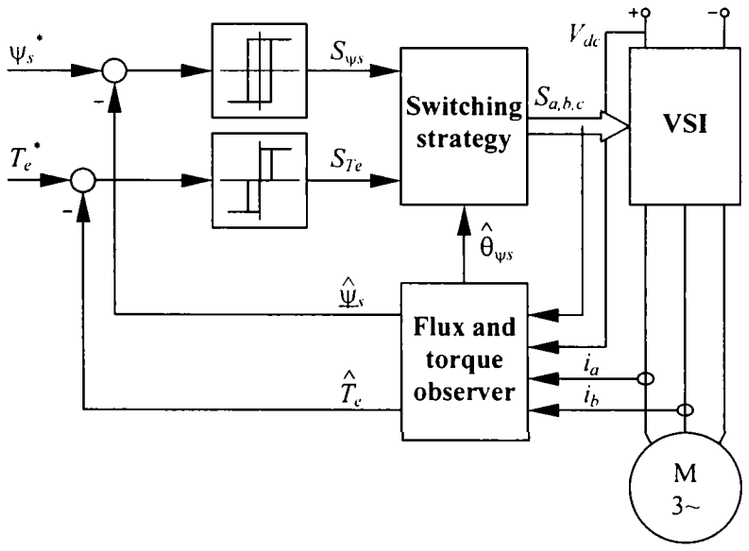

Figure 1.3 Direct Torque and Flux Control for induction machine drives

1.3 Sensorless Control of Induction Machine Drives

State Estimation

A sensorless drive is an ASD that realizes motion control (torque, speed or position control), without using motion sensors to detect the mechanical quantities. In general, the motor's terminal quantities are measured and an estimator is employed to calculate the unknown mechanical quantities.

Sensorless speed and torque control of induction machine ASD-s has become a well-established technology in a broad range of applications. The field has developed to a point where sensorless control is not considered a major difficulty, excepting in the low speed range. Many commercial drives include some sort of sensorless speed and torque control. However their performance at very low speed is poor [11].

In sensorless drives, quantities that are estimated are the stator and rotor fluxes, the electromagnetic toque and the rotor speed. The stator currents and voltages are the only measured quantities and the estimation is performed by a digital signal processor.

Induction machines are high-order nonlinear systems. The classical approach to induction machine modeling for vector control is to determine linear, time-variable state space models, under simplifying assumptions. The most important nonlinearities that remain unmodeled are the magnetic saturation, iron loses, that account for half of the total machine losses, and the presence of slots. These effects act as disturbances or model uncertainties, deteriorating the system's performance.

There are two possible approaches of this problem: either developing advanced nonlinear models, or employing robust control and observation techniques. While the former approach offers a unique theoretical fascination and challenge, the later is very attractive for practical implementation of high performance motion control systems.

The estimation of internal state variables of the induction machine is based exclusively on measured terminal voltages and currents. Low cost, medium performance sensorless drives employ simple open-loop estimators. High-performance drives employ complex observers based on full order state space models.

There are two categories of state observers: linear observers and nonlinear observers. The most important linear observers for state estimation are: full order linear observers, known as Luenberger observers and reduced order observers.

The nonlinear observers for induction machine state estimation are:

- The Extended Kalman Filter (EKF). It is the extension to nonlinear systems of the optimal linear filter that minimizes the mean square estimation error, known as Kalman Filter. This filter assumes perfect system knowledge and requires precise information on noise statistics.
- The Variable Structure Observer or Sliding Mode Observer (SMO). It is a nonlinear state observer supported by the theory of Variable Structure Systems. It possesses excellent robustness over a specified magnitude range of system parameter uncertainties and disturbances.
- The Neural Network Observer (NNO) or Fuzzy Neural Observer (FNO). These belong to the area of Artificial Intelligence. These observers require intensive training for each particular application without need of detailed information on system's model. Performances displayed by NNO-s are only moderate. The application of these techniques in ASD-s is at the beginning and shows promising potential.

The EKF appeared to be the ultimate solution for sensorless drives. It has the advantage that is able to handle nonlinear systems and copes well with the fifth order complete model (2.15)-(2.20) of the induction machine.

However, EKF has limitations. It suffers from lack of inherent robustness, perfect knowledge of the system model and noise characteristics are assumed, it does not guarantee adequate bandwidth for disturbance rejection. The EKF implementation involves significant computation complexity and requires powerful processors. Recent studies have demonstrated the superiority of other observers, over EKF [12].

The speed estimation is the most difficult part of the estimation process. There are two categories of speed estimators in induction machine drives:

- Estimation based on fundamental excitation includes all methods that employ the fundamental components of stator voltages and currents. By proper processing of these quantities, the speed information can be extracted. These

methods are not able to provide speed estimation at zero stator frequency. The most important methods in this category are presented in Chapter 6.

- Estimation based on magnetic saliency and signal injection includes methods that use as test signals injected high frequency flux or current components. Some methods detect the speed related harmonics caused by rotor slots, while other methods detect the magnetic saliencies caused by the main flux saturation. These methods provide accurate speed estimation at zero stator frequency.

Methods in the second category appear to be very promising, since they provide speed estimate at zero frequency. However, there are problems at high speeds, since injected high frequency components cause torque ripple, loss increasing and acoustical noise. This constitutes a major drawback that makes them unattractive.

Sensorless control

Apart from the vector control strategies, there are other control techniques that are employed for motion control in ASD-s.

Variable Structure Control (VSC), due to its disturbance rejection, strong robustness, order reduction and simple implementation by means of power converter, is one of the most promising control philosophies for electrical drives [13].

Variable Structure Control forces the system's trajectories to intersect a surface of the state space, designated by the designer. After intersection, system's trajectories are constrained to this surface for all subsequent time, via the use of high speed switching controls. The most important characteristics of VSC are:

- The surface can be selected so that the system is robust to system parameters changes and disturbances as long as system's trajectories lie along the surface.
- If the system's nonlinearities and disturbances are bounded, then the system can be forced to behave like a linear system by the use of VSC. As long as the system remains in sliding mode, it emulates a reduced order system.
- The control algorithm is very simple in most cases.

The feedback linearization control achieves decoupling and linearization of the induction machine dynamics by using nonlinear state transformations [14]. This method is relatively complex, but appears very promising [1].

1.4 Thesis Objective

This thesis is devoted to direct torque and flux control of sensorless induction machine drives. It provides an insightful analysis of DTC sensorless drives and attempts to develop several new concepts related to: (1) induction machine state estimation and (2) direct torque control.

Solutions for induction machine state estimation are discussed in two chapters that present existing solutions, as well as new solutions of linear and nonlinear state observers. Speed observers are introduced next, while the last chapter approaches the DTC. New DTC solutions based on VSC are presented.

The most important objectives of this thesis are:

- Analysis of the classical DTC and development of alternative high performance control strategies that maintain the advantages of DTC and reduce or eliminate its shortcomings.
- Development of high performance state observers that may be operated in wide speed range induction machine sensorless drives. In particular, the very low speed range performance is targeted.
- Building and testing a high performance induction machine sensorless drive that uses concepts previously developed.

Nevertheless that the sensorless control of induction machine drives is a very popular subject and the literature devoted to this topic is very rich. Herewith, only solutions considered the most representative, that show the best results in terms of DTC sensorless control, were presented under the title "State of the art". Solutions that are not confirmed by meaningful experiments, or that claim spectacular experimental results, without theoretical fundaments, were neglected.

References

[1] I. Boldea. S.A. Nasar, *Electric Drives.*, CRC Press Boca Raton, London, New York, Washington, D.C., 1999.

[2] I. Boldea, S.A. Nasar, *Vector Control of AC Drives.*, C.R.C. Press Florida, Boca Raton, Ann Arbor, London, Tokyo, 1992.

[3] Werner Leonhard, *Control of Electrical Drives.*, Springer-Verlag, Berlin, Heidelberg, New-York, Tokyo, 1985.

[4] A.M. Trzynadlowski, *The Field Orientation Principle in Control of Induction Motors.*, Kluwer Academic Press, Boston, 1994.

[5] D.W. Novotny, T.A. Lipo, *Vector Control and Dynamics of AC Drives.*, Clarendon Press - Oxford, Oxford University Press, New York, 1996.

[6] Bimal K. Bose (editor) et al., *Power Electronics and Variable Frequency Drives. Technology and Applications.*, IEEE Press, 1997.

[7] B.K. Bose, *Energy, Environment and Advances in Power Electronics.*, IEEE Transactions on Power Electronics, vol. 15, no. 4, July 2000, pp. 688-701.

[8] R.J. Kerkman, G.L. Skibinski, D.W. Schlegel, *AC Drives: Year 2000 (Y2K) and Beyond.*, APEC'99, The Annual Applied Power Electronics Conference, 1999, vol. 1, pp. 28-39.

[9] T.M. Jahns, E.L. Owen, *AC Adjustable-Speed Drives at the Millennium: How Did We Get Here.*, IEEE Transactions on Power Electronics, vol. 16, no. 1, Jan. 2001, pp. 17-25.

[10]D. Casadei, F. Profumo, G. Serra, A. Tani, *FOC and DTC: Two Viable Schemes for Induction Motors Torque Control.*, Proc. of EPE-PEMC 2000, 2000, pp. 1-128 - 1-135.

[11]J. Holtz, *Methods for Speed Sensorless Control of AC Drives.*, in K. Rajashekara (Editor) "Sensorless Control of AC Motors", IEEE Press, 1996.

[12]F. Chen, M.W. Dunnigan, *Comparative Study of a Sliding-Mode Observer and Kalman Filters for Full State Estimation in an Induction Machine.*, IEE Proceedings on Electric Power Applications, vol. 149, no. 1, January 2002, pp. 53-64.

[13]Vadim Utkin, Jurgen Guldner, Jingxin Shi, *Sliding Mode Control in Electromechanical Systems.*, Taylor & Francis, 1999.

[14]Jean-Jacques E. Slotine, Weiping Li, *Applied Nonlinear Control.*, Prentice Hall, Englewood Cliffs, New Jersey, 1991

2 INDUCTION MACHINE MODELING

2.1 Introduction

The induction motor is recognized to be the workhorse of the industrial electromechanical conversion systems. Induction motors are simple in structure, robust, reliable, require little maintenance, can be operated in difficult environments and their cost is substantially less than for DC motors. All these features make them attractive for use in today's industrial drives and possibly to remain so in the future. Conventional induction motor drives are supplied from the constant voltage and frequency industrial power grid and are limited only to driving loads which require nearly constant speed or, at best, several discrete speeds. Operating such a conventional drive on a wide speed range below the rated speed is rather difficult and involves a significant degradation of the motor efficiency. The problem has been overcame by using variable voltage-frequency power supplies that allow operating the motor below and above the base speed.

The analysis of induction machine for constant speed drives is typically done by means of the steady state per phase equivalent circuit. This model proves to be inadequate when dealing with dynamic electromechanical processes encountered in adjustable speed drives (ASD). In order to drive the induction motor at any speed in a certain speed range and also to manage fast transients, complex control systems are required. It is well known that high performance control systems require adequate knowledge and modeling of plant dynamic model. Furthermore, sensorless AC drives employ advanced state observation techniques based, once more, on the plant dynamic

model. Although simple in structure, the induction machine owns the most complex dynamic model when compared to other electric machines and is the most challenging in terms of control engineering.

In the next sections, the induction machine modeling begins with the definition of space vectors and continues with the development of state space dynamic models. Models that account for saturation effects and iron losses are also presented.

2.2 Space Vector Definition

In order to describe and study the mechanical motion of different objects it is necessary to define a space-time frame that allows to specify objects' positions and the time flow. Such a space-time frame is called *reference system* or *reference frame*. Any reference system can be fixed or in relative motion with respect to other reference systems. Finding an absolutely fixed system is an exceptionally difficult problem.

According to classical Newtonian-Galilean[1] mechanical principles, the space and time are absolute and invariant and the motion laws are the same for all *inertial reference systems*. With a very good approximation, the Earth is such an inertial reference system and this is the primary reference system in the following induction machine study. All reference frames used herewith are two-dimensional complex frames (complex planes) and all mobile frames exhibit only rotary motion with respect to stationary references. Any fixed frame with respect to Earth is called *stationary reference frame* or *stator reference frame* and is identified by "α" and "β" orthogonal axes. The rotating frame attached to the rotor is the *rotor reference frame*. A reference frame can also be attached to a vector and, in this case, inherits the name of that vector. For example, a reference frame attached to rotor flux space vector is a *rotor flux reference frame*. A useful generalization is the *arbitrary reference frame* that

[1] Galileo Galilei 1654-1642, Isaac Newton 1642-1727

represents a reference system rotating with undefined, arbitrary angular speed. Herewith, all rotating frames are identified by "*d*" and "*q*" orthogonal axes.

The concept of complex space vectors is a very powerful tool and an essential aspect of electric machines analysis. It provides a compact notation, easy algebraic manipulation, very simple graphical interpretations and often a very logical and straightforward development of concepts that are difficult to develop using real variable analysis. In the case of induction machines, a very convenient and compact form of the machine equations is obtained and there is a great deal of manipulative and conceptual value in their use [1] – [6].

Consider a symmetrical three phase winding located in the stator of an elementary two pole electric machine, with the configuration shown in Figure 2.1. In this case, the winding placement is conceptually shown with the symmetry axes of the equivalent inductors directed along the real magnetic *a*, *b* and *c* axes of the windings. In complex notation, with respect to a stationary (α, β) reference frame, the three phase axes are defined by the respective unity vectors $\underline{1}$, $\underline{a}$ and $\underline{a}^2$.

$$\underline{1}=1, \qquad \underline{a}=e^{j\frac{2\pi}{3}}, \qquad \underline{a}^2=e^{-j\frac{2\pi}{3}} \tag{2.1}$$

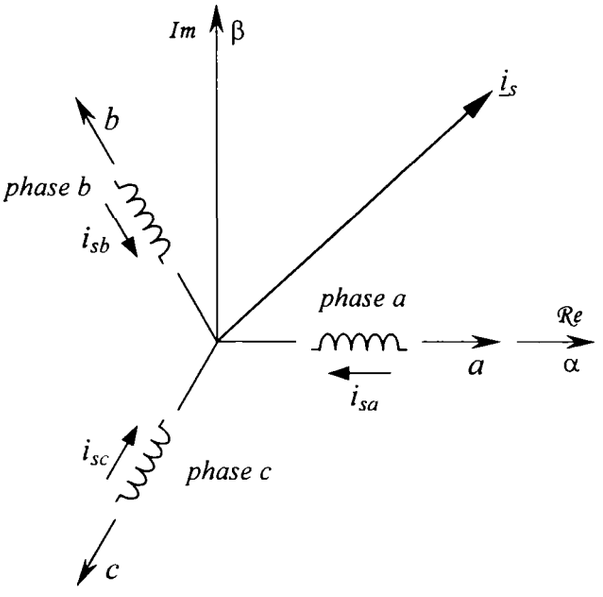

Figure 2.1 Stator winding of an induction machine and associated magnetic axes

A generic three phase system, related to the stator winding shown in Figure 2.1, can be uniquely described by a *complex space vector* $\underline{x}^s$ and a *zero sequence component* x_0.

$$\underline{x}^s = \frac{2}{3}(x_a + \underline{a}x_b + \underline{a}^2 x_c) \tag{2.2}$$

$$x_0 = \frac{1}{3}(x_a + x_b + x_c) \tag{2.3}$$

where x_a, x_b, x_c are the phase variables and superscript "s" denotes the stator reference frame. In Figure 2.1 the stator current space vector $\underline{i}_s$ is represented, but, in general, $x_{a,b,c}$ can be any quantity related to that winding, such as voltage, flux linkage, etc.

In terms of stationary complex reference frame (α, β), the space vector $\underline{x}^s$ is

$$\underline{x}^s = x_\alpha + jx_\beta \tag{2.4}$$

$$x_\alpha = x_a - \frac{1}{3}(x_a + x_b + x_c) \tag{2.5a}$$

$$x_\beta = \frac{1}{\sqrt{3}}(x_b - x_c) \tag{2.5b}$$

In most practical situations the neutral connection of the three phase system is opened so that the zero sequence component x_0 equals zero. In this case, from (2.4a), the real component of $\underline{x}^s$ is $x_\alpha = x_a$. In voltage source inverter analysis, however, this is not true and the zero sequence component must be taken into account.

Equations (2.2) to (2.5) define the (a, b, c) to (α, β) coordinate transformation. The choice of 2/3 coefficient in (2.2) is somewhat arbitrary; this value is usually selected in order to maintain the length of the voltage and current vectors equal to the magnitude of the phase voltage and current sinusoids from the sinusoidal steady state operation. Another choice is to use the coefficient $\sqrt{2/3}$ in order to obtain a power invariant transformation.

The inverse relations, for finding the phase variables associated with the space vector $\underline{x}^s$, are obtained from the projections of this vector to respective (a, b, c) axes with $x_0 = 0$.

$$x_a = \Re e(\underline{x}^s), \qquad x_b = \Re e(a^2 \underline{x}^s), \qquad x_c = \Re e(a\underline{x}^s) \tag{2.6}$$

The complex space vector $\underline{x}^s$ defined by (2.2) to (2.5) is represented in stationary reference frame (α, β). A generalization of interest is to represent the same vector in an arbitrary reference frame defined by (d, q) axes, rotating with angular speed $\omega_e = d\theta_e / dt$, as shown in Figure 2.2. In (d, q) coordinates, denoted by superscript "e", the vector $\underline{x}^e$ is

$$\underline{x}^e = \underline{x}^s \cdot e^{-j\theta e} \tag{2.7}$$

where θ_e is the arbitrary (d, q) frame position with respect to stationary (α, β) system. Using the well known Euler's relation $e^{j\theta e} = \cos(\theta_e) + j\sin(\theta_e)$, in terms of ($d$, q) coordinates, the space vector $\underline{x}^e$ is

$$\underline{x}^e = x_d + jx_q \tag{2.8}$$

$$x_d = x_\alpha \cos(\theta_e) + x_\beta \sin(\theta_e) \tag{2.9a}$$

$$x_q = -x_\alpha \sin(\theta_e) + x_\beta \cos(\theta_e) \tag{2.9b}$$

In matrix notation, (2.9) is

$$\begin{bmatrix} x_d \\ x_q \end{bmatrix} = \begin{bmatrix} \cos(\theta_e) & \sin(\theta_e) \\ -\sin(\theta_e) & \cos(\theta_e) \end{bmatrix} \cdot \begin{bmatrix} x_\alpha \\ x_\beta \end{bmatrix} \tag{2.10}$$

The inverse transformation from (d, q) frame to (α, β) frame is

$$\underline{x}^s = \underline{x}^e \cdot e^{j\theta e} \tag{2.11}$$

$$x_\alpha = x_d \cos(\theta_e) - x_q \sin(\theta_e) \tag{2.12a}$$

$$x_\beta = x_d \sin(\theta_e) + x_q \cos(\theta_e) \tag{2.12b}$$

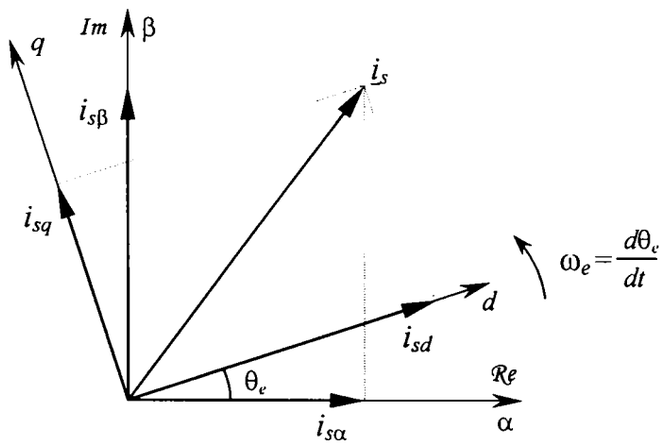

Figure 2.2 Transformation from stationary (α, β) to rotating (d, q) reference system

In matrix notation, (2.12) is

$$\begin{bmatrix} x_\alpha \\ x_\beta \end{bmatrix} = \begin{bmatrix} \cos(\theta_e) & -\sin(\theta_e) \\ \sin(\theta_e) & \cos(\theta_e) \end{bmatrix} \cdot \begin{bmatrix} x_d \\ x_q \end{bmatrix} \tag{2.13}$$

In order to simplify the formulas and for clarity, whenever this is not confusing, the superscripts "*e*" and "*s*", denoting the respective frames, will be dropped.

The transformation (2.2) from (*a*, *b*, *c*) to (α, β) together with transformation (2.7) from (α, β) to (*d*, *q*) is a general coordinate transformation from a three phase system to a two phase rotating one, known as the *Park transformation*. From (2.2) and (2.7) the space vector definition, in (*d*, *q*) system, is

$$\underline{x}^e = \frac{2}{3} e^{-j\theta e} (x_a + \underline{a} x_b + \underline{a}^2 x_c) \tag{2.14}$$

The inverse Park transformation could be easily obtained from (2.11) and (2.6).

Although (2.14) appears to be very compact, the digital implementation requires more operations than (2.2) and (2.7) computed separately. For efficiency reasons, in practice, the preferred relations are (2.5), (2.9) for direct Park transformation and (2.13), (2.6) for the inverse Park transformation.

It must be noted at this point that the space vector concept represents a *spatial and time variable* entity. The best analogy is that with the revolving field (air gap flux density) which, being *spatial* in nature, is sinusoidally distributed *spatially* even for arbitrary *temporal* values of stator winding current and travels with finite speed from one phase to another around the air gap when the winding current is modified. Mathematically speaking, the complex vectors respect the complex numbers algebra rules.

All definitions presented imply a great degree of generality. The generic variable "*x*" can be replaced with any stator and rotor quantity and the arbitrary system "*e*" can be any rotating reference frame. Furthermore, the space vector concept can be generalized to any three phase power supply and three phase load. Although not distributed in space, such a load circuit behaves exactly in the same way as a motor load. It is permitted and a common practice, therefore, to extend the space vector approach to the analysis of equivalent lumped parameter circuits.

2.3 Space Vector Modeling of Induction Machine

2.3.1 General assumptions

Most induction machines are designed to operate from a three phase power source of alternating voltage. For ASD-s, the source is normally an inverter that uses solid-state switching devices to produce approximately sinusoidal voltage and currents of controllable magnitude and frequency.

The induction machine has a three phase stator winding as the one shown simplified in Figure 2.2. The turns in each coil are distributed so that a current flowing trough the stator winding produces an approximately sinusoidally spatial distributed flux density around the air gap periphery. The most common type of induction machine has a squirrel cage rotor which can be conceptually replaced with a three phase sinusoidally distributed winding, similar with the stator winding. The wound rotor machines, on the other hand, have a true three phase rotor winding, similar with the stator one.

The induction machine modeling for vector controlled ASD-s is based on several assumptions [1]-[5]:

- The air gap is uniform and the machine is symmetrical from electromagnetic perspective. This assumption is true in today's induction machines.
- The stator and rotor windings are sinusoidally spatial distributed along the inner periphery of the stator and the outer periphery of the rotor, respectively. This assumption implies that the flux density has sinusoidal distribution along the air gap periphery and is true to a certain degree in all machines.
- The slotting effects are neglected, so that the windings can be visualized as being of negligible depth and located in the air gap. This in an idealization since all machines have slots in both sides.
- Space harmonics of the stator and rotor flux, arising from the placement of the actual conductors in the discrete slots (harmonic leakage flux), are neglected.

- Magnetic saturation and iron losses are neglected. This will be assumed in derivation of general induction machine models, but in the last sections, advanced models that take into account saturation and iron losses will be developed.
- Windings' resistances are assumed constant or very slowly variable compared with machine's dynamics. In the drive implementation, the resistances deviation from nominal values will be taken into account and compensated for.
- End winding effects, magnetic anisotropy effect and skin effect are neglected.
- The permeability of the stator and rotor iron is assumed to be infinite.

The modeling and analysis of induction machines can be done using real three phase quantities in stationary (a, b, c) reference frame. Analyzing the machine physical structure and using the Maxwell[2] electromagnetic field theory, the three phase model could be obtained. In this case, the machine's electromagnetic model consists of six circuits with extensive amount of coupling between them, making the analysis rather complicated. This model is not used anymore in electric drives analysis.

A significant simplification and system's order reduction from six to four is obtained if the analysis is carried out in terms of real variable (d, q) differential equations. The approach involves the topic of referenced frame theory and constitutes an essential aspect of machine analysis. The real variable orthogonal model is used mostly when the external constraints are unsymmetrical (single phase operation, unequal parameters, failure analysis, etc.).

In those situations when the fundamental polyphase symmetry is retained, analysis can be conveniently carried out in complex vector form. The result is that the model is reduced to a powerful and compact second order complex variable model. This order reduction permits considerable simplification and is especially valuable in the constant speed analysis when the electrical equations reduce to linear differential equations with constant coefficients – linear time invariant dynamic model. Equivalent circuits that correctly represent the machine model are also easily derived using

[2] James Clerk Maxwell 1831-1879

complex vector modeling. Therefore, the space vectors based modeling of induction machine has become the standard approach in the analysis and synthesis of ASD-s.

The literature dedicated to induction machine modeling and vector control is very rich and detailed [1]-[5]. Different machine models and equivalent circuits are thoroughly derived and in detail analyzed, valuable conclusions are presented. All authors conclude that the best way to approach the induction machine control is throughout the complex space vector analysis. The same procedure is adopted herewith. Only the most important space vector based models are presented in the following subsections. State space models are derived and analyzed from the perspective of ASD design and control systems engineering. All models and equivalent diagrams are valid in transient operation if not otherwise specified.

2.3.2 The Induction Machine General Model

As mentioned before, the space vector model can be developed starting with the analysis of the physical machine and using the Maxwell's equations and the space vector theory [1]–[5]. This derivation is skipped herewith.

An induction machine with zero applied rotor voltage (short-circuited rotor) is considered. The induction machine space vector general model in *arbitrary reference frame* rotating with ω_e angular speed, including the mechanical equations is

$$\underline{u}_s = R_s \underline{i}_s + \frac{d\underline{\Psi}_s}{dt} + j\omega_e \underline{\Psi}_s \tag{2.15}$$

$$\underline{0} = R_r \underline{i}_r + \frac{d\underline{\Psi}_r}{dt} + j(\omega_e - \omega_r)\underline{\Psi}_r \tag{2.16}$$

$$\underline{\Psi}_s = L_s \underline{i}_s + L_m \underline{i}_r \tag{2.17}$$

$$\underline{\Psi}_r = L_r \underline{i}_r + L_m \underline{i}_s \tag{2.18}$$

$$T_e = \frac{3}{2} p(\Psi_{sd} i_{sq} - \Psi_{sq} i_{sd}) \tag{2.19}$$

$$\frac{J}{p}\frac{d\omega_r}{dt} = T_e - T_L \tag{2.20}$$

where

$\underline{u}_s = u_{sd} + ju_{sq}$ is the stator voltage space vector,

$\underline{i}_s = i_{sd} + ji_{sq}$ is the stator current space vector,

$\underline{i}_r = i_{rd} + ji_{rq}$ is the rotor current (stator referred),

$\underline{\psi}_s = \psi_{sd} + j\psi_{sq}$ is the stator flux linkage space vector,

$\underline{\psi}_r = \psi_{rd} + j\psi_{rq}$ is the rotor flux linkage (stator referred) space vector,

R_s, R_r are the stator and rotor (stator referred) resistances,

L_m is the magnetizing inductance,

$L_s = L_m + L_{s\sigma}$ is the stator inductance,

$L_r = L_m + L_{r\sigma}$ is the rotor inductance (stator referred),

$L_{s\sigma}$, $L_{r\sigma}$ the stator and rotor (stator referred) leakage inductances,

$\omega_e = d\theta_e/dt$ is the arbitrary reference frame speed,

$\omega_r = d\theta_r/dt$ is the rotor electrical speed and θ_r is the rotor position,

T_e is the electromagnetic torque,

T_L is the load torque,

J is the rotor and load inertia

p is the number of pole pairs,

Equations (2.15) to (2.18) represent the complex vector electromagnetic model, (2.19) is the torque equation and (2.20) is the mechanical model. The entire model represents a fifth order, nonlinear, cross-coupled, dynamic system, which cannot be analytically solved. The complex vector equivalent "T" circuit, corresponding to electromagnetic model (2.15) - (2.18), is illustrated in Figure 2.3.

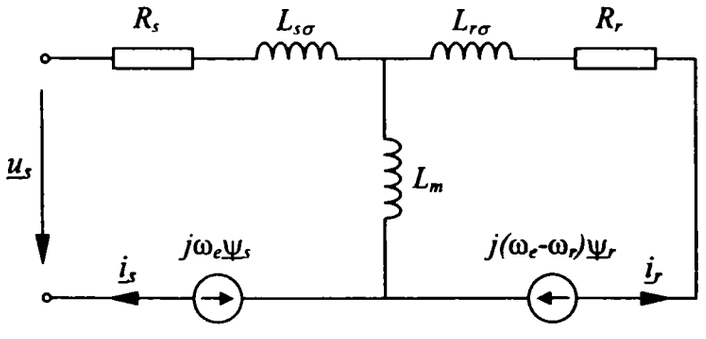

Figure 2.3 Induction machine equivalent circuit in arbitrary reference frame

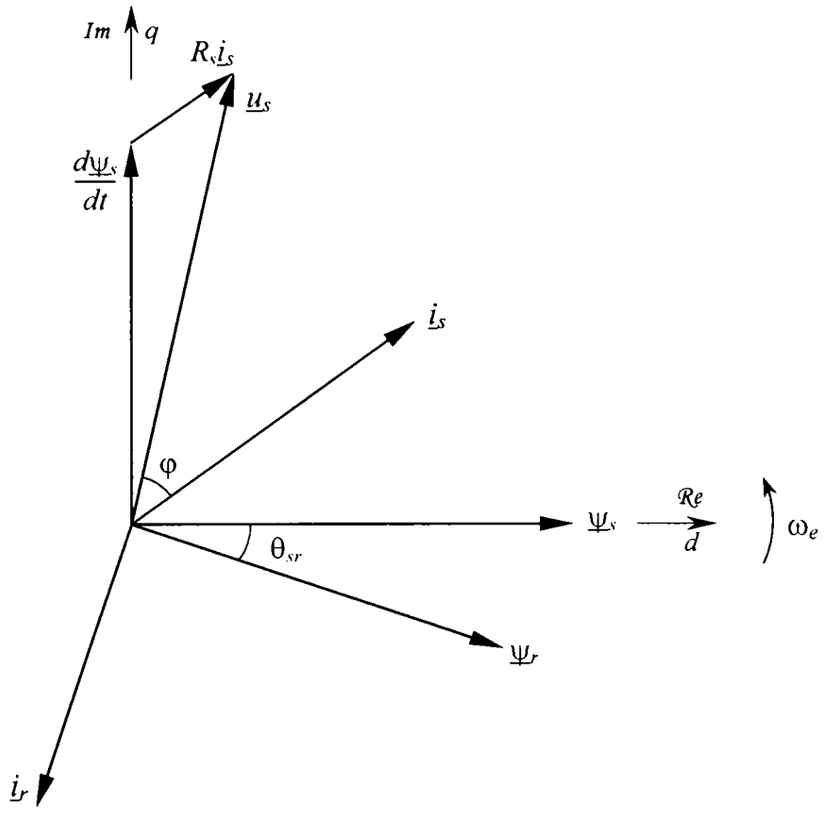

Figure 2.4 Induction machine space vector diagram in arbitrary reference system

The space vector diagram of the induction motor, with the stator flux vector alongside the "*d*" axis, is represented in Figure 2.4. The diagram is valid for both transient and steady state operation. In transient operation the relative position of the space vectors changes because each individual vector rotates with different instantaneous angular speed.

The rotor current, rotor flux and rotor parameters are stator referred using the turn ratio (the ratio $k=N_s/N_r$ between the number of turns in stator and rotor windings). This means that the real rotor flux has been multiplied with the turn ratio, the real rotor current with its reciprocal, N_r/N_s and the real rotor resistance and leakage inductance with $(N_s/N_r)^2$. It can be shown that the selection of turn ratio between the stator and rotor circuits of the (*d*, *q*) model is essentially completely arbitrary when the machine is operated with zero applied rotor voltage [4].

It is of interest to detail the general model for some particular reference frames. Depending on application requirements, it may be useful to rotate the reference system synchronously with the rotor or with one of the complex vectors denoting stator or

rotor flux, current or voltage. While (2.17) to (2.20) are reference frame invariant, equations (2.15) and (2.16) turn out to be simpler.

In *stator reference frame*, with ω_e=0, the electromagnetic model is

$$\underline{u}_s = R_s \underline{i}_s + \frac{d\underline{\Psi}_s}{dt} \tag{2.21}$$

$$\underline{0} = R_r \underline{i}_r + \frac{d\underline{\Psi}_r}{dt} - j\omega_r \underline{\Psi}_r \tag{2.22}$$

$$\underline{\Psi}_s = L_s \underline{i}_s + L_m \underline{i}_r \tag{2.23}$$

$$\underline{\Psi}_r = L_r \underline{i}_r + L_m \underline{i}_s \tag{2.24}$$

In this case, the equivalent circuit is illustrated in Figure 2.5.

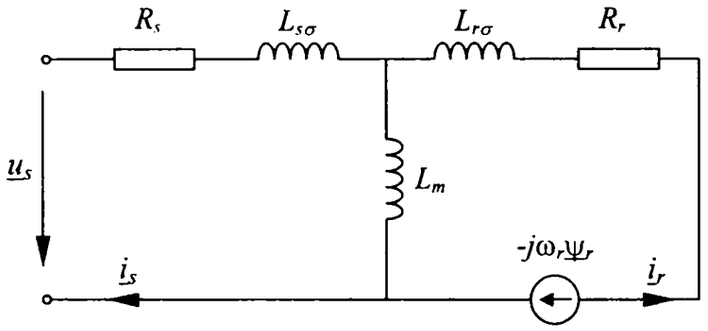

Figure 2.5 Induction machine equivalent circuit in stator reference frame

In *rotor reference frame*, with ω_e=ω_r, the electromagnetic model is

$$\underline{u}_s = R_s \underline{i}_s + \frac{d\underline{\Psi}_s}{dt} + j\omega_r \underline{\Psi}_s \tag{2.25}$$

$$\underline{0} = R_r \underline{i}_r + \frac{d\underline{\Psi}_r}{dt} \tag{2.26}$$

$$\underline{\Psi}_s = L_s \underline{i}_s + L_m \underline{i}_r \tag{2.27}$$

$$\underline{\Psi}_r = L_r \underline{i}_r + L_m \underline{i}_s \tag{2.28}$$

In this case, the equivalent circuit is illustrated in Figure 2.6. This time, the rotor equation (2.26) has become speed independent. Another choice of interest for the reference frame is the *rotor flux reference frame* with ω_e=$\omega_{\psi r}$, the rotor flux speed. In this case the model is similar with (2.15) - (2.20), with ω_e replaced by $\omega_{\psi r}$.

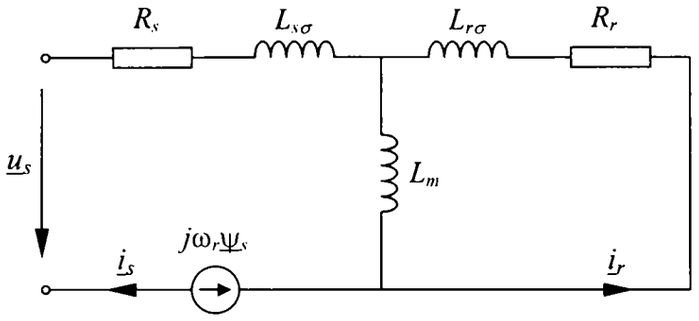

Figure 2.6 Induction machine equivalent circuit in rotor reference frame

Regardless of the reference frame, the model still remains nonlinear. It is well known that the electromagnetic time constants are smaller than the mechanical time constants. Based on this observation, the fifth order system can be divided in two separate subsystems, a fast electromagnetic system and a slow mechanical system. The electromagnetic system (2.15) - (2.18) is linear and contains the rotor speed only as a time variable (assumed slowly variable) parameter. This is a fourth order, linear time variable dynamic system. The mechanical system (2.20) is also linear and the algebraic torque equation (2.19) remains the only nonlinear connection between those two systems.

Equations (2.17) and (2.18) are linear algebraic relations between currents and fluxes and, eventually, will be eliminated together with two complex variables. Before that, several useful relations are directly derived from (2.17) and (2.18), as follows.

The stator and rotor currents, in terms of stator and rotor flux, are

$$\underline{i}_s = \frac{L_r\underline{\Psi}_s - L_m\underline{\Psi}_r}{L_sL_r - L_m^2} \tag{2.29}$$

$$\underline{i}_r = \frac{L_s\underline{\Psi}_r - L_m\underline{\Psi}_s}{L_sL_r - L_m^2} \tag{2.30}$$

From (2.29), the relations between stator flux, rotor flux and stator current are

$$\underline{\Psi}_s = \frac{L_m}{L_r}\underline{\Psi}_r + \frac{L_sL_r - L_m^2}{L_r}\underline{i}_s \tag{2.31}$$

$$\underline{\Psi}_r = \frac{L_r}{L_m}\underline{\Psi}_s - \frac{L_sL_r - L_m^2}{L_m}\underline{i}_s \tag{2.32}$$

The model presented so far allows the induction machine to be easily analyzed

in either transient or steady state operation, regardless of the supply method used. However, if an attempt to develop a control system and a state estimator for an induction motor drive is made, the model turns out to be somehow unsystematic and inefficient. It contains too many variables (four complex), and too many equations, some of them algebraic.

Elimination of two complex variables using (2.17) and (2.18) turns out to be an important simplification and systematization, and produces the state space models of the induction machine. The selection of the two variables to be removed is carried out taking into account the control system requirements and the control strategies adopted. In most cases, the rotor current is not accessible for measurements (in squirrel-cage type motors), is not controlled and is disregarded. In most cases, the stator current is measured and appears either as a state variable and/or as output. In general, when stator flux control is desired, the rotor flux is eliminated and the *stator flux model* is obtained. When rotor flux control is desired, the stator flux is eliminated and the *rotor flux model* is obtained. If both stator and rotor fluxes are defined as state variables and the stator current is output, the *stator flux-rotor flux model*, or, simply, the *flux model* is found. The last model is the most appropriate when saturation effects are considered. Models involving the magnetizing flux are also possible, but are not discussed herewith.

Furthermore, the selection of reference frames is made in the same way, taking into account the control requirements. In general, stator flux orientation and control is carried out in stator or stator flux reference frame, while rotor flux orientation and control is carried out in rotor flux reference frame.

The above considerations on induction machine state space models are valid if the machine is supplied from a voltage source, in general, and from a Voltage Source Inverter (VSI), in particular. If the machine is supplied from a Current Source Inverter (CSI), it is natural to select the stator current as the input and the voltage as the output. In this case different models can be obtained.

The most important state space models for the induction machine are developed next. These models are appropriate for machines supplied by voltage source inverters.

2.4 State Space Models of Induction Machine

Control systems engineering is a vast, well established and advanced scientific domain with a variety of powerful methods and a long history of successful industrial applications. Therefore, it is natural to exploit those methods in designing induction motor control systems.

Control systems theory requires dynamic systems to be modeled in standard canonic forms [7], [8]. For multivariable linear systems like the induction motor's electromagnetic model, the typical canonic form is the so-called *state space model.* The advantage of using state space forms is that the considerable achievements of the linear control theory can be directly applied once the model parameters have been identified.

The generic state space model of a linear multivariable dynamic system is

$$\frac{d}{dt}x = Ax + Bu \tag{2.33}$$

$$y = Cx \tag{2.34}$$

where $x \in \Re^n$ is an $n \times 1$ state vector, $u \in \Re^r$ is an $r \times 1$ input vector, $y \in \Re^m$ is an $m \times 1$ output vector, $\boldsymbol{A} \in \Re^{n \times n}$ is the $n \times n$ system matrix, $\boldsymbol{B} \in \Re^{n \times r}$ is the $n \times r$ input matrix and $\boldsymbol{C} \in \Re^{m \times n}$ is the $m \times n$ observability matrix.

The state trajectory is obtained as a solution of state equation (2.33) for a given input vector u(t) and a known initial state x_0.

$$x(t) = e^{At}x_0 + \int_0^t e^{A(t-\tau)}Bu(\tau)d\tau \tag{2.35}$$

This equation is difficult to be evaluated in most practical situations.

The system's *eigenvalues*, or *poles*, are solutions of the characteristic equation

$$\det(sI - A) = 0 \tag{2.36}$$

where $\boldsymbol{I} \in \Re^{n \times n}$ is the $n \times n$ unity matrix and "det" is the determinant of the respective matrix. The number of eigenvalues represents the system's order.

A very important topic in control systems analysis and design is the stability concept. Qualitatively, a dynamic system is described as *stable* if starting the system somewhere near its desired operating point implies that it will stay around that point ever after that. Fundamental definitions for nonlinear systems stability are given in Appendix. Nonlinear systems stability analysis is performed by means of Lyapunov stability theory, also summarized in Appendix, [8].

A linear time-invariant system (2.33) is stable if and only if all its eigenvalues have negative real parts. Linear time-invariant systems are either asymptotically stable, or marginally stable, or unstable as can be seen from the modal decomposition of linear system solution (2.35).

In the case of induction motors, several state space models will be presented in subsequent sections. In all cases, if not otherwise specified, the system's input is the stator voltage vector $u = \underline{u}_s$ and the system's output is the stator current vector $y = \underline{i}_s$, while the state vector x remains to be specified. The generic structural block diagram of the induction machine state space model (2.33) - (2.34) with input $u = \underline{u}_s$ and output $y = \underline{i}_s$ is presented in Figure 2.7.

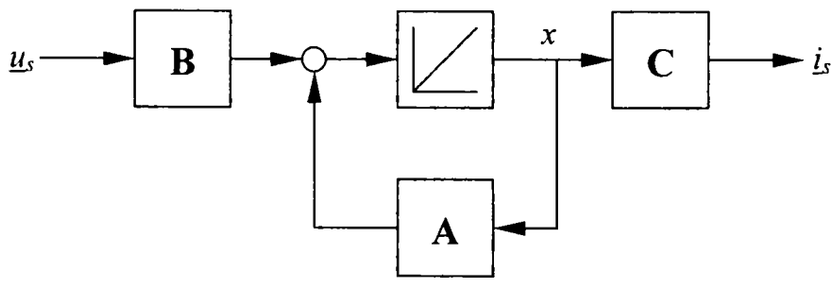

Figure 2.7 General block diagram of the induction machine state space model

2.4.1 The Flux Model

The *flux model* (stator flux-rotor flux model) is obtained by using (2.29) and (2.30) to eliminate the stator and rotor current from (2.15) and (2.16) and incorporating the stator and rotor flux vectors into the system's state vector, $x = [\underline{\Psi}_s, \underline{\Psi}_r]^T$ (superscript "T" denotes the transposition).

The induction motor flux model in arbitrary reference frame is

$$\frac{d}{dt}\underline{\Psi}_s = -(\frac{1}{T_s\sigma} + j\omega_e)\underline{\Psi}_s + \frac{L_m}{L_r T_s \sigma}\underline{\Psi}_r + \underline{u}_s \tag{2.37}$$

$$\frac{d}{dt}\underline{\Psi}_r = \frac{L_m}{L_s T_r \sigma}\underline{\Psi}_s - (\frac{1}{T_r\sigma} + j(\omega_e - \omega_r))\underline{\Psi}_r \tag{2.38}$$

$$\underline{i}_s = \frac{1}{L_s\sigma}\underline{\Psi}_s - \frac{L_m}{L_s L_r \sigma}\underline{\Psi}_r \tag{2.39}$$

where σ is the leakage coefficient

$$\sigma = \frac{L_s L_r - L_m^2}{L_s L_r} \tag{2.40}$$

and $T_s = L_s / R_s$, $T_r = L_r / R_r$ are the stator and rotor time constants, respectively.

The state space model is described by the following complex matrices

$$A = \begin{bmatrix} -(\frac{1}{T_s\sigma} + j\omega_e) & \frac{L_m}{L_r T_s \sigma} \\ \frac{L_m}{L_s T_r \sigma} & -(\frac{1}{T_r\sigma} + j(\omega_e - \omega_r)) \end{bmatrix} \tag{2.41}$$

$$C = \begin{bmatrix} \frac{1}{L_s\sigma} & -\frac{L_m}{L_s L_r \sigma} \end{bmatrix}, \qquad B = [1 \quad 0]^T \tag{2.42}$$

The structural block diagram of the flux model, with space vector variables, is shown in Figure 2.8 [9]. The flux model is a second order complex (fourth order real) linear time variable system. The variable parameter is the rotor speed ω_r represented in Figure 2.8 as an additional input. Equation (2.37) is the *voltage model* and equation (2.38) is the *current model*.

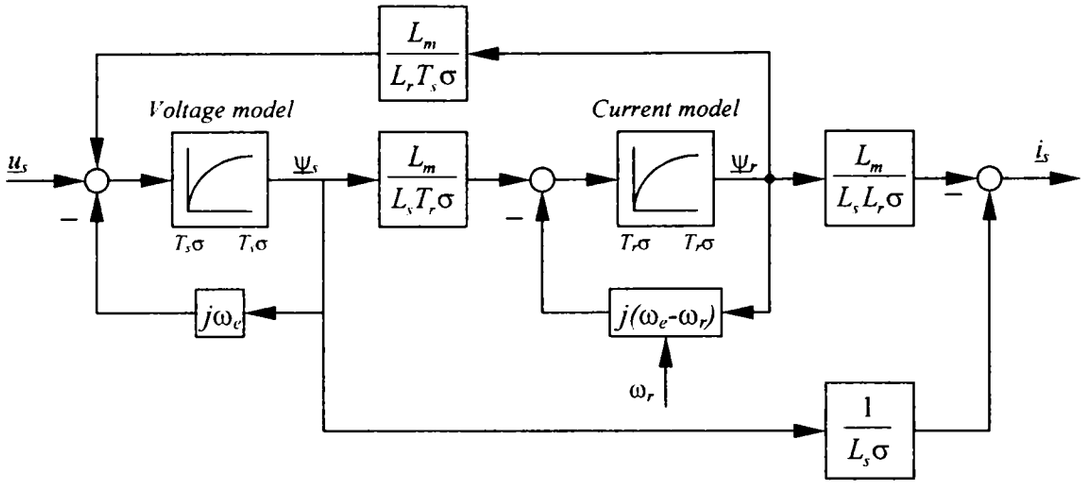

Figure 2.8 Structural block diagram of the induction machine flux model

The system's complex eigenvalues $s_{1,2}$ are solutions of the characteristic equation $\det(sI - A) = 0$, that is

$$\det\begin{bmatrix} s-(\frac{1}{T_s\sigma}+j\omega_e) & -\frac{L_m}{L_r T_s \sigma} \\ -\frac{L_m}{L_s T_r \sigma} & s-(\frac{1}{T_r\sigma}+j(\omega_e-\omega_r)) \end{bmatrix} = 0 \tag{2.43}$$

It is of interest to write the model in particular reference frames where either stator equation (2.37) or rotor equation (2.38) become speed independent, while the output equation (2.39) remains the same.

In stator reference frame, with ω_e=0, the flux model is

$$\frac{d}{dt}\underline{\Psi}_s = -\frac{1}{T_s\sigma}\underline{\Psi}_s + \frac{L_m}{L_r T_s \sigma}\underline{\Psi}_r + \underline{u}_s \tag{2.44}$$

$$\frac{d}{dt}\underline{\Psi}_r = \frac{L_m}{L_s T_r \sigma}\underline{\Psi}_s - (\frac{1}{T_r\sigma} - j\omega_r)\underline{\Psi}_r \tag{2.45}$$

In rotor reference frame, with ω_e=ω_r, the flux model is

$$\frac{d}{dt}\underline{\Psi}_s = -(\frac{1}{T_s\sigma} + j\omega_r)\underline{\Psi}_s + \frac{L_m}{L_r T_s \sigma}\underline{\Psi}_r + \underline{u}_s \tag{2.46}$$

$$\frac{d}{dt}\underline{\Psi}_r = \frac{L_m}{L_s T_r \sigma}\underline{\Psi}_s - \frac{1}{T_r\sigma}\underline{\Psi}_r \tag{2.47}$$

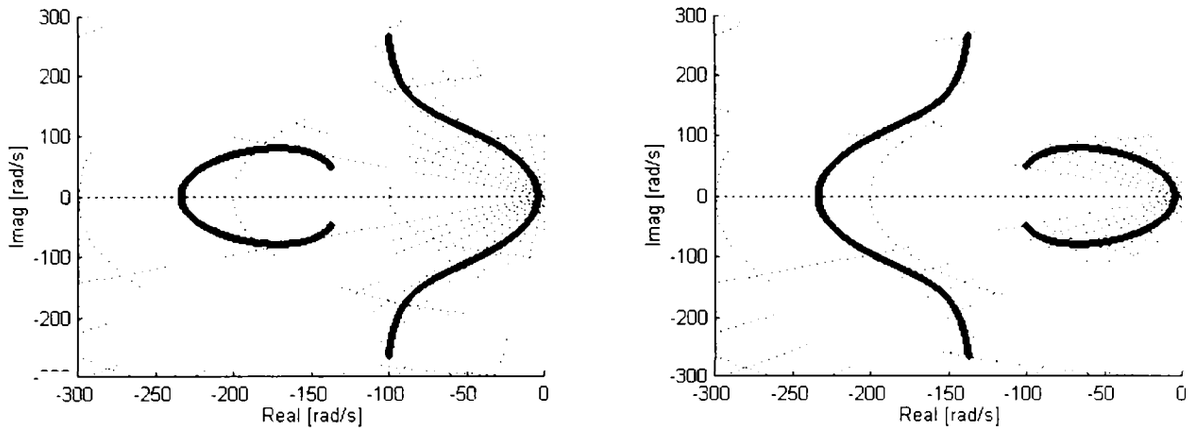

Figure 2.9 Eigenvalues trajectories for stator reference frame – left and rotor reference frame – right, for $\omega_r = 0$ to 314 rad/s

Eigenvalues trajectories of a 4 kW induction motor (Machine 1, Appendix B), with rotor speed as parameter, modified from zero to base value ($\omega_{r,N} = 314$ rad/s), are presented in Figure 2.9 for both stator reference frame (left) and rotor reference frame (right). Figure 2.9 shows the locus of $s_{1,2}$ solutions of equation (2.43) (above the real axis), as well as the locus of their complex conjugates (below the real axis). An important propriety is that the four eigenvalues always add to a constant real value that is independent of the rotor speed [4].

It must be noted that, regardless of the reference system, the model remains time variable, speed dependent. In sensorless drives, when state observers have to be implemented, but the rotor speed is yet unknown, this is an important disadvantage. State observers, based on the flux model as it appears here, have to be speed adaptive observers. On the other hand, the fact, that only flux linkages are present, is an advantage when saturation is included within the model.

2.4.2 The Stator Flux Model

The *stator flux model* contains as states the stator current and the stator flux linkage vectors, $x = [\underline{i}_s, \underline{\Psi}_s]^T$. The rotor current and rotor flux are eliminated from the general model using (2.28) and (2.30).

The induction motor stator flux model in arbitrary reference frame is

$$\frac{d}{dt}\underline{i}_s = -(\frac{1}{T_s\sigma}+\frac{1}{T_r\sigma}+j(\omega_e-\omega_r))\underline{i}_s+\frac{1}{L_s\sigma}(\frac{1}{T_r}-j\omega_r)\underline{\Psi}_s+\frac{1}{L_s\sigma}\underline{u}_s \tag{2.48}$$

$$\frac{d}{dt}\underline{\Psi}_s = -R_s\underline{i}_s - j\omega_e\underline{\Psi}_s+\underline{u}_s \tag{2.49}$$

The state space model is described by the following complex matrices

$$A=\begin{bmatrix} -(\frac{1}{T_s\sigma}+\frac{1}{T_r\sigma}+j(\omega_e-\omega_r)) & \frac{1}{L_s\sigma}(\frac{1}{T_r}-j\omega_r) \\ -R_s & -j\omega_e \end{bmatrix} \tag{2.50}$$

$$C=\begin{bmatrix}1 & 0\end{bmatrix}, \qquad B=\begin{bmatrix}\frac{1}{L_s\sigma} & 1\end{bmatrix}^T \tag{2.51}$$

The structural block diagram of the stator flux model, with space vector variables, is shown in Figure 2.10. Again, the stator flux model is a second order complex (fourth order real) linear time variable system with rotor speed ω_r as adaptive parameter. Equation (2.49) is the *voltage model* and equation (2.48) is the *current model*. The eigenvalues are the same as for flux model (2.43). Indeed, the eigenvalues are an intrinsic characteristic of the physical system and, since the modeled motor remains physically the same, they are unique, regardless of the model – Figure 2.9.

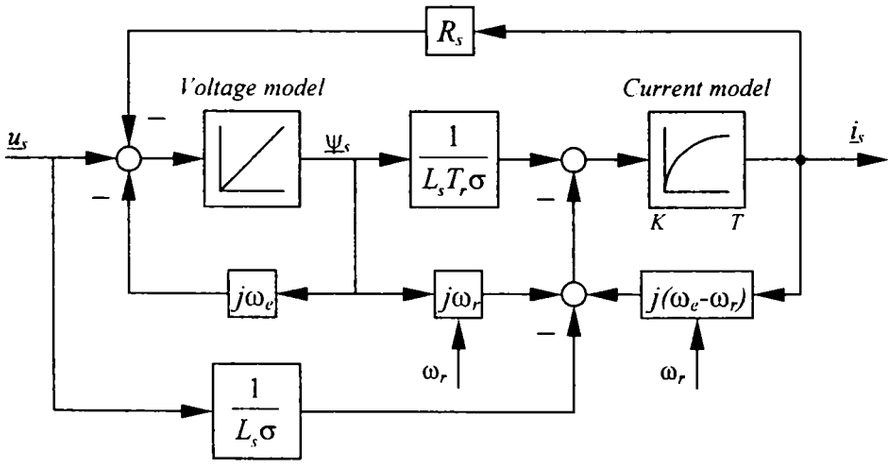

Figure 2.10 Structural block diagram of the induction machine stator flux model

In stator reference frame, with ω_e=0, the stator flux model is

$$\frac{d}{dt}\underline{i}_s = (-\frac{1}{T_s\sigma} - \frac{1}{T_r\sigma} + j\omega_r)\underline{i}_s + \frac{1}{L_s\sigma}(\frac{1}{T_r} - j\omega_r)\underline{\Psi}_s + \frac{1}{L_s\sigma}\underline{u}_s \tag{2.52}$$

$$\frac{d}{dt}\underline{\Psi}_s = -R_s\underline{i}_s + \underline{u}_s \tag{2.53}$$

In *stator flux reference frame*, with ω_e=$\omega_{\psi s}$, the (d, q) frame rotates with stator flux angular speed and for stator flux orientation the flux has only real component $\underline{\Psi}_s$=Ψ_{sd}.

In stator flux reference frame, the stator flux model is

$$\frac{d}{dt}\underline{i}_s = -(\frac{1}{T_s\sigma} + \frac{1}{T_r\sigma} + j(\omega_{\psi s} - \omega_r))\underline{i}_s + \frac{1}{L_s\sigma}(\frac{1}{T_r} - j\omega_r)\underline{\Psi}_s + \frac{1}{L_s\sigma}\underline{u}_s \tag{2.54}$$

$$\frac{d}{dt}\underline{\Psi}_s = -R_s\underline{i}_s - j\omega_{\psi s}\underline{\Psi}_s + \underline{u}_s \tag{2.55}$$

The model (2.54), (2.55) is employed whenever stator flux orientation and/or stator flux control is desired. This is the case for direct torque and flux control. The very simple voltage model (2.53) is the basic equation for simple stator flux estimators. However, as will be discussed later, the precision of flux estimation is very poor if only (2.53) is employed for that purpose.

2.4.3 The Rotor Flux Model

The *rotor flux model* contains as states the stator current and the rotor flux linkage vectors, x = [$\underline{i}_s$, $\underline{\Psi}_r$]^T. The rotor current and stator flux are eliminated from the general model using (2.27) and (2.30).

The induction motor rotor flux model in arbitrary reference frame is

$$\frac{d}{dt}\underline{i}_s = -(\frac{1}{T_s\sigma} + \frac{1-\sigma}{T_r\sigma} + j\omega_e)\underline{i}_s + \frac{L_m}{L_sL_r\sigma}(\frac{1}{T_r} - j\omega_r)\underline{\Psi}_r + \frac{1}{L_s\sigma}\underline{u}_s \tag{2.56}$$

$$\frac{d}{dt}\underline{\Psi}_r = \frac{L_m}{T_r}\underline{i}_s - (\frac{1}{T_r} + j(\omega_e - \omega_r))\underline{\Psi}_r \tag{2.57}$$

The state space model is described by the following complex matrices

$$A=\begin{bmatrix} -(\frac{1}{T_s\sigma}+\frac{1-\sigma}{T_r\sigma}+j\omega_e) & \frac{L_m}{L_sL_r\sigma}(\frac{1}{T_r}-j\omega_r) \\ \frac{L_m}{T_r} & -(\frac{1}{T_r}+j(\omega_e-\omega_r)) \end{bmatrix} \tag{2.58}$$

$$C=\begin{bmatrix}1 & 0\end{bmatrix}, \qquad B=\begin{bmatrix}\frac{1}{L_s\sigma} & 0\end{bmatrix}^T \tag{2.59}$$

The structural block diagram of the rotor flux model, with space vector variables, is shown in Figure 2.11. Equation (2.56) is the *voltage model* and equation (2.57) is the *current model*. Once more, the stator flux model is a second order complex (fourth order real) linear time variable system with rotor speed ω_r as adaptive parameter.

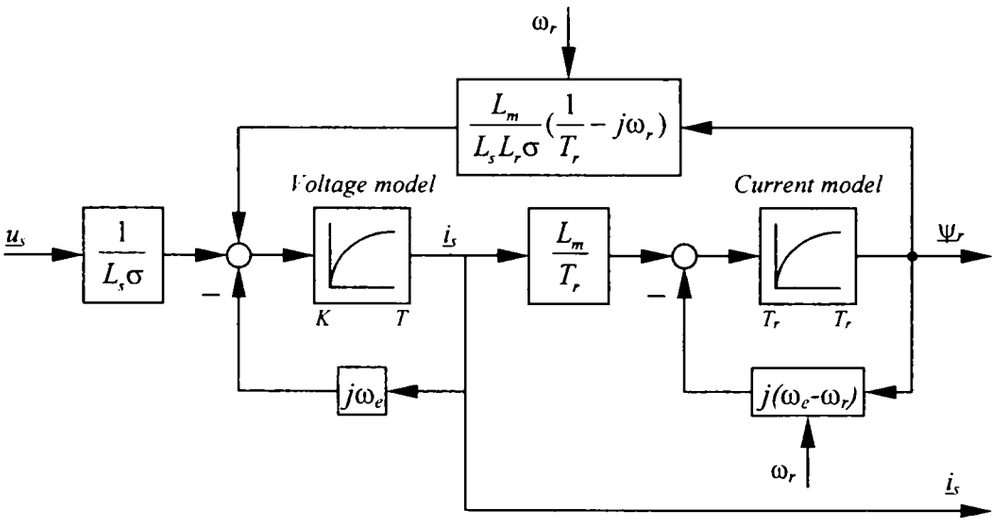

Figure 2.11 Structural block diagram of the induction machine rotor flux model

In stator reference frame, with ω_e=0, the rotor flux model is

$$\frac{d}{dt}\underline{i}_s=-\frac{1}{L_s\sigma}(R_s+\frac{L_m^2}{L_rT_r})\underline{i}_s+\frac{L_m}{L_sL_r\sigma}(\frac{1}{T_r}-j\omega_r)\underline{\Psi}_r+\frac{1}{L_s\sigma}\underline{u}_s \tag{2.60}$$

$$\frac{d}{dt}\underline{\Psi}_r=\frac{L_m}{T_r}\underline{i}_s+(j\omega_r-\frac{1}{T_r})\underline{\Psi}_r \tag{2.61}$$

In *rotor flux reference frame*, with $\omega_e=\omega_{\psi r}$, the rotor flux model is

$$\frac{d}{dt}\underline{i}_s = -(\frac{1}{T_s\sigma}+\frac{1-\sigma}{T_r\sigma}+j\omega_{\psi r})\underline{i}_s+\frac{L_m}{L_sL_r\sigma}(\frac{1}{T_r}-j\omega_r)\underline{\psi}_r+\frac{1}{L_s\sigma}\underline{u}_s \tag{2.62}$$

$$\frac{d}{dt}\underline{\psi}_r = \frac{L_m}{T_r}\underline{i}_s-(\frac{1}{T_r}+j(\omega_{\psi r}-\omega_r))\underline{\psi}_r \tag{2.63}$$

where $\omega_{\psi r}$ is the rotor flux vector angular speed.

The rotor flux model is employed whenever rotor flux orientation and/or rotor flux control is desired. This is the case of classical direct and indirect vector control. The current model (2.61) is used for rotor flux estimation, provided that the rotor speed is known. In rotor flux orientation ($\underline{\psi}_r = \psi_{rd}$), (2.63) is also used for rotor flux estimation and to calculate the rotor flux slip speed ω_s

$$\omega_s = \omega_{\psi r}-\omega_r = \frac{L_m}{T_r}\cdot\frac{i_{sq}}{\psi_{rd}} \tag{2.64}$$

All state space models presented so far do not contain the rotor current as state variable. The reason is, that in most cases, the rotor current is not accessible for measurements and is disregarded. However, when wound rotor motors are used, for example in dual feed motors, adequate models, based on rotor current measurement, can be developed in a similar way.

2.4.4 Models Including Saturation

In previous sections the magnetic nonlinearity has been neglected. In the general induction machine model, the flux-current relations (2.17) and (2.18) are linear with constant inductances. In this kind of linear modeling, the iron of both the stator and the rotor is assumed to be of negligible reluctance. The main inductance L_m remains to be inversely proportional with the air gap reluctance and is mostly influenced by the length of the air gap. In practical design, it would generally be inefficient to operate at maximum flux levels, which would produce negligible iron reluctance. A considerable increase in torque output can be achieved for a given machine frame by operating at flux densities in the stator and rotor for which the iron

reluctances are significant in comparison with the air gap reluctance. Thus, considering the effects of magnetic saturation would bring an improvement in the machine model [10]-[12].

It is assumed first that the saturation is predominantly dependent on the radially directed air gap flux and the leakage fluxes have a negligible effect on saturation. This implies that the *B/H* curves are functions of the resultant magnetizing current i_m only. The effect of main path magnetic saturation is associated with the main inductance L_m, while the leakage inductances are considered constant [10], [12].

The *magnetization functions* represent the flux-current functions $\psi_m(i_m)$ and the magnetization (main) flux vector can be obtained from tests in the form

$$\underline{\Psi}_m = L_m(i_m)\underline{i}_m \tag{2.65}$$

where the magnetizing current vector is $\underline{i}_m = \underline{i}_s + \underline{i}_r$ and i_m is its magnitude.

In this case L_m is current dependent and incorporates the main-path saturation effects. It can be determined from the same tests either as a function of magnetizing current magnitude, as in (2.65), or as a function of main flux magnitude ψ_m.

The stator and rotor inductances L_s and L_r are

$$L_s(i_m) = L_m(i_m) + L_{s\sigma} \tag{2.66}$$

$$L_r(i_m) = L_m(i_m) + L_{r\sigma} \tag{2.67}$$

Recalling the general model (2.15) to (2.18) and replacing (2.66) and (2.67), the general induction machine model including saturation effects is

$$\underline{u}_s = R_s\underline{i}_s + \frac{d\underline{\Psi}_s}{dt} + j\omega_e\underline{\Psi}_s \tag{2.68}$$

$$\underline{0} = R_r\underline{i}_r + \frac{d\underline{\Psi}_r}{dt} + j(\omega_e - \omega_r)\underline{\Psi}_r \tag{2.69}$$

$$\underline{\Psi}_s = L_s(i_m)\underline{i}_s + L_m(i_m)\underline{i}_r \tag{2.70}$$

$$\underline{\Psi}_r = L_r(i_m)\underline{i}_r + L_m(i_m)\underline{i}_s \tag{2.71}$$

The equivalent circuit of the saturated induction machine is shown in Figure 2.12 where $L_{mt}(i_m)$ is the transient magnetizing inductance defined as

$$L_{mt}(i_m) = \frac{d\psi_m}{di_m} \tag{2.72}$$

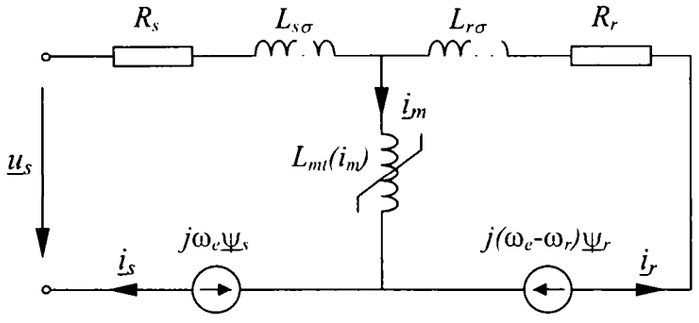

Figure 2.12 Induction machine equivalent circuit including saturation effects

It is evident that the saturated model is almost identical with the linear model, with the only difference that the main inductance is function of the magnetizing current. In the same way as the rotor speed is, the inductances are now time variable parameters and the model is linear time variable. State space modeling remains entirely the same with the difference that any controller or observer based on those models has to be speed and inductance adaptive. The inductances adaptation law is (2.66) and (2.67).

From the vector control perspective, however, (2.65) is not adequate because, in general, the rotor current is not measured or estimated. The control quantities are the torque and flux, (stator, rotor or main flux). In general, that flux is kept constant or is slowly modified for high speed operation and its value is known at any moment by the control system. It is, thus, advantageous to determine the main, stator and rotor inductances as functions of the main flux magnitude ψ_m.

$$L_m(\psi_m) = \frac{\Psi_m}{i_m} \tag{2.73}$$

$$L_s(\psi_m) = L_m(\psi_m) + L_{s\sigma} \tag{2.74}$$

$$L_r(\psi_m) = L_m(\psi_m) + L_{r\sigma} \tag{2.75}$$

Now, the flux-current equations are

$$\underline{\Psi}_s = L_s(\psi_m)\underline{i}_s + L_m(\psi_m)\underline{i}_r \tag{2.76}$$

$$\underline{\Psi}_r = L_r(\psi_m)\underline{i}_r + L_m(\psi_m)\underline{i}_s \tag{2.77}$$

In practice, (2.73) is approximated by ratios of polynomials, by exponentials, or can be memorized as a look-up table with linear interpolation between points [10].

The model presented so far assumed that the leakage fluxes have a negligible effect on the state of saturation in the rotor and stator iron because these fluxes are mainly circumferentially directed across the tooth tips, while the main flux is radially directed across the air gap. In highly saturated machines this assumption is incorrect.

In fact, the flux densities in the stator teeth and yoke are dependent primarily on the total stator flux linkage that results from the air gap flux plus the leakage flux. Similarly, the flux density in the rotor iron depends on the rotor flux linkage that is derived from the air gap flux minus the effect of the rotor leakage flux. The additional magnetizing current i_{si} required by the stator iron is mainly dependent on the stator flux linkage ψ_s and is structurally modeled by means of a nonlinear inductance $L_{si}(\psi_s)$. Saturation in the rotor iron is similarly dependent on the rotor flux linkage ψ_r and is represented by the nonlinear inductance $L_{ri}(\psi_r)$. The main L_m inductance remains linear and accounts only for the air gap reluctance.

Typical curves for $L_{si}(\psi_s)$ and $L_{ri}(\psi_r)$ are presented in Figure 2.13 [11]. The equivalent circuit including these elements is presented in Figure 2.14.

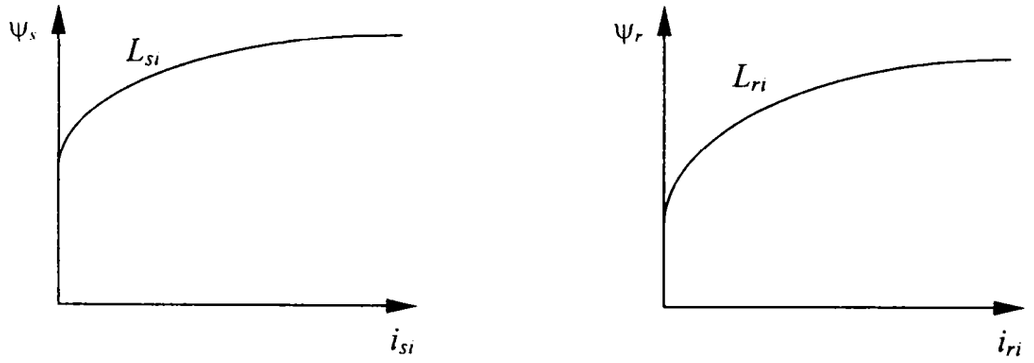

Figure 2.13 Typical saturation characteristics $L_{si}(\psi_s)$ - left and $L_{ri}(\psi_r)$ - right

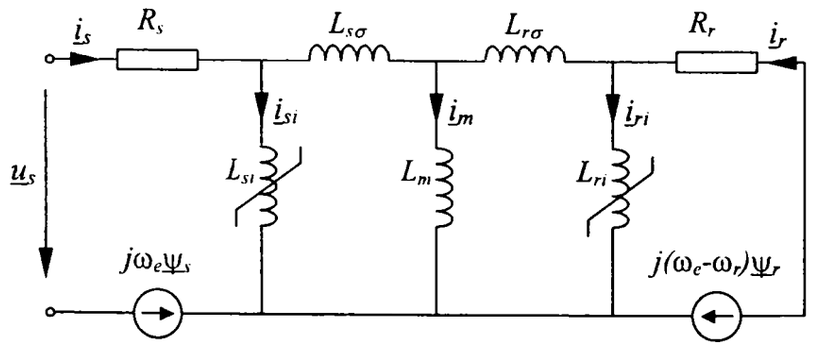

Figure 2.14 Equivalent circuit of highly saturated induction machine

The leakage inductances $L_{s\sigma}$ and $L_{r\sigma}$ account for the leakage flux that is present in air and nonmagnetic parts: end windings connections leakage, plus slot leakage, plus differential leakage. They have the same name and the same significance with leakage inductances in Figure 2.4, where the iron permeability was considered infinite and, the iron reluctance was neglected. In Figure 2.14, the iron effects are accounted for by $L_{si}(\psi_s)$ and $L_{ri}(\psi_r)$. Obviously, diagram 2.14 reduces to 2.4 when L_{si} and L_{ri} are removed, that is, when the iron permeability is considered infinite.

For any instantaneous values of winding currents, the flux linkages may still be represented by their fundamental space vectors in spite of magnetic saturation.

$$\underline{\Psi}_s = L_{si}(\psi_s)\underline{i}_s \tag{2.78}$$

$$\underline{\Psi}_r = L_{ri}(\psi_r)\underline{i}_r \tag{2.79}$$

$$\underline{\Psi}_g = L_m \underline{i}_m \tag{2.80}$$

where $\underline{\Psi}_g$ is the air gap flux vector.

From Figure 2.14, the flux-current equations are obtained as follows

$$\underline{\Psi}_s(1+\frac{L_s}{L_{si}}) = L_s\underline{i}_s + L_m\underline{i}_r - \frac{L_m}{L_{ri}}\underline{\Psi}_r \tag{2.81}$$

$$\underline{\Psi}_r(1+\frac{L_r}{L_{ri}}) = L_r\underline{i}_r + L_m\underline{i}_s - \frac{L_m}{L_{si}}\underline{\Psi}_s \tag{2.82}$$

where $L_s = L_m + L_{s\sigma}$ and $L_r = L_m + L_{r\sigma}$ are constant inductances.

After some simple manipulations, the currents are

$$\underline{i}_s = \frac{L_r^*\underline{\Psi}_s - L_m\underline{\Psi}_r}{L_sL_r - L_m^2} \tag{2.83}$$

$$\underline{i}_r = \frac{L_s^*\underline{\Psi}_r - L_m\underline{\Psi}_s}{L_sL_r - L_m^2} \tag{2.84}$$

where $L_s^* = L_s + (L_sL_r - L_m^2)/L_{ri}$ and $L_r^* = L_r + (L_sL_r - L_m^2)/L_{si}$.

The similarity with (2.29) and (2.30) is evident and now (2.83) and (2.84) can be used to eliminate two variables from the general model and to determine the state space models, in the same way as (2.17) and (2.18) were used before. In this case only

L_s^* and L_r^* are time dependent, while the other inductances are constant. All considerations regarding the state space models remain the same.

For example, the flux model of the highly saturated induction machine is

$$\frac{d}{dt}\underline{\Psi}_s = -(\frac{L_r^*}{L_r T_s \sigma} + j\omega_e)\underline{\Psi}_s + \frac{L_m}{L_r T_s \sigma}\underline{\Psi}_r + \underline{u}_s \tag{2.85}$$

$$\frac{d}{dt}\underline{\Psi}_r = \frac{L_m}{L_s T_r \sigma}\underline{\Psi}_s - (\frac{L_s^*}{L_s T_r \sigma} + j(\omega_e - \omega_r))\underline{\Psi}_r \tag{2.86}$$

$$\underline{i}_s = \frac{L_r^*\underline{\Psi}_s - L_m\underline{\Psi}_r}{L_s L_r - L_m^2} \tag{2.87}$$

2.4.5 Models Including Core Losses

Core losses, together with saturation, are the main effects of non-ideal nature of the magnetic core. In general, in vector control literature, core losses are almost always neglected, although they account for a significant part of the total losses in induction motors and their omission can cause the loss of decoupled torque and flux control.

The common approach in steady state analysis of induction machine is to model the core looses with an equivalent resistance. In induction machines, most of the core loss occurs in stator and it is assumed, for simplicity, that core losses are concentrated in stator only. The core losses are modeled by a short-circuited, fictive stator winding, with stator referred resistance R_{Fe} and leakage inductance $L_{Fe\sigma}$ [10], [13]. There is no need for a similar rotor winding provided that the above assumption holds.

The equations that describe the core loss winding are

$$\underline{0} = R_{Fe}\underline{i}_{Fe} + L_{Fe\sigma}\frac{d\underline{i}_{Fe}}{dt} + \frac{d\underline{\Psi}_m}{dt} + j\omega_e\underline{\Psi}_m \tag{2.88}$$

$$\underline{i}_m - \underline{i}_{Fe} = \underline{i}_s + \underline{i}_r \tag{2.89}$$

where the magnetizing flux $\underline{\Psi}_m = L_m(i_m)\underline{i}_m$ includes the saturation effects as in (2.65) and $\underline{i}_{Fe}$ is the core loss current.

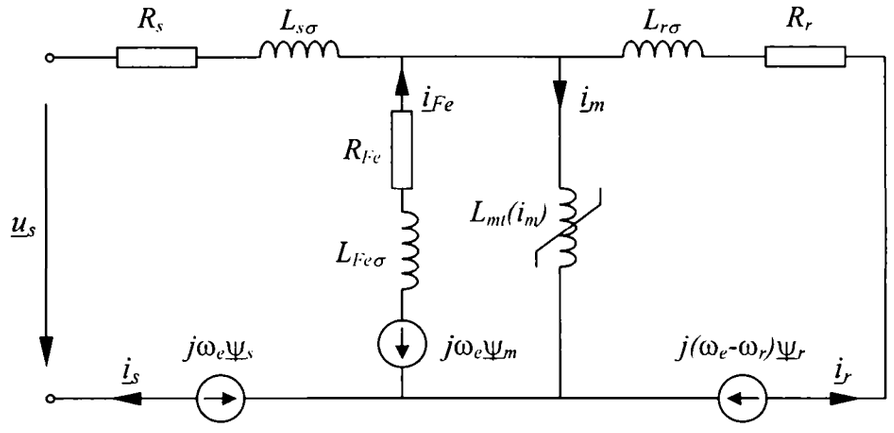

Figure 2.15 Induction machine equivalent circuit including core losses and saturation

The space vector equivalent circuit of the induction machine, including core losses and saturation effects, is shown in Figure 2.15.

The leakage inductance of the core loss winding, $L_{Fe\sigma}$, is very small, in general $T_{Fe} = R_{Fe} / L_{Fe\sigma} < 0.003\ s$ and, at the same time, adds certain unnecessary complexity to the model [13]. Therefore, it can be neglected. In this case, the core loss winding model is

$$\underline{0} = R_{Fe}\underline{i}_{Fe} + \frac{d\underline{\Psi}_m}{dt} + j\omega_e\underline{\Psi}_m \tag{2.90}$$

Eliminating the core loss current $\underline{i}_{Fe}$ from (2.88)-(2.90) and adding the stator and rotor equations, the general model of the induction machine, including core losses and saturation effects, is

$$\underline{u}_s = R_s\underline{i}_s + \frac{d\underline{\Psi}_s}{dt} + j\omega_e\underline{\Psi}_s \tag{2.91}$$

$$\underline{0} = R_r\underline{i}_r + \frac{d\underline{\Psi}_r}{dt} + j(\omega_e - \omega_r)\underline{\Psi}_r \tag{2.92}$$

$$\underline{0} = -R_{Fe}(\underline{i}_s + \underline{i}_r) + \frac{d\underline{\Psi}_m}{dt} + (j\omega_e + \frac{R_{Fe}}{L_m})\underline{\Psi}_m \tag{2.93}$$

$$\underline{\Psi}_s = L_{s\sigma}\underline{i}_s + \underline{\Psi}_m \tag{2.94}$$

$$\underline{\Psi}_r = L_{r\sigma}\underline{i}_r + \underline{\Psi}_m \tag{2.95}$$

where, for clarity, L_m was used instead of $L_m(\psi_m)$, but it will be recalled that L_m is a variable parameter.

The model represents a third order complex (sixth order real) linear time variable dynamic system. Determination of state space models, using the same procedure as before, is straightforward.

For example, the flux model, with stator, rotor and main fluxes as independent states, $x = [\underline{\Psi}_s, \underline{\Psi}_r, \underline{\Psi}_m]^T$, input $\underline{u}_s$ and output $\underline{i}_s$, is

$$\frac{d}{dt}\underline{\Psi}_s = -(\frac{R_s}{L_{s\sigma}} + j\omega_e)\underline{\Psi}_s + \frac{R_s}{L_{s\sigma}}\underline{\Psi}_m + \underline{u}_s \tag{2.96}$$

$$\frac{d}{dt}\underline{\Psi}_r = -(\frac{R_r}{L_{r\sigma}} + j(\omega_e - \omega_r))\underline{\Psi}_r + \frac{R_r}{L_{r\sigma}}\underline{\Psi}_m \tag{2.97}$$

$$\frac{d}{dt}\underline{\Psi}_m = \frac{R_{Fe}}{L_{s\sigma}}\underline{\Psi}_s + \frac{R_{Fe}}{L_{r\sigma}}\underline{\Psi}_r + (R_{Fe}(\frac{1}{L_{s\sigma}} + \frac{1}{L_{r\sigma}} - \frac{1}{L_m}) - j\omega_e)\underline{\Psi}_m \tag{2.98}$$

$$\underline{i}_s = \frac{1}{L_{s\sigma}}(\underline{\Psi}_s - \underline{\Psi}_m) \tag{2.99}$$

The system's complexity has increased, but the model can be easily implemented within a digital control system using the Digital Signal Processors available today.

2.5 The Electromagnetic Torque

The induction machine is an electromechanical energy converter. The active power flowing into an *n* phase induction machine is clearly the instantaneous product of the voltages across and currents through the *n* phases of the machine. Considering the three phase short-circuited rotor machine, the power and torque are as follows.

The *apparent power S*, in terms of space vectors, is

$$S = \frac{3}{2}\underline{u}_s \underline{i}_s^* = P + jQ \tag{2.100}$$

where superscript "*" denotes the complex conjugate.

The *active power P*, flowing into machine, is the real component of *S*.

$$P = \frac{3}{2}(u_{sd}i_{sd} + u_{sq}i_{sq}) \tag{2.101}$$

The *reactive power Q* is the imaginary component of *S*.

$$Q = \frac{3}{2}(u_{sq}i_{sd} - u_{sd}i_{sq}) \tag{2.102}$$

The *electromagnetic power* P_{em} is the one that accounts for energy conversion

$$P_{em} = \frac{3}{2}\omega_r L_m \operatorname{Im}(\underline{i}_s \underline{i}_r^*) \tag{2.103}$$

The electromagnetic torque is the electromagnetic power divided by the mechanical rotor speed $\omega_m=\omega_r/p$

$$T_e = \frac{3}{2} pL_m \operatorname{Im}(\underline{i}_s \underline{i}_r^*) \tag{2.104}$$

Apart from equation (2.19) that defines the torque in terms of stator current and stator flux, several other forms are possible. Two torque definitions of interest, which can be easily derived from (2.19), (2.29) and (2.31), are given below.

$$T_e = \frac{3}{2} p \frac{L_m}{L_r}(\psi_{rd}i_{sq} - \psi_{rq}i_{sd}) \tag{2.105}$$

$$T_e = \frac{3}{2} p \frac{L_m}{L_s L_r \sigma}(\psi_{sq}\psi_{rd} - \psi_{sd}\psi_{rq}) \tag{2.106}$$

References

[1] I. Boldea, S.A. Nasar, *Vector control of a.c. drives.*, C.R.C. Press Florida, Boca Raton, Ann Arbor, London, Tokyo, 1992.

[2] I. Boldea, S.A. Nasar, *Electric machines: dynamics and control.*, CRC Press Florida, Boca Raton, Ann Arbor, London, Tokyo, 1992.

[3] I. Boldea, S.A. Nasar, *Electric Drives.*, CRC Press Boca Raton, London, New York, Washington, D.C., 1999.

[4] D.W. Novotny, T.A. Lipo, *Vector Control and Dynamics of AC Drives.*, Clarendon Press - Oxford, Oxford University Press, New York, 1996.

[5] A.M. Trzynadlowski, *The field orientation principle in control of induction motors.*, Kluwer Academic Press, Boston, 1994.

[6] Bimal K. Bose (editor) et al., *Power Electronics and Variable Frequency Drives. Technology and Applications.*, IEEE Press, 1997.

[7] Karl J. Astrom, Bjorn Wittenmark, *Computer Controlled Systems: Theory and Design.*, Prentice Hall International, Englewood Cliffs, New Jersey, 1984.

[8] Jean-Jacques E. Slotine, Weiping Li, *Applied Nonlinear Control.*, Prentice Hall, Englewood Cliffs, New Jersey, 1991

[9] J. Holtz, *The Representation of AC Machine Dynamics by Complex Signal Flow Graphics.*, IEEE Transactions on Industrial Electronics, vol. 42, no. 3, June 1995, pp. 263-271.

[10]I. Boldea, S.A. Nasar, *Unified treatment of core losses and saturation in the orthogonal-axis model of electric machines.*, IEE Proceedings, vol. 134, Pt. B, No.6, November 1987, pp. 355-363.

[11]G.R. Slemon, *Modeling of Induction Machines for Electric Drives.*, IEEE Transactions on Industry Applications, vol. 25, no. 6, Nov./Dec. 1989, pp. 1126-1131.

[12]E. Levi, V. Vuckovic, *Field-Oriented Control of Induction Machines in the Presence of Magnetic Saturation.* Electric Machines and Power Systems, vol. 16, no. 2, March/April 1989, pp. 133-147.

[13]Emil Levi, *Rotor Flux Oriented Control of Induction Machines Considering the Core Loss.* Electric Machines and Power Systems, vol. 24, no. 1, Jan./Feb. 1996, pp. 37-50.

3 VOLTAGE SOURCE INVERTER MODEL

3.1 Solid State Inverters

The solid state switching inverter is a power electronic DC-to-AC converter, that is, a static device that transfers energy between a DC source and an AC load. The process of conversion is called inversion and the inverter produces approximately sinusoidal voltage and currents, of controllable magnitude and frequency, which are used to drive an AC motor at variable speed. The control of the energy flow between the DC source and the AC load is achieved in a quantized fashion, by means of a pulse width modulation function [1]-[4].

Inverters for motion control applications are subjected to operational and parametric conditions fixed by the electrical machines that are connected to these converters as loads. Regardless of type, electric machines have common characteristics that are important considerations for power converter topology, modulation functions and control, as follows:

- The load is inductive.
- The load is active; they contain sources of induced electromotive force, EMF.
- The load requires two directions of power and current flow.
- The load is dynamic; it requires large variations in power and direction of power flow, depending on the specific application.

In ASD-s with induction machines the power inverter must accomplish a dual control function: changing the fundamental frequency of the output voltage and adjusting the voltage amplitude. Variation of stator fundamental frequency of an induction machine changes the speed of rotation of the magnetic field in the air gap

and, therefore, also the rotor mechanical speed. In order to maintain the magnetic flux density in the machine unchanged, the adaptation of the stator voltage magnitude directly proportional to the frequency is mandatory whenever the machine is operated below base speed. For high-speed applications, when the machine is operated in field weakening region, the voltage is constant and only the frequency is increased.

From the point of view of the DC power supply, two basic inverter classes, which are totally different in their behavior, are currently in use:

- The *Voltage Source Inverter* (VSI) is supplied from a constant DC voltage bus and generates a well-defined switched voltage waveform. The resulting load current waveform is then governed by the motor load and speed.
- The *Current Source Inverter* (CSI) is supplied from a constant DC current bus and generates a well-defined switched current waveform. The resulting load voltage waveform is now governed by the motor load and speed.

Both types can be operated in either *six-step* mode or in *Pulse Width Modulation* (PWM) mode, with the later being more advantageous and widely used in ASD-s. Each type has advantages and limitations. The CSI is robust in operation and reliable due to insensitivity to short circuits and a noisy environment, but needs symmetrical devices as far as blocking voltage is concerned. The VSI is more prone to reliability problems in a harsh environment, with output short-circuit and simultaneous conduction of two devices in one leg being the most dangerous, but does not need reverse blocking devices, favoring the modern devices such as IGBT-s and GTO-s.

Traditionally, the CSI has found widespread practical application in large power industrial and traction drives, while the VSI has been used for low and medium power applications. However, over the past years, the current controlled voltage source PWM inverter has gradually been superseding the CSI technology, especially since the availability of GTO-s extended the applicability of turn-off devices in VSI-s up to the highest power levels.

In most ASD-s the power is obtained from the constant frequency AC supply grid. This requires the use of an AC to DC converter and a DC link circuit. In VSI-s the DC bus is maintained voltage stiff by the use of a large capacitor. From the line converter perspective, two basic VSI topologies, shown in Figure 3.1, are used today.

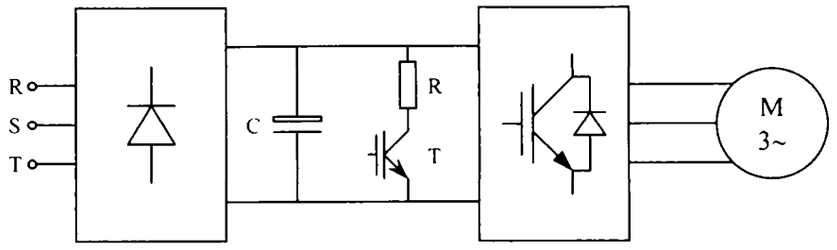

a. Diode rectifier – PWM inverter

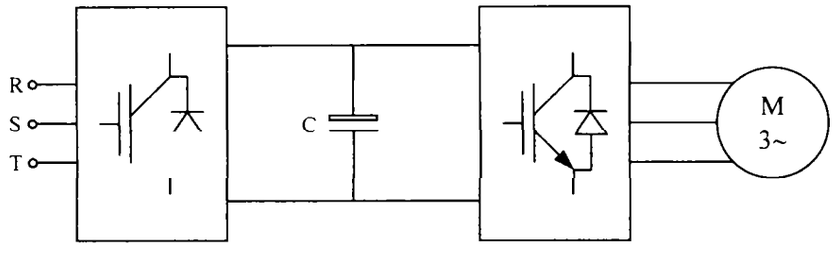

b. Back-to-back PWM converter

Figure 3.1 Modern voltage source inverter topologies

While the PWM inverter itself is always bidirectional, the nonregenerative front-end diode rectifier in Figure 3.1.a is a cost-effective solution for low power drives. In such drives, in order to eliminate the energy returned from the motor side, a power dissipation circuit, as a chopper in series with a power resistor, is connected to the DC bus. The back-to-back system in Figure 3.1.b gives regeneration capability with the price of increased complexity. The topology in this system can be either two level or multi level. The three-level inverter, used in high voltage and high power applications, gives better harmonic performance without increasing the switching frequency. Unity power factor operation with sinusoidal line currents is also possible with the back-to-back converter.

In CSI-s, the DC bus is maintained current stiff by the use of a large inductor. Figure 3.2 shows two basic topologies of CSI. The thyristor phase-controlled rectifier-inverter in Figure 3.2.a is widely used today. High power, load-commutated thyristor inverters for synchronous motor drives, where machines operate at leading power factor, are very popular in industry. For induction motor drives, the same converter has been used with a capacitor bank at machine terminals, for load commutation. Current feed, auto-sequential commutated inverters have been used for induction motor drives, but recently, with the advent of GTO technology, they have become obsolete.

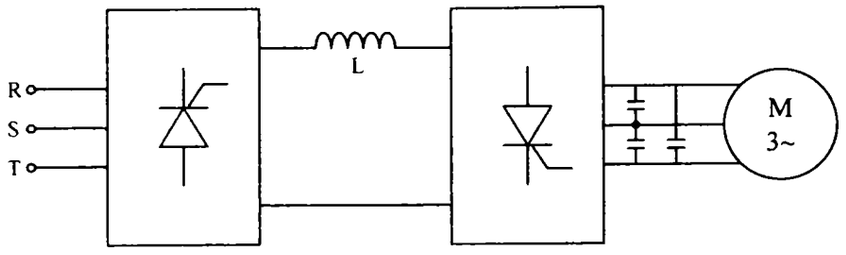

a. Thyristor phase-controlled rectifier-inverter

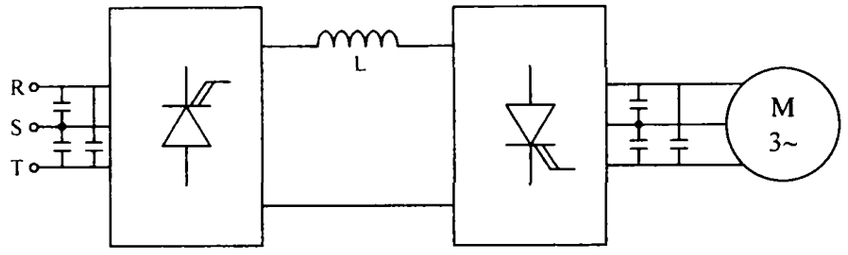

b. Back-to-back PWM converter

Figure 3.2 Modern current source inverter topologies

The back-to-back PWM current-source converter in Figure 3.2.b, which uses self-controlled reverse blocking devices (GTO-s), has essentially the same features as the voltage source topology presented in Figure 3.1.b. However, the voltage source topology is superior and far more popular in industrial drive applications.

Traditional converters with self-controlled devices use hard switching. Soft switching technology at zero current and/or zero voltage has been applied to inverters. It improves the converter's efficiency by minimizing or eliminating the device switching loss. Soft switching converters can be classified as resonant DC link, resonant DC pole and high frequency AC link systems. However, in spite of potential advantages, the need of extra components and control complexity are the main reasons that limited the expansion of resonant technology in industrial ASD-s.

This thesis is devoted to direct torque control of induction motor ASD-s supplied by standard three phase voltage source inverters shown in Figure 3.1. A description of the standard VSI, together with the PWM strategy employed, the inverter nonlinearity compensation technique and other related topics are presented in the following sections of this chapter.

3.2 The Voltage Source Inverter

The structure of the basic three phase voltage source inverter (VSI), with insulated gate bipolar transistors as switching devices, is shown in Figure 3.3. The diagram includes the inverter, the three phase active load and the DC link capacitor that provides a path for the rapidly changing currents drawn by the inverter. In general, the capacitor is of appreciable size (thousands of microfarads) and is a major cost item in the system. Sometimes, an inductive reactance is also present in the DC link circuit, in order to smooth the current peaks. The load is an induction machine modeled by its transient impedance in series with the counter EMF voltage.

The three phase inverter bridge is composed from three "legs", a, b, c, each one containing two switching power devices and two return current diodes. Diodes must be provided in order to allow for an alternative path for the inductive load current that continues to flow when the power devices are turned off. At present, the choice for power devices is: Insulated Gate Bipolar Transistors (IGBT), MOS Field Effect Transistors (MOSFET), Bipolar Junction Transistors (BJT), Gate Turn Off Thyristors (GTO), MOS Controlled Thyristors (MCT) and fast Thyristors.

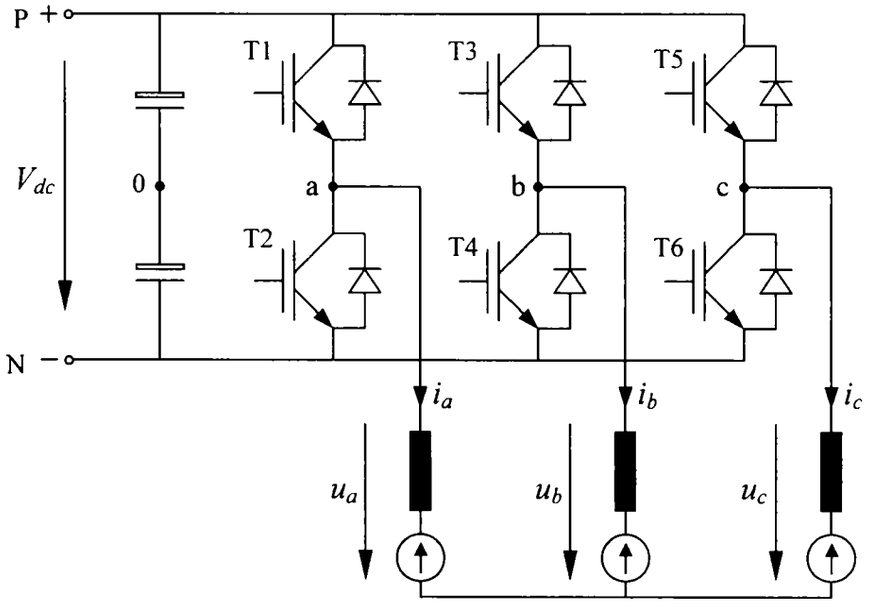

Figure 3.3 The voltage source inverter

In order to simplify and linearize the inverter model, the following hypotheses are assumed first:

- The DC link voltage V_{dc} is considered constant or slowly variable. In general the inverter switching frequency is much higher than the frequency of the DC link voltage ripples and this assumption is always realistic.
- The power switching devices are assumed identical. The turn on time T_{on} and turn off time T_{off} are the same for each device.
- The power diodes are assumed identical. The reverse recovery current, associated to the diodes turn off process, is neglected.
- The switching process is considered ideal, with rise time, fall time and reverse recovery time incorporated into T_{on} and T_{off} times, respectively.
- The voltage drop on the power devices is neglected if not otherwise specified.
- The dead time is neglected if not otherwise specified.

Inverter's nonlinearities are discussed and taken into account in Section 3.5.

During normal controlled operation, if the dead time is neglected, within each inverter leg, one and only one transistor must be in conduction. Simultaneous conduction of both transistors within one leg produces DC link voltage short-circuit, while simultaneous turn-off disconnects the respective load phase from the power supply. In order to simplify the analysis, it is useful to define the *switching signals* S_a, S_b and S_c as binary numbers that describe the legs' states, as follows: for a certain leg x ($x = a, b, c$), the switching signal $S_x = 1$ if the upper transistor in that leg (T1, T3 or T5, respectively) is on and $S_x = 0$ if the lower transistor in that leg (T2, T4 or T6, respectively) is on.

$$S_x = \begin{cases} 1 & \text{if } T_{2k-1} \text{ is on} \\ 0 & \text{if } T_{2k} \text{ is on} \end{cases} \tag{3.1}$$

where index k is 1, 2, or 3 when x is a, b or c, respectively.

It must be noted that the switching signals have similar waveforms with the gating signals of the upper transistors, respectively, while the binary-negate of the switching signals have the same waveforms as the gating signals of the lower transistors, respectively, if the dead time is neglected.

Employing the switching signals, the instantaneous line-to-line voltages are

$$u_{ab} = V_{dc} \cdot (S_a - S_b) \tag{3.2}$$

$$u_{bc} = V_{dc} \cdot (S_b - S_c) \tag{3.3}$$

$$u_{ca} = V_{dc} \cdot (S_c - S_a) \tag{3.4}$$

The instantaneous phase voltages of the three phase load are

$$u_a = V_{dc} \cdot (S_a - \frac{1}{3}(S_a + S_b + S_c)) \tag{3.5}$$

$$u_b = V_{dc} \cdot (S_b - \frac{1}{3}(S_a + S_b + S_c)) \tag{3.6}$$

$$u_c = V_{dc} \cdot (S_c - \frac{1}{3}(S_a + S_b + S_c)) \tag{3.7}$$

if the zero sequence voltage $u_0 = u_a + u_b + u_c$ is zero.

The voltage space vector obtained from (3.5) – (3.7) and (2.2) – (2.5) is

$$\underline{V} = V_\alpha + jV_\beta \tag{3.8}$$

$$V_\alpha = V_{dc}(S_a - \frac{1}{3}(S_a + S_b + S_c)) \tag{3.9a}$$

$$V_\beta = V_{dc}\frac{1}{\sqrt{3}}(S_b - S_c) \tag{3.9b}$$

Since each switching signal can assume two discrete states, the three-phase VSI can only assume a total of eight distinct and independent physical states (VSI modes). The three phase output voltage associated with each state is regarded as the voltage space vector produced by the VSI, when it is placed in that particular state defined by (S_a, S_b, S_c) triplet. When all switching signals have the same value, (0, 0, 0) or (1, 1, 1), the output voltage is zero and the two associated vectors, $\underline{V}_0$ and $\underline{V}_7$, are called *zero vectors*. In the remaining six modes the instantaneous output of the VSI consist of six *active vectors* equally spaced sixty degrees apart and having constant amplitude of $2 \cdot V_{dc}/3$. In complex notation, the six active voltage vectors are

$$\underline{V}_k = \frac{2}{3}V_{dc} \cdot e^{j(k-1)\frac{\pi}{3}} \qquad k = 1, 2, 3, 4, 5, 6 \tag{3.10}$$

where k is the vector count. The basic voltage vectors, identified as $\underline{V}_k$ (S_a S_b S_c), are illustrated in Figure 3.4.

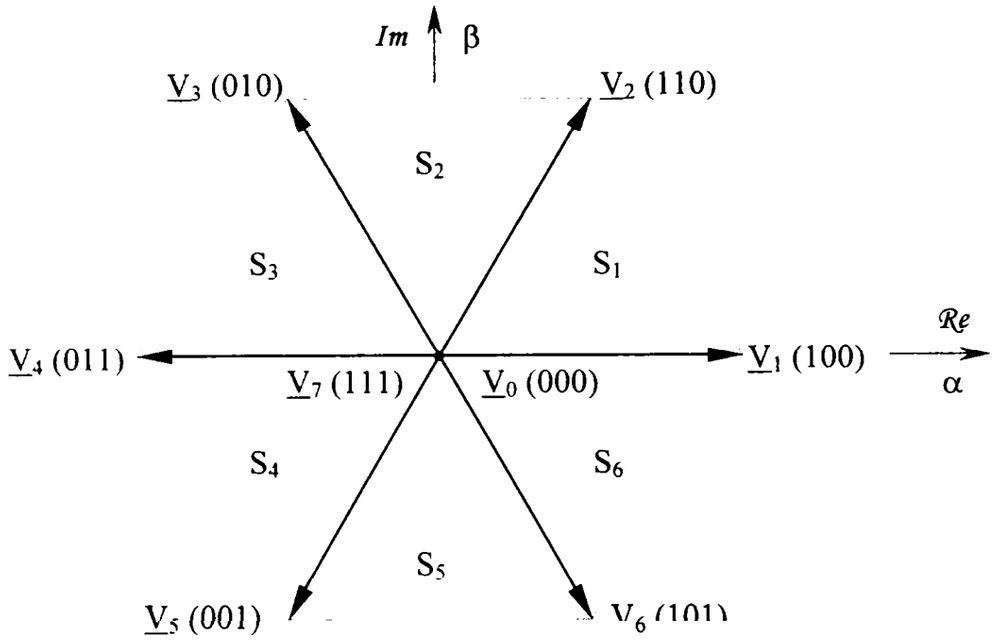

Figure 3.4 Basic voltage vectors of the voltage source inverter

The six active voltage vectors $\underline{V}_k$, k=1…6, define a hexagonal boundary (dotted line in Figure 3.4) which represents the VSI voltage capability, that is the maximum available output voltage when PWM is used. The hexagon dimensions are determined only by the DC kink voltage V_{dc}. The complex plane is divided into six *sectors*, S_1 to S_6 in Figure 3.4, each of these located between two adjacent voltage vectors.

The simplest method for VSI control is the *six-step mode*. This switching strategy is mostly employed for high voltage, high frequency operation, when the entire VSI's voltage capability is needed. Along one fundamental period of the reference voltage, the switching sequence is: $\underline{V}_1$-$\underline{V}_2$-$\underline{V}_3$-$\underline{V}_4$-$\underline{V}_5$-$\underline{V}_6$. The active voltage vectors are successively activated, each for the duration of one sixth of fundamental period. Neither zero vectors, nor modulation techniques are engaged in this process.

Six-step operation has the merit to produce the highest possible output voltage with the lowest switching looses. However, voltage control cannot be achieved in this way. The line-to-line output RMS voltage is $U_{ab\ six-step} = \sqrt{2/3} \cdot V_{dc} = 0.816 \cdot V_{dc}$, always, while the machine phase RMS voltage is $U_{a\ six-step} = \sqrt{2}/3 \cdot V_{dc} = 0.471 \cdot V_{dc}$. Furthermore, the load current is heavily distorted. Although voltage control is not possible, the fundamental frequency still can be modified.

3.3 Pulse Width Modulation Overview

Modern automated industrial applications rely on efficient and fast control of the electric power flow. The electric power conversion is performed by solid state electronic converters that operate exclusively in switched mode. These power converters use fast transitions of electronic switches to convert electrical energy from a power supply into sequences of high frequency voltage or current pulses that represent a target average low frequency output waveform. The actual power flow is controlled by the on/off ratio (duty ratio, or duty cycle) of the respective switches. The process of creating the desired waveform by varying the duty cycle of a sequence of high frequency pulses is called *Pulse Width Modulation* (PWM) and is the basis of all modern power electronic conversion systems [1]-[4].

The switched mode operation is mandatory in order to ensure high efficiency of power conversion. The switching frequency should be high, in order to allow the load, by its low-pass filter characteristic, to attenuate the undesired side effects of discontinuous power flow. On the other side, upper limitations of the switching frequency are imposed by the increased switching losses in power devices and this creates a conflicting situation. Along with the switching capability of the power devices, any PWM strategy involves a tradeoff between the quality of the output current and the amount of switching looses incurred in the converter.

Pulse Width Modulation techniques for VSI have been the subject of considerable research in the past decades [1]-[22]. Over this period, there have been some trends in the development of PWM strategies, including:

- Development of PWM strategies with low harmonic distortion and increased output voltage magnitude for a given switching frequency [5]-[8];
- Identification of the most efficient methods in terms of inverter's losses or with respect to another optimization criteria [9]-[12].
- Efficient PWM integration within modern DSP based drive systems [13]-[15].
- Application of known modulation strategies to new inverter topologies.

In order to examine the theoretical performance of a particular PWM strategy in a specific application, the harmonics, produced in the output voltage and current waveforms by that strategy, switching frequency and modulation depth, must be evaluated. These harmonic effects arrive from two sources: *interference* and *distortion*. These two sources are quite independent and need to be separately evaluated if a full assessment of the PWM performance is to be made [15].

Interference is the corruption of the frequency baseband by the intrusion of the PWM switching frequency sidebands into the baseband. Interference is the result of high frequency switching and is strongly dependent on the PWM strategy and on the low pass filter characteristics of the load.

Distortion is the corruption of the baseband region by nonlinear effects of the VSI and PWM process, operating directly in the baseband, independent of the switching frequency. Distortion is produced by power devices switching time and dead time, by time sampling quantization, reference amplitude quantization, and reference angle quantization effects of the PWM process.

Performance Criteria

Performance criteria provide the means of comparing the qualities of different PWM methods and to support the selection of a certain strategy for a particular application. The most important performance criteria are [3], [4], [9], [10], [15]:

1. Total Harmonic Distortion factor - THD

$$THD = \frac{100}{I_1}\sqrt{\sum_{n=2}^{\infty}(I_n)^2} = 100\sqrt{\left(\frac{I_{rms}}{I_1}\right)^2 - 1} \quad \% \tag{3.11}$$

where I_1 is the RMS value of the fundamental current, I_n is the RMS value of the n^{th} harmonic current and I_{rms} is the RMS value of the entire current waveform.

2. Weighted Total Harmonic Distortion factor - WTHD

$$WTHD = \frac{100}{I_1}\sqrt{\sum_{n=2}^{\infty}\left(\frac{I_n}{n}\right)^2} \quad \% \tag{3.12}$$

WTHD has a first order low pass filter characteristic and is the same as the RMS noise to signal ratio of the overall motor current [15].

3. Distortion factor and current harmonics

The Distortion Factor d, (3.13), is a figure of merit of the PWM strategy with regard to increase of copper losses in the machine due to harmonic current.

$$d = \frac{I_{h\,rms}}{I_{h\,rms\ six-step}} \tag{3.13}$$

where the RMS harmonic current $I_{h\,rms}$ is

$$I_{h\,rms} = \sqrt{\frac{1}{T}\int_0^T (i(t) - i_1(t))^2\,dt} \tag{3.14}$$

and $I_{h\,rms\ six\text{-}step}$ is the harmonic current of same motor operated in the six-step mode.

Harmonic copper losses in the motor are proportional to the square of the harmonic current, $P_{Cu} \approx d^2$, where d^2 is the loss factor. Definition (3.13) values the current distortion of a PWM method independently from the load properties.

4. Harmonic spectrum

With the advent of powerful signal processing tools, it has become a common practice to determine and compare the discrete harmonic amplitude spectrum or the continuous amplitude density spectrum of the most important quantities involved within a motor drive, for different control and modulation strategies. It represents a more detailed and comprehensive description than the global distortion factor d.

5. Maximum modulation index

$$m_{\max} = \frac{U_{1\,\max}}{U_{1\ six-step}} \tag{3.15}$$

where $U_{1\ max}$ is the maximum fundamental RMS voltage obtained with a given PWM scheme and $U_{1\ six-step} = 2 \cdot V_{dc} / \pi$, the fundamental RMS voltage at six-step operation. The maximum modulation index is an important utilization factor of the VSI.

6. Torque harmonics

$$\Delta T = \frac{T_{\max} - T_{av}}{T_N} \tag{3.16}$$

where T_{max} is the maximum torque, T_{av} is the average torque and T_N is the rated torque.

7. Switching frequency and inverter looses

The harmonic distortion on AC side currents reduces almost linearly with increase in switching frequency. However, power devices switching looses increase

proportional to switching frequency. Finding a good balance in this contradictory situation is of paramount practical and economical interest.

Another important issue related to switching frequency is the acoustical noise radiated by a load supplied with switched voltages or currents. It is known that the human ear is most sensitive to frequencies in the 0.5-10 kHz range, with a maximum at about 1-2 kHz. Therefore, increasing the switching frequency above 10 kHz would provide an important environmental improvement.

Although distortion factors were discussed in relation with current harmonics that are of interest in a VSI drive, equations (3.11) to (3.14) may also be employed for voltage harmonics analysis.

Pulse Width Modulation Strategies

A large number of Pulse Width Modulation techniques have been developed and are widely investigated in the literature [1]-[15]. Only a short overview follows.

1. Feedforward PWM Control

Feedforward or open-loop schemes for VSI inject voltages into the motor. They receive as input a reference voltage space vector $\underline{u}_s^*$ and generate a switched three phase voltage $\underline{u}_s$, such that the output fundamental space vector $\underline{u}_{s1}$ equals the reference voltage $\underline{u}_s^*$. The general feedforward PWM topology is presented in Figure 3.5.a.

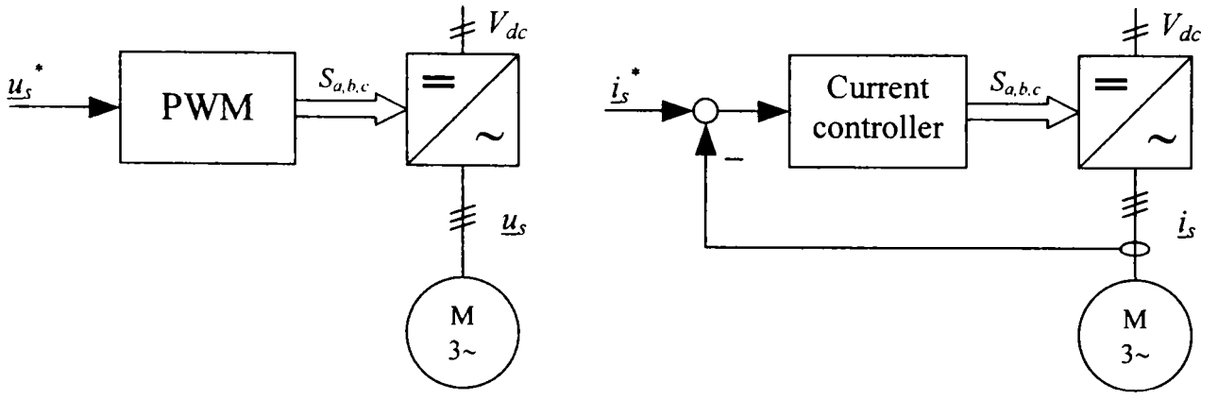

a. Feedforward PWM scheme

b. Feedback PWM scheme

Figure 3.5 Basic PWM topologies

1.1 Carrier based PWM

Carrier based strategies are the most widely used PWM methods. They have, as common characteristic, cycles of constant time duration, during which, each inverter leg assumes two consecutive switching states of opposite voltage polarity. Operation at constant carrier frequency is reflected in the harmonic spectrum by pairs of salient sidebands symmetric about the carrier frequency and about integer multiples of it.

1.1.1 Suboscillation method

The method is based on individual modulators for each of the three phases. The three phase components (u_a^*, u_b^*, u_c^*), of the reference vector $\underline{u_s}^*$, are compared with a triangular, high frequency, constant amplitude carrier signal using three bang-bang comparators (electronic comparators). The one-bit outputs of the three comparators are directly applied to VSI as switching signals S_a, S_b, S_c.

If the reference voltages are sinusoidal, the maximum value of the modulation index, (3.15), is $m_{max} = \pi/4 = 0.785$ and this value is reached at a point where the amplitudes of the reference and the carrier signals become equal. The maximum line to line voltage amplitude in this operating point is $u_{ab} = \sqrt{3} \cdot V_{dc} / 2 = 0.866 \cdot V_{dc}$. For this reason, the method exhibits a poor utilization of the available DC voltage, V_{dc}.

The drawback of low DC voltage utilization ratio can be avoided if distorted reference voltages are used. Such waveforms contain only zero sequence systems (third order harmonics) in addition to the fundamental. If the star point of the load is isolated, no distortions are produced in the machine currents and the fundamental content of the voltage waveform is increased. Two subclasses of distorted reference waveforms, continuous and discontinuous, are identified and widely investigated in literature [3], [4], [9], [10].

The maximum value of the modulation index, which can be obtained with the technique of adding zero sequence components to the reference voltage, without employing overmodulation techniques, is $m_{max} = 0.907$, [3], [4].

Today, the suboscillation method is easily implemented with classical analogue electronic circuits, as well as within modern digital DSP based systems.

1.1.2 Space Vector Modulation

The Space Vector Modulation (SVM) processes the reference voltage vector $\underline{u_s}^*$ as a whole instead of using separate modulators for each phase, as is the case of the suboscillation method. This approach is well matched with the space vector theory and is capable of producing the highest available fundamental output voltage, with low harmonic distortion of the output current [3]-[6]. The method is also well suited for digital implementation [11]-[13] and optimization techniques are available [9], [10]. A detailed description of this method is presented in the next section.

1.1.3 Synchronized Carrier Modulation

High power inverters are operated at low switching frequency (hundreds of Hz). In this case, the carrier frequency must be an integer multiple of the reference voltage frequency and the two signals must be synchronized in order to avoid the appearance of subharmonic components in the current waveform. These subharmonics are undesired as they produce relatively high losses and low-frequency torque harmonics. Methods in this class are referred as synchronized PWM methods.

1.2 Carrierless PWM

Carrierless modulation or random modulation strategies are those techniques where the carrier frequency is not constant. In general, the carrier frequency is varied in a random, or pseudo-random manner, over a certain frequency pool [10]. In random PWM the spectral distribution of the harmonic energy is equalized over a large frequency range, instead of being concentrated in salient sidebands located at several fixed frequencies. In this way, the acoustical noise radiated by load is almost white noise.

1.3 Optimized open-loop PWM

High power inverters are operated at low switching frequency with synchronized carrier. The number of pulses per fundamental period is small and it is advantageous to determine off-line the switching instants (switching angles) of a finite number of pulses, by optimization procedures.

1.3.1 Harmonic elimination

This technique determines the switching instants of N pulses, such that, a well defined number, $n=(N-1)/2$ of lower order harmonics from the discrete Fourier spectrum, are eliminated. The method is applied when specific harmonic torque frequencies must be avoided, but is suboptimal with respect to other performance criteria.

1.3.2 Objective functions

Several objective functions can be selected for optimization: the harmonic distortion factor d (3.13) or the loss factor d^2, the overall drive system efficiency, the highest peak current and other. In general, the numerical solution is time consuming.

1.3.3 Optimal subcycle method

This method considers the duration of switching subcycles as optimization variable, a subcycle being the time sequence of three consecutive switching vectors. The sequence is arranged such that the instantaneous distortion current equals zero at the beginning and at the end of the subcycle. The modulation process is based on space vector approach with variable, off-line optimized subcycle length [7].

2. Feedback PWM Control

Feedback or closed-loop schemes for VSI inject currents into the motor. They receive as input a reference current space vector $\underline{i}_s^*$ and generate a switched three phase voltage such that the output fundamental current vector $\underline{i}_{s1}$ equals the reference current $\underline{i}_s^*$. The feedback loop is established either for the stator current vector or for the stator flux vector. The general feedback PWM scheme is presented in Figure 3.5.b.

2.1 Nonoptimal feedback PWM

2.1.1 Hysteresis current control

This method uses three hysteresis current controllers, one for each phase. The one-bit outputs of the three controllers are the inverter switching signals S_a, S_b, S_c. The control method is simple and its dynamic performance is excellent.

However, the quality of the modulation process is low and favors the generation of subharmonic components. The switching frequency of hysteresis current controllers is not constant, being strongly dependent on the modulation index and, therefore, the switching capability of the inverter is not entirely utilized. This method is preferred for higher switching frequency operation to compensate for the poor modulation quality.

2.1.2 Suboscillation current control

The basic disadvantages of the hysteresis controller are eliminated by a carrier modulation scheme as part of the current control loop. In this case, a PI current vector controller outputs the reference voltage vector $\underline{u}_s^*$ that is used by the carrier-based modulator to generate the switching signals. The PI controller gain must be relatively high, in order to ensure low steady-state current tracking error and fast dynamic current response.

2.1.3 Space vector current control

Basically, this scheme is similar with the subocillation current control, with the only particularity that a space vector modulator is used. This method is well suited for vector control and digital implementation. Many solutions are proposed in the literature [13], [14]. Various improvements are possible: feedforward current control and EMF compensation for improved dynamics [3], [4], cross-coupling decoupling [14], synchronous regular sampling.

2.2 Optimized feedback PWM

2.2.1 Predictive current control

In this method the current vector $\underline{i}_s$ is maintained within a two-dimensional current error bounded area, symmetric about the tip of the reference current $\underline{i}_s^*$. When the motor current $\underline{i}_s$ reaches the boundary, a new switching state is applied, such that the current is retained inside the restricted area. The best switching state vector is determined by prediction of the current trajectory and minimization, or optimization of the switching frequency. The prediction of the switching instants is based on a simplified model of the machine.

2.2.2 PWM with field orientation

Further reduction of the switching frequency for high power applications can be achieved by defining a current error boundary of rectangular shape, aligned with the machine rotor flux vector. This transfers a major portion of the unavoidable current harmonics to the rotor field axis where they have no direct influence on the machine torque because of the large rotor time constant. The selection of switching state vectors is based on prediction, such that the switching frequency and the torque current ripple are minimized [1], [3], [4].

2.2.3 Trajectory tracking control

The trajectory tracking approach uses a combination of off-line optimization methods for steady-state operation and on-line optimization techniques for transient operation. In this way the advantages of both methods are exploited. The steady-state current vector trajectories, precalculated off-line from the optimal pulse sequences, are used as steady-state templates for the actual current waveform. Once an optimal trajectory is selected, this is used to define a time-moving target point. At transient operation, an on-line tracking controller counteracts if the actual current vector deviates from this given path. This approach defines a tracking problem to be solved in real time. High quality dynamic performance and minimum harmonic distortion have been reported [8].

Although a large number of PWM techniques have been proposed in the literature, only a handful of them gained a foothold in the industry. Apart from the very popular SVM method, with or without current control loop, probably the most common are the DSP implemented regular sampling strategies that have replaced the classic, natural sampling triangular carrier analog technique. In this work, the open-loop SVM method was selected for practical implementation. A detailed description of this modulation technique follows.

3.4 Space Vector Modulation

The space vector approach to pulse width modulation owes its popularity to the clear simplicity and elegance of implementation. Space Vector Modulation (SVM) is an open-loop PWM strategy, based on space vectors theory and, therefore, suitable for vector controlled ASD-s. SVM has gained widespread recognition after its introduction in two simultaneous papers, [5] and [6], in the mid-eighties.

Since then, research efforts have been directed toward further improvement of the classical technique, [9]-[18], and the SVM has proven its numerous advantages:

- It is capable of producing the highest available fundamental output voltage.
- It is suitable for variable torque loads and for large power drives.
- It generates low harmonic distortion of the output current.
- It is simple and appropriate for digital implementation.

The SVM principle is illustrated in Figure 3.6. The modulation algorithm is derived with reference to the first sector and generalized afterwards for the entire complex plane. The input reference voltage vector $\underline{V}^*$ is sampled at constant frequency $f_s=1/T_s$, synchronously with the modulator, whose switching frequency is also f_s.

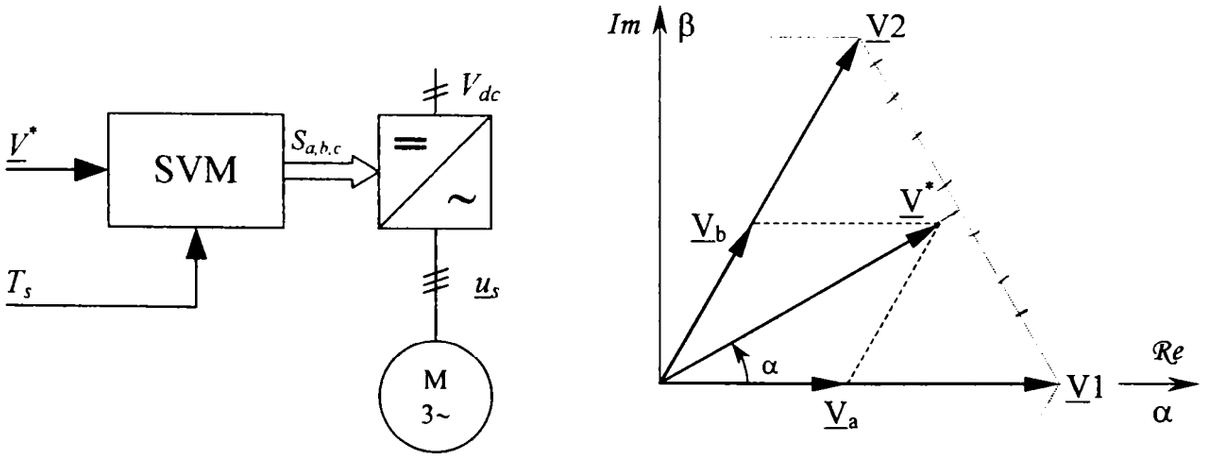

a. SVM block diagram

b. SVM principle

Figure 3.6 The Space Vector Modulation principle

Considering the two active vectors, adjacent to sector S_1, $\underline{V}_1$ and $\underline{V}_2$, as coordinate axes, the reference vector $\underline{V}^*$, located in S_1, can be decomposed as

$$\underline{V}^* = \underline{V}_a + \underline{V}_b \tag{3.17}$$

where $\underline{V}_a$ and $\underline{V}_b$ are its components in axes directions, as shown in Figure 3.6.b.

Since only eight voltage vectors are available as instantaneous outputs, during each sampling/switching interval of duration T_s, the reference vector $\underline{V}^* = \underline{V}_\alpha + j\underline{V}_\beta$ is realized as a linear combination of the two adjacent active voltage vectors, $\underline{V}_1$ and $\underline{V}_2$, and the two zero vectors, $\underline{V}_0$ and $\underline{V}_7$. The volt-second balance equation, over the sampling period T_s, is

$$\underline{V}^* T_s = \underline{V}_1 T_1 + \underline{V}_2 T_2 + \underline{V}_0 T_0 + \underline{V}_7 T_7 \tag{3.18}$$

Employing $\underline{V}_1$ and $\underline{V}_2$ from (3.10), and $\underline{V}_0 = \underline{V}_7 = 0$, this complex equation is solved for time durations T_1 and T_2 of the active vectors

$$T_1 = T_s \frac{\sqrt{3}}{2V_{dc}} (\sqrt{3} V_\alpha - V_\beta) \tag{3.19}$$

$$T_2 = T_s \frac{\sqrt{3}}{V_{dc}} V_\beta \tag{3.20}$$

As long as the linear modulation range is addressed, the condition $T_1 + T_2 < T_s$ holds and one or both zero vectors are inserted for the remaining time

$$T_0 + T_7 = T_s - T_1 - T_2 \tag{3.21}$$

Alternatively, the active vectors duty cycles D_1 and D_2 are calculated as the time average of T_1 and T_2 over the switching period T_s.

$$D_1 = M \cdot \sin(\pi/3 - \alpha) \tag{3.22}$$

$$D_2 = M \cdot \sin(\alpha) \tag{3.23}$$

$$D_0 + D_7 = 1 - D_1 - D_2 \tag{3.24}$$

where $M = \sqrt{3} V^* / V_{dc}$ is the space vector modulation index, V^* is the magnitude of $\underline{V}^*$ and α is the argument of $\underline{V}^*$ with respect to the beginning of the sector. Obviously, the foregoing equations apply only when $\underline{V}^*$ is located in the first sector, $0 < \alpha < \pi/3$.

For the general case, when $\underline{V}^*$ is located within any sector S_k, (k=1…6), the problem is solved by rotating $\underline{V}^*$ backward with the angle $\beta - \alpha = (k-1)\pi/3$.

$$D_k = M \cdot \sin(k\pi/3 - \beta) \tag{3.25}$$

$$D_{k+1} = M \cdot \sin(\beta - (k-1)\pi/3) \tag{3.26}$$

where k=1…6 is the modulo-six vector count ($\underline{V}_{6+1} \equiv \underline{V}_1$), D_k is the duty cycle of vector $\underline{V}_k$ and $\beta = \tan^{-1}(V_\beta / V_\alpha)$ is the argument of $\underline{V}^*$, as shown in Figure 3.7.a.

For further simplification of the signal processing algorithm, in case of digital implementation, the reference vector is subjected to a linear coordinate transformation that gives the normalized reference voltage vector [13]

$$\underline{u}^* = u_\alpha^* + j u_\beta^* = \frac{3}{2}\frac{V_\alpha^*}{V_{dc}} + j\frac{\sqrt{3}}{2}\frac{V_\beta^*}{V_{dc}} \tag{3.27}$$

Employing $\underline{u}^*$, from (3.22) and (3.23) the duty cycles for all sectors are

Sector S_1 $\quad D_1 = u_\alpha^* - u_\beta^* \quad D_2 = 2u_\beta^*$ (3.28a)

Sector S_2 $\quad D_2 = u_\alpha^* + u_\beta^* \quad D_3 = u_\beta^* - u_\alpha^*$ (3.28b)

Sector S_3 $\quad D_3 = 2u_\beta^* \quad D_4 = -u_\alpha^* - u_\beta^*$ (3.28c)

Sector S_4 $\quad D_4 = u_\beta^* - u_\alpha^* \quad D_5 = -2u_\beta^*$ (3.28d)

Sector S_5 $\quad D_5 = -u_\alpha^* - u_\beta^* \quad D_6 = u_\alpha^* - u_\beta^*$ (3.28e)

Sector S_6 $\quad D_6 = -2u_\beta^* \quad D_1 = u_\alpha^* + u_\beta^*$ (3.28f)

All sectors $\quad D_0 + D_7 = 1 - D_k - D_{k+1}$ (3.29)

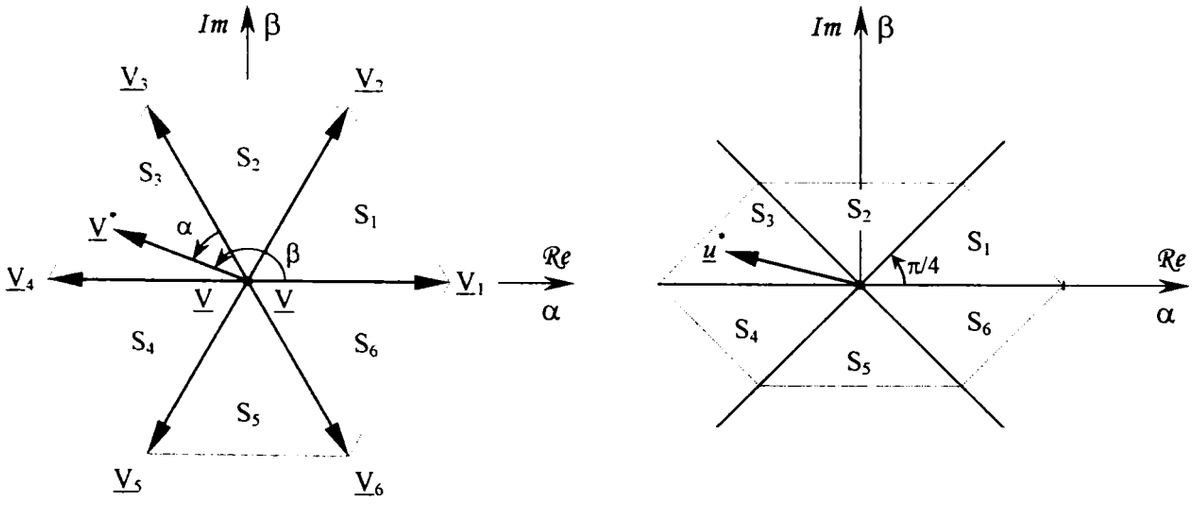

a. original reference voltage b. normalized reference voltage

Figure 3.7 Space Vector Modulation reference voltage and VSI voltage limit

The transformation (3.27) does not change the SVM algorithm, but drastically simplifies the voltage sector identification procedure and the duty cycle computation, Figure 3.7.b. It is just a different way of doing the signal processing.

The distribution of switching states within a subcycle determines the harmonic content of the motor currents and the switching frequency of the VSI. According to (3.29), there is a degree of freedom in the choice of zero vectors, $\underline{V}_0$ and/or $\underline{V}_7$, and their distribution in one subcycle. Continuous SVM schemes are obtained employing both zero vectors, $T_0>0$, and $T_7>0$, while discontinuous schemes are yielded using only one zero vector, $T_0=0$ or $T_7=0$, [3], [4], [9], [10].

The standard, symmetrical, continuous SVM scheme employs both zero vectors with equal time durations, $T_0 = T_7 = (T_s - T_1 - T_2)/2$, and distributed so that the transition from one state to another involves switching of only one inverter leg.

Within the first sector S_1, the standard SVM switching sequence is

$\underline{V}_0(T_0/2)$, $\underline{V}_1(T_1/2)$, $\underline{V}_2(T_2/2)$, $\underline{V}_7(T_7)$, $\underline{V}_2(T_2/2)$, $\underline{V}_1(T_1/2)$, $\underline{V}_0(T_0/2)$.

where $\underline{V}_k(t)$ associates each vector $\underline{V}_k$ to its time duration t, as shown in Figure 3.8.

In general, the switching sequence is

$\underline{V}_0(T_0/2)$, $\underline{V}_k(T_k/2)$, $\underline{V}_{k+1}(T_{k+1}/2)$, $\underline{V}_7(T_7)$, $\underline{V}_{k+1}(T_{k+1}/2)$, $\underline{V}_k(T_k/2)$, $\underline{V}_0(T_0/2)$

for all odd sectors (S_1, S_3 and S_5) and

$\underline{V}_0(T_0/2)$, $\underline{V}_{k+1}(T_{k+1}/2)$, $\underline{V}_k(T_k/2)$, $\underline{V}_7(T_7)$, $\underline{V}_k(T_k/2)$, $\underline{V}_{k+1}(T_{k+1}/2)$, $\underline{V}_0(T_0/2)$

for all even sectors (S_2, S_4 and S_6), where $\underline{V}_{6+1}\equiv\underline{V}_1$.

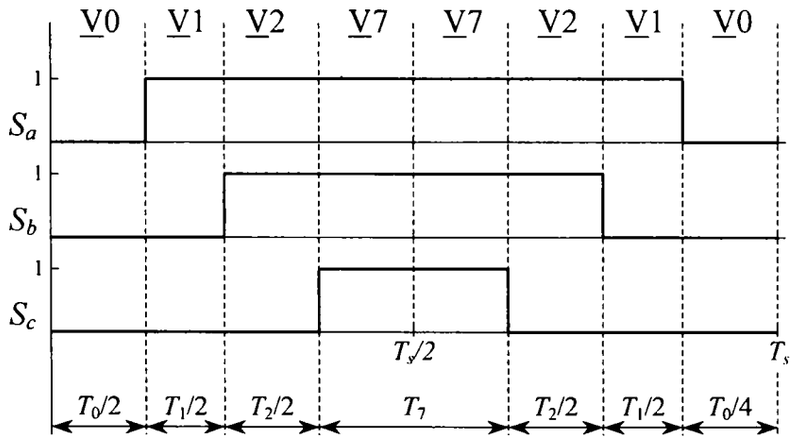

Figure 3.8 Space Vector Modulation switching sequence for sector S_1

With this arrangement, there are only six switchings during T_s. As shown in Figure 3.8, during each cycle T_s, the switching signals S_a, S_b, S_c are single-pulse signals, meaning that each transistor switches exactly twice during this time. Therefore, the transistors' switching frequency is always f_s. Moreover, the symmetry of the pulse pattern permits sampling of the undistorted fundamental current at the same frequency as the modulation rate f_s.

The *modulation functions*, or duty cycles, of each phase are determined as the time average, over one period T_s, of the switching signals S_a, S_b, S_c.

$$D_x = \frac{1}{T_s}\int_0^{Ts} S_x dt, \qquad x=a,\ b,\ c \tag{3.30}$$

Phase duty cycles, in terms of D_k from (2.28), are given in Table 3.1 for all six sectors.

Table 3.1 Modulation functions for standard continuous SVM

Sector	D_a	D_b	D_c
S_1	$(1+D_1+D_2)/2$	$(1-D_1+D_2)/2$	$(1-D_1-D_2)/2$
S_2	$(1+D_2-D_3)/2$	$(1+D_2+D_3)/2$	$(1-D_2-D_3)/2$
S_3	$(1-D_3-D_4)/2$	$(1+D_3+D_4)/2$	$(1-D_3+D_4)/2$
S_4	$(1-D_4-D_5)/2$	$(1+D_4-D_5)/2$	$(1+D_4+D_5)/2$
S_5	$(1-D_5+D_6)/2$	$(1-D_5-D_6)/2$	$(1+D_5+D_6)/2$
S_6	$(1+D_6+D_1)/2$	$(1-D_6-D_1)/2$	$(1+D_6-D_1)/2$

A discontinuous regular-sampled SVM scheme, which employs only one zero vector, is the Minimum Loss Space Vector Modulation (MLSVM), introduced in [9] and [10]. The MLSVM switching sequence within sector S_1, shown in Figure 3.9, is

$\underline{V}_1(T_1/2)$, $\underline{V}_2(T_2/2)$, $\underline{V}_7(T_7)$, $\underline{V}_2(T_2/2)$, $\underline{V}_1(T_1/2)$.

In general, the switching sequence is

$\underline{V}_k(T_k/2)$, $\underline{V}_{k+1}(T_{k+1}/2)$, $\underline{V}_7(T_7)$, $\underline{V}_{k+1}(T_{k+1}/2)$, $\underline{V}_k(T_k/2)$

for all odd sectors (S_1, S_3 and S_5) and

$\underline{V}_{k+1}(T_{k+1}/2)$, $\underline{V}_k(T_k/2)$, $\underline{V}_0(T_0)$, $\underline{V}_k(T_k/2)$, $\underline{V}_{k+1}(T_{k+1}/2)$

for all even sectors (S_2, S_4 and S_6), where $\underline{V}_{6+1}\equiv\underline{V}_1$.

Phase duty cycles, D_a, D_b, D_c, are given in Table 3.2 for all six sectors.

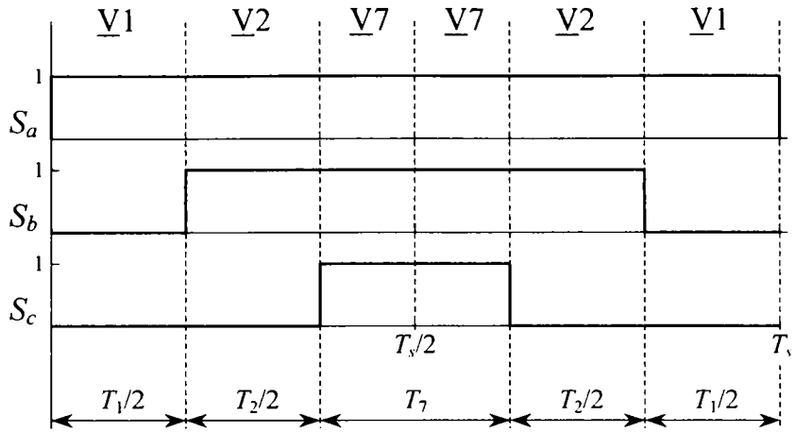

Figure 3.9 Minimum Loss Space Vector Modulation switching sequence for S1

Table 3.2 Modulation functions for minimum loss SVM

Sector	D_a	D_b	D_c
S_1	D_1+D_2	D_2	0
S_2	$1-D_3$	1	$1-D_2-D_3$
S_3	0	D_3+D_4	D_4
S_4	$1-D_4-D_5$	$1-D_5$	1
S_5	D_6	0	D_5+D_6
S_6	1	$1-D_6-D_1$	$1-D_1$

As shown in Figure 3.9, within one sector, one switching signal is always constant and the number of switchings is decreased from six to four. This pattern results in reduction of the power devices switching frequency with one third, for the same modulation frequency as in the standard SVM case.

The name of the method implies minimization of the inverter switching losses. This minimization results from the reduction of power devices switching frequency and from the absence of switching in the vicinity of load current peaks in a given phase. This favorable property is exploited whenever the power devices are driven toward their margin of thermal overload [9]. The disadvantage of MLSVM is that, for medium values of the modulation index, it exhibits larger current distortion factor than standard SVM, Figure 3.10.a. However, the harmonic distortion of the current decreases at higher modulation indexes, approaching that of SVM [13].

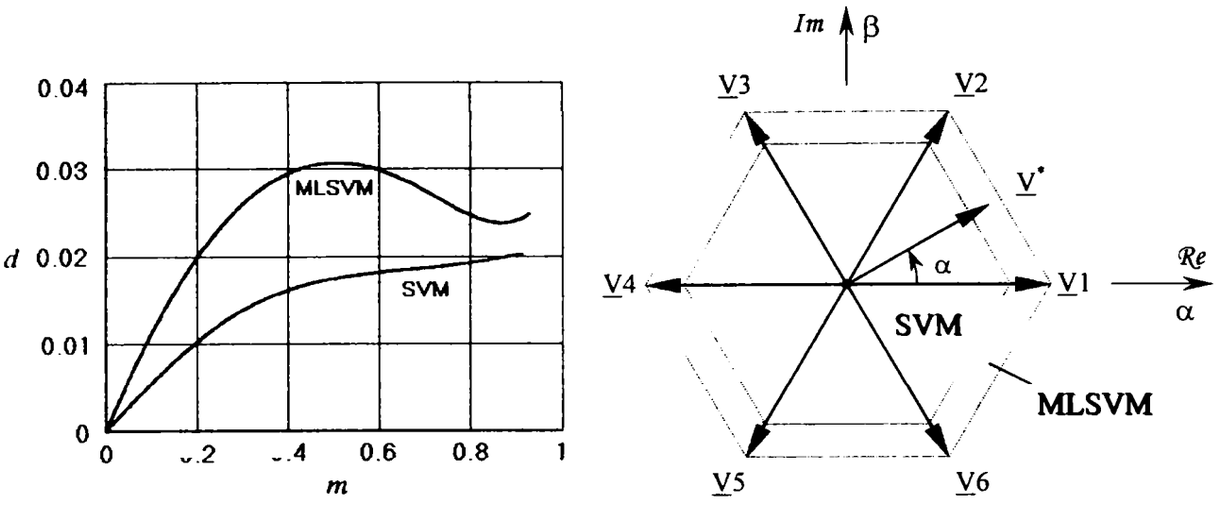

a. SVM and MLSVM distortion factor b. SVM and MLSVM operation range

Figure 3.10 SVM and MLSVM distortion factor versus *m* and operation range [13]

The harmonic distortion factor, *d* (3.13), versus modulation index, *m* (3.15), for SVM and MLSVM, is shown in Figure 3.10.a [13]. In both cases, the center-pulse switching pattern results in minimization of the current harmonic distortion. Within the linear modulation range, the SVM strategy is employed at low modulation indexes and MLSVM at high indexes, as in Figure 3.10.b.

The work described here uses either this SVM-MLSVM mixed strategy, or the standard SVM scheme for the entire linear modulation range.

Considerations presented so far addressed the linear modulation range. This is characterized by the condition $T_k + T_{k+1} < T_s$, that is, the reference voltage vector $\underline{V}^*$ points inside the voltage hexagon defined by the VSI basic vectors. If the reference vector exceeds the voltage hexagon boundary, then this reference cannot be realized as demanded and the control is achieved by *overmodulation techniques* (OVM).

Traditionally, the linear modulation range was characterized by the condition $V^* \le V_{dc}/\sqrt{3}$, that is, $\underline{V}^*$ points inside the circle tangent to VSI hexagon, [3], [4]. The exterior area of that circle was considered the OVM range and two OVM modes have been defined and studied in [16]. This approach relies on the fact that the voltage vector trajectory is circular in steady-state operation and the relationship between that trajectory and the voltage hexagon has been considered in a global manner.

For a servo-drive system, whose dynamic behavior is very important, this philosophy is not necessarily the best and, as shown in [13], different approaches can be considered. In the most general case, no assumption is made about the shape of the reference voltage trajectory. If, at any moment, the reference vector points outside the hexagon, this is an indication that the DC link voltage, V_{dc}, is not large enough to meet the control system's requirements and a tradeoff with respect to system's dynamic performances must be found [16]-[18].

The OVM trades a phase angle error against a higher voltage magnitude and leads to increased lower order harmonics in the machine current. Two OVM strategies combined with DTC, for improved dynamic behavior, have been implemented and tested. In both cases, the limit between linear modulation, either SVM or MLSVM, and OVM, is the voltage hexagon, characterized by $T_k+T_{k+1} = T_s$.

The simplest OVM strategy, called *proportional OVM*, is to apply a shorter reference vector $\underline{V}$, with the same direction as the original reference vector $\underline{V}^*$. The phase angle α, of $\underline{V}^*$, is maintained unchanged, while its magnitude is decreased, so that the new reference points to the intersection between the original reference and the voltage hexagon. The merit of this approach is that the current distortion is kept low, with the price of sacrificing the system's dynamic response.

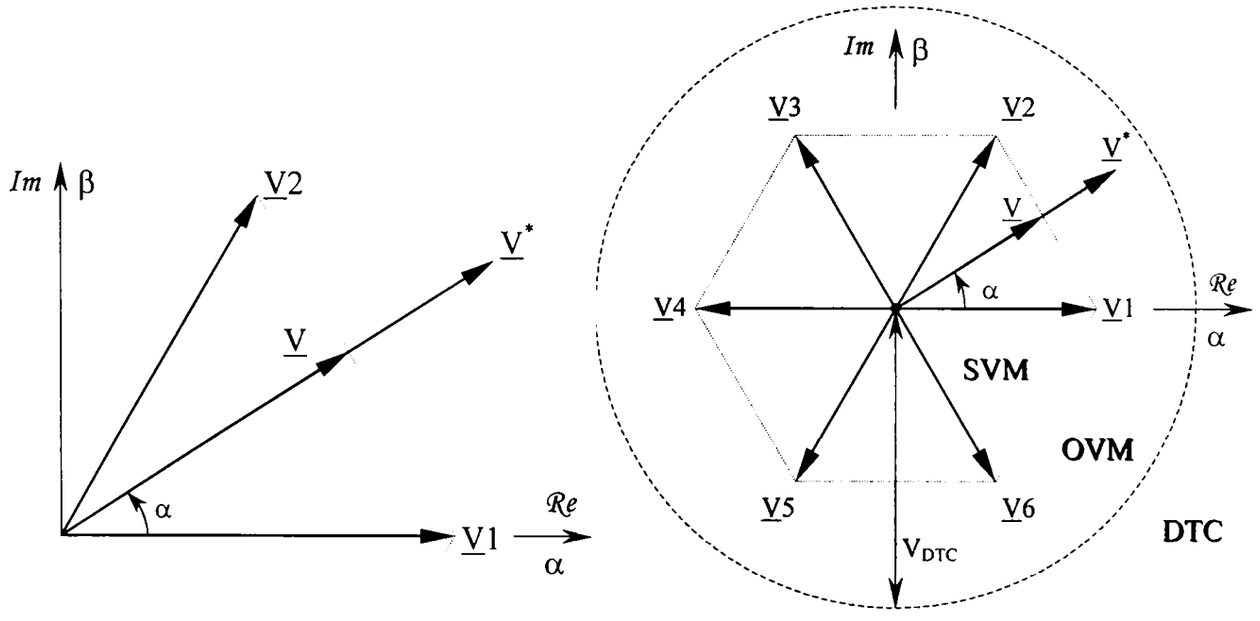

a. Principle of proportional OVM b. Operation range of SVM, OVM and DTC

Figure 3.11 The principle and operation range of proportional OVM

The new duty cycles D'_k and D'_{k+1}, of the active vectors $\underline{V}_k$ and $\underline{V}_{k+1}$, employed to realize the new reference $\underline{V}$, are determined from geometric considerations.

$$D'_k = \frac{D_k}{D_k + D_{k+1}} \tag{3.31}$$

$$D'_{k+1} = \frac{D_{k+1}}{D_k + D_{k+1}} \tag{3.32}$$

where D_k and D_{k+1} are duty cycles of the original reference $\underline{V}^*$, obtained from (3.28).

In order to improve the dynamic behavior, enhancement of OVM with DTC has been proposed and tested herewith. If the reference vector magnitude is greater than a certain circular limit V_{DTC}, $V^* > V_{DTC}$, it means that system's dynamic requirements are very large and there is no benefit in maintaining the reference vector phase angle. In this case, the reference $\underline{V}^*$ is disregarded and the fast response classical DTC is applied. The principle of proportional OVM is illustrated in Figure 3.11.a, while Figure 3.11.b shows operation ranges for linear SVM, OVM and DTC.

The second OVM strategy, implemented and tested in this work, achieves better utilization of the VSI voltage capability, together with simple implementation. It is called *triangular OVM* and its principle is illustrated in Figure 3.12 [13].

If the reference voltage vector $\underline{V}^*$ points outside the voltage hexagon, $T_k + T_{k+1} > T_s$, and both time durations, T_k and T_{k+1} are smaller than T_s, then the longest time is maintained unchanged, while the other is decreased, such that they sum to T_s.

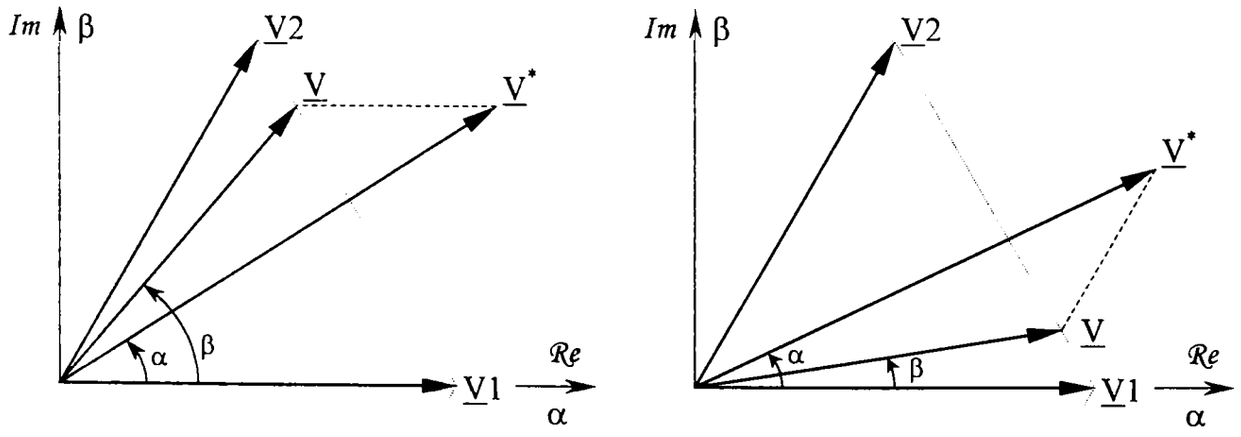

a. Upper segment triangular OVM

b. Lower segment triangular OVM

Figure 3.12 The principle of triangular OVM for upper and lower half-sectors of S_1

The new reference $\underline{V}$ points to hexagon border and is obtained by moving the original reference vector $\underline{V}^*$ along either one of dashed lines in Figure 3.12.

The new duty cycles D'_k and D'_{k+1}, of the active vectors $\underline{V}_k$ and $\underline{V}_{k+1}$, are

$$D'_k = D_k \qquad D'_{k+1} = 1 - D_{k+1} \qquad \text{if } D_k > D_{k+1} \tag{3.33}$$

$$D'_k = 1 - D_k \qquad D'_{k+1} = D_{k+1} \qquad \text{if } D_{k+1} > D_k \tag{3.34}$$

where D_k and D_{k+1} are duty cycles for the original reference $\underline{V}^*$, obtained from (3.28).

Obviously, the above formulas apply only if $D_k<1$and $D_{k+1}<1$. This condition restricts the application of OVM strategy to six equilateral triangles, adjacent to the basic hexagon, one for each sector, as shown by shaded areas in Figure 3.13. If the reference $\underline{V}^*$ exceeds the triangular boundary, $D_k>1$ in the lower half of the sector, or $D_{k+1}>1$ in the upper half of the sector, and a bang-bang control strategy must be employed. In this case, the reference $\underline{V}^*$ is disregarded and the fast response classical DTC is applied. SVM, OVM and DTC regions are shown in Figure 3.13.

Triangular OVM strategy achieves better utilization of the DC voltage, with the price of increased current distortion. In comparison with proportional OVM, the magnitude of $\underline{V}$ is increased, but a phase angle error is introduced.

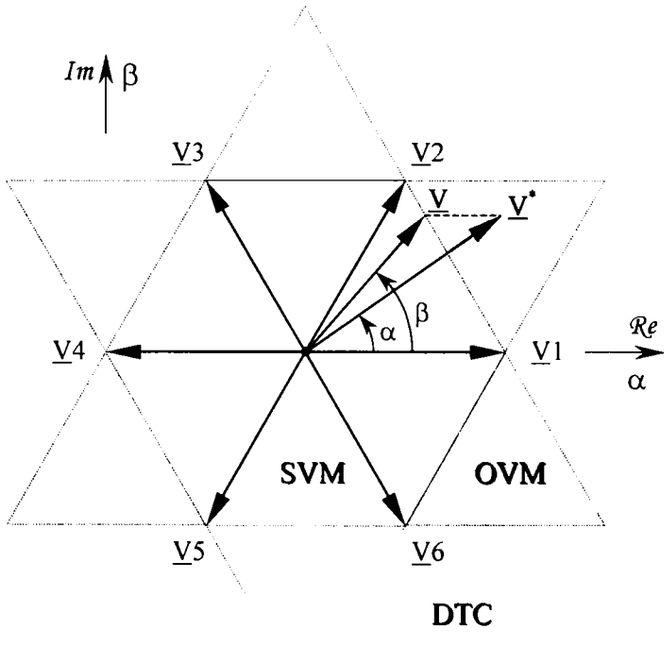

Figure 3.13 The operation region of SVM, triangular OVM and DTC

For both OVM strategies, using DTC in the high modulation range, as proposed herewith, offers several important benefits:

- The robust, high band-with torque and flux control is maintained. In this way, the drive's dynamic performance is preserved or improved.
- In each sampling period the voltage vector magnitude, is either zero, or at its maximum possible value, $2 \cdot V_{dc}/3$.
- Switching frequency and switching looses are decreased about six times.
- The volt-second loss caused by the VSI deadtime is reduced.

Since steady-state DTC operation is characterized by high torque and current ripple, it is desirable to operate the drive with linear modulation or overmodulation, in steady-state, and to reach the DTC region only during transients. In this way, DTC's dynamic merits are exploited without significant current distortion in steady-state. This strategy was called *DTC dynamic overmodulation.*

While triangular OVM precisely defines the OVM-DTC boundary, the proportional OVM offers the freedom to implement this limit, V_{DTC}, as a design parameter. This allows the drive's dynamic behavior to be optimized.

When the steady-state voltage demand increases, the DTC mode gets selected for continuous operation. Six-step operation, as suggested in [13] for triangular OVM, is not possible with this arrangement. The advantage of DTC over six-step mode is that the fast and robust torque control is maintained and the low frequency current distortions are smaller in DTC operation. Since six-step mode is an open loop uncontrolled switching strategy, the fact that the control is still active with DTC, is regarded as an important merit of the proposed DTC-OVM enhancement.

However, if the six-step operation is desired, because of its higher output voltage capability and lower switching looses, the control system must be adequately designed [16]. In particular, straightforward implementation of the six-step mode is easily achieved with triangular OVM [13].

Other OVM dynamic strategies are also possible [17], [18], but only the two techniques presented here, proportional and triangular OVM have been implemented and tested.

3.5 Inverter Nonlinearities

The development of fast switching power devices and complex modulation techniques made possible the production of high performance ASD-s with fast torque response, low current harmonics and low audible noise. In such applications, the exact knowledge of the inverter output voltage is needed to calculate the system's state. The output voltage can be determined from direct measurements or calculated.

It is rather difficult to measure the output voltage of a PWM VSI because it is composed of discrete pulses. Since only the low frequency content is of interest, a low pass filter should remove the high frequencies. Due to the low pass filter, the filtered voltage is subjected to phase delay and is not adequate for control purposes.

Calculating the voltage means using the reference voltage as the output voltage. Only the average voltage over one switching period is needed because only that can follow the commanded voltage. Since the reference voltage vector $\underline{V}^*$ is modified in OVM, the best approach is to measure the DC link voltage V_{dc} and to use the modulation functions, determined in Section 3.5 for either SVM or MLSVM.

Analytically, taking the average over T_s, of the instantaneous voltage vector (3.8), gives the VSI output *momentary-average voltage* vector

$$\underline{V} = V_\alpha + jV_\beta \tag{3.35}$$

$$V_\alpha = V_{dc}(D_a - \frac{1}{3}(D_a + D_b + D_c)) \tag{3.36a}$$

$$V_\beta = V_{dc}\frac{1}{\sqrt{3}}(D_b - D_c) \tag{3.36b}$$

Similarly, the momentary-average phase voltages can be determined from (3.5)-(3.7) by formally replacing switching signals (S_a, S_b, S_c) with duty cycles (D_a, D_b, D_c).

The VSI linear model (3.35)-(3.36), obtained under simplifying assumptions invoked in Section 3.2, represents an idealization of the inverter, but provides to be very useful and straightforward in most cases when the VSI behavior is investigated.

However, compared to the reference voltage, the inverter real output voltage is distorted due to VSI nonlinear behavior.

The most important sources of voltage distortion are:

- The VSI dead time introduced to avoid the DC link short-circuit;
- The nonideal turn on and off characteristic of switching power devices;
- The inherent voltage drop across the power devices during the on state;
- Quantization and sampling effects in digital implemented SVM.

Compensation techniques for these nonlinearities are discussed next.

Dead time analysis and compensation

To guarantee that both power devices in an inverter leg (see Figure 3.3) never conduct simultaneously, a small time delay, T_d, called dead time, is added to the gate signal of the turning-on device, Figure 3.14. This delay, added to the device's finite turn on and turn off times, introduces a load dependent, magnitude and phase error in the output voltage. Since the delay occurs in every PWM cycle, the magnitude of the error grows in inverse proportion to the fundamental frequency, introducing a serious waveform distortion. The voltage distortion increases also with switching frequency, introducing harmonic components that, if not compensated, may cause instabilities and additional looses in the machine being driven [3], [4], [12], [19]-[21].

The SVM typical signals – ideal switching signal S_a^* and gating signals u_{g1} and u_{g2} – in the first inverter leg, over one carrier period T_s are shown in Figure 3.14.

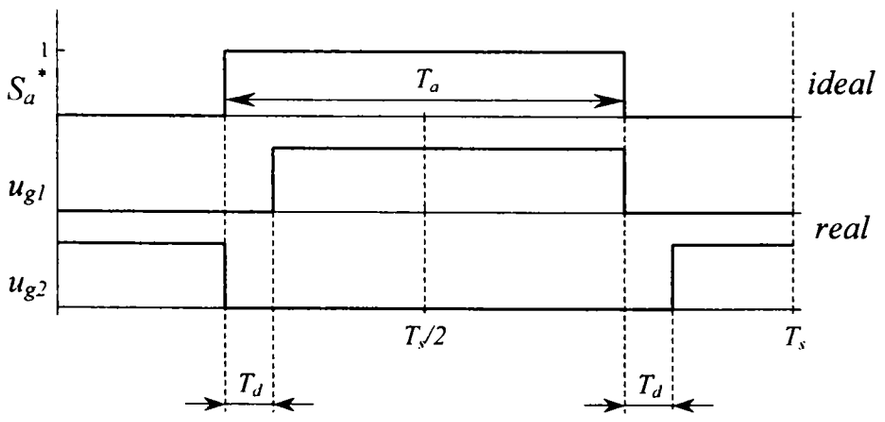

Figure 3.14 Ideal switching signal S_a^*, T1 gating signal u_{g1} and T2 gating signal u_{g2}, taking into account the dead time T_d

During the dead time T_d, both power devices in the same leg cease to conduct and one diode conducts. If the first leg current flows to load, i_a>0, the lower diode conducts and the load phase "a" is connected to negative pole "N". Otherwise, the current flows from load, i_a<0, the upper diode conducts and the load phase "a" is connected to positive pole "P". The VSI effective output phase-to-N voltage, u_{aN}, in both situations, is shown in Figure 3.15, where $u_{aN}^* = S_a^* \cdot V_{dc}$ is the desired (ideal) voltage. Compared to ideal case, in reality there is a volt-second loss of $V_{dc}T_d$ if i_a>0, or a volt-second gain of the same magnitude if i_a<0. The effective turn-on duration of the upper device is $T_a^{'} = T_a - T_d \,\mathrm{sgn}(i_a)$, where T_a is the commanded duration and $\mathrm{sgn}(i_a)$ is 1 if i_a>0 and –1 if i_a<0.

At this point, nonlinear effects of power devices turn-on and turn-off delay times, T_{on} and T_{off}, respectively, can be taken into account. It is easy to see that T_{on} delays the positive edge of u_{aN}, producing a volt-second loss if i_a>0, or a volt-second gain if i_a<0, in the same manner as T_d does. On the other side, T_{off} delays the negative edge of u_{aN}, achieving an opposite effect.

The total time error resulting from dead time, turn-on and turn-off times is

$$T_\Delta = T_d + T_{on} - T_{off} \tag{3.37}$$

For safe operation of the VSI, the dead time T_d must be selected so that T_Δ is always positive. Usually, T_d is in the range of 1 to 5 microseconds.

Since $u_{aN} = S_a \cdot V_{dc}$, the apparent pulse-width of S_a is modified, as in Figure 3.16. It follows from (3.30) that the duty cycle D_a is modified with $\Delta = T_\Delta / T_s$.

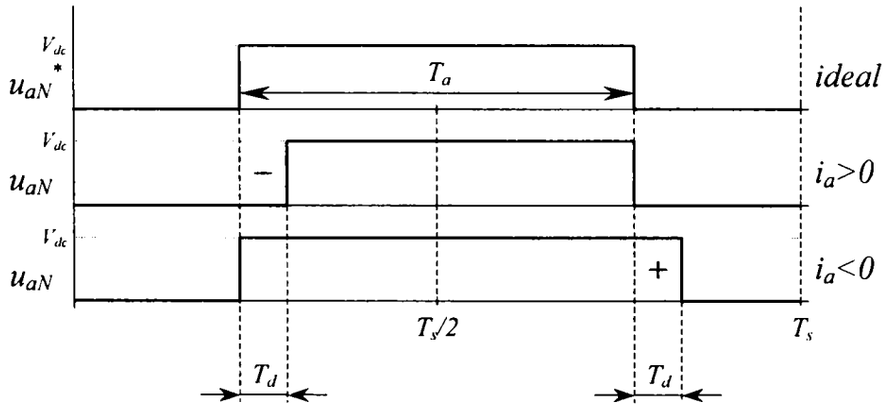

Figure 3.15 Ideal phase voltage u_{aN}^* and real phase voltage u_{aN}, for i_a>0 and i_a<0

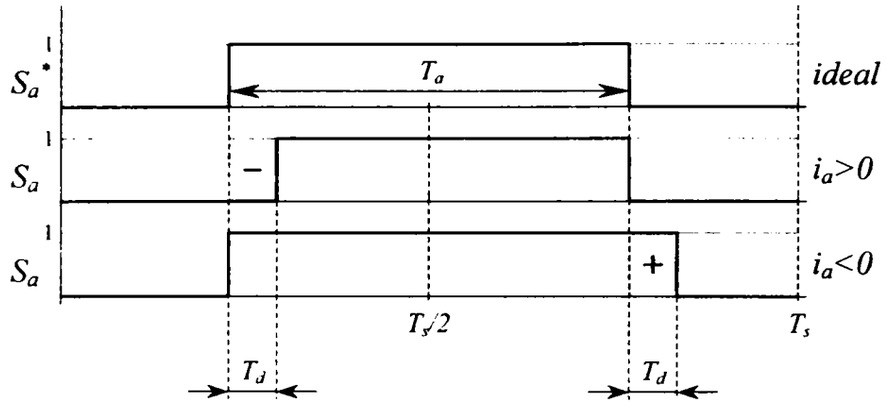

Figure 3.16 Ideal switching signal S_a^* and real switching signal S_a, for $i_a>0$ and $i_a<0$

If similar analysis is performed for all three phases, the real duty cycles are

$$D_a = D_a^* - \Delta \operatorname{sgn}(i_a) \tag{3.38a}$$

$$D_b = D_b^* - \Delta \operatorname{sgn}(i_b) \tag{3.38b}$$

$$D_c = D_c^* - \Delta \operatorname{sgn}(i_c) \tag{3.38c}$$

where superscript "*" denotes reference values, i_a, i_b, i_c are the load phase currents and Δ is the relative time error that takes into account the effects of T_d, T_{on} and T_{off}

$$\Delta = (T_d + T_{on} - T_{off})/T_s \tag{3.39}$$

The voltage vector produced by VSI can be determined from (3.35) and (3.38)

$$\underline{V} = \underline{V}^* - \underline{V}_\Delta \tag{3.40}$$

where $\underline{V}^*$ is the reference (commanded) voltage vector and the voltage error vector is

$$\underline{V}_\Delta = V_{\Delta\alpha} + jV_{\Delta\beta} \tag{3.41}$$

$$V_{\Delta\alpha} = V_{dc}\Delta\left(\operatorname{sgn}(i_a) - \frac{1}{3}(\operatorname{sgn}(i_a) + \operatorname{sgn}(i_b) + \operatorname{sgn}(i_c))\right) \tag{3.42a}$$

$$V_{\Delta\beta} = V_{dc}\Delta\frac{1}{\sqrt{3}}(\operatorname{sgn}(i_b) - \operatorname{sgn}(i_c)) \tag{3.42b}$$

In a symmetrical three phase voltage system, only six combinations of current directions exist. Following the concept of voltage sectors, six current sectors are identified, one for each signs combination, as shown in Figure 3.17.a. The error vector $\underline{V}_\Delta$ can assume exactly six distinct values of same magnitude, shown in Figure 3.17.b.

$$\underline{V}_{\Delta k} = \frac{4}{3}V_{dc}\Delta \cdot e^{j(k-1)\frac{\pi}{3}} \qquad k = 1, 2, 3, 4, 5, 6 \tag{3.43}$$

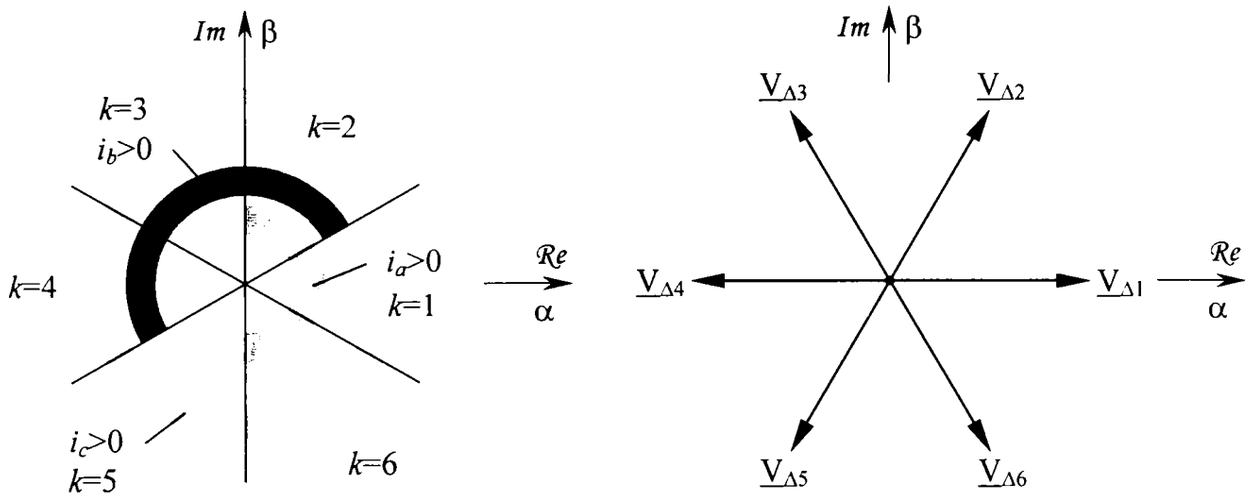

Figure 3.17 Current sectors and voltage error vectors

The dead time compensation is based on (3.38) or (3.40). The effective duty cycles, which must be applied to the modulator, are

$$D_x^* = D_x + \Delta \operatorname{sgn}(i_x), \qquad x = a, b, c \tag{3.44}$$

where D_x are the duty cycles produced by the SVM algorithm in the ideal case.

Alternatively, the reference voltage vector for the SVM modulator must be

$$\underline{V}^* = \underline{V} + \underline{V}_\Delta \tag{3.45}$$

where $\underline{V}$ is the required/desired VSI output voltage vector.

This compensation method relies on direct current measurement to determine the sign of the compensation needed. Accurate measurement of the current polarity is difficult and inaccurate around zero crossing because of the PWM noise and current clamping. Therefore, it appears that it is better to deactivate the compensation whenever the instantaneous current becomes very small.

A less conservative approach is proposed here. Statistically, the measurement is not completely erroneous, especially if provisions for synchronous current sampling have been taken. Hence, instead of signum function, the softer saturation function is employed in (3.44). This introduces a variable gain for Δ in the low current range that decreases with the increase of the measurement error probability.

$$D_x^* = D_x + \Delta \operatorname{sat}(i_x) \qquad x = a, b, c \tag{3.46}$$

where $\operatorname{sat}(i_x)$ is 1 if $i_x > h$, -1 if $i_x < -h$, and i_x/h if $-h < i_x < h$, with h a small positive value.

Voltage drop analysis and compensation

The voltage drop across the power devices, either transistors or diodes is also a source of voltage distortion. Depending on the current polarity, the voltage drop of the current conducting device will add or subtract to the output voltage, Figure 3.18.

The inverter phase "*a*" voltage, taking into account the voltage drop, is

$$u_{aN} = S_a^* V_{dc} - S_a^* u_T - (1 - S_a^*) u_D \qquad \text{if } i_a>0 \tag{3.47}$$

$$u_{aN} = S_a^* V_{dc} + S_a^* u_D + (1 - S_a^*) u_T \qquad \text{if } i_a<0 \tag{3.48}$$

where u_T and u_D are voltage drops across the transistor and the diode, respectively

$$u_T = u_{T0} + r_T \mid i_a \mid \tag{3.49}$$

$$u_D = u_{D0} + r_D \mid i_a \mid \tag{3.50}$$

where u_{T0} and u_{D0} are the threshold voltages and r_T and r_D are the on-state dynamic resistances of transistor and diode, respectively.

Combining (3.47) and (3.48) into one equation yields

$$u_{aN} = S_a^* V_{dc} + (S_a^* - 1/2)(u_D - u_T) - \text{sgn}(i_a)(u_D + u_T)/2 \tag{3.51}$$

If it is assumed that the transistor and diode have almost identical voltage drop, $u_D \cong u_T$, the second term in (3.51) may be neglected. The phase voltage becomes

$$u_{aN} = S_a^* V_{dc} - \text{sgn}(i_a)(u_D + u_T)/2 \tag{3.52}$$

Taking into account (3.49)-(3.50), the final result for the phase-to-N voltage is

$$u_{aN} = S_a^* V_{dc} - \text{sgn}(i_a)(u_{D0} + u_{T0})/2 - i_a(r_D + r_T)/2 \tag{3.53}$$

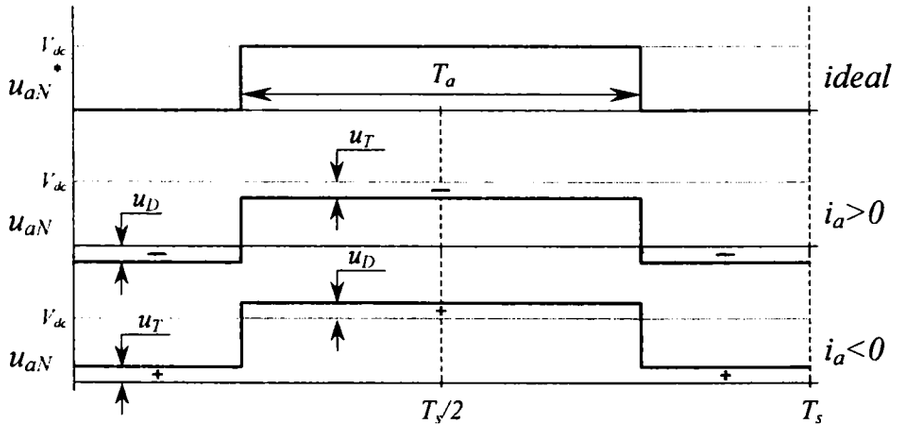

Figure 3.18 Ideal phase voltage u_{aN}^* and real phase voltage u_{aN}, for $i_a>0$ and $i_a<0$, taking into account the power devices voltage drop, u_T and u_D

Two important conclusions can be derived from (3.53). First, the last term is an ohmic voltage drop and $(r_D + r_T)/2$ acts as a load resistance. In AC machine drives this adds to the real stator resistance R_s, yielding the apparent stator resistance

$$R_s^{'} = R_s + (r_D + r_T)/2 \tag{3.54}$$

With on-line stator resistance identification and adaptation, as it is the case here, the effect of $(r_D + r_T)/2$ is accounted for and there is no need for compensation.

The second observation is that the second term in (3.53) has dead time voltage loss likewise behavior. From (3.53), without the last term, it is evident that the apparent switching signal is

$$S_a = \frac{u_{aN}}{V_{dc}} = S_a^* - \frac{(u_{D0} + u_{T0})}{2V_{dc}} \text{sgn}(i_a) \tag{3.55}$$

Taking the average over one carrier period of S_a, according to (3.30), gives the apparent duty cycle D_a. The result can now be generalized for all thee legs

$$D_x = D_x^* - \frac{(u_{D0} + u_{T0})}{2V_{dc}} \text{sgn}(i_x) \qquad x = a,\ b,\ c \tag{3.56}$$

Finally, taking into account the effects of T_d, T_{on} and T_{off} from (3.38) and the voltage drop error from (3.56), the combined duty cycle error is

$$\Delta = \frac{T_d + T_{on} - T_{off}}{T_s} + \frac{(u_{D0} + u_{T0})}{2V_{dc}} \tag{3.57}$$

This replaces (3.39) in (3.40)-(3.46) and all considerations presented for the dead time compensation remain the same. The combined dead time-voltage drop compensation is implemented with (3.46) and (3.57).

The compensation technique described above is the most popular strategy and is called current feedforward compensation of dead time [12], [20]. It is relatively simple and gives relatively good results. However, it suffers from the drawback that power devices parameters are sometimes uncertain or unknown. Solutions to this problem are to measure the VSI output voltage and to perform voltage feedback compensation [12], [19], or to employ apriori-measured values for voltage distortion compensation and to employ those values in feedforward compensation, as in [21].

Quantization and samplig effects in digital implemented SVM

Digital modulators introduce further distortions due to limited resolution of the digital system that implements the modulation algorithm. Three error sources can be identified: the finite word-length of the microprocessor, the limited time resolution of the digital modulator and the dead time resolution.

The finite word-length quantization error is characteristic to all digital control systems. All quantities involved in digital computations are quantised by rounding or truncation. Since truncation of a time signal generates even harmonics in a Fourier series because of the DC offset it introduces, a rounding type quantisation is always preferable and should always be used when signal processing is performed [15]. Using 16 or 32 bit word length devices and floating point processors, whenever it is possible, is desirable, in order to keep this error at a negligible level.

The limited time resolution of the digital timer that implements the carrier signal is determined by the master clock frequency of the digital system. For example, the time resolution of a system with 20 MHz clock frequency is 50 ns. Within a carrier period of 100 μs, there are only 2000 time increments. Hence, the duty cycles D_x will assume only 2000 distinct values, regardless of the word-length resolution. This effect can be accounted for if the quantised duty cycles are employed in (3.36).

The dead time resolution error occurs due to the fact that the value of dead time determines the minimum width of the output voltage pulses. If the desired duty cycle for a certain leg is smaller than Δ (3.39), no switching will occur in that leg because the turn on instant is delayed with the time T_Δ (3.37), which is longer than the desired pulse width. Compensating for this effect involves the so-called *pulse drop* technique. The simplest way to achieve this is to modify the duty cycles to feasible values, whenever the calculated values cannot be realized because of the dead time delay. In particular, when $0<D_x<\Delta$, D_x is rounded to 0 or Δ, and when $1-\Delta<D_x<1$, D_x is rounded to $1-\Delta$ or 1. Once more, the modified duty cycles are employed in (3.36) whenever the output voltage is calculated.

References

[1] Bimal K. Bose (Editor) et al., *Power Electronics and Variable Frequency Drives. Technology and Applications.*, IEEE Press, 1997.

[2] N. Mohan, T.M. Undeland, W.P. Robbins, *Power Electronics: Converters, Applications and Design.*, Second Edition, John Wiley & Sons, New York, 1995.

[3] J. Holtz, *Pulsewidth Modulation for Electronic Power Conversion.*, Proceedings of IEEE, vol. 82, no. 8, August 1994, pp. 1194-1214.

[4] J. Holtz, *Pulsewidth Modulation - A Survey.*, IEEE Transactions on Industrial Electronics, vol. 39, no. 5, Dec. 1992, pp. 410-420.

[5] H.W. van der Broeck, H.-C. Skudelny, G.V. Stanke, *Analysis and Realization of a Pulsewidth Modulator Based on Voltage Space Vectors.*, IEEE Transactions on Industry Applications, vol. 24, no. 1, Jan./Feb. 1988, pp. 142-150.

[6] J. Holtz, P. Lammert, W. Lotzkat, *High-Speed Drive System with Ultrasonic MOSFET PWM Inverter and Single-Chip Microprocessor Control.*, IEEE Trans. on Industry Applications, vol. IA-23, no. 6, Nov./Dec. 1987, pp. 1010-1015.

[7] J. Holtz, B. Bayer, *Optimal Pulse-width Modulation for AC Servos and Low-Cost Industrial Drives*, IEEE Trans. on Industry Applications, vol. 30, no. 4, July/Aug. 1994, pp. 1039-1047.

[8] J. Holtz, B. Bayer, *The Trajectory Tracking Approach – A New Method for Minimum Distortion PWM in Dynamic High-Power Drives.*, IEEE Transactions on Industry Applications, vol. 30, no. 4, July/Aug. 1994, pp. 1048-1057.

[9] A.M. Trzynadlowski, S. Legowski, *Minimum-Loss Vector PWM Strategy for Three Phase Inverters.*, IEEE Transactions on Power Electronics, vol. 9, no. 1, January 1994, pp. 26-34.

[10]A.M. Trzynadlowski, R.L. Kirlin, S.F. Legowski, *Space Vector PWM Technique with Minimum Switching Losses and a Variable Pulse Rate.*, IEEE Transactions on Industrial Electronics, vol. 44, no. 2, April 1997, pp. 173-181.

[11]P. Thoegersen, J.K. Pedersen, *Stator Flux Oriented Asynchronous Vector Modulation for AC-Drives.*, Proceedings of PESC'90, 1990, pp. 641-648.

[12]F. Blaabjerg, J.K. Pedersen, P. Thoegersen, *Improved Modulation Techniques for PWM - VSI Drives.*, IEEE Trans. on Industrial Electronics, vol. 44, no. 1, Feb. 1997, pp. 87-95.

[13]J.-O. Krah, J. Holtz, *High Performance Current Regulation and Efficient PWM Implementation for Low-Inductance Servo Motors.*, IEEE Transactions on Industry Applications, vol. 35, no. 5, Sept./Oct. 1999, pp. 1039-1049.

[14]F. Briz, M.W. Degner, R.D. Lorenz, *Analysis and Design of Current Regulators Using Complex Vectors.*, IEEE Transactions on Industry Applications, vol. 36, no. 3, May/June 2000, pp. 817-825.

[15]D. Zmood, D.G. Holmes, *Practical Performance Limitations for PWM Strategies.* The 33rd IEEE IAS Annual Meeting, 1998, St. Louis, CD-ROM paper 27.6.

[16]J. Holtz, W. Lotzkat, A.M. Khambadkone, *On Continuous Control of PWM Inverters in the Overmodulation Range Including the Six-Step Mode.*, IEEE Transactions on Power Electronics, vol. 8, no. 4, Oct. 1993, pp. 546-553.

[17]A.M. Hava, S.-K. Sul, R.J. Kerkman, T.A. Lipo, *Dynamic Overmodulation Characteristics of Triangle Intersection PWM Methods.*, IEEE Transactions on Industry Applications, vol. 35, no. 4, July/Aug. 1999, pp. 896-907.

[18]J.-K. Seok, J.-S. Kim, S.-K. Sul, *Overmodulation Strategy for High-Performance Torque Control.*, IEEE Transactions on Power Electronics, vol. 13, no. 4, July 1998, pp. 786-792.

[19]D. Leggate, R.J. Kerkman, *Pulse-Based Dead-Time Compensator for PWM Voltage Inverters.*, IEEE Trans. on Industrial Electronics, vol. 44, no. 2, April 1997, pp. 191-197.

[20]A.R. Muñoz, T.A. Lipo, *On-Line Dead-Time Compensation Technique for Open Loop PWM-VSI Drives.*, IEEE Trans. on Power Electronics, vol. 14, no. 4, July 1999, pp. 683-689.

[21]J.-W. Choi, S.-K. Sul, *Inverter Output Voltage Synthesis Using Novel Dead Time Compensation.*, IEEE Trans. on Power Electronics, vol. 11, no. 2, March 1996, pp. 221-227.

[22]K. Zhou, D. Wang, *Relationship Between Space-Vector Modulation and Three-Phase Carrier-Based PWM: A Comprehensive Analysis.*, IEEE Transactions on Industrial Electronics, vol. 49, no. 1, Feb. 2002, pp. 186-196.

4 STATE OBSERVERS FOR INDUCTION MACHINE DRIVES

4.1 Introduction

The vast majority of induction machine control strategies are developed with the assumption that either full or partial system state information is available. The precision and robustness of those controllers depends significantly on accurate knowledge of the system state variables. In induction machine drives it is impractical to measure all those variables. Therefore, a state observer is needed to estimate the unknown states and in some cases this can also provide better estimates of the known states that are contaminated by noise.

The state observer is a dynamic system that produces an approximation of the state vector of a real system and whose characteristics are somewhat free to be determined by the designer [1]. This system has as inputs the inputs and available outputs of the system whose state is to be estimated and has a state vector that is the desired estimation. Observers for linear systems have been proposed and developed by D.G. Luenberger in 1972 [1] and further extended for nonlinear systems [2]. In 1960 R.E. Kalman has proposed observers for stochastic systems [3].

The theory associated to state observer is intimately related to the fundamental concepts of controllability, observability, stability and dynamic response. These are exhaustively discussed in literature for linear [4] and nonlinear systems [5]. Stability definitions and fundamentals of Lyapunov theory for nonlinear systems stability are summarized in Appendix A.

There are three observer categories employed in adjustable speed drives:

- Full order and reduced order asymptotical observers have linear structure and are used for state estimation of well-defined linear systems [1]. Probably the most popular, these observers suffer from lack of robustness.
- Nonlinear observers are suitable for nonlinear or uncertain systems, exhibiting high performance and improved robustness. This category includes variable structure observers, stochastic observers and adaptive observers [2], [3].
- Artificial intelligence based observers are newcomers in this field and display high development potential. This category includes observers based on fuzzy logic, neural networks and genetic algorithms.

Observers for ASD-s are subjected to several performance criteria:

- Accuracy is the observer ability to precisely follow the actual states during steady-state operation, as well as, during transient operation.
- Robustness represents the insensitivity to perturbations (dynamic stiffness or disturbance rejection capability) and to model and parameter uncertainties.
- Fast speed of convergence between estimated and actual states.
- Behavior at very low and zero rotor speed and at very high rotor speed.
- Complexity of digital implementation versus performance.

Nowadays, research efforts are directed toward development of new solutions for induction machine state observation and improvement of robustness, accuracy and low speed behavior of existing schemes. From this perspective, nonlinear observers are very promising due to their recognized robustness and versatility.

An overview of the most popular asymptotical and adaptive observers for induction machine drives is presented in section 4.2. New state observer topologies and improvements of existing schemes are proposed in section 4.3. Simulations and experimental results are also provided.

4.2 Asymptotical Observers – State of the Art

Asymptotical observers exhibit linear dynamics and are widely employed, with good results, for state estimation of sensorless induction motor drives.

A multivariable linear system is governed by the state space model

$$dx/dt = Ax + Bu \tag{4.1a}$$

$$y = Cx \tag{4.1b}$$

where $x \in \Re^n$ is an $n\times 1$ state vector, $u \in \Re^r$ is an $r\times 1$ input vector, $y \in \Re^m$ is an $m\times 1$ measurable output vector, $\boldsymbol{A} \in \Re^{n\times n}$ is the $n\times n$ system matrix, $\boldsymbol{B} \in \Re^{n\times r}$ is the $n\times r$ input matrix and $\boldsymbol{C} \in \Re^{m\times n}$ is the $m\times n$ observability matrix.

The following theorem is a cornerstone of the observation theory [1].

Theorem 4.1 A state observer, having arbitrary dynamics, can be designed for the linear time-invariant system (4.1) if and only if the system is completely observable, that is, if the matrix $[\boldsymbol{C}^T \mid \boldsymbol{A}^T\boldsymbol{C}^T \mid (\boldsymbol{A}^T)^2\boldsymbol{C}^T \mid \ldots \mid (\boldsymbol{A}^T)^{n-1}\boldsymbol{C}^T]$ has rank n.

The *Luenberger observer* [1], is designed having the same form as the observed system, with an additional input depending on the mismatch between the measured and estimated output vectors

$$d\hat{x}/dt = A\hat{x} + Bu + K(y - \hat{y}) \tag{4.2a}$$

$$\hat{y} = C\hat{x} \tag{4.2b}$$

where $\boldsymbol{K} \in \Re^{n\times m}$ is the $n\times m$ observer gain matrix and "^" denotes estimated quantities.

Defining the estimation error as $e = x - \hat{x}$, the observer motion equation is

$$de/dt = (A - KC)e \tag{4.3}$$

The set of eigenvalues of $\boldsymbol{A}$-$\boldsymbol{KC}$ can be made to correspond to the set of eigenvalues of any $n\times n$ real matrix by suitable choice of the real matrix K, if and only if the system (4.1) is completely observable. In practice, the observer eigenvalues are selected to be negative, more negative than the eigenvalues of the observed system, so that the observer state will converge to the state of the observed system faster than other system effects.

The observer (4.2) is simple, but also possesses a certain degree of redundancy, due to the fact that, while the observer constructs an estimate of the entire state, part of that state, as given by the system outputs is already available by direct measurements. This redundancy can be eliminated and an observer of lower dimension, called *reduced-order observer*, still of arbitrary dynamics, can be designed [1].

Theorem 4.2 Corresponding to the n-th order, completely controllable, linear time-invariant system (4.1), having m linearly independent outputs (i.e. $\boldsymbol{C}$ has rank m), a state observer of order n-m can be constructed having arbitrary eigenvalues.

One way to find a reduced-order observer is to transform the system into a canonical form in which the output vector is part of the state vector. Due to the fact that $\boldsymbol{C}$ has rank m, the output vector can be written as

$$y = C_1 x_1 + C_2 x_2 \tag{4.4}$$

where the state vector has been conveniently partitioned as $x^T=[x_1^T\ x_2^T]$, $x_1 \in \Re^{n-m}$, $x_2 \in \Re^m$, $\boldsymbol{C}_1 \in \Re^{m\times(n-m)}$, $\boldsymbol{C}_2 \in \Re^{m\times m}$, and $\det(\boldsymbol{C}_2)\neq 0$.

Using a nonsingular coordinates transformation, $\boldsymbol{T} \in \Re^{n\times n}$, the observed system (4.1) can be represented in space (x_1, y) as

$$dx_1 / dt = A_{11} x_1 + A_{12} y + B_1 u \tag{4.5a}$$

$$dy / dt = A_{21} x_1 + A_{22} y + B_2 u \tag{4.5b}$$

where $TAT^{-1} = \begin{bmatrix} A_{11} & A_{12} \\ A_{21} & A_{22} \end{bmatrix}$, $TB = \begin{bmatrix} B_1 \\ B_2 \end{bmatrix}$ and $T = \begin{bmatrix} I_{n-m} & 0 \\ C_1 & C_2 \end{bmatrix}$, with $\det(\boldsymbol{T})\neq 0$.

It is now sufficient to design for x_1, an observer of order n-m, in the form

$$d\hat{x}_1 / dt = (A_{11} - LA_{21})\hat{x}_1 + (A_{12} - LA_{22})y + (B_1 - LB_2)u + L\dot{y} \tag{4.6}$$

where $\boldsymbol{L} \in \Re^{(n-m)\times m}$ is the observer gain and, from (4.4), the components of state x_2 are

$$x_2 = C_2^{-1}(y - C_1 x_1) \tag{4.7}$$

The output derivative is avoided by using the coordinate transformation

$$x' = x_1 - Ly \tag{4.8}$$

Finally, from (4.6), the desired form of the reduced-order observer, for x', is

$$d\hat{x}' / dt = (A_{11} - LA_{21})\hat{x}' + (A_{12} - LA_{22})y + (A_{11} - LA_{21})Ly + (B_1 - LB_2)u \tag{4.9}$$

The estimation error $e' = x' - \hat{x}'$ is governed by

$$de'/dt = (A_{11} - LA_{21})e' \tag{4.10}$$

It can be proved that, if the original system is observable, then so is ($\boldsymbol{A}_{11}$, $\boldsymbol{A}_{21}$) [1] and the eigenvalues of $\boldsymbol{A}_{11}$-$\boldsymbol{LA}_{21}$ can be arbitrarily assigned, so that (4.10) is stable. The components of the original state vector x are found from (4.7) and (4.8).

It is of paramount importance to determine the effect of an observer on the closed-loop stability properties of the system. It would be undesirable if, an otherwise stable, control design became unstable when realized by introduction of an observer. Fortunately, observers do not disturb stability properties when they are introduced. It can be proved that an observer does not change the closed-loop eigenvalues of a design, but merely adjoins its own eigenvalues. Thus, a very general key result is that *stability is not affected by a stable observer* [1].

It is obvious that the observer gain selection is very important. It is designed so that the observer exhibits fast and stable dynamics. The observer poles can be moved arbitrarily far toward minus infinity, yielding extremely rapid convergence, but this tends to make the observer to act like a differentiator and to become noise sensitive. The unavoidable presence of system disturbances and model uncertainties requires trading off speed of convergence against lowered noise sensitivity.

Several approaches for the selection of gain $\boldsymbol{K}$ are possible:

a. With $\boldsymbol{K}$=0 an open-loop simulator of the real process, called *estimator* is obtained. The estimation is not corrected by an error term and the error dynamics is the same as that of the real system. For sluggish or unstable systems this is, typically, unacceptable.

b. With $\boldsymbol{K}$ constant, the Luenberger observer is obtained. In this case, $\boldsymbol{K}$ is designed by standard pole placement techniques, as explained before.

c. With $\boldsymbol{K}$ variable, a wide class of adaptive observers is obtained. In nonlinear and/or time-variable systems, the gain $\boldsymbol{K}$ can be on-line adapted to compensate for certain nonlinearities or parameter deviations. The celebrated Kalman filter is precisely a variable gain observer in which $\boldsymbol{K}$ is on-line adapted to give optimal (minimum) mean square estimation error when the system perturbation is modeled as a Gaussian white noise process [3].

4.2.1 Stator and rotor flux estimators

The voltage model

The most simple and attractive approach to induction machine flux estimation relies on the integration of the back EMF, in stator reference frame. Once the stator voltages and currents are measured, the stator and rotor fluxes are

$$\underline{\hat{\psi}}_s = \frac{1}{s}(\underline{u}_s - R_s \underline{i}_s) \tag{4.11}$$

$$\underline{\hat{\psi}}_r = \frac{L_r}{L_m}\underline{\hat{\psi}}_s - \frac{L_s L_r - L_m^2}{L_m}\underline{i}_s \tag{4.12}$$

The pure integrator (4.11) is marginally stable (has infinite DC gain) and is impractical in this form. Unavoidable offsets and quantization errors, always present in the voltage and current measurements, make its outputs to progressively drift away beyond acceptable limits. Sometimes, initial conditions for (4.11) are unknown and this causes additional DC errors.

Instead of the integrator, a *low pass filter* (LPF) usually serves as substitute [6]

$$\underline{\hat{\psi}}_s = \frac{1}{s+\omega_0}(\underline{u}_s - R_s \underline{i}_s) \tag{4.13}$$

where $\omega_0=2\pi f_0$ and f_0 is the low pass filter cutoff frequency.

The LPF has finite DC gain that reduces, but does not eliminate the offset problem. By choosing f_0 very small, normally at f_0 = 0.5 – 2 Hz, (4.13) approximates well the pure integral (4.11) at high stator frequencies. However, the LPF introduces severe phase angle and amplitude errors at stator frequencies around and below f_0. The drive behavior degrades at stator frequencies below two-three times f_0.

An improvement of the LPF is to compensate for the phase and gain errors at stator fundamental pulsation $\omega_s=2\pi f_s$. The estimated flux vector is rotated with an angle φ corresponding to phase error between the pure integrator and LPF, and its magnitude is multiplied with a gain compensation term [7].

$$\underline{\hat{\psi}}_s = \frac{1}{s+\omega_0}\frac{\sqrt{\omega_s+\omega_0}}{|\omega_s|}(\underline{u}_s - R_s \underline{i}_s)e^{-j\varphi} \tag{4.14}$$

where the phase error angle is $\varphi = \pi/2 - \tan^{-1}(\omega_s/\omega_0)$ and ω_s must be known.

Since (4.14) compensates only for errors at f_s, the LPF cutoff frequency f_0 can be on-line modified, proportionally to stator frequency, so that to remain below stator frequency for any operation point. An adaptive LPF is obtained in this way [7].

$$\omega_0 = k \mid \omega_s \mid \qquad 0 < k < 0.5 \tag{4.15}$$

In this way, errors at frequencies of interest around f_s are maintained small.

Another realization of the pure integrator is based on adaptive cascaded LPF-s approach [8]. The single stage LPF is resolved into a number of identical, adaptive, cascaded LPF-s, designed such that the total phase shift angle is -π/2, the same as the one produced by the integrator. The amplitude correction is performed at the filter output, by using the same gain correction as in (4.14), $K = \sqrt{\omega_s + \omega_0} / \mid \omega_s \mid$.

The low pass filter solution is appropriate for low-cost drives, with speed range of about 1 to 10. Sensorless operation results at 50 rpm rotor speed, with simple LPF and with adaptive LPF, have been reported in [6] and [7], respectively. Very low speed sensorless operation is problematic because of the LPF bandwidth limitations and increased sensitivity to stator resistance variations.

The low pass filter stabilizes the estimation by introducing negative feedback. This concept, of impressing some form of feedback, has been recognized as an important performance improvement of the flux estimation in the low frequency range and has been widely applied. Even if that feedback does not depend on the machine states and is not necessary derived from any control theory or mathematical models, it is able to stabilize and improve the estimation [6]-[11].

The most general form of stator flux estimator, incorporating a feedback compensation term $\underline{u}_{comp}$, that remains to be specified, is

$$\underline{\hat{\psi}}_s = \frac{1}{s}(\underline{u}_s - R_s \underline{i}_s + \underline{u}_{comp}) \tag{4.16}$$

A simple and practical selection for $\underline{u}_{comp}$ is to make it proportional with the error between the reference stator flux vector $\underline{\psi}_s^*$ and the estimated flux vector [9].

$$\underline{u}_{comp} = \omega_0(\psi_s^* e^{j\alpha} - \underline{\hat{\psi}}_s) \tag{4.17}$$

where ψ_s^* is the reference stator flux magnitude, $\alpha = \tan^{-1}(\hat{\psi}_{s\beta} / \hat{\psi}_{s\alpha})$ is the estimated stator field angle and ω_0 is the compensation gain.

From (4.16) and (4.17), the estimated flux, in stator reference frame, is

$$\underline{\hat{\psi}}_s = \frac{1}{s+\omega_0}(\underline{u}_s - R_s \underline{i}_s) + \frac{\omega_0}{s+\omega_0}\psi_s^* e^{j\alpha} \tag{4.18}$$

The first term is the LPF (4.13) that is dominant at high frequencies while the last term prevails the estimation at lower frequencies. As frequency decreases, the reference flux compensates for the LPF errors. The bandwidth ω_0 may be constant or adapted as in (4.15). Values in the range ω_0=0.4 ... 0.8 rad/s are suggested in [9].

Although this estimator inherits the advantages and limitations of the LPF estimator. lower speed sensorless operation is possible. Speeds as low as 10 rpm, obtained with a system that compensates for VSI nonlinearities, are reported in [9].

A superior solution, based on the same flux vector error, is to generate the compensation voltage $\underline{u}_{comp}$ as the output of a dynamic system. A proportional-integral compensator (PI) forces the flux vector onto a circular trajectory, [10], Figure 4.25.

$$\underline{u}_{comp} = (K_P + \frac{K_I}{s})(\psi_s^* e^{j\alpha} - \underline{\hat{\psi}}_s) \tag{4.19}$$

From (4.16) and (4.19), the estimated flux, in stator reference frame, is

$$\underline{\hat{\psi}}_s = \frac{s}{s^2 + K_P s + K_I}(\underline{u}_s - R_s \underline{i}_s) + \frac{K_P s + K_I}{s^2 + K_P s + K_I}\psi_s^* e^{j\alpha} \tag{4.20}$$

The first term is a band pass filter (BPF) whose eigenvalues ω_1, ω_2 are given by

$$K_P = \omega_1 + \omega_2 \qquad K_I = \omega_1 \omega_2 \tag{4.21}$$

Practical values for ω_1 and ω_2 are in the range of 1 ... 10 rad/s.

At frequencies approaching zero, the first term in (4.20) vanishes, as expected, since the BPF has zero DC gain, and the estimation is performed by the last term. In this way, the measurement offset is completely rejected. At high frequencies, the first term approximates the integral (4.11) and takes over in a smooth transition. The most important advantage of this estimator is that it operates without phase lag.

An important limitation of estimators based on reference flux is that $\underline{\psi}_s \cong \underline{\psi}_s^*$ at lower frequencies, which means that the flux controller is virtually deactivated. Nevertheless, field orientation may be lost at very low stator frequency. The PI based estimator (4.20) is superior to (4.18) because the integrator memorizes its output when $\underline{\psi}_s = \underline{\psi}_s^*$ and continues to perform the compensation in open loop.

An interesting solution, based on LPF and a nonlinear compensation strategy that takes advantage of the orthogonality between the back EMF vector and the stator flux vector, has been proposed in [11]. However, no practical implementation of this method has been reported. It appears that the method exhibits instability and loss of field orientation at and after transient operation [9].

Advantages of voltage model flux estimators are implementation simplicity, absence of coordinate transformation and robustness with respect to motor parameters variation. At high speeds, the voltage model provides accurate stator flux estimates because the back EMF dominates the measured voltage. At low speeds, the stator $i_s R_s$ drop becomes significant causing the flux estimate to be sensitive to stator resistance variation. However, the stator resistance can be accurately measured offline and/or adapted online. Due to that sensitivity and to inherent drift problems at low speeds, the voltage model practical applicability is restricted at higher speeds.

The current model

The current model relies on the rotor equation (2.57) in rotor reference frame. With measured stator current and rotor position, the rotor and stator fluxes are

$$\underline{\hat{\psi}}_r = \frac{L_m}{1+sT_r}\underline{i}_s \tag{4.22}$$

$$\underline{\hat{\psi}}_s = \frac{L_m}{L_r}\underline{\hat{\psi}}_r + \frac{L_s L_r - L_m^2}{L_r}\underline{i}_s \tag{4.23}$$

The current model (4.22) is globally stable and works well at low and zero frequency, provided that the rotor position is known, in order to perform the coordinate transformation to rotor frame. It is still parameter sensitive (to L_m and T_r), however, and has been demonstrated to be less accurate than the voltage model at high speeds [12]. Besides, it requires a rotor speed or position sensor. An insightful analysis of the estimation accuracy, under parameter detuning, for voltage and current models, is presented in [12].

4.2.2 Stator and rotor flux asymptotical observers

Jansen-Lorenz observers

It is possible to apply close loop observer techniques to form closed-loop flux observers based on the full order induction motor models. Several configurations are possible, depending on the quantities used to build up the error correction term.

The Jansen-Lorenz observer takes advantage of the best features of both, current and voltage models, [12], [13]. It implements a PI correction mechanism based on stator flux error for the voltage model, Figure 4.1. The current model operates without any correction. The voltage model and the PI feedback compensation are implemented in stator reference frame.

$$\underline{\hat{\psi}}_s = \frac{1}{s}(\underline{u}_s - R_s \underline{i}_s + \underline{u}_{comp}) \tag{4.24}$$

$$\underline{u}_{comp} = (K_P + \frac{K_I}{s})(\underline{\hat{\psi}}_s^s - \underline{\hat{\psi}}_s) \tag{4.25}$$

The current model operates open-loop, in rotor reference frame.

$$\underline{\hat{\psi}}_r^r = \frac{L_m}{1+sT_r}\underline{i}_s^r \tag{4.26}$$

$$\underline{\hat{\psi}}_s^s = \frac{L_m}{L_r}\underline{\hat{\psi}}_r^s + \frac{L_s L_r - L_m^2}{L_r}\underline{i}_s \tag{4.27}$$

$$\underline{i}_s^r = \underline{i}_s e^{-j\theta r} \qquad \underline{\hat{\psi}}_r^s = \underline{\hat{\psi}}_r^r e^{j\theta r} \tag{4.28}$$

where θ_r is the measured rotor position, superscript "s" denotes the stator frame and superscript "r" denotes the rotor frame.

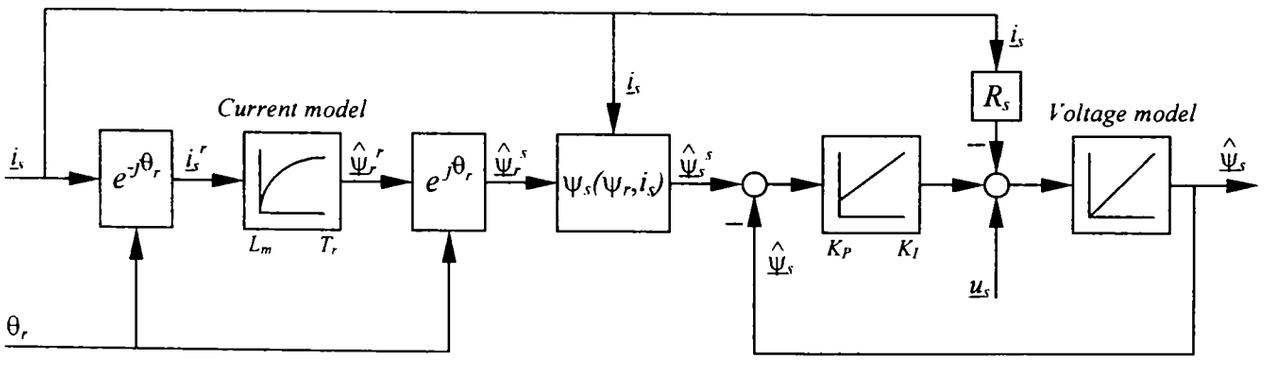

Figure 4.1 Jansen-Lorenz observer using the stator flux error

From (4.24) and (4.25), the estimated stator flux, in stator reference frame, is

$$\underline{\hat{\psi}}_s = \frac{s}{s^2 + K_P s + K_I}(\underline{u}_s - R_s \underline{i}_s) + \frac{K_P s + K_I}{s^2 + K_P s + K_I}\underline{\hat{\psi}}_s^s \tag{4.29}$$

At frequencies approaching zero, the first term in (4.29) vanishes, since it is the same BPF as in (4.20), and the observer tracks the current model reference. At high frequencies, the first term approximates the integral (4.11) and takes over the current model in a smooth transition. In this way, the best features of both models are utilized.

The transition between the two models is governed by the BPF eigenvalues ω_1 and ω_2, which may be arbitrarily allocated by selecting K_P and K_I so that

$$K_P = \omega_1 + \omega_2 \qquad K_I = \omega_1 \omega_2 \tag{4.30}$$

Practical values for ω_1 and ω_2 are in the range of 3 ... 30 rad/s.

An alternative form is obtained if the rotor flux error is employed for the PI correction of the voltage model, in stator reference frame, Figure 4.2, [13].

$$\underline{\hat{\psi}}_s = \frac{1}{s}(\underline{u}_s - R_s \underline{i}_s + \underline{u}_{comp}) \tag{4.31}$$

$$\underline{\hat{\psi}}_r = \frac{L_r}{L_m}\underline{\hat{\psi}}_s - \frac{L_s L_r - L_m^2}{L_m}\underline{i}_s \tag{4.32}$$

$$\underline{u}_{comp} = (K_P + \frac{K_I}{s})(\underline{\hat{\psi}}_r^s - \underline{\hat{\psi}}_r) \tag{4.33}$$

The current model, in rotor reference frame is

$$\underline{\hat{\psi}}_r^r = \frac{L_m}{1 + sT_r}\underline{i}_s^r \tag{4.34}$$

where coordinate transformations are given by (4.28).

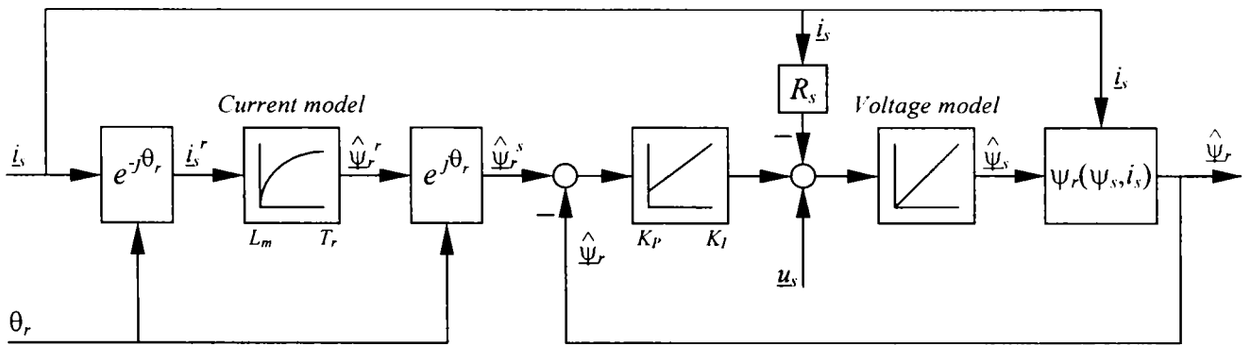

Figure 4.2 Jansen-Lorenz observer using the rotor flux error

All design considerations, presented for the first variant, remain the same.

The main drawback of Jansen-Lorenz observers is that no correction feedback is provided for the parameter sensitive current model. In some way, this plays the same role as the reference model in a model reference adaptive system, where the voltage model would be the adaptive model. Therefore, a lower BPF bandwidth is selected when parameter estimation for the current model (L_m and T_r) is poor. This forces the transition to the voltage model at lower frequencies, increasing robustness, as the voltage model is insensitive to these parameters. The estimation accuracy analysis for this observer is presented in [12] and [13].

Recalling (4.29), it may be noticed that, in mid-frequencies range, the first term behavior is still far from the ideal integrator and the current model estimate is already filtered out by the last term. Therefore, the transition range operation is problematic.

Luenberger observers

The linear time variable state space models for induction machines, introduced in Chapter 2, are adequate for Luenberger observers implementation. Since all models are in form (4.1), a full-order observer can be designed as (4.2). The block diagram of the Luenberger observer for induction machine is shown in Figure 4.3, where the input is the stator voltage, $u=\underline{u}_s$ and the measurable output is the stator current, $y=\underline{i}_s$.

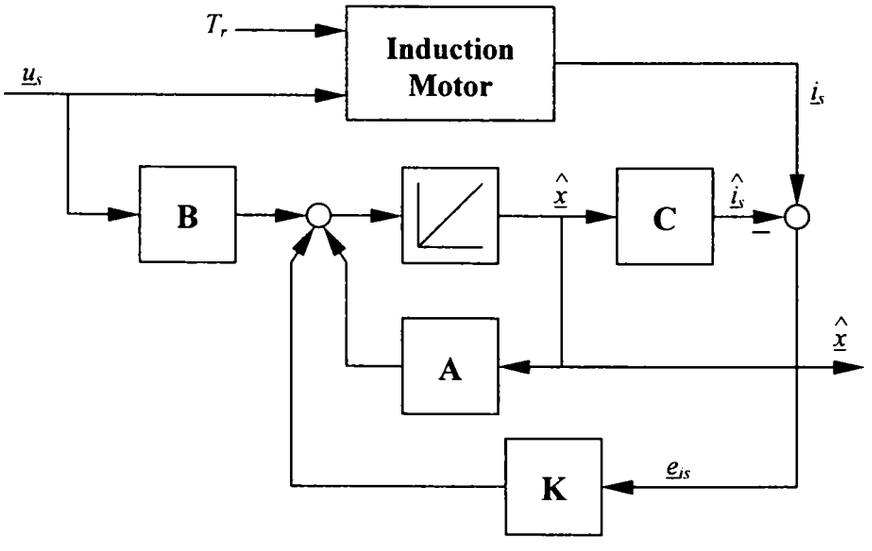

Figure 4.3 Generic Luenberger observer for induction machines

The most common approach is to design the observer based on the rotor flux model in stator reference frame, (2.60)-(2.61), as follows [14], [15]:

$$\frac{d}{dt}\begin{bmatrix}\hat{\underline{i}}_s\\ \hat{\underline{\psi}}_r\end{bmatrix}=\begin{bmatrix}A_{11} & A_{12}\\ A_{21} & A_{22}\end{bmatrix}\cdot\begin{bmatrix}\hat{\underline{i}}_s\\ \hat{\underline{\psi}}_r\end{bmatrix}+\begin{bmatrix}B_1\\ 0\end{bmatrix}\underline{u}_s+\begin{bmatrix}K_1\\ K_2\end{bmatrix}(\underline{i}_s-\hat{\underline{i}}_s) \tag{4.35}$$

where A_{ij} , i=1,2, j=1,2 are elements of $\boldsymbol{A}$ from (2.58)-(2.59), with ω_e=0.

Another approach is to use the flux model in rotor frame (2.46)-(2.47), [16].

$$\frac{d}{dt}\begin{bmatrix}\hat{\underline{\psi}}_s\\ \hat{\underline{\psi}}_r\end{bmatrix}=\begin{bmatrix}A_{11} & A_{12}\\ A_{21} & A_{22}\end{bmatrix}\cdot\begin{bmatrix}\hat{\underline{\psi}}_s\\ \hat{\underline{\psi}}_r\end{bmatrix}+\begin{bmatrix}1\\ 0\end{bmatrix}\underline{u}_s+\begin{bmatrix}K_1\\ K_2\end{bmatrix}(\underline{i}_s-\hat{\underline{i}}_s) \tag{4.36}$$

$$\hat{\underline{i}}_s=C_1\hat{\underline{\psi}}_s+C_2\hat{\underline{\psi}}_r \tag{4.37}$$

where A_{ij} , i=1,2, j=1,2 are elements of $\boldsymbol{A}$ and C_1, C_2 are elements of $\boldsymbol{C}$, from (2.41)-(2.42), with ω_e=ω_r. A signal flow diagram is shown in Figure 4.4.

Selection of gain matrix $\boldsymbol{K}$ is of paramount importance for stability, dynamic response and low sensitivity to parameter errors. The classical approach is to select the observer poles, $S_{o1,2}$ (eigenvalues of $\boldsymbol{A}$-$\boldsymbol{KC}$) proportional to the machine poles $S_{m1,2}$, i.e. $S_{o1,2}=k\cdot S_{m1,2}$, Figure 4.5.a, [15]. At very high speed operation, this method may lead to instability, in discrete time implementation because of the very large imaginary parts the observer poles reach. At lower speeds the slow pole is closer to the imaginary axis than the motor pole, giving unsatisfactory damping.

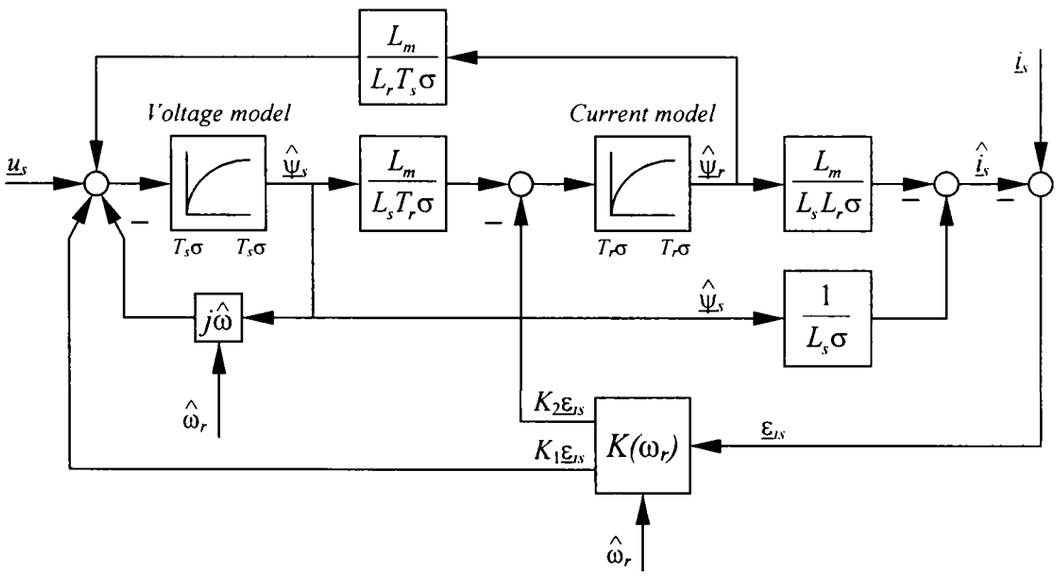

Figure 4.4 Luenberger observer based on flux model in rotor reference frame

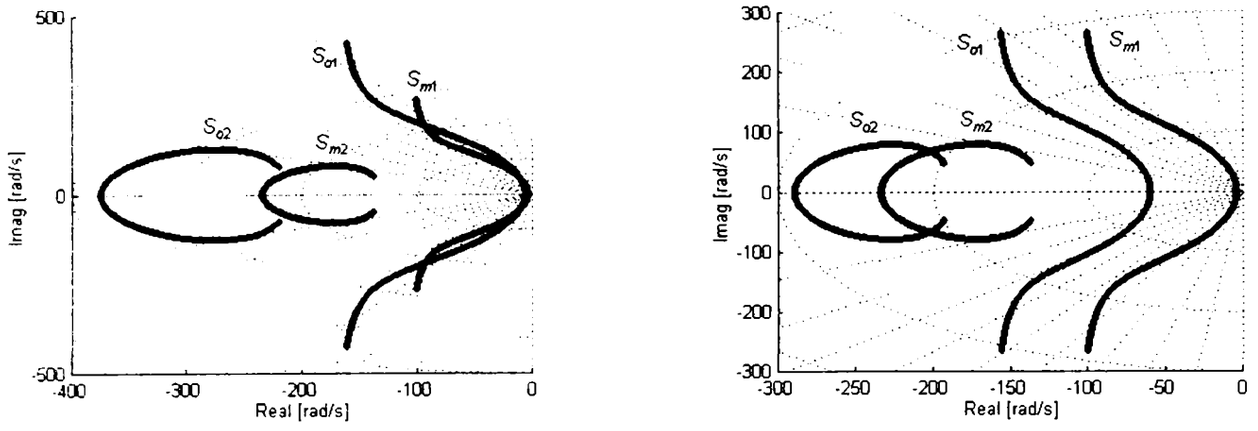

a. $S_{o1,2} = k \cdot S_{m1,2}$, $k = 1.6$, [15]

b. $S_{o1,2} = S_{m1,2} - k$, $k = 55$, [16]

Figure 4.5 Luenberger observer poles $S_{o1,2}$: and motor poles $S_{m1,2}$ for $\omega_r = 0$ to 314 rad/s

In order to have better damping control, the motor poles complex components can be multiplied with constants, k_r and k_i: $S_{o1,2} = k_r \Re e(S_{m1,2}) + jk_i \Im m(S_{m1,2})$. Rather complicated solution for $\boldsymbol{K}$ results in this way.

Another approach is to select the observer poles having the same imaginary component as the motor poles, but shifted to the left in the s-plane, by a constant positive amount k, [16]. In this way, the observer is faster than machine for the whole speed range. For rotor flux model in stator reference frame, in order to place the observer poles at $S_{o1,2} = S_{m1,2} - k$, as in Figure 4.5.b, the observer gain $\boldsymbol{K}$ is

$$K = \begin{bmatrix} K_1 \\ K_2 \end{bmatrix} = \begin{bmatrix} 2k \\ k(A_{22} - A_{11} + k)A_{12}^{-1} \end{bmatrix} \tag{4.38}$$

where A_{ij} , i=1,2, j=1,2 are elements of $\boldsymbol{A}$ from (2.58) and k>0. These gains can either be calculated online, or precalculated offline and stored in memory [17]. Figure 4.5 shows the observer and motor (Machine 1, Appendix B) eigenvalues trajectories for observer proportional poles (k=1.6) and left-shifted poles (k=55).

The observer error dynamics is given by (4.3). It is speed adaptive, as matrix $\boldsymbol{A}$ is speed dependent. Nevertheless, it is stable and performs equally well at low and high speeds. It depends on all machine parameters. However, it is less sensitive than Jansen-Lorenz observer to parameter detuning. Parameter adaptation, as proposed in [15], [16], is a solution to increase the robustness. Low speed sensorless operation at 10 rpm has been reported in [16], with a stator resistance adaptive scheme.

Reduced order observers

Since the stator current is a measurable quantity, there is no immediate need for estimating it. Rather, a reduced order observer can be constructed from the rotor flux model, in stator reference frame (2.60)-(2.61), with voltage error for corrective (predictive) feedback [14].

$$\frac{d}{dt}\hat{\underline{\psi}}_r = \frac{L_m}{T_r}\underline{i}_s + (j\omega_r - \frac{1}{T_r})\hat{\underline{\psi}}_r + L(u_s - \hat{u}_s) \tag{4.39}$$

$$\hat{\underline{u}}_s = L_s\sigma\frac{d}{dt}\underline{i}_s + (R_s + \frac{L_m^2}{L_r T_r})\underline{i}_s - \frac{L_m}{L_r}(\frac{1}{T_r} - j\omega_r)\hat{\underline{\psi}}_r \tag{4.40}$$

There is no loss of information as compared to a full order observer; both equations (2.60), (2.61) have been used. With (4.40) in (4.39), an observer equivalent to (4.6) is obtained. Indeed, model (2.60)-(2.61) is already in canonical form (4.5), with $x_1=\underline{\psi}_r$ and $y=\underline{i}_s$, and observer synthesis in form (4.6) is straightforward [18].

$$\frac{d}{dt}\hat{\underline{\psi}}_r = (A_{22} - LA_{12})\hat{\underline{\psi}}_r + (A_{21} - LA_{11})\underline{i}_s - LB_1\underline{u}_s + L\frac{d}{dt}\underline{i}_s \tag{4.41}$$

where A_{ij} , i=1,2, j=1,2 are elements of $\boldsymbol{A}$ from (2.58)-(2.59), with ω_e=0.

To avoid the current derivative, $d\underline{i}_s/dt$ calculation, the coordinate transformation (4.8) may be used, or it is avoided at implementation, as the flux estimate is obtained by integrating (4.41). The rotor flux error dynamics results from (4.10) and (2.58).

$$\frac{d}{dt}\underline{e}_{\psi r} = (j\omega_r - \frac{1}{T_r})(1 + L\frac{L_m}{L_s L_r\sigma})\underline{e}_{\psi r} \tag{4.42}$$

Several possible selections for gain $\boldsymbol{L}$ in (4.39) are suggested in [19]. With $\boldsymbol{L}$=0 the current model is obtained, while $\boldsymbol{L}$=1 gives the voltage model. It is advantageous to select $\boldsymbol{L}$ so that a seamless transition between the current and the voltage models takes place within a finite frequency band (ω_1 ω_2). Possible observer gain selections are: $L = |z|$, or $L = -jz$, or $L = 1 - j(z + i_q / i_d)$, where

$$z = z_0\begin{cases} 0, & |\omega_r| \le \omega_1 \\ (|\omega_r| - \omega_1)/(\omega_2 - \omega_1), & \omega_1 < |\omega_r| < \omega_2 \\ \mathrm{sgn}(\omega_r), & |\omega_r| \ge \omega_2 \end{cases} \tag{4.43}$$

Typical transition band is at about 5%-30% of base speed and z_0 is constant.

Another method for selecting $\boldsymbol{L}$ in (4.42) is described in [18]. In this case, the observer pole (the observer equation is first order complex) is allocated such that to minimize the observer sensitivity to rotor resistance detuning.

At high and low speeds, the reduced order observer inherits advantages and limitations of the voltage and current models, respectively. In [19], a detailed analysis of the reduced order observer is carried out and experiments at 50 rpm are reported. Experiments at 150 rpm and an attempt to run a 0 rpm are reported in [18].

Conclusions

Nevertheless, a multitude of linear estimators and observers can be constructed for induction machines. The voltage and current models are the most basic schemes, but their stand-alone performance is very modest. Estimators derived from the voltage model are very attractive due to their simplicity and relative robustness. Speeds as low as 10 rpm have been reported in [9] with a stator resistance adaptive scheme.

The best and, probably, the most popular topology is the adaptive Luenberger observer that exhibits the best overall performance with the price of highest complexity. Its behavior is good in the whole speed range, including very low speeds; 10 rpm is the best low speed performance reported with an adaptive observer [16].

Less complex and also less performant, are the reduced order and Jansen-Lorenz observers. Both are sensitive to current model parameters detuning, especially at low speeds, and Jansen-Lorenz observer shows rather poor performance in the mid speed range. Continuous operation at about 50 rpm is reported in [19] with a reduced order observer.

The most important drawback of all linear observers is the sensitivity to model parameter detuning. This lack of robustness has negative impact on low speed behavior, producing loss of field orientation and overall performance degradation. As mentioned, many of the proposed schemes that display low speed performance are parameter adaptive.

4.3 Asymptotical Observers – Proposed Solutions

4.3.1 Inherent sensorless Luenberger observers

Observer synthesis

Standard Luenberger observers, given by (4.35) and (4.36), are speed adaptive schemes, Figure 4.6, [14]-[16]. Various machine models and various reference frames can be used to implement them, but always the implementation is carried out in one frame. Whatever the model and the reference frame are, at least one element of system matrix $\boldsymbol{A}$ contains the rotor speed as an adaptive parameter.

Rather than being an advantage, this is an inconvenience. The speed estimator, labeled "Adaptation mechanism" in Figure 4.6, employs the estimated state and, in general, in a digital controlled system that operates sequential, it is the last step of the state estimation process. Hence, the speed estimate is affected by cumulative errors, noise and, most important, is time-delayed. This slightly erroneous estimate is fed-back to the state observer in the same or in the subsequent sampling cycle.

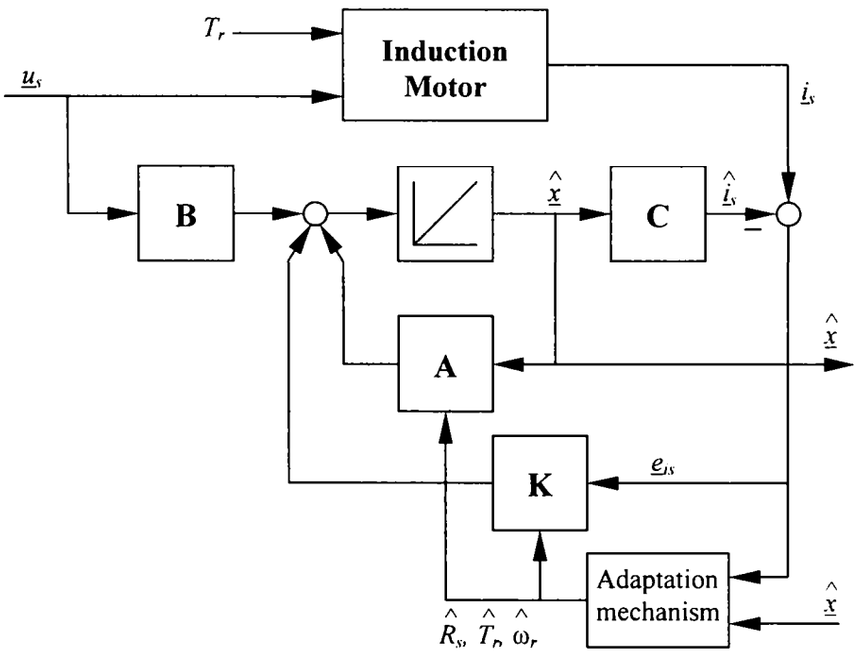

Figure 4.6 Adaptive Luenberger observer for induction machines

In this way the accuracy of state estimation may progressively worsen. Although the speed adaptive observer is stable, undesirable effects, such as limit cycles, high sensitivity to noise, or phase shifting, tend to occur and to deteriorate the overall system's performance.

The *inherent sensorless observer* proposed here and illustrated in Figure 4.7 is input-output equivalent to Luenberger observer in Figure 4.4. However, using two reference frames – stator frame for stator equation and rotor flux frame for rotor equation – allows eliminating the speed feedback.

Consider the flux model in arbitrary reference frame (2.37)-(2.38). An observer in form (4.36) can be constructed, with A_{ij} given by (2.41).

$$\frac{d}{dt}\begin{bmatrix}\hat{\underline{\psi}}_s\\ \hat{\underline{\psi}}_r\end{bmatrix}=\begin{bmatrix}A_{11} & A_{12}\\ A_{21} & A_{22}\end{bmatrix}\cdot\begin{bmatrix}\hat{\underline{\psi}}_s\\ \hat{\underline{\psi}}_r\end{bmatrix}+\begin{bmatrix}1\\ 0\end{bmatrix}\underline{u}_s+\begin{bmatrix}K_1\\ K_2\end{bmatrix}(\underline{i}_s-\hat{\underline{i}}_s) \tag{4.44}$$

From (2.32), the estimated rotor flux is

$$\hat{\underline{\psi}}_r=\frac{L_r}{L_m}\hat{\underline{\psi}}_s-\frac{L_sL_r-L_m^2}{L_m}\underline{i}_s \tag{4.45}$$

With (4.44) in the first equation of (4.44), the observer is

$$\frac{d}{dt}\hat{\underline{\psi}}_s=-R_s\underline{i}_s-j\omega_e\hat{\underline{\psi}}_s+\underline{u}_s+K_1(\underline{i}_s-\hat{\underline{i}}_s) \tag{4.46}$$

$$\frac{d}{dt}\hat{\underline{\psi}}_r=\frac{L_m}{L_sT_r\sigma}\hat{\underline{\psi}}_s-\left(\frac{1}{T_r\sigma}+j(\omega_e-\omega_r)\right)\hat{\underline{\psi}}_r+K_2(\underline{i}_s-\hat{\underline{i}}_s) \tag{4.47}$$

In (4.45), the current $\underline{i}_s$ is the measured value rather than the estimated one.

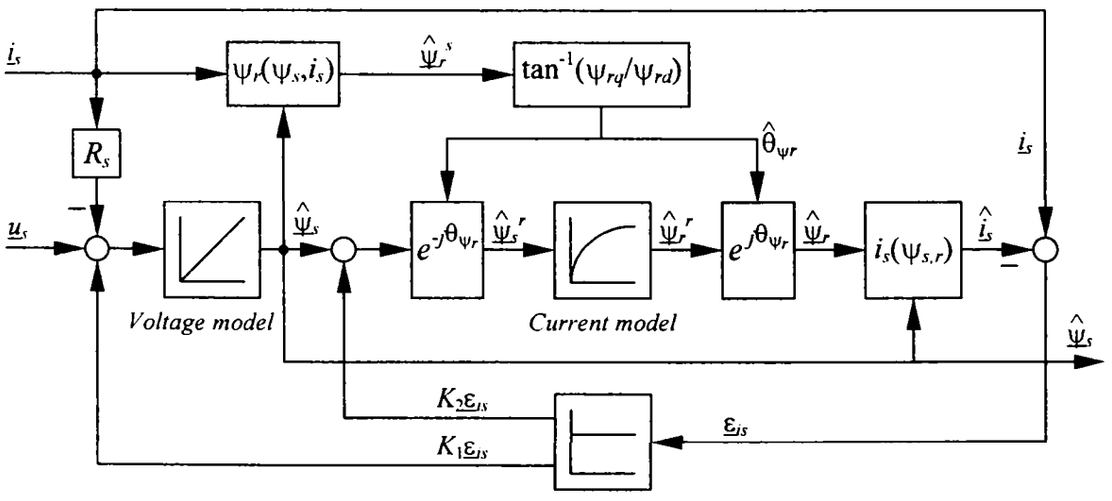

Figure 4.7 Inherent sensorless Luenberger observer for induction machines

Equation (4.46) is implemented in stator reference frame (voltage model), ω_e=0

$$\frac{d}{dt}\hat{\underline{\psi}}_s = -R_s\underline{i}_s + \underline{u}_s + K_1(\underline{i}_s - \hat{\underline{i}}_s) \tag{4.48}$$

Equation (4.47) is implemented in rotor flux reference frame, $\omega_e=\omega_{\psi r}$

$$\frac{d}{dt}\hat{\underline{\psi}}_r^r = \frac{L_m}{L_s T_r \sigma}\hat{\underline{\psi}}_s^r - (\frac{1}{T_r\sigma} + j(\omega_{\psi r} - \omega_r))\hat{\underline{\psi}}_r^r + K_2(\underline{i}_s^r - \hat{\underline{i}}_s^r) \tag{4.49}$$

In rotor flux frame the rotor flux is $\hat{\underline{\psi}}_r^r = \hat{\psi}_{rd}^r$ and (4.49) separates into

$$\frac{d}{dt}\hat{\psi}_{rd}^r = \frac{L_m}{L_s T_r \sigma}\hat{\psi}_{sd}^r - \frac{1}{T_r\sigma}\hat{\psi}_{rd}^r + \Re e(K_2(\underline{i}_s^r - \hat{\underline{i}}_s^r)) \tag{4.50a}$$

$$\hat{\psi}_{rq}^r = 0 \tag{4.50b}$$

Finally the estimated stator current in stator frame is calculated with (4.51).

$$\hat{\underline{i}}_s = \frac{1}{L_s\sigma}\hat{\underline{\psi}}_s - \frac{L_m}{L_s L_r \sigma}\hat{\underline{\psi}}_r \tag{4.51}$$

The estimated rotor flux in stator frame is obtained using the transformation $\hat{\underline{\psi}}_r = \hat{\underline{\psi}}_r^r e^{j\theta\psi r}$. The estimated rotor flux position, needed for coordinate transformations, is $\hat{\theta}_{\psi r} = \tan^{-1}(\hat{\psi}_{rq}^s / \hat{\psi}_{rd}^s)$, where the estimated rotor flux, $\underline{\psi}_r^s$ is obtained from (4.45), using the estimated stator flux and the measured current.

The observer is realized with (4.48)-(4.51) and the coordinate transformations to and from rotor flux reference frame. It is input-output equivalent to observer (4.44) and there is no rotor speed is involved. This scheme is extremely useful for drives that don't need the speed estimate for other purposes, e.g. electric vehicles.

The observer gain ***K*** can be determined by pole placement methods described by Figure 4.5. These methods are computation intensive and, sometimes, inconvenient for digital implementation. Several simple and practical methods are discussed next.

If the rotor speed is available, it is advantageous to make ***K*** speed adaptive

$$K = \begin{bmatrix} K_1 \\ K_2 \end{bmatrix} = \begin{bmatrix} k_{1r} + j\omega_r k_{1i} \\ k_{2r} + j\omega_r k_{2i} \end{bmatrix} \tag{4.52}$$

The observer matrix is ***E=A-KC***, with ***A*** and ***C*** from (2.41)-(2.42), based on equivalence with (4.44). Its eigenvalues, $S_{o1,2}$ and Motor 1 poles, $S_{m1,2}$ are shown in Figure 4.8.a for gains K_1=1.5+$j\omega_r$0.012, K_2=-1.2+$j\omega_r$0.012 and ω_r = 0… 314 rad/s.

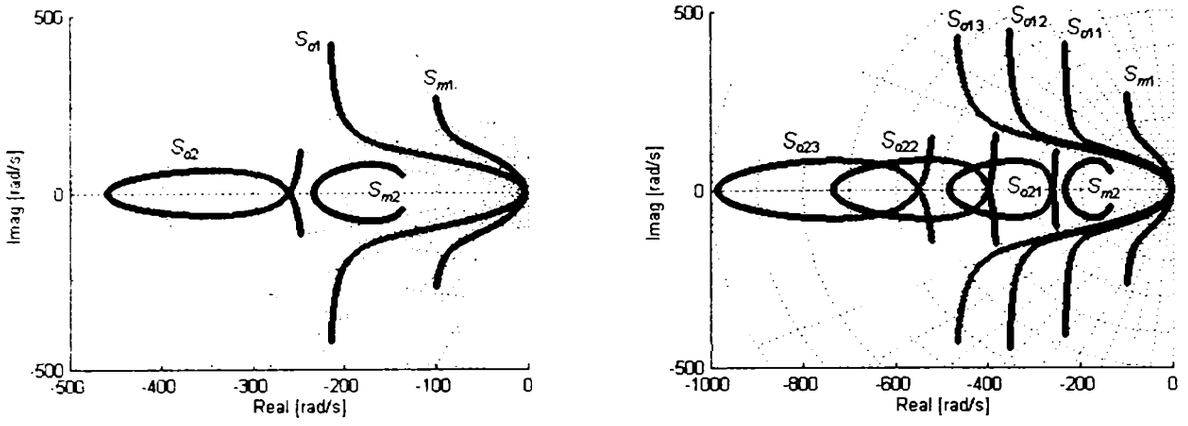

a. $K_1 = 1.5+j\omega_r 0.012$, $K_2 = -1.2+j\omega_r 0.012$ b. $\boldsymbol{K}_z = z\boldsymbol{K}$, $z = 1, 2, 3$, same K_1 and K_2

Figure 4.8 Observer poles $S_{o1,2}$ and motor poles $S_{m1,2}$ for speed adaptive gains

Once K_1 and K_2 have been determined for a motor, a family of curves for $S_{o1,2}$ can be obtained by multiplying $\boldsymbol{K}$ with a constant z, $\boldsymbol{K}_z=z\boldsymbol{K}$. Figure 4.8.b shows this family for z=1,2,3 with same K_1, K_2 as above. For the entire speed range the observer poles are located to the left of motor poles, better than those in Figure 4.5.a.

Although this method appears simple, there isn't a general design methodology adequate for design of $\boldsymbol{K}$. A trial-and-error approach, with the aid of some dedicated software, is a practical solution. Equation (4.52) offers more flexibility.

For example, if (4.52) is designed in the form

$$K = \begin{bmatrix} K_1 \\ K_2 \end{bmatrix} = \begin{bmatrix} -R_s + (1/T_r - j\omega_r)k_1 \\ L_m/T_r + (1/T_r - j\omega_r)k_2 \end{bmatrix} \tag{4.53}$$

then the observer matrix, $\boldsymbol{E}=\boldsymbol{A}-\boldsymbol{KC}$, with $\boldsymbol{A}$ and $\boldsymbol{C}$ from (2.41)-(2.42), is

$$E = (-\frac{1}{T_r} + j\omega_r)\begin{bmatrix} k_1C_1 & k_1C_2 \\ k_2C_1 & k_2C_2+1 \end{bmatrix} = (-\frac{1}{T_r} + j\omega_r)H \tag{4.54}$$

It is easy to prove that, if h_1 and h_2 are eigenvalues of $\boldsymbol{H}$, then the observer eigenvalues are $S_{o1,2} = (-1/T_r + j\omega_r)h_{1,2}$. Once $S_{o1,2}$ have been allocated by selection of h_1 and h_2, observer gains k_1 and k_2 can easily be determined using (4.55).

$$k_1 = L_s\sigma h_1 h_2, \qquad k_2 = L_s L_r \sigma(h_1h_2 - h_1 - h_2 + 1)/L_m \tag{4.55}$$

This method creates poles with constant real component, if h_1, h_2 are real. Figure 4.9.a shows the motor and observer pole locus for $h_1 = 0.4+j1.2$ and $h_2 = 1.2+j$.

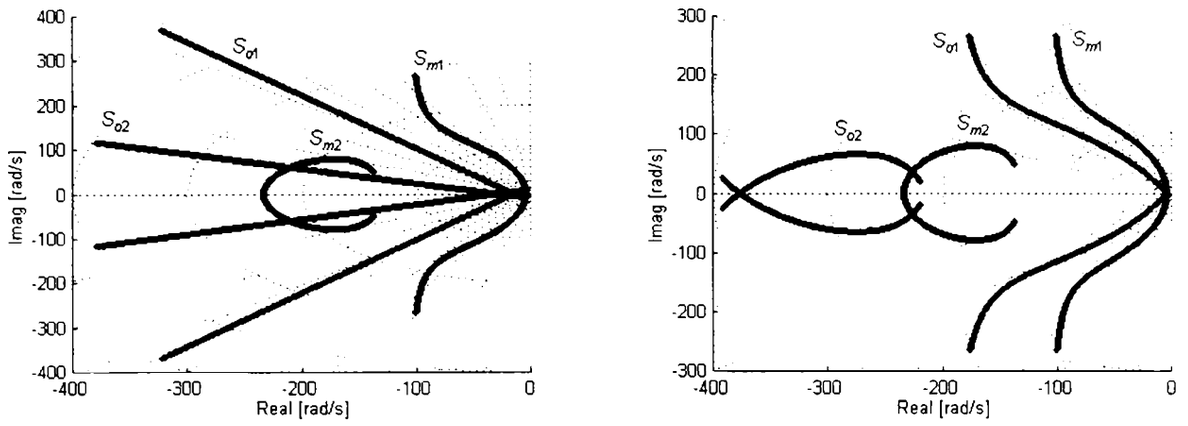

a. $h_1 = 0.4+j1.2$ and $h_2 = 1.2+j$.

b. $K_1 = 0.8 + j\ 1.2$ and $K_2 = -1.1 + j\ 0.9$

Figure 4.9 Observer and motor poles for speed adaptive gain (a) versus constant gain (b)

The disadvantage of this technique is that, at low speeds, all observer poles have very small real components, even smaller than motor poles real components.

A solution, consistent with the inherent sensorless observer philosophy, would be to design a completely speed-independent gain. Hence, the simplest, and yet practical, selection for $\boldsymbol{K}$ is a constant matrix.

$$K = \begin{bmatrix} K_1 \\ K_2 \end{bmatrix} = \begin{bmatrix} k_{1r} + jk_{1i} \\ k_{2r} + jk_{2i} \end{bmatrix} \tag{4.56}$$

Observer and motor pole locus, obtained with constant gains K_1=0.8+j1.2 and K_2=-1.1+j0.9 are shown in Figure 4.9.b. At low speeds, the position of poles is more advantageous than that of the speed adaptive solution from Figure 4.9.a.

The main limitation of all design methods described here is that, at low speeds, the observer poles are close to motor poles. Sometimes, this gives unsatisfactory dynamic behavior. At high speed, despite their simplicity, all methods respect the requirement to place the observer poles to the left of motor poles and display good performance.

The observer's stability depends on gain $\boldsymbol{K}$ selection. The common practice is to assume that the speed is slowly variable if compared to other quantities. Therefore, it can be considered a constant parameter and the observer matrix $\boldsymbol{E}$ becomes time-invariant. In this case, the observer is stable because $\boldsymbol{E}$ is Hurwitz, i.e. its eigenvalues are located in the left-half plane, as can bee noticed from Figures 4.5, 4.8 and 4.9.

Solutions for offset sensitivity compensation

Extensive simulations have been performed in order to determine the observer's performance with respect to perturbations and model parameter deviations. The most important simulation results and conclusions are presented herewith.

Figure 4.10 shows simulation results with a sensorless drive that employs the Linear-DTC and the proposed inherent sensorless observer, under perfect tuning of observer and controller. In these conditions, the estimated stator flux and rotor flux magnitudes match their actual values without errors. Also, the torque estimation error (not shown) is practically zero. As can be observed, the observer's robustness with respect to perturbations (dynamic stiffness) is excellent.

The speed and torque scenario in Figure 4.10 is repeated for all subsequent simulations. The motor (Machine 1) is started at rated speed n_N and decelerated at $0.01n_N$ after 2 sec. Load torque of 27 Nm (motor's rated torque) is applied at 1 sec.

The stator flux magnitude, rotor flux magnitude, torque and speed estimation errors for operation with 0.3 V offset, added on voltage measurements, are shown in Figure 4.11. The flux estimation at low speed is significantly deteriorated.

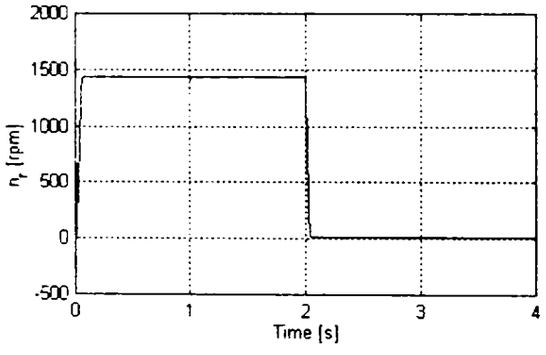

a. Actual speed

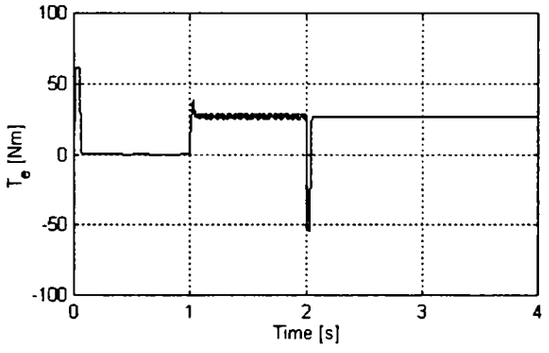

b. Actual torque

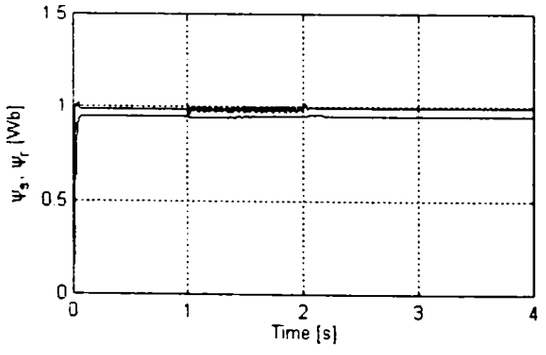

c. Actual stator flux and rotor flux

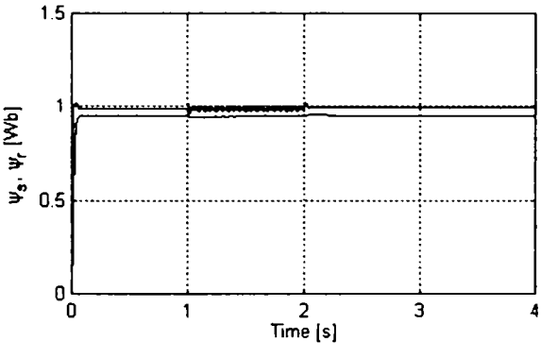

d. Estimated stator and rotor flux

Figure 4.10 Sensorless operation of Linear-DTC with asymptotical observer - simulations

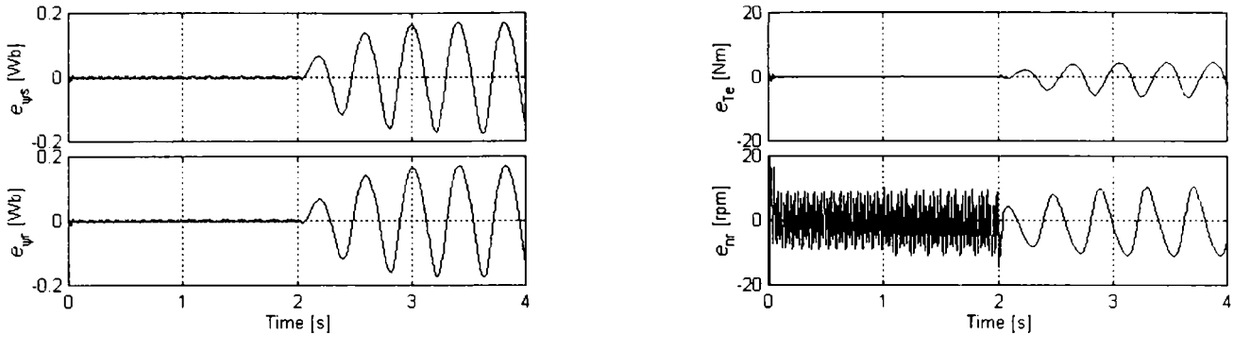

a. Stator and rotor flux errors

b. Torque and speed errors

Figure 4.11 Estimation errors for asymptotical observer, with 0.3 V measurement offset

This sensitivity to measurement offset is unacceptable for high performance drives. In order to compensate for this, two observers, derived from the basic scheme in Figure 4.7, are proposed in Figures 4.12 and 4.14.

An inherent sensorless asymptotical observer, with PI dynamics on the voltage model feedback compensation, is depicted in Figure 4.12. The observer model remains (4.46)-(4.47) and only the gain $\boldsymbol{K}$ is redesigned as

$$K = \begin{bmatrix} K_P + K_I / s \\ K_2 \end{bmatrix} \tag{4.57}$$

where K_P, K_I and K_2 are determined such that the observer is stable. K_P is the same as K_1 from (4.48) and K_I design is based on the BPF design procedure (4.21).

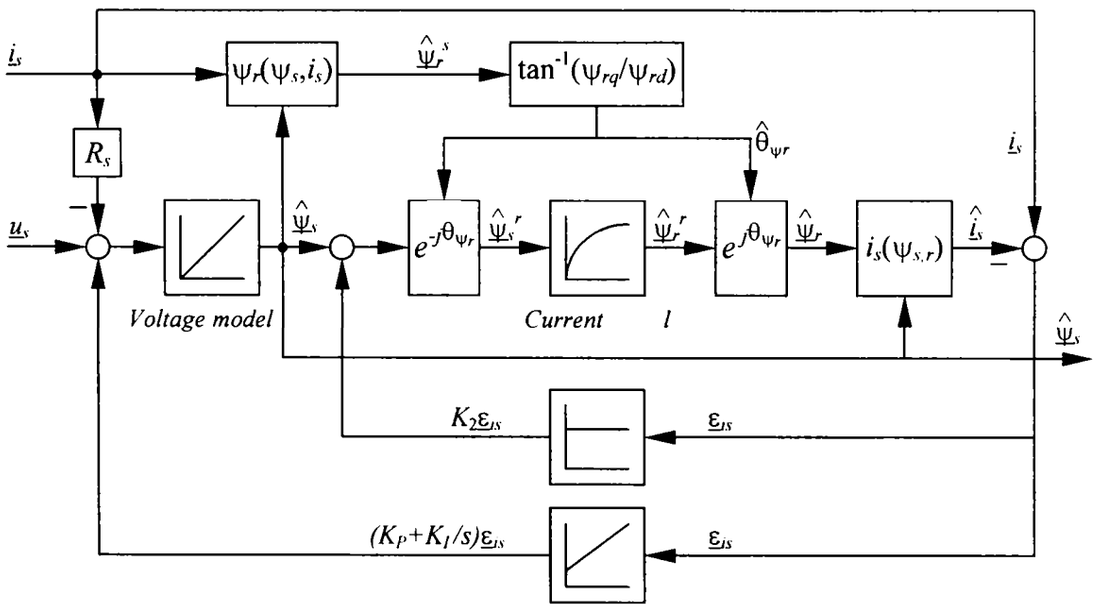

Figure 4.12 Inherent sensorless observer with added dynamics for offset compensation

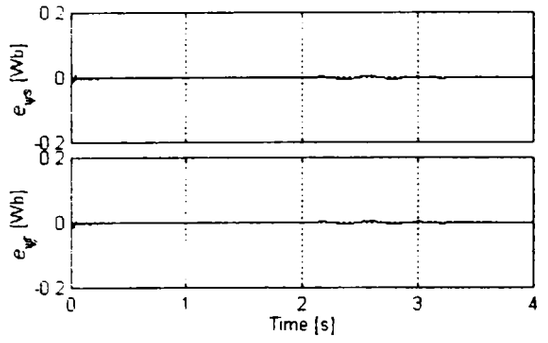

a. Stator and rotor flux estimation errors

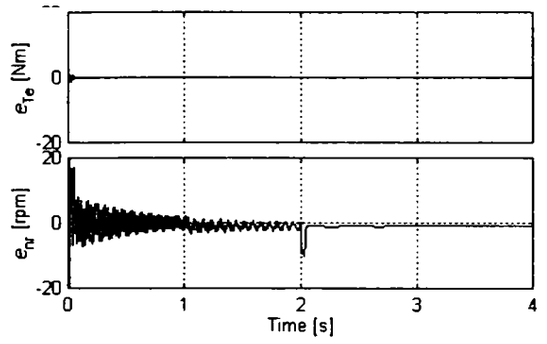

b. Torque and speed estimation errors

Figure 4.13 Estimation errors for modified asymptotical observer, with 0.3 V offset

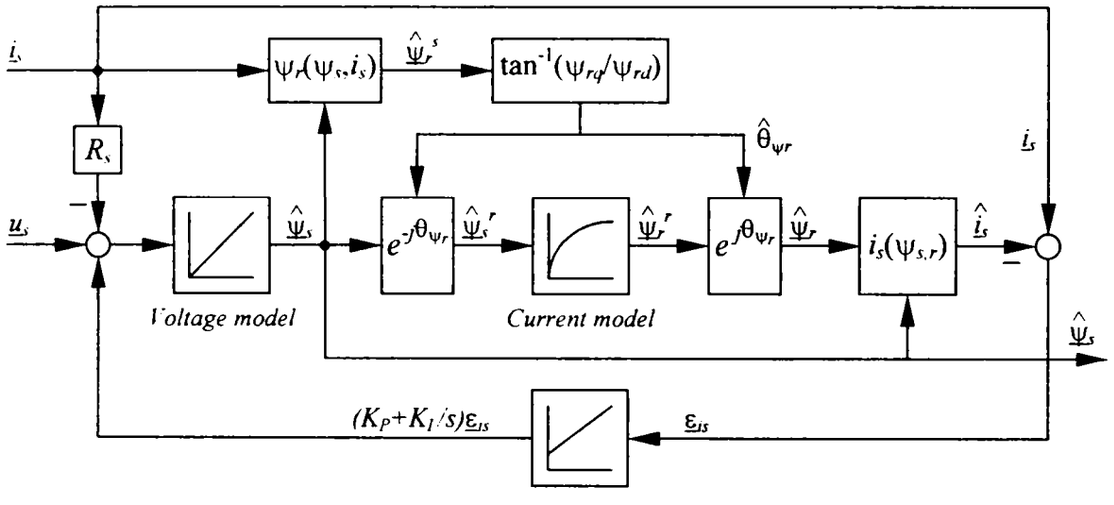

Figure 4.14 Simplified observer with added dynamics for offset compensation

Simulation results with the modified observer, with K_P=40, K_I=80 and 0.3 V offset, are shown in Figure 4.13. The flux magnitude and torque estimation errors are practically zero for the whole speed range and the speed shows some errors at startup and at low speed. This is an indication that, at high speeds, the offset has a stronger influence on flux vector phase, influence that is eventually removed. Overall, the modified observer is stable and robust with respect to measurement offset.

If the current model parameters, L_m and T_r are precisely known, the observer can be simplified by eliminating the current model feedback compensation (K_2=0), as shown in Figure 4.14. It was determined by simulations that both observers with PI voltage model compensator exhibit the same, very good performance (Figure 4.13), in the presence of measurement offset.

Parameter sensitivity analysis

Like most sensorless schemes, the performance of this observer depends on accurate estimation of model parameters, which vary as a function of temperature, saturation and load. Model parameter mismatch degrades the accuracy of flux and speed estimation, at very low speed, eventually leading to unstable operation.

Simulations with detuned observer have been carried out in order to determine the overall system's performance and stability limits in face of parameter detuning. The estimated stator and rotor flux magnitude errors, $e_{\psi s} = \psi_s - \hat{\psi}_s$ and $e_{\psi r} = \psi_r - \hat{\psi}_r$, with inaccurate L_m, R_r and R_s are shown in Figure 4.15.

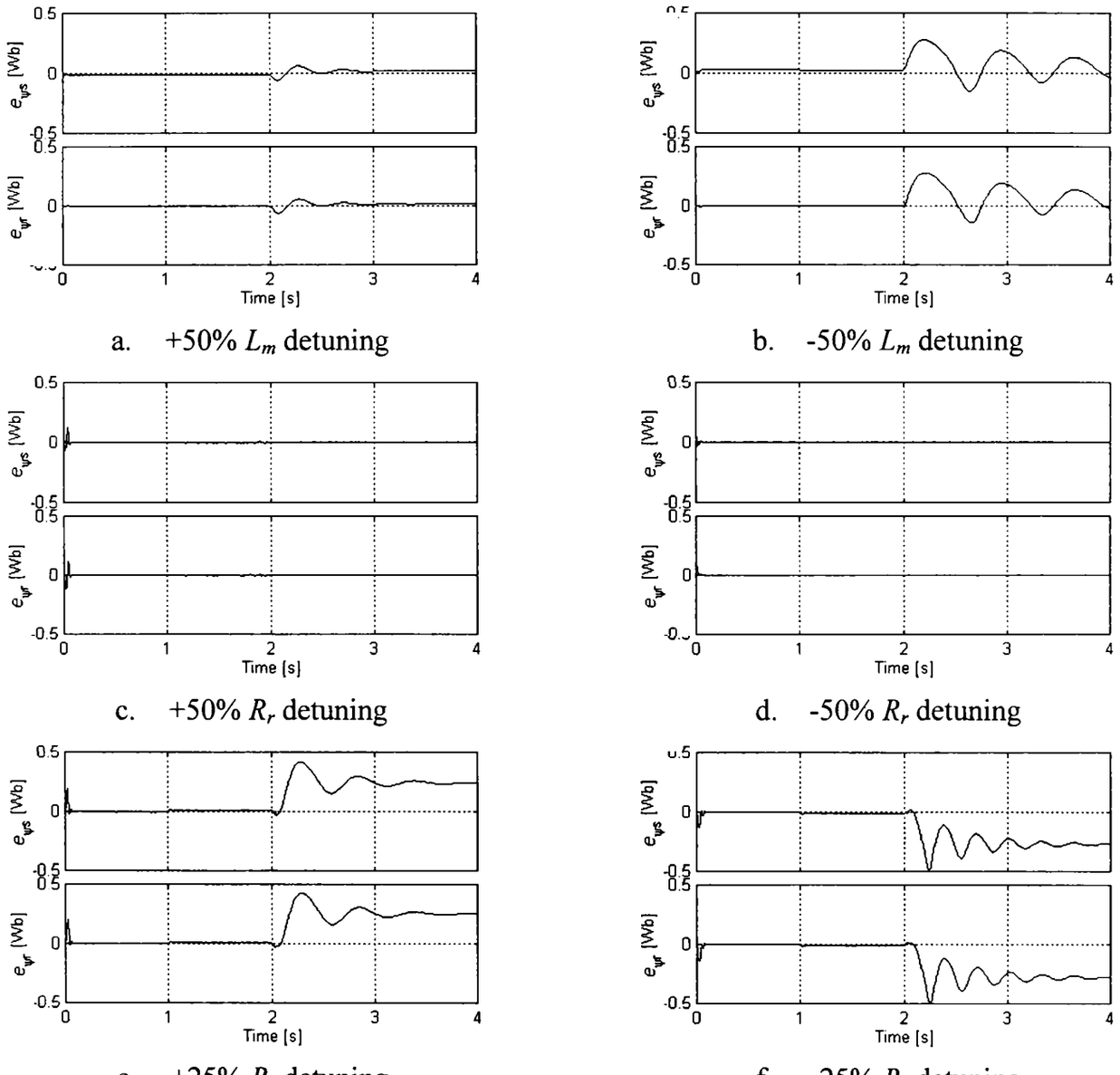

a. +50% L_m detuning

b. -50% L_m detuning

c. +50% R_r detuning

d. -50% R_r detuning

e. +25% R_s detuning

f. -25% R_s detuning

Figure 4.15 Stator and rotor flux estimation errors with L_m, R_r and R_s detuning - simulations

System's sensitivity to magnetizing inductance detuning is illustrated in Figure 4.15.a, b. Large overestimation of L_m, even larger than +50%, has only a marginal impact on flux estimation at low speeds and during transients, Figure 4.15.a. However, underestimation below -50% produces instability. Thus, in the case when L_m is not very well known, an overestimation of it is recommended.

The magnetizing inductance is saturation dependent (Appendix B, Figure B.1). The simplest method to take saturation into account is to consider the magnetizing inductance as a function of the main flux $L_m(\psi_m)$, and to employ models including saturation, as determined in Chapter 2. The functional $L_m(\psi_m)$ can be implemented analytically, as exemplified in Appendix B (B.1), or as a lookup table.

In vector-controlled drives, the flux is constant for operation below base speed and L_m can be considered constant. This is the case here and in all subsequent simulations and experiments L_m has been implemented constant.

The observer is insensitive to rotor resistance detuning, as shown by Figure 4.15.c, d. There are only small errors during flux transients, due to rotor time constant detuning. Errors, even larger than ±100% in R_r value have no significant influence on flux estimation. This is a very important advantage of the proposed observer.

Stator resistance adaptation

Simulated stator and rotor flux estimation errors with ±25% stator resistance detuning are shown in Figure 4.15.e, f. High-speed operation is marginally affected, but low speed operation is ruined. Errors larger than ±25% produce instability at low speeds. At no load, the observer is completely insensitive to R_s mismatch, at both, high and low speeds. A stator resistance adaptation mechanism is mandatory.

There are two basic approaches to parameter estimation or adaptation: statistical fitting of parameters from measured data and adaptive control to modify parameters and force convergence. In general, statistical approaches are most widely used for self commissioning at startup, while adaptive control approaches are used for continuous self-tuning during use, as in Figure 4.6.

A simple solution for stator resistance online tuning, based on voltage model (2.15) in stator current reference frame, $\omega_e=\omega_{is}$, is described in [9] and [20].

At sinusoidal steady state operation, the flux is constant, $d\underline{\psi}_s/dt=0$ and (2.15) is

$$\underline{u}_s = R_s \underline{i}_s + j\omega_{is} \underline{\psi}_s \tag{4.58}$$

Taking into account that, in current frame, $\underline{i}_s = i_{sd}$, the stator resistance is determined using the measured voltage and current, and the estimated stator flux.

$$\hat{R}_s = \frac{1}{i_{sd}}(u_{sd} + u_{sq}\frac{\hat{\psi}_{sq}}{\hat{\psi}_{sd}}) \tag{4.59}$$

This method is applicable at steady state, with the stator flux estimated by the current model. Using the voltage model for both, flux and resistance estimation may result in estimation errors. At high frequencies, R_s is obtained as the difference of two large quantities ($\psi_{sq}<0$) and this also induces some estimation errors. However, a sensorless drive that operates at very low speed (10 rpm), using the voltage model flux estimator (4.18) and the resistance estimator (4.59), is reported in [9].

Stator resistance adaptation methods based on model reference adaptive system (MRAS) are very popular and more accurate. The MRAS approach is based upon comparing actual measurements with a feasible model. The adaptation mechanism is excited by a nonlinear error that is a cross-correlation product that averages out the signals that are uncorrelated with the reference model.

A MRAS scheme for stator resistance estimation, determined from Lyapunov stability analysis, is described [15] and [16]. In stator frame, the estimated resistance is

$$\hat{R}_s = -K_{Rs}\frac{1}{s}(\hat{i}_{s\alpha}e_{is\alpha} + \hat{i}_{s\beta}e_{is\beta}) \tag{4.60}$$

where K_{Rs} is a positive gain and $e_{is} = \underline{i}_s - \underline{\hat{i}}_s$ is the current estimation error. A standard Luenberger observer (4.35) is used for current estimation, Figure 4.6.

Simulations and experiments with the proposed observer indicated that (4.60) is able to accurately estimate the resistance in load conditions, at high and low speeds. However, at no-load, a disturbing, undesired drift appears in R_s estimation.

Several forms for the nonlinear error have been experimented and it was found that the new stator resistance estimator (4.61) is superior to (4.60).

$$\hat{R}_s = -K_{Rs}\frac{1}{s}(\hat{i}_{r\alpha}e_{is\beta} - \hat{i}_{r\beta}e_{is\alpha}) \tag{4.61}$$

where $\underline{\hat{i}}_r = (\underline{\hat{\psi}}_r - L_m\underline{i}_s)/L_r$ is the estimated rotor current.

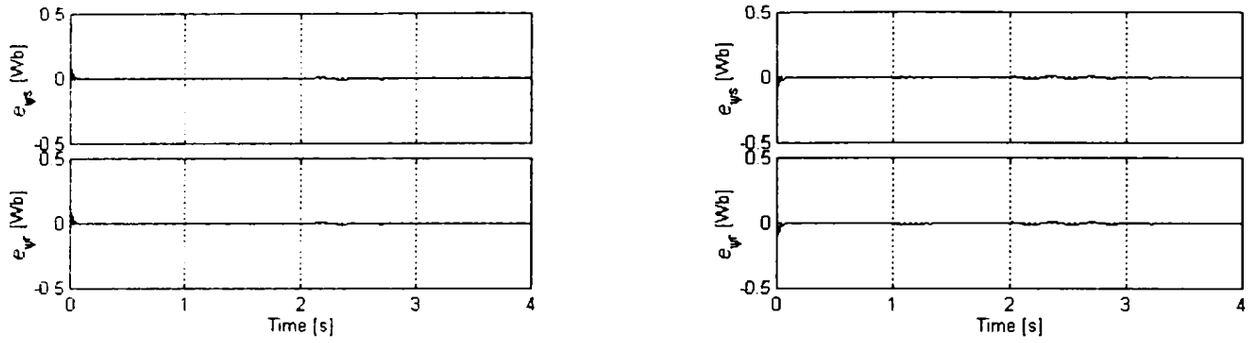

Figure 4.16 Stator and rotor flux errors with ±50% R_s detuning and adaptation (4.61)

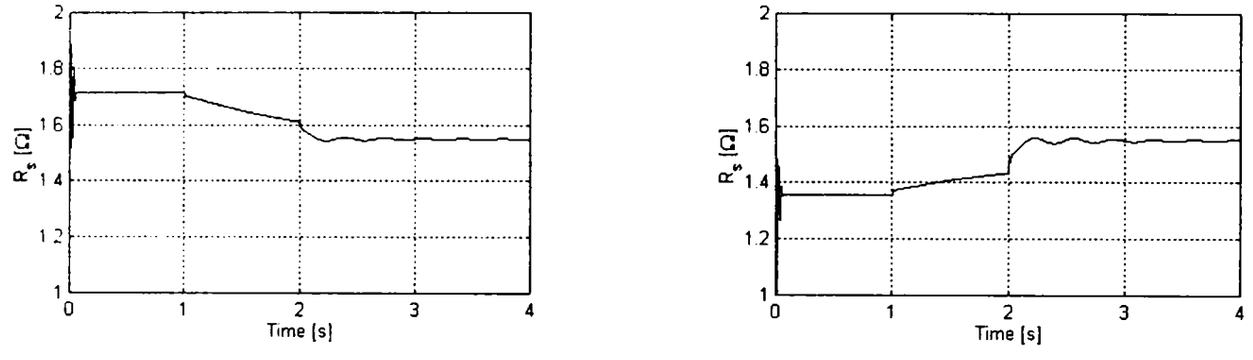

Figure 4.17 Stator resistance estimation with ±50% initial detuning and adaptation (4.61)

Simulated stator and rotor flux estimation errors, with ±50% R_s initial detuning, twice as in Figure 4.15, using R_s adaptation (4.61), are presented in Figure 4.16. The estimated stator resistance is shown in Figure 4.17. The correct value, R_s=1.55 Ω, is accurately estimated in powering operation. As expected, there is no adaptation during no-load. The speed and load scenario is the same as in Figure 4.10.

Experimental results

Extensive experiments have been carried out in order to demonstrate the performance of the proposed observers and adaptation techniques. Very low speed sensorless operation was targeted and the system's ability, to operate stable, under full load, at zero and very low speed, has been confirmed.

Zero speed, full load, sensorless operation, with Luenberger inherent sensorless observer, is presented in Figure 4.18 (estimated and measured speed, estimated torque, stator and rotor flux, and stator current). The control strategy is RCG-VSC, with PLL speed estimation and the motor under test is Machine 2 (1.1 kW, Appendix B).

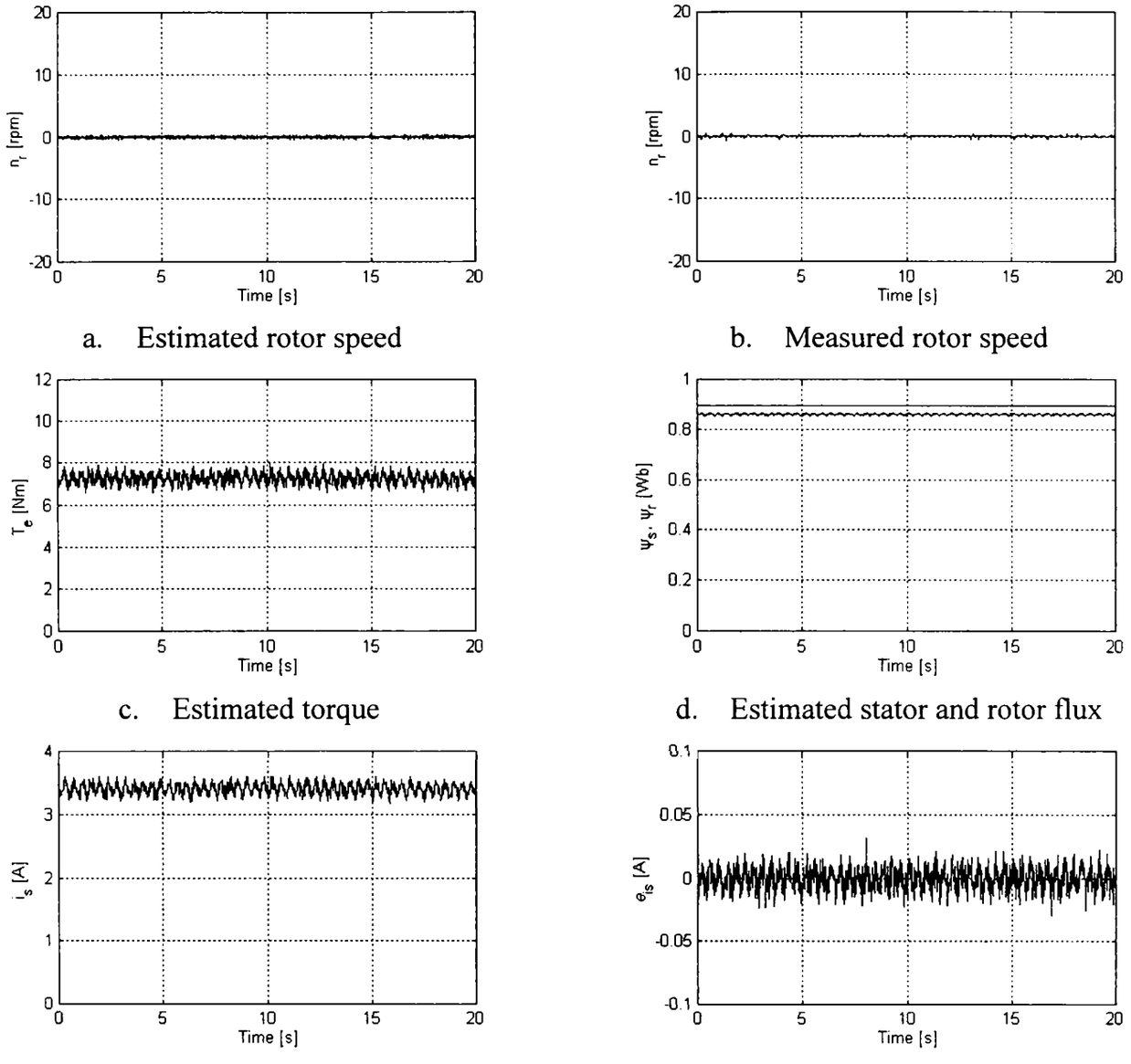

a. Estimated rotor speed

b. Measured rotor speed

c. Estimated torque

d. Estimated stator and rotor flux

e. Estimated stator current magnitude

f. Current magnitude estimation error

Figure 4.18 Zero speed sensorless operation with RCG Control and Luenberger observer

The overall system's performance is excellent and the fact that the estimated current matches very well the measured one (Figure 4.18.e and f) and estimated speed matches the measured speed, with the exception of some high frequency noise, is an indication that the estimation system performs very well.

It is difficult to separate the flux observer and the speed observer contributions. In order to prove that the flux observer behaves well in various conditions, speed transients and high-speed operation with a different system, are shown in Figure 4.19. The system employs Linear-DTC with constant stator flux control, inherent sensorless observer, speed estimator and the motor under test is Machine 1 (4 kW).

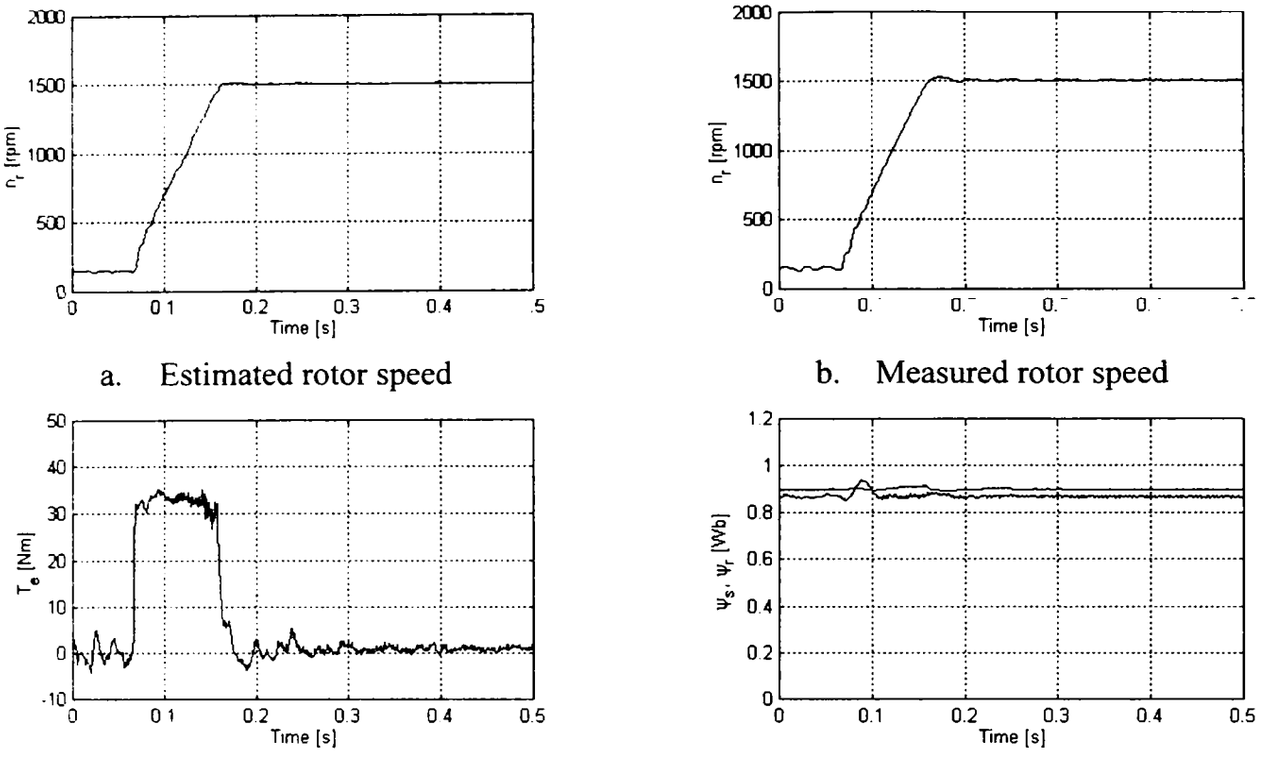

Figure 4.19 Acceleration from 150 to 1500 rpm with Linear-DTC and Luenberger observer

Although Linear-DTC is inferior to RCG-VSC in terms of robustness and the speed estimator is inferior to PLL observer during fast transients, the overall system's performance is good and the estimated speed matches well the measured one. More experiments with this system have been reported in [21].

Conclusions

A new asymptotical observer for induction machines state estimation has been developed and analyzed. It is called inherent sensorless observer because there is no rotor speed information involved, that is, the observer is not speed adaptive. Design considerations for the observer gain selection are presented.

Two modified observer topologies, insensitive to measurement offset, have been derived from the basic scheme. A novel stator resistance adaptation mechanism has been proposed and successfully tested. The observer's good performance, including zero speed and very low speed, full load operation, has been demonstrated by experiments.

4.3.2 Modified Jansen-Lorenz observers

Observer synthesis

Jansen-Lorenz observers presented in Figures 4.1 and 4.2, employ the measured rotor position for coordinate transformations [12], [13]. In a sensorless drive, the rotor position is not measured and using the estimated rotor position, if available, presents the same inconveniences as for Luenberger observers. An inherent sensorless observer based on Jansen-Lorenz approach is developed next.

The observer is easily obtained if the current model is implemented in rotor flux reference frame, as in (2.63), Figure 4.20. From (2.63) one obtain

$$\frac{d}{dt}\hat{\underline{\psi}}_r^r = \frac{L_m}{T_r}\underline{i}_s^r - \left(\frac{1}{T_r} + j(\omega_{\psi r} - \omega_r)\right)\hat{\underline{\psi}}_r^r \tag{4.62}$$

In rotor flux frame, $\hat{\psi}_{rq}^r = 0$ and (4.62) provides the estimated rotor flux

$$\hat{\underline{\psi}}_r^r = \hat{\psi}_{rd}^r = \frac{L_m}{1+sT_r} i_{sd}^r \tag{4.63}$$

The second equation in (4.62) provides the estimate for rotor slip speed, (2.64).

The voltage model, the PI compensation and the primary estimation for rotor flux remain unchanged, given by (4.31)-(4.33) if rotor flux error is used, or by (4.24), (4.25) and (4.27) if stator flux error is used. The coordinate transformation (4.28) uses the estimated rotor flux position $\hat{\theta}_{\psi r} = \tan^{-1}(\hat{\psi}_{rq} / \hat{\psi}_{rd})$.

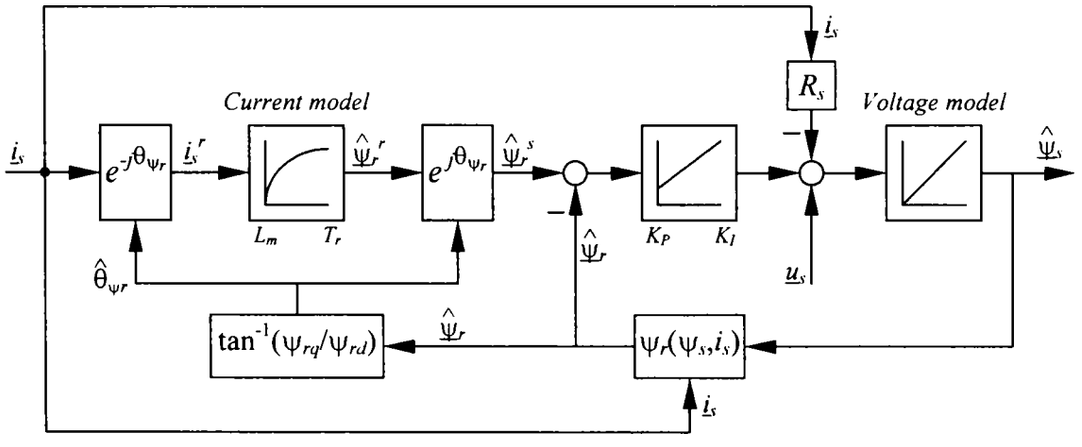

Figure 4.20 Inherent sensorless Jansen-Lorenz observer using the rotor flux error

The observer based on rotor flux error, depicted in Figure 4.20, is equivalent to the one in Figure 4.2 and can be directly used in sensorless drives, as it doesn't require the rotor position. An observer based on stator flux error can be constructed in the same way, using (4.63), (4.24), (4.25) and (4.27).

The inherent sensorless observer inherits qualities of the original Jansen-Lorenz observer. In particular, since the current model is open loop operated, it is expected to be sensitive to model parameter detuning. All considerations on gain selection remain the same as for Jansen-Lorenz observers.

Parameter and offset sensitivity analysis

Simulations with the modified Jansen-Lorenz observer and Linear-DTC have been carried out in the same scenario as for Figure 4.10. Simulations under perfect tuning of controller and observer are similar with those in Figure 4.10 and not shown.

Simulations with 0.5 V offset, added on voltage measurements, are presented in Figure 4.21. The estimated stator and rotor flux magnitudes show negligible errors. The estimated speed is affected at startup, but the error decays as the BPF compensates for the offset. As expected, due to the BPF from (4.29), the observer is robust with respect to offset. However, its performance is inferior to that of the modified Luenberger observer, as demonstrated by Figures 4.13 and 4.21. The same PI compensator gains have been used in both cases.

The estimated stator and rotor flux magnitude errors, with L_m, R_r and R_s detuning, are shown in Figure 4.22. Figure 4.15 is referred for comparison.

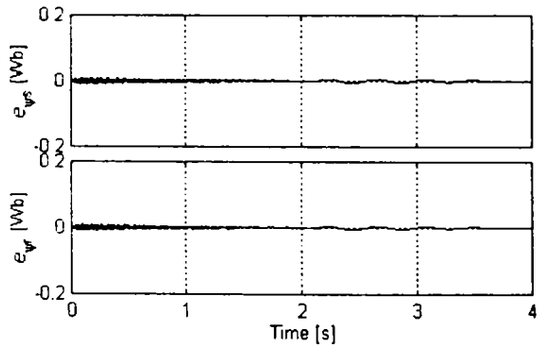

a. Stator and rotor flux estimation errors

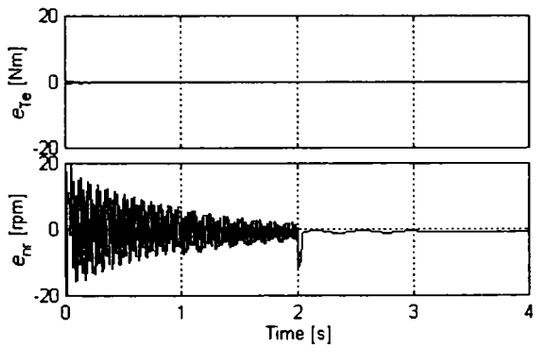

b. Torque and speed estimation errors

Figure 4.21 Estimation errors for modified Jansen-Lorenz observer in the presence of offset

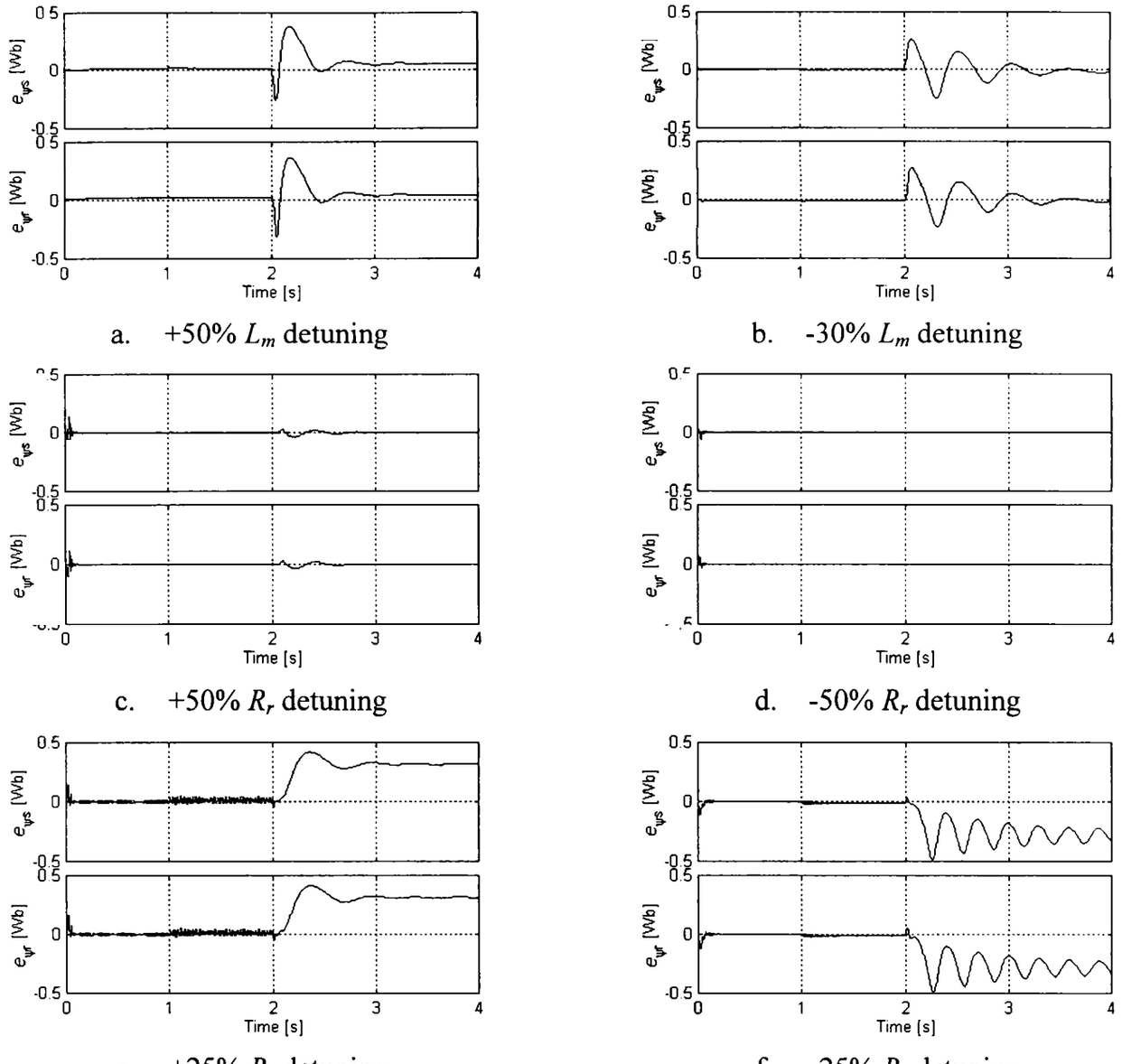

a. +50% L_m detuning

b. -30% L_m detuning

c. +50% R_r detuning

d. -50% R_r detuning

e. +25% R_s detuning

f. -25% R_s detuning

Figure 4.22 Stator and rotor flux estimation errors with L_m, R_r and R_s detuning - simulations

This time, the impact of L_m detuning on estimation accuracy is severe at low speeds. Underestimation below –30% determine a dramatic increase of oscillations leading, eventually, to instability. As expected, at high speeds L_m has no influence.

The rotor resistance detuning affects only the rotor time constant that has minor influence on estimation, during flux transients. Since there is no compensation for the current model, the errors are higher than those for Luenberger observer, Figure 4.15.

The stator resistance detuning has the most serious impact on performance. Errors higher than ±25% lead to large oscillations and instability. Since a current estimate is not available, adaptations (4.60) or (4.61) are not applicable.

Experimental results

Experimental results at 30 rpm (1 Hz stator frequency), no load, with classical DTC, inherent sensorless Jansen-Lorenz observer and MRAS speed observer, are shown in Figure 4.23 (estimated and measured speed, estimated torque, estimated stator and rotor flux). This represents the best low speed result that was obtained with Jansen-Lorenz observer and Machine 1 (4 kW). Very low speed operation, lower than 30 rpm, was not possible, partly due to the low accuracy of the flux observer that was operated without parameters adaptation and partly due to the poor dynamic performance of the MRAS speed observer.

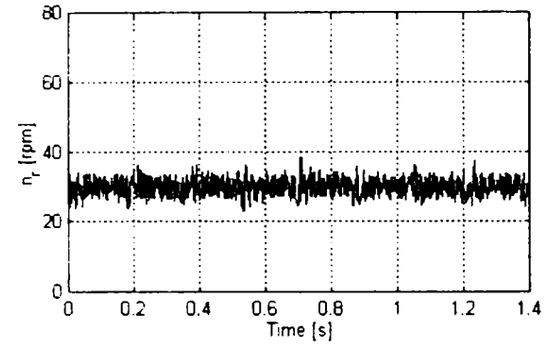

a. Estimated rotor speed

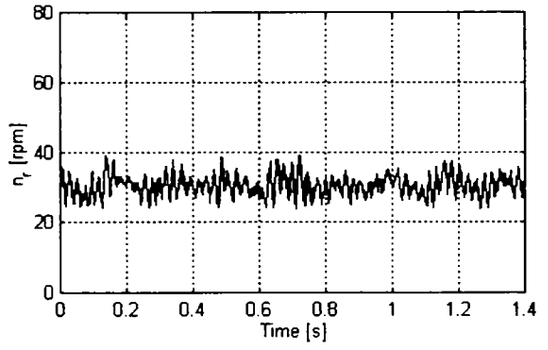

b. Measured rotor speed

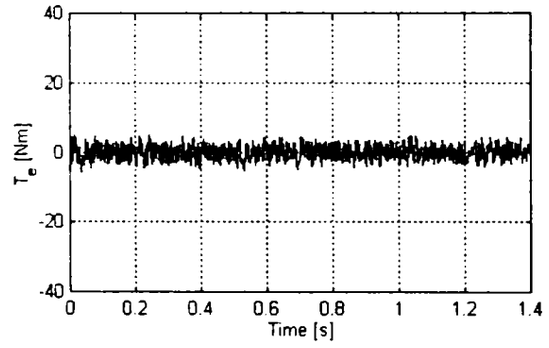

c. Estimated torque

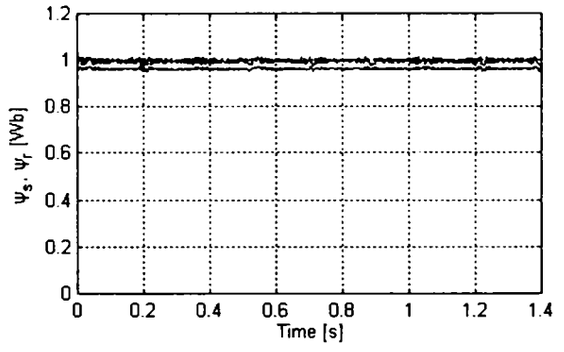

d. Estimated stator and rotor flux

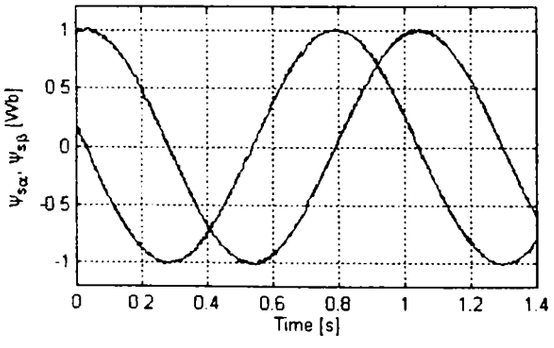

e. Estimated stator flux (α,β) components

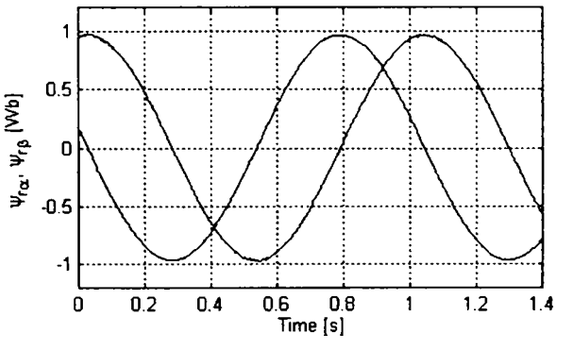

f. Estimated rotor flux (α,β) components

Figure 4.23 Low speed sensorless operation with DTC and Jansen-Lorenz observer

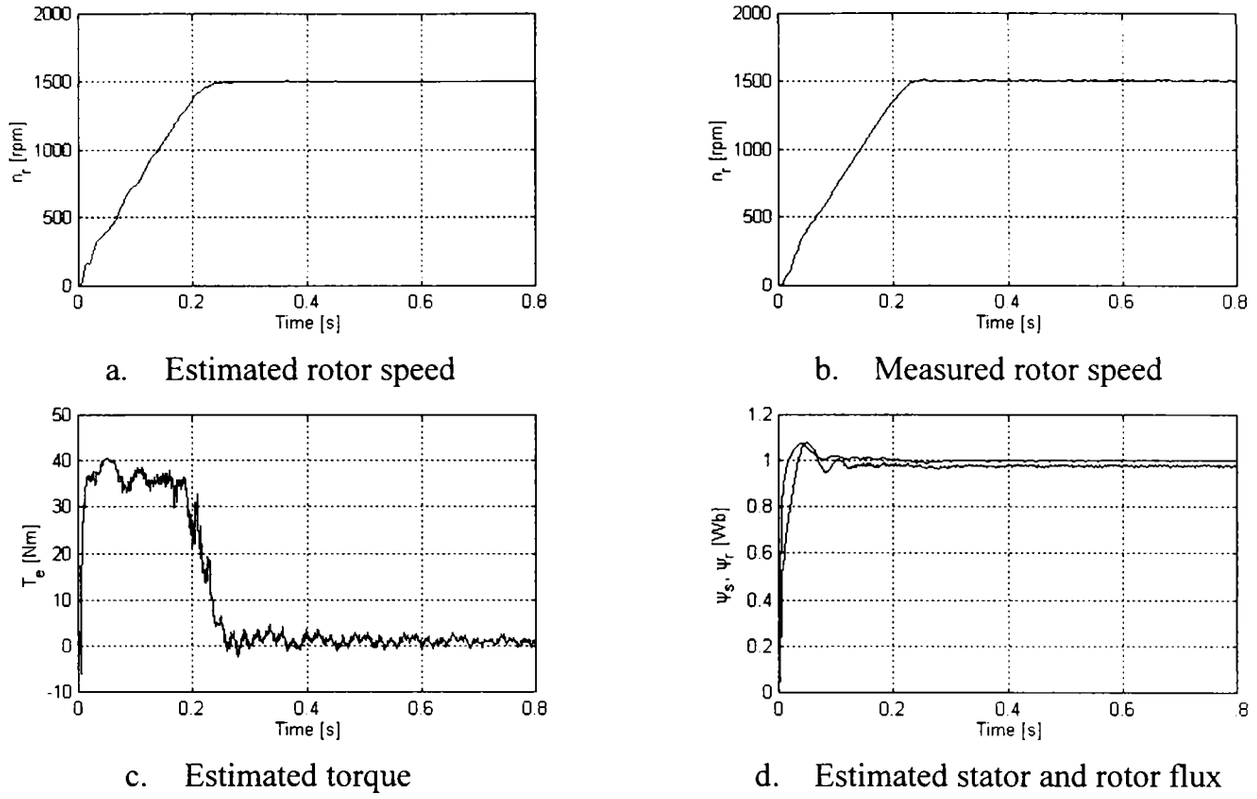

Figure 4.24 Starting transients with Linear-DTC and Jansen-Lorenz observer

The observer was tested with Linear-DTC also. Starting transients and no load operation at 1500 rpm are presented in Figure 4.24. As can be noticed, at high speeds, the overall behavior is good. More experiments with the modified Jansen-Lorenz observer, Linear-DTC and DTC have been reported in [22].

Conclusions

An inherent sensorless Jansen-Lorenz observer has been proposed and analyzed by means of simulations. It was determined that the observer sensitivity to model parameters detuning is higher than that of Luenberger observer. The stator resistance adaptation schemes developed for Luenberger observers are not applicable.

Experiments with the modified Jansen-Lorenz observer and two control strategies, DTC and Linear-DTC have been presented and discussed. The lowest rotor speed that was possible in continuous and stable operation was 30 rpm.

4.3.3 Improved Voltage Model Estimator - Experiments

The voltage model flux estimator is very attractive due to inherent robustness with respect to motor parameter detuning, but suffers from sensitivity to measurement offset. A voltage model based flux estimator that forces the flux vector onto a circular trajectory by means of a PI offset correction loop has been theoretically introduced in [10] and is described by (4.20), Figure 4.25. The loop compensates for errors caused by the input DC offset and wrong initial conditions. Together with the author of [10], experiments have been carried out in order to confirm the validity of this scheme.

Zero speed, full load, sensorless operation, with improved voltage model based estimator, is shown in Figure 4.26. The control strategy is Linear-VSC, with PLL speed estimation and the motor under test is Machine 2 (1.1 kW). The system is able to develop full torque at standstill, while the stator frequency is about 2.5 Hz.

Very low speed sensorless operation, with the same estimation and control system, is illustrated in Figure 4.27. Motoring and regenerating sensorless operation, at 6rpm and reversal under full load are shown. Despite its simplicity, the flux estimator is stable and performs well at any speed.

Starting transients and high-speed sensorless operation of Machine 2 are shown in Figure 4.28. The system's behavior is good and the estimated speed matches the measured one very well. This is an indication that the flux estimator exhibits adequate performance in the whole speed range.

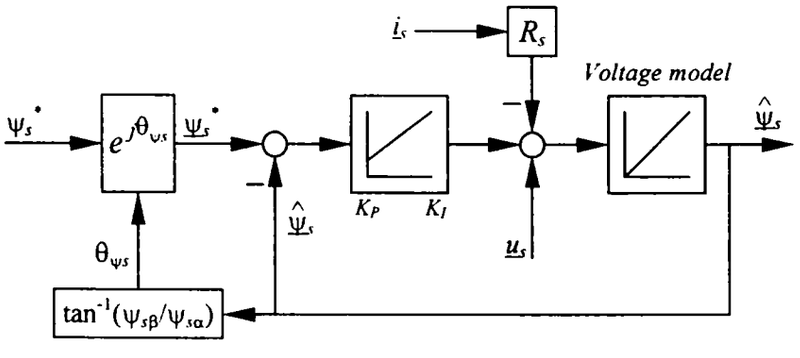

Figure 4.25 Improved voltage model estimator

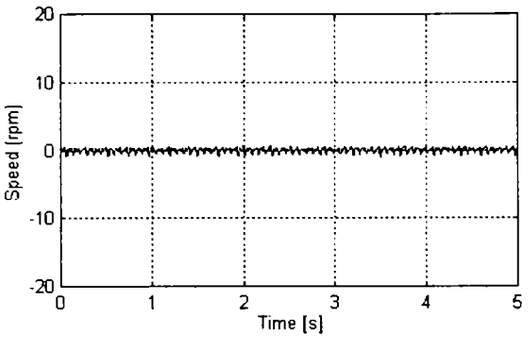

a. Estimated rotor speed

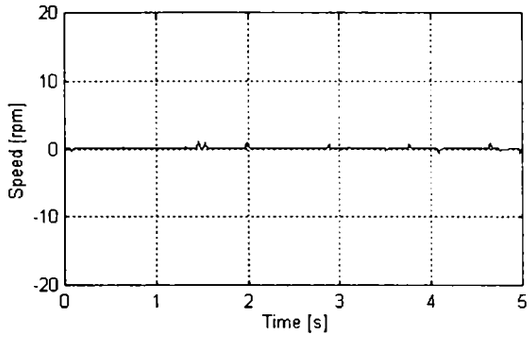

b. Measured rotor speed

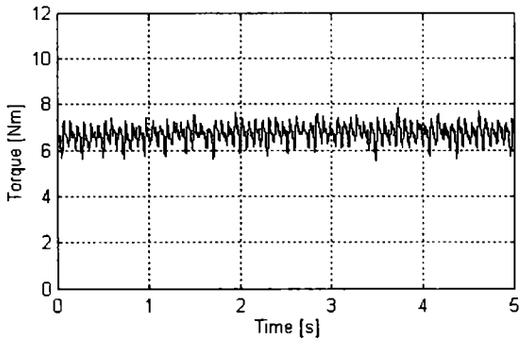

c. Estimated torque

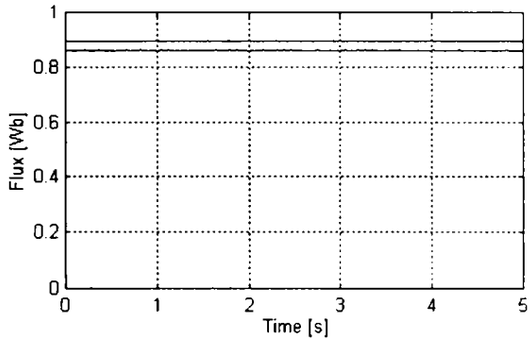

d. Estimated stator and rotor flux

Figure 4.26 Zero speed sensorless Linear-VSC with improved voltage model observer

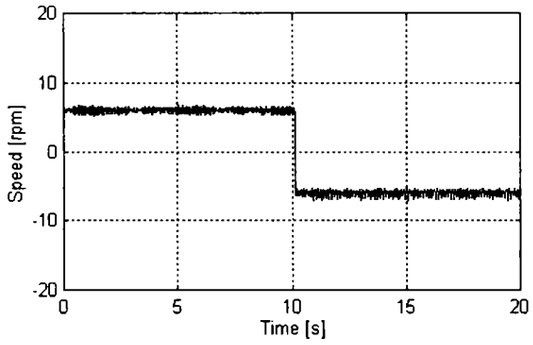

a. Estimated rotor speed

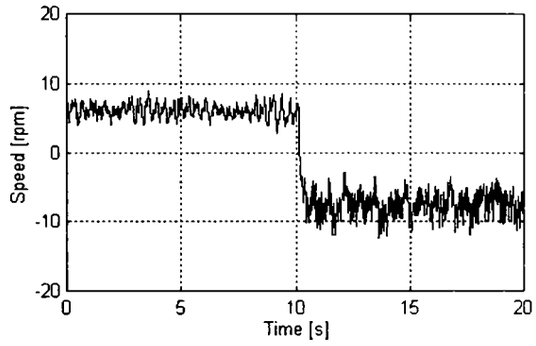

b. Measured rotor speed

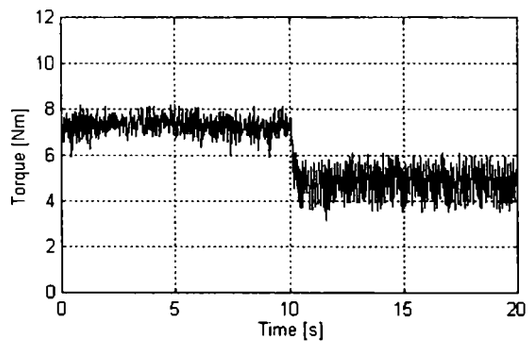

c. Estimated torque

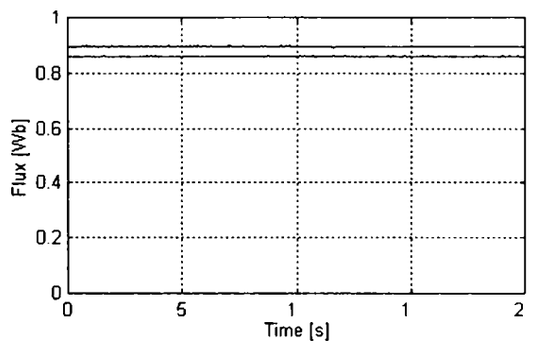

d. Estimated stator and rotor flux

Figure 4.27 Motoring and regenerating sensorless operation at ±6 rpm with Linear-VSC, improved voltage model observer and PLL speed estimation

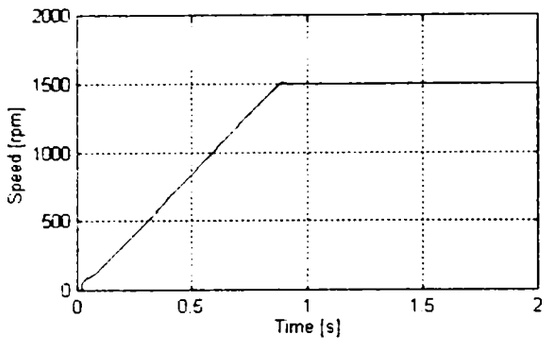

a. Estimated rotor speed

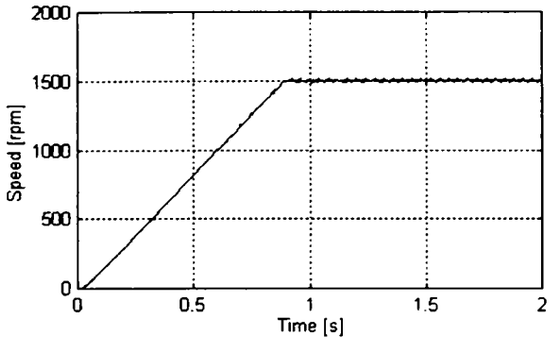

b. Measured rotor speed

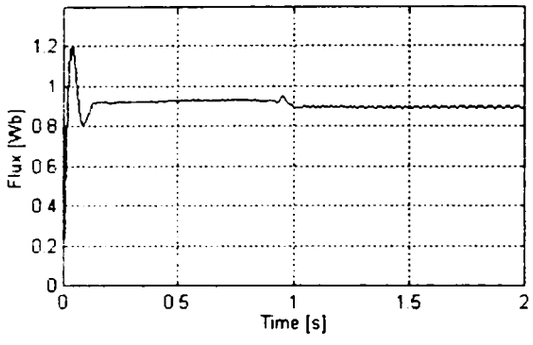

c. Estimated stator flux

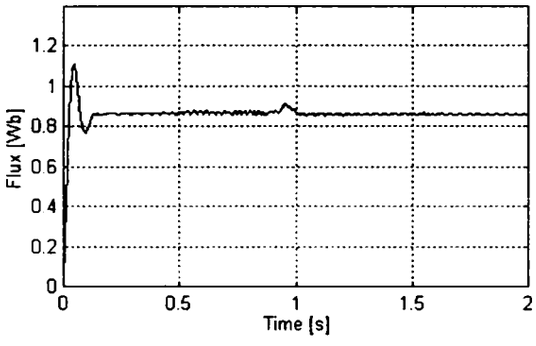

d. Estimated rotor flux

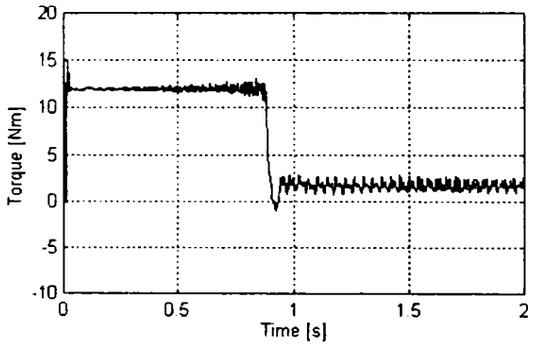

e. Estimated torque

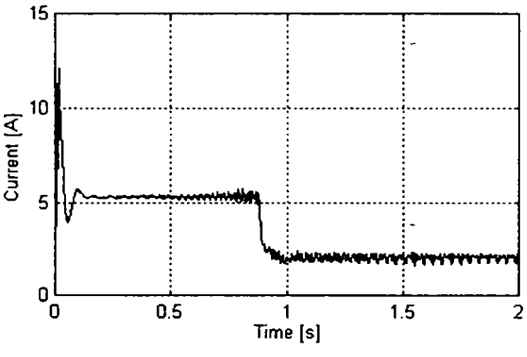

f. Measured current magnitude

Figure 4.28 Starting transients with Linear-VSC and improved voltage model observer

Conclusions

Experimental results, with a system that employs the improved voltage model flux estimator proposed in [10], are presented. Zero and very low speed, full load sensorless operation is possible. Motoring and regenerating sensorless operation has been demonstrated at 6 rpm. It was proved that, despite its simplicity, the estimator is able to achieve very good performance in a wide speed range. The solution is robust with respect to measurement offset.

References

[1] D.G. Luenberger, *An Introduction to Observers.*, IEEE Transactions on Automatic Control, vol. AC-16, no. 6, Dec. 1971, pp. 596-602.

[2] E.A. Misawa, J.K. Hedrick, *Nonlinear Observers – A State-of-the-Art Survey.*, Transactions of the ASME Journal of Dynamic Systems, Measurement and Control, vol. 111, Sept. 1989, pp. 344-352.

[3] Robert Grover Brown, Patrick Y. C. Hwang, *Introduction to Random Signals and Applied Kalman Filtering, third edition.*, John Wiley & Sons, USA, 1997.

[4] Karl J. Astrom, Bjorn Wittenmark, *Computer Controlled Systems: Theory and Design.*, Prentice Hall International, Englewood Cliffs, New Jersey, 1984.

[5] Jean-Jacques E. Slotine, Weiping Li, *Applied Nonlinear Control.*, Prentice Hall, Englewood Cliffs, New Jersey, 1991

[6] K.D. Hurst, T.G. Habetler, G. Griva, F. Profumo, *Zero-Speed Tacholess IM Torque Control: Simply a Matter of Stator Voltage Integration.*, IEEE Transactions on Industry Applications, vol. 34, no. 4, July/Aug. 1998, pp. 790-795.

[7] M.-H. Shin, D.-S. Hyun, S.-B. Cho, S.-Y. Choe, *An Improved Stator Flux Estimation for Speed Sensorless Stator Flux Orientation Control of Induction Motors.*, IEEE Transactions on Power Electronics, vol. 15, no. 2, Sept. 2000, pp. 312-318.

[8] B.K. Bose, N.R. Patel, *A Programmable Cascaded Low-Pass Filter-Based Flux Synthesis for a Stator Flux-Oriented Vector-Controlled Induction Motor.*, IEEE Transactions on Industrial Electronics, vol. 44, no. 1, Feb. 1997, pp. 140-143.

[9] J. Holtz, J. Quan, *Sensorless Vector Control of Induction Motors at Very Low Speed Using a Nonlinear Inverter Model and Parameter Identification.*, The 36th IEEE Industry Applications Society Annual Meeting, 2001, CD-ROM paper 62.3.

[10]G.D. Andreescu, *Flux Estimator with Offset Correction Loop for Low Speed Sensorless Control of AC Drives.*, Proc. of OPTIM 2002, Brasov Romania, 2002, vol. 2, pp. 531-538.

[11]J. Hu, B. Wu, *New Integration Algorithms for Estimating Motor Flux Over a Wide Speed range.*, IEEE Transactions on Power Electronics, vol. 13, no. 5, Sept. 1998, pp. 969-977.

[12]P.L. Jansen, R.D. Lorenz, *A Physically Insightful Approach to the Design and Accuracy Assessment of Flux Observers for Field Oriented I.M. Drives.*, IEEE Transactions on Industry Applications, vol. 30, no. 1, Jan./Feb. 1994, pp 101-110.

[13]P.L. Jansen, R.D. Lorenz, D.W. Novotny, *Observer-Based Direct Field Orientation: Analysis and Comparison of Alternative Methods.*, IEEE Transactions on Industry Applications, vol. 30, no. 4, July/Aug. 1994, pp. 945-953.

[14]G. Verghese, S.R. Sanders, *Observers for Flux Estimation in Induction Machines.*, IEEE Transactions on Industrial Electronics, vol. 35, no. 1, Feb. 1988, pp. 85-94.

[15]H. Kubota, K. Matsuse, T. Nakano, *DSP Based Speed Adaptive Flux Observer for Induction Motor Applications.*, IEEE Transactions on Industry Applications, vol. 29, no. 2, Mar./Apr. 1993, pp. 344-348.

[16]J. Maes, J. Melkebeek, *Speed Sensorless Direct Torque Control of Induction Motors using an Adaptive Flux Observer.*, IEEE Transactions on Industry Applications, vol. 36, no. 3, May/June 2000, pp. 778-785.

[17]M. Abrate, G. Griva, F. Profumo, A. Tenconi, *High Speed Sensorless Fuzzy-Like Luenberger Observer.*, The 30th IEEE PESC99 Record, 1999, vol. 1, pp. 477-481.

[18]H. Tajima,Y. Hori, *Speed Sensorless Field-Oriented Control of the Induction Machine.*, IEEE Transactions on Industry Applications, vol. 29, no.1, Jan./Feb. 1993, pp. 175-180.

[19]L. Harnefors, *Design and Analysis of General Rotor-Flux-Oriented Vector Control Systems.* IEEE Transactions on Industrial Electronics, vol. 48, no. 2, April 2001, pp. 383-390.

[20]R.J. Kerkman, B.J. Seibel, T.M. Rowan, D.W. Schlegel, *A New Flux and Stator Resistance Identifier for AC Drive Systems.*, IEEE Transactions on Industry Applications, vol. 32, no. 3, May/June 1996, pp. 585-593.

[21]Cristian Lascu, Andrzej M. Trzynadlowski, *A Sensorless Hybrid DTC Drive for High-Volume Applications Using the TMS320F243 DSP Controller.*, The 36th IEEE Industry Applications Society Annual Meeting 2001, Chicago, IL, USA, vol. 1, pp. 482-489.

[22]Cristian Lascu, Ion Boldea, Frede Blaabjerg, *A Modified Direct Torque Control for Induction Motor Sensorless Drive.*, IEEE Transactions on Industry Applications, vol. 36, no. 1, Jan./Feb. 2000, pp. 122-130.

5 VARIABLE STRUCTURE OBSERVERS FOR INDUCTION MACHINE DRIVES

5.1 Introduction

Induction machines are nonlinear systems. Dynamic models, currently used for induction machine drives, are linear time variable models, obtained by neglecting iron losses, magnetic saturation and other nonlinearities. In order to compensate for these unmodeled effects that tend to deteriorate the system's overall performance, robust control and observation techniques must be employed.

The popular Luenberger observer is only one possibility to find the unknown states of linear dynamic systems. Whether the observed system is nonlinear, uncertain or affected by noise, nonlinear approaches are preferable [1]-[3]. Among nonlinear observers for ASD-s, the (Extended) Kalman Filter (EKF) is, probably, the most popular, but not necessary the best [2]. It suffers from lack of inherent robustness against modeling errors and disturbances [3].

The *Variable Structure Observer* or *Sliding Mode Observer* (SMO) is a nonlinear state observer supported by the theory of Variable Structure Systems [5], [6]. The SMO features excellent robustness properties over a specified magnitude range of system parameter uncertainties, unmodeled dynamics and disturbances. It possesses invariant dynamic modes, whose performance can be assigned by setting different poles, and guaranties finite time convergence. If the nonlinearitites are bounded and satisfy certain matching conditions, then the SMO behaves as a reduced order linear observer [1]-[9].

The SMO concept has been introduced some time ago and, since then, several theoretical solutions evolved. An early SMO appeared as the sliding mode realization of a reduced order asymptotic observer [5], [6]. In this formulation, the original system is transformed into a canonical form and the sliding mode is induced, on the known output error variables, by a discontinuous function. Later, the equivalent control methodology has been exploited from different perspectives and used to design the observer for systems transformed in block-observable form [5]-[8].

Sliding observers for general nonlinear systems, as well as for nonlinear systems in companion form, $x^{(n)}=f$ and for multi-output nonlinear systems, have been studied in [4]. The generalization of the sliding mode concept for discrete time sliding observers is presented in [9] and [10].

Despite of the extensive theory available, only few sliding mode observers have been related to ASD-s. In all cases, a framework, similar to a Luenberger observer with the linear innovative term replaced by a discontinuous function of the output estimation mismatch, was used, [6], [11]-[17]. A recent study has demonstrated the superiority of SMO over EKF for induction machine state estimation [2].

The main drawback of the sliding-mode method is the existence of high frequency chattering that is highly undesirable in practice. Contrary to the case of controller design, chattering issues in SMO design are related only to numerical implementation. Different methods to reduce the chattering have been proposed and the most simple is the introduction of the so-called boundary layer.

Existing SMO solutions for induction machine state estimation are presented in the next section. New sliding observers topologies are proposed subsequently. Simulation and experiments are given and discussed.

5.2 Variable Structure Observers – State of the Art

Similarly to VSC design, the SMO design procedure consists of two steps. First, a set of *sliding surfaces*, $S(y, t)\in\Re^m$ is designed, such that the estimation error trajectories, restricted to $S(y, t)$, exhibit the desired stable dynamics. Secondly, the observer structure and gain are determined, so that to drive the estimation errors trajectories to S and, once intercepted, to maintain them on this set for all subsequent time. System's behavior on S is called *sliding mode*.

Consider the linear system (4.1), in canonical form (4.5), in which the output vector is part of the state vector. A sliding mode observer for it is (5.1), [6].

$$d\hat{x}_1 / dt = A_{11}\hat{x}_1 + A_{12}\hat{y} + B_1 u + L\nu \tag{5.1a}$$

$$d\hat{y} / dt = A_{21}\hat{x}_1 + A_{22}\hat{y} + B_2 u + \nu \tag{5.1b}$$

$$\nu = K\,\mathrm{sgn}(y - \hat{y}), \qquad K > 0 \tag{5.1c}$$

Equations describing the error dynamics, $e_x = x_1 - \hat{x}_1$ and $e_y = y - \hat{y}$ are obtained by subtracting (5.1) from (4.5)

$$de_x / dt = A_{11}e_x + A_{12}e_y - L\nu \tag{5.2a}$$

$$de_y / dt = A_{21}e_x + A_{22}e_y - \nu \tag{5.2b}$$

The discontinuous switching function $\nu\in\Re^m$ is designed such that the sliding mode is enforced on surface $S = y - \hat{y} = 0$. It is shown in [6], that a large, but finite value of K will accomplish that. For bounded initial conditions, sliding mode will occur on S=0. According to the equivalent control method, the system in sliding mode behaves as if ν is replaced by its equivalent value ν_{eq}, which is the solution of equation $dS / dt = 0$. From (5.2b), the *equivalent control* is $\nu_{eq} = A_{21}e_x$, [6].

The error dynamics of x_1 in sliding mode is determined from (5.2a) using ν_{eq}

$$de_x / dt = (A_{11} - LA_{21})e_x \tag{5.3}$$

which coincide with the reduced order observer dynamics (4.10). Hence, the SMO in sliding mode is equivalent to the reduced order observer (4.9).

However, if the plant and the observed signals are affected by noise, the nonlinear observer may turn out to be preferable, due to its filtering proprieties, which coincide to those of a Kalman filter [6]. The gain $\boldsymbol{L}$ remains to be found so that (5.3) is stable and exhibits the desired convergence rate. Finally, x_2 is given by (4.7).

Another method of designing the observer is to transform the original system (4.1) in block-observable form and to use sliding modes to reconstruct the states of the transformed system [5]-[8]. However, since most induction motor models are in form (4.5), the SMO design (5.1) is more advantageous.

The SMO provides a systematic approach to the problem of maintaining stability and consistent performance in the face of model imprecision and noise.

Let the model of a nonlinear and/or uncertain dynamic system be

$$dx_1 / dt = f_1(x,t) + B_1 u \tag{5.4a}$$

$$dy / dt = f_2(x,t) + B_2 u \tag{5.4b}$$

where the function $f = [f_1\ f_2]^T$ is not exactly known, but estimated, as $\hat{f}$ and the estimation error is assumed to be upper bounded by a known continuous function

$$F_i \geq | f_i - \hat{f}_i |, \qquad i = 1, 2 \tag{5.5}$$

Following the same procedure as before, a SMO for (5.4) is constructed as

$$d\hat{x}_1 / dt = \hat{f}_1(\hat{x},t) + B_1 u + LK \operatorname{sgn}(y - \hat{y}) \tag{5.6a}$$

$$d\hat{y} / dt = \hat{f}_2(\hat{x},t) + B_2 u + K \operatorname{sgn}(y - \hat{y}) \tag{5.6b}$$

The estimation error dynamics is obtained by subtracting (5.6) from (5.4)

$$de_x / dt = f_1(x,t) - \hat{f}_1(\hat{x},t) - LK \operatorname{sgn}(y - \hat{y}) \tag{5.7a}$$

$$de_y / dt = f_2(x,t) - \hat{f}_2(\hat{x},t) - K \operatorname{sgn}(y - \hat{y}) \tag{5.7b}$$

Sliding mode will occur on the sliding surface $S = y - \hat{y} = 0$ if the reaching and stability condition, $S^T \cdot dS / dt < 0$ is satisfied, [4]-[8]. From (5.7b),

$$S^T \cdot dS / dt = S^T (f_2(x,t) - \hat{f}_2(\hat{x},t)) - K | S | < 0 \tag{5.8}$$

In order to fulfill (5.8), the SMO gain K is selected so that

$$K > F_2 \geq | f_2(x,t) - \hat{f}_2(\hat{x},t) | \tag{5.9}$$

Satisfying (5.8) guaranties the observer stability and finite reaching time.

During sliding mode, the system is effectively reduced to an equivalent *n-m* order system. The approximate dynamics of this system is found by using the equivalent control method [4]-[8]. In sliding mode $S = 0$ and, formally, $dS/dt = 0$.

The equivalent control ν_{eq}, is found from (5.7b).

$$\nu_{eq} = f_2(x,t) - \hat{f}_2(\hat{x},t) \tag{5.10}$$

With (5.10) in (5.7a), the equivalent dynamics on the sliding surface is

$$de_x/dt = f_1(x,t) - \hat{f}_1(\hat{x},t) - L(f_2(x,t) - \hat{f}_2(\hat{x},t)) \tag{5.11}$$

The gain $\boldsymbol{L}$ is selected so that the SMO dynamics (5.11) is fast and stable. The system must be observable, in order for any observer structure to be successful in reconstructing the state x_1 from the measurement y. Intuitively, for system (5.4) to be observable, f_2 must be a single valued function of x_1, in order for the control term $L(f_2(x,t) - \hat{f}_2(\hat{x},t))$ to have an influence on error dynamics (5.11) [4].

In general, the observability condition is strongly linked to condition (5.8) and an unobservable system will result in uncontrollable error dynamics. Condition (5.8) is the stability condition derived from Lyapunov stability theory (Appendix A). Indeed, the positive definite function $V = S^T \cdot S/2$ is a Lyapunov function for system (5.7) if $dV/dt = S^T \cdot dS/dt < 0$, that is, if (5.8) is satisfied. Hence, selection of gain K according to (5.9) guaranties the observer's stability in face of bounded model imprecision. Moreover, it guaranties that, after startup, the surface S will nonetheless be reached in finite time.

Sometimes, in practice, the equivalent control is needed. Since (5.10) cannot be computed, it is a common practice to determine ν_{eq} as an average value of the actual control ν. It is obtained by using a low pass filter whose time constant is sufficiently small to pass the slow component of the motion, which is ν_{eq}, but is large enough to eliminate the high frequency component caused by the finite frequency switching.

The induction machine state space models are adequate for observer design. Almost invariably, the rotor flux model in stationary reference frame (2.60)-(2.61) is used for the SMO design [2], [6], [11]-[15]. The stator flux model, in stator frame (2.52)-(2.53), is employed for the same purpose, in [16].

The SMO for the rotor flux model in stator frame can be constructed as in (5.1)

$$\frac{d}{dt}\begin{bmatrix}\hat{\underline{i}}_s \\ \hat{\underline{\psi}}_r\end{bmatrix}=\begin{bmatrix}A_{11} & A_{12} \\ A_{21} & A_{22}\end{bmatrix}\cdot\begin{bmatrix}\hat{\underline{i}}_s \\ \hat{\underline{\psi}}_r\end{bmatrix}+\begin{bmatrix}B_1 \\ 0\end{bmatrix}\underline{u}_s+\begin{bmatrix}1 \\ L\end{bmatrix}K\,\mathrm{sgn}(S) \tag{5.12}$$

where, L and $K>0$ are observer gains, S is the sliding surface, A_{ij}, i=1,2, j=1,2 are elements of $\boldsymbol{A}$ from (2.58), with ω_e=0, and B_1 is the first element of $\boldsymbol{B}$, from (2.59).

The most common choice for the sliding surface is $S=\underline{i}_s-\hat{\underline{i}}_s$, [13]-[16] and

$$\mathrm{sgn}(S)=\mathrm{sgn}(i_{sd}-\hat{i}_{sd})+j\,\mathrm{sgn}(i_{sq}-\hat{i}_{sq}) \tag{5.13}$$

The real gain K is selected large enough, so that to satisfy the stability condition (5.9), $K>F_i$, where F_i is the modeling uncertainty bound of the first equation in (5.12). The most general form for the innovation term ν is

$$\nu=K\,\mathrm{sgn}(S)=k_1\,\mathrm{sgn}(i_{sd}-\hat{i}_{sd})+jk_2\,\mathrm{sgn}(i_{sq}-\hat{i}_{sq}) \tag{5.14}$$

where $k_1>F_{id}$, $k_2>F_{iq}$ and F_{id}, F_{iq} are separate bounds for the real and imaginary components of the first equation in (5.12). It is possible $k_1=k_2=K>\max(F_{id},F_{iq})$.

In sliding mode, $S=0$, $dS/dt=0$ and the flux estimation error is

$$\frac{d}{dt}\underline{e}_{\psi r}=(A_{22}-LA_{12})\underline{e}_{\psi r} \tag{5.15}$$

As expected, the SMO is equivalent to a reduced order observer since (5.15) is precisely (4.42), the error dynamics of the asymptotical reduced order observer.

The observer gain L is selected so that to allocate the pole of A_{22}-LA_{12} at a desired location. If $p=a+jb$ is the desired pole of A_{22}-LA_{12}, then L is

$$L=(A_{22}-p)A_{12}^{-1} \tag{5.16}$$

In [13], L is selected with speed dependent imaginary component

$$L=(q-1)\varepsilon+\gamma/T_r\varepsilon+j\omega_r\gamma/\varepsilon \tag{5.17}$$

where q and γ are constant design parameters and $\varepsilon=L_sL_r\sigma/L_m$. By adjusting q and γ, the real and imaginary components, of the observer pole, can be freely modified. Similar solutions, based on pole placement methods, are suggested in [2], [14]-[16].

Experimental results with systems using SMO-s and sliding mode speed estimators are reported in [13] and [15]. In both cases, the lowest speed obtained in sensorless operation was 50 rpm.

A different and more elaborate SMO design is presented in [11]. Simultaneous estimation of rotor flux and speed is achieved by defining the complex sliding surface

$$S = (\underline{i}_s - \hat{\underline{i}}_s)\hat{\underline{\psi}}_r^* = S_\alpha + jS_\beta \tag{5.18a}$$

$$S_\alpha = (i_{s\alpha} - \hat{i}_{s\alpha})\hat{\psi}_{r\alpha} + (i_{s\beta} - \hat{i}_{s\beta})\hat{\psi}_{r\beta} \tag{5.19a}$$

$$S_\beta = (i_{s\beta} - \hat{i}_{s\beta})\hat{\psi}_{r\alpha} - (i_{s\alpha} - \hat{i}_{s\alpha})\hat{\psi}_{r\beta} \tag{5.19b}$$

where superscript "*" denotes the complex conjugate.

The selection of S is based on energetic considerations (S_β is proportional to the torque error, etc) and allows decoupling of the current estimation problem into two independent ones, one for the real axis and the other for the imaginary axis.

Two nonlinear innovation terms are also defined.

$$\nu_1 = k_1 \hat{\underline{\psi}}_r \operatorname{sgn}(S_\alpha) \tag{5.20}$$

$$\nu_2 = jk_2 \hat{\underline{\psi}}_r \operatorname{sgn}(S_\alpha) \tag{5.21}$$

The speed adaptive sliding mode observer, for the rotor flux model, is

$$\frac{d}{dt}\begin{bmatrix} \hat{\underline{i}}_s \\ \hat{\underline{\psi}}_r \end{bmatrix} = \begin{bmatrix} A_{11} & A_{12} \\ A_{21} & A_{22} \end{bmatrix} \cdot \begin{bmatrix} \hat{\underline{i}}_s \\ \hat{\underline{\psi}}_r \end{bmatrix} + \begin{bmatrix} B_1 \\ 0 \end{bmatrix} \underline{u}_s + \begin{bmatrix} \nu_1 \\ L\nu_2 \end{bmatrix} \tag{5.22}$$

The rotor speed is the adaptive parameter in (5.22) and it is estimated by

$$\hat{\omega}_r = n_0 \operatorname{sgn}(S_\beta) \tag{5.23}$$

where S_β is given by (5.19) and n_0, k_1 and k_2 are design constants. In fact, the average value of the discontinuous function (5.22) is the estimate of the rotor speed.

A complex stability analysis of the composite observer-controller system has been performed in [11] and it was proved that constant values n_0, k_1 and k_2 exist, such that $S_\alpha \cdot dS_\alpha / dt < 0$ and $S_\beta \cdot dS_\beta / dt < 0$. Hence, sliding mode occurs on surfaces S_α=0 and S_β=0. After the sliding mode arises on the intersection of both surfaces, the current estimation errors are equal to zero and the flux estimation errors converge to zero asymptotically. In sliding mode, the SMO exhibits reduced order dynamics.

Sensorless speed control at 300rpm continuous operation is reported in [11]. Lower speed operation was possible only with speed sensor. A simplified version of this observer is proposed in [6] and an implementation is presented in [12] where low speed sensorless operation at 19 rpm is reported.

5.3 Variable Structure Observers – Proposed Solutions

Observer synthesis

The inherent robustness and the existence of invariant dynamic modes make the sliding observer an attractive solution for high performance sensorless drives. Since the estimation accuracy is also very important in such drives, several solutions based on the inherent sensorless scheme have been investigated, in order to determine the one that exhibits the best static and dynamic performance.

The motivation of using the inherent sensorless topology is the same as for asymptotical observers. The speed estimate is affected by cumulative errors, noise and is time-delayed. Employing this estimate, as an adaptive parameter for the observer, may result in progressive deterioration of the estimation accuracy. Although the SMO guaranties stability over a specified magnitude range of model uncertainties and disturbances, it does not necessary provide high accuracy.

It is convenient to develop the SMO using the stator flux model in stator reference frame, (2.52)-(2.53) and later to transform it into inherent sensorless form.

Let the sliding surface be $S = \underline{i}_s - \hat{\underline{i}}_s$. The simplest SMO is

$$\frac{d}{dt}\begin{bmatrix}\hat{\underline{i}}_s \\ \hat{\underline{\psi}}_s\end{bmatrix} = \begin{bmatrix}A_{11} & A_{12} \\ A_{21} & A_{22}\end{bmatrix}\cdot\begin{bmatrix}\hat{\underline{i}}_s \\ \hat{\underline{\psi}}_s\end{bmatrix} + \begin{bmatrix}B_1 \\ 1\end{bmatrix}\underline{u}_s + \begin{bmatrix}1 \\ L\end{bmatrix}K\,\mathrm{sgn}(S) \tag{5.24}$$

where A_{ij}, and B_1 are elements of $\boldsymbol{A}$ and $\boldsymbol{B}$, respectively, from (2.50)-(2.51).

The current and flux errors, $\underline{e}_{is} = \underline{i}_s - \hat{\underline{i}}_s$ and $\underline{e}_{\psi s} = \underline{\psi}_s - \hat{\underline{\psi}}_s$ dynamics are

$$\frac{d}{dt}\begin{bmatrix}\underline{e}_{is} \\ \underline{e}_{\psi s}\end{bmatrix} = \begin{bmatrix}A_{11} & A_{12} \\ A_{21} & A_{22}\end{bmatrix}\cdot\begin{bmatrix}\underline{e}_{is} \\ \underline{e}_{\psi s}\end{bmatrix} - \begin{bmatrix}1 \\ L\end{bmatrix}K\,\mathrm{sgn}(S) \tag{5.25}$$

In sliding mode $S = 0$ and, formally, $dS/dt = 0$, and the equivalent control is obtained from the first equation in (5.25): $\underline{v}_{eq} = A_{12}\underline{e}_{\psi s}$. The flux error dynamics is

$$\frac{d}{dt}\underline{e}_{\psi s} = (A_{22} - LA_{12})\underline{e}_{\psi s} \tag{5.26}$$

This represents the dynamics of a reduced order observer.

The SMO real gain K is determined from stability considerations. The positive definite function $V = 0.5S^2$ is a Lyapunov function for system (5.24) if

$$\frac{dV}{dt} = S\frac{dS}{dt} = \underline{e}_{is}(A_{11}\underline{e}_{is} + A_{12}\underline{e}_{\psi s}) - K\,|\,\underline{e}_{is}\,| < 0 \tag{5.27}$$

This condition is accomplished if K is large enough, such that

$$K > \left|A_{11}\underline{e}_{is} + A_{12}\underline{e}_{\psi s}\right| \tag{5.28}$$

Although not explicitly shown, the SMO uses estimated values for A_{ij} that differ from the real ones. Equation (5.28) is understand in the best sense of (5.9), that is, the gain K must dominate the flux and current errors, as well as the model uncertainties that are included within estimated A_{ij}.

The complex gain L is selected such that (5.26) is fast and stable. If $L = x + jy$, then, from (2.50) in stator frame, with $\omega_e=\omega_r$, the observer dynamics (5.26) is

$$\frac{d}{dt}\underline{e}_{\psi s} = \frac{1}{L_s\sigma}(-\frac{x}{T_r} - y\omega_r + j(-\frac{y}{T_r} + x\omega_r))\underline{e}_{\psi s} \tag{5.29}$$

Allocating the pole $p = a + jb$ of (5.29) requires determining $L = x + jy$ from (5.16). Several simple and practical selections for L are proposed here.

With $x = kL_s\sigma$ and $y = kL_s\sigma T_r\omega_r$, k constant, p results real and stable

$$p = -k(1/T_r + T_r\omega_r^2) \tag{5.30}$$

With $x = kL_s\sigma$ and $y = (k - z)L_s\sigma T_r\omega_r$, k and z design constants, p results

$$p = -k/T_r - (k - z)T_r\omega_r^2 + jz\omega_r \tag{5.31}$$

In both cases, the real component of p can be adapted by means of k, while, in the second case, z is employed to adjust the imaginary component of p.

Another approach is to select the observer poles shifted to the left in the s-plane by a constant amount k, so that to constrain p to take the form

$$p = \frac{1}{L_s\sigma}(-\frac{1}{T_r} - k + j\omega_r) \tag{5.32}$$

In this case, from (5.15), L is obtained as

$$L = 1 + \frac{kT_r}{1 + T_r^2\omega_r^2} + j\frac{k\omega_r T_r^2}{1 + T_r^2\omega_r^2} \tag{5.33}$$

For practical implementation the method illustrated by (5.31) has been adopted.

Once the gains have been selected, the stator flux model based observer (5.24) is transformed into a flux model based observer. This is achieved by means of a nonsingular coordinate transformation $\boldsymbol{T}\in\Re^{n\times n}$

$$\begin{bmatrix}\hat{\underline{\psi}}_r\\ \hat{\underline{\psi}}_s\end{bmatrix}=T\begin{bmatrix}\hat{\underline{i}}_s\\ \hat{\underline{\psi}}_s\end{bmatrix}=\begin{bmatrix}-L_sL_r\sigma/L_m & L_r/L_m\\ 0 & 1\end{bmatrix}\cdot\begin{bmatrix}\hat{\underline{i}}_s\\ \hat{\underline{\psi}}_s\end{bmatrix} \tag{5.34}$$

Using this linear transformation, the observer (5.24) becomes

$$\frac{d}{dt}\begin{bmatrix}\hat{\underline{\psi}}_r\\ \hat{\underline{\psi}}_s\end{bmatrix}=T\begin{bmatrix}A_{11} & A_{12}\\ A_{21} & A_{22}\end{bmatrix}T^{-1}\cdot\begin{bmatrix}\hat{\underline{\psi}}_r\\ \hat{\underline{\psi}}_s\end{bmatrix}+T\begin{bmatrix}B_1\\ 1\end{bmatrix}\underline{u}_s+T\begin{bmatrix}1\\ L\end{bmatrix}K\,\mathrm{sgn}(S) \tag{5.35}$$

Recalling that the matrix $\boldsymbol{A}$ of the original observer (5.24) was given by (2.50), it is obvious that the matrix $A'=TAT^{-1}$ of (5.35) is given by (2.41). Similarly, $B'=TB$ is given by (2.42). The flux model based SMO has been obtained in this way.

The *inherent sensorless observer* is constructed by taking the second equation from (5.24) and the first equation from (5.35). From (2.38) and (2.49), one obtain:

$$\frac{d}{dt}\hat{\underline{\psi}}_s=-R_s\underline{i}_s-j\omega_e\hat{\underline{\psi}}_s+\underline{u}_s+K_1\,\mathrm{sgn}(\underline{i}_s-\hat{\underline{i}}_s) \tag{5.36}$$

$$\frac{d}{dt}\hat{\underline{\psi}}_r=\frac{L_m}{L_sT_r\sigma}\hat{\underline{\psi}}_s-\left(\frac{1}{T_r\sigma}+j(\omega_e-\omega_r)\right)\hat{\underline{\psi}}_r+K_2\,\mathrm{sgn}(\underline{i}_s-\hat{\underline{i}}_s) \tag{5.37}$$

where $K_1=LK$ and $K_2=K(LL_r-L_sL_r\sigma)/L_m$ are redefined gains.

Equation (5.36) is implemented in stator reference frame, with ω_e=0

$$\frac{d}{dt}\hat{\underline{\psi}}_s=-R_s\underline{i}_s+\underline{u}_s+K_1\,\mathrm{sgn}(\underline{i}_s-\hat{\underline{i}}_s) \tag{5.38}$$

Equation (5.37) is implemented in rotor flux reference frame, with $\omega_e=\omega_{\psi r}$

$$\frac{d}{dt}\hat{\underline{\psi}}_r^r=\frac{L_m}{L_sT_r\sigma}\hat{\underline{\psi}}_s^r-\left(\frac{1}{T_r\sigma}+j(\omega_{\psi r}-\omega_r)\right)\hat{\underline{\psi}}_r^r+K_2\,\mathrm{sgn}(\underline{i}_s^r-\hat{\underline{i}}_s^r) \tag{5.39}$$

In rotor flux frame, the rotor flux is $\hat{\underline{\psi}}_r^r=\hat{\psi}_{rd}^r$, $\hat{\psi}_{rq}^r=0$, and (5.39) gives

$$\frac{d}{dt}\hat{\psi}_{rd}^r=\frac{L_m}{L_sT_r\sigma}\hat{\psi}_{sd}^r-\frac{1}{T_r\sigma}\hat{\psi}_{rd}^r+\Re e(K_2\,\mathrm{sgn}(\underline{i}_s^r-\hat{\underline{i}}_s^r)) \tag{5.40}$$

Finally, the estimated stator current, in stator reference frame, is

$$\hat{\underline{i}}_s=\frac{1}{L_s\sigma}\hat{\underline{\psi}}_s-\frac{L_m}{L_sL_r\sigma}\hat{\underline{\psi}}_r \tag{5.41}$$

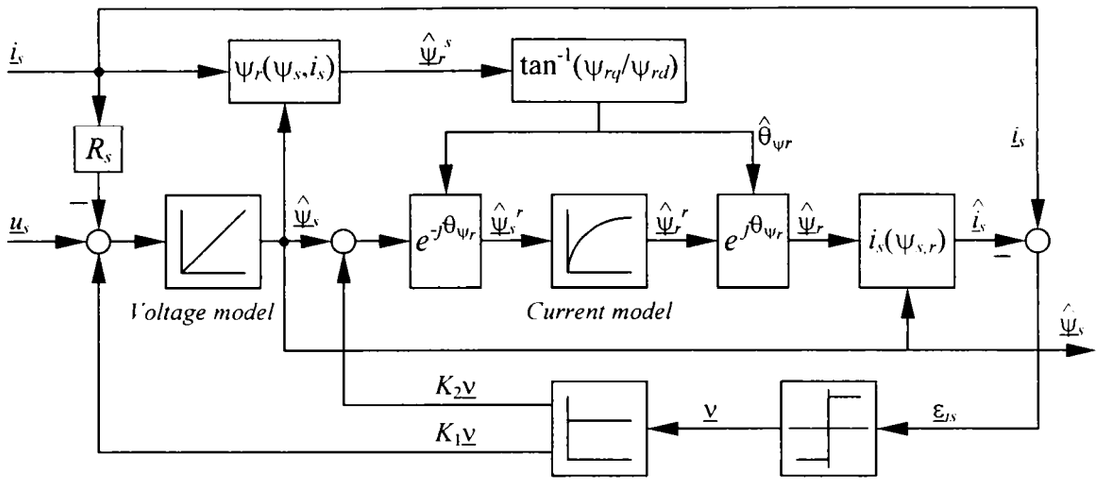

Figure 5.1 Inherent sensorless sliding mode observer for induction machines

The inherent sensorless sliding mode observer diagram is shown in Figure 5.1.

The estimated rotor flux position, needed for all coordinate transformations, is $\hat{\theta}_{\psi r} = \tan^{-1}(\hat{\psi}_{rq}^s / \hat{\psi}_{rd}^s)$, where the estimated rotor flux, $\hat{\underline{\psi}}_r^s$ is

$$\hat{\underline{\psi}}_r^s = \frac{L_r}{L_m}\hat{\underline{\psi}}_s - \frac{L_s L_r - L_m^2}{L_m}\underline{i}_s \tag{5.42}$$

Although (5.36) and (5.37) arrive from two different models, they are distinct. As shown in section 4.3.1, (5.36) can be transformed into second equation of (5.35) by using the linear, algebraic equation (5.41) that gives the estimated stator current. The stator flux model (5.24) has been employed just to obtain simpler synthesis for the observer gain L. Obviously, (5.24) and (5.38)-(5.41) are input-output equivalent.

At this point, the generalization of the inherent sensorless observer concept is possible. The only difference between the linear observer, Figure 4.7 and SMO, Figure 5.1, is the linear feedback in the former case, versus nonlinear feedback in the later. The most general scheme is the one that employs both methods, as in Figure 5.2.

The generalized inherent sensorless observer is described by

$$\frac{d}{dt}\hat{\underline{\psi}}_s = -R_s\underline{i}_s + \underline{u}_s + K_1\,\mathrm{sgn}(\underline{i}_s - \hat{\underline{i}}_s) + K_1'(\underline{i}_s - \hat{\underline{i}}_s) \tag{5.43}$$

$$\frac{d}{dt}\hat{\underline{\psi}}_r^r = \frac{L_m}{L_s T_r \sigma}\hat{\underline{\psi}}_s^r - \left(\frac{1}{T_r\sigma} + j(\omega_{\psi r} - \omega_r)\right)\hat{\underline{\psi}}_r^r + K_2\,\mathrm{sgn}(\underline{i}_s^r - \hat{\underline{i}}_s^r) + K_2'(\underline{i}_s^r - \hat{\underline{i}}_s^r) \tag{5.44}$$

where (5.43) is in stationary frame and (5.44) is in rotor flux frame.

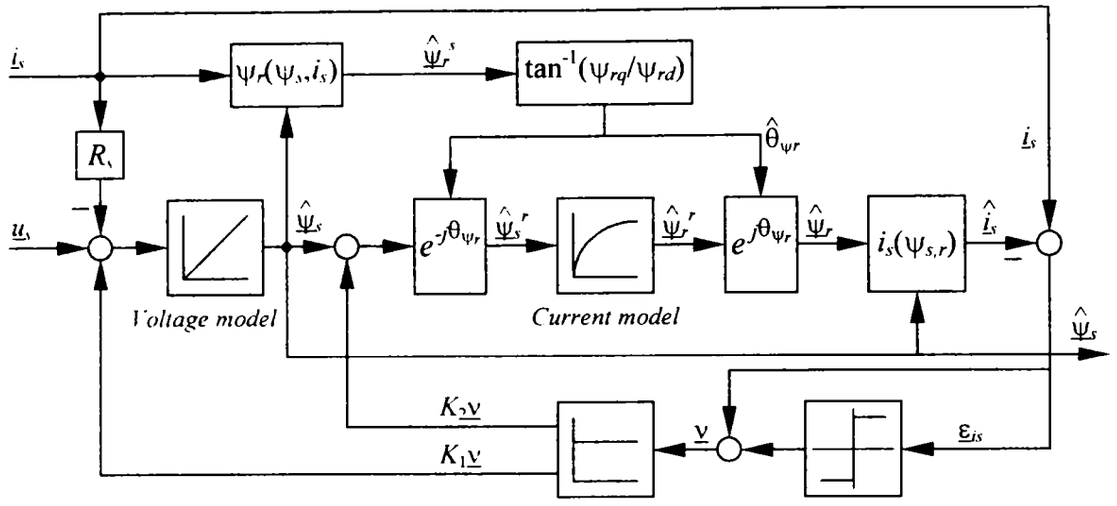

Figure 5.2 Generalized inherent sensorless observer for induction machines

The topology in Figure 5.2 offers flexibility. Finding the right balance, between the linear behavior and the nonlinear one, is possible by adjusting gains $\boldsymbol{K}$ and $\boldsymbol{K'}$. If the model parameters are precisely known, the linear gain $\boldsymbol{K'} = [K_1\ K_2]^T$ is increased. When the model is uncertain, the SMO gain $\boldsymbol{K} = [K'_1\ K'_2]^T$ is increased.

The most important drawback of the variable structure approach is the existence of chattering. It is present in the estimated stator flux, rotor flux and current, and increases with the increase of the SMO gain K. However, it was determined by simulations and confirmed by experiments that the chattering has only a marginal impact and it is not a matter of concern in this case.

In order to smooth out the control discontinuity, a thin *boundary layer*, neighboring the switching surface, can be introduced, [5], [6], [18]. This is simply implemented by replacing the "sign" function with the "saturation" function.

$$\text{sat}(x) = \begin{cases} \text{sgn}(x) & if \quad |x| > h \\ x/h & if \quad -h < x < h \end{cases} \tag{5.45}$$

where the small quantity $2h$ defines the boundary layer width.

The boundary layer has the effect of a low pass filter on the local dynamics of the variable S. The invariance property of sliding mode is preserved only outside the boundary layer, [5], [6], while inside the layer, the system exhibits linear behavior, like an asymptotical observer. Without boundary layer, the robustness of the sliding mode approach ensures zero error of the estimated stator current.

Offset sensitivity compensation

Extensive simulations have been performed in order to determine the observer's performance. However it is quite difficult to prove the SMO robustness and invariance properties by means of simulations because the simulated induction machine is based on the same "uncertain" model employed by the state observer. As for the linear observer, simulations under detuned conditions have been carried out.

Simulation results with SMO and Linear-DTC, under perfect tuning of observer and controller are identical with those shown in Figure 4.10 for the linear observer. All estimation errors are zero and only some chattering appears when the SMO gain K is too much increased. Torque and speed scenario, for all subsequent simulations, is the same as in Figure 4.10. The simulated motor is Machine 1.

The stator flux magnitude, rotor flux magnitude, torque and speed estimation errors for operation with 0.3 V offset added on voltage measurements, are shown in Figure 5.3. For subfigures a and b, that are very similar with Figure 4.11, the SMO gain was K=0.5, while for subfigures c and d, the gain was K=2.5. The robustness of the SMO, with large gain, in face of measurement offset is evident.

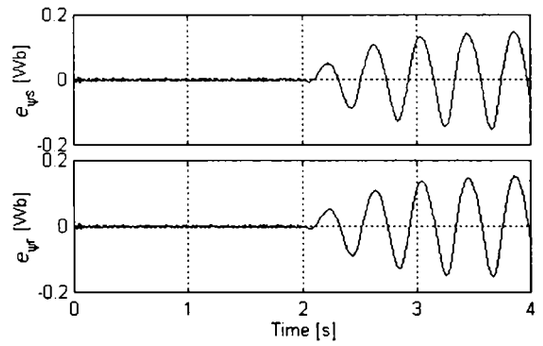

a. Stator and rotor flux errors, K=0.5

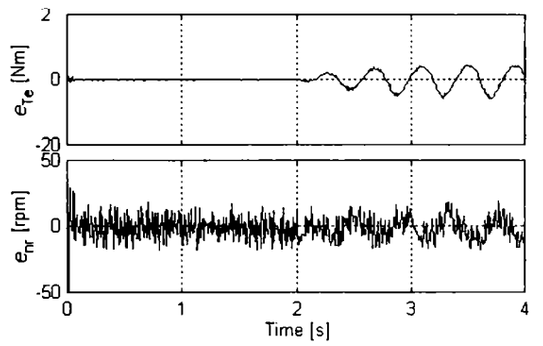

b. Torque and speed errors, K=0.5

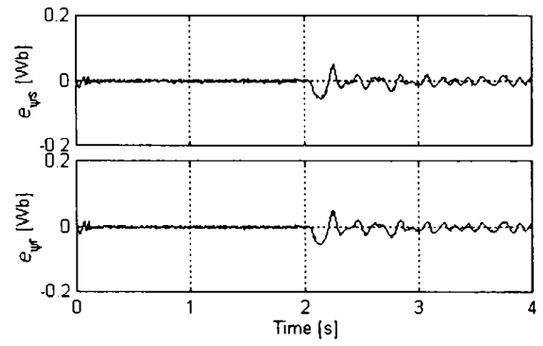

a. Stator and rotor flux errors, K=2.5

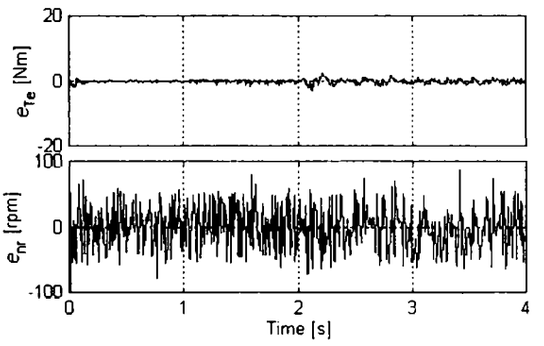

b. Torque and speed errors, K=2.5

Figure 5.3 Estimation errors for SMO, with 0.3 V offset and two different SMO gains

If not otherwise specified, for all subsequent simulations, the SMO gains are: K=0.5, L=10+$j\omega_r$ and h=0.01. This was the case for Figure 4.11.

Unfortunately, the increased gain produces larger chattering. As can be noticed from Figure 4.11.d, the speed estimation is quite sensitive to this and, although the offset error is canceled, the low speed operation is deteriorated. Therefore, in this particular case, it is advantageous to employ offset-free schemes.

As shown for the linear observer, adding dynamics on the observer feedback path can solve the offset problem. A scheme with PI dynamics on the nonlinear switching term, for the voltage model, is shown in Figure 5.4. Recalling the SMO model, (5.38)-(5.39), the gain matrix $\boldsymbol{K} = [K_1\ K_2]^T$ is redesigned as

$$K = \begin{bmatrix} K_P + K_I / s \\ K_2 \end{bmatrix} \tag{4.46}$$

where K_P, K_I and K_2 are determined such that the observer is stable. In general, K_P is the same as K_1, while K_I is selected based on the BPF design considerations.

The second scheme proposed in Figure 5.5 is derived from the generalized observer model (5.43)-(5.44). At this time, the nonlinear compensation mechanism remains unchanged and a linear PI compensation, completely separate from the nonlinear path, is added on the voltage model feedback.

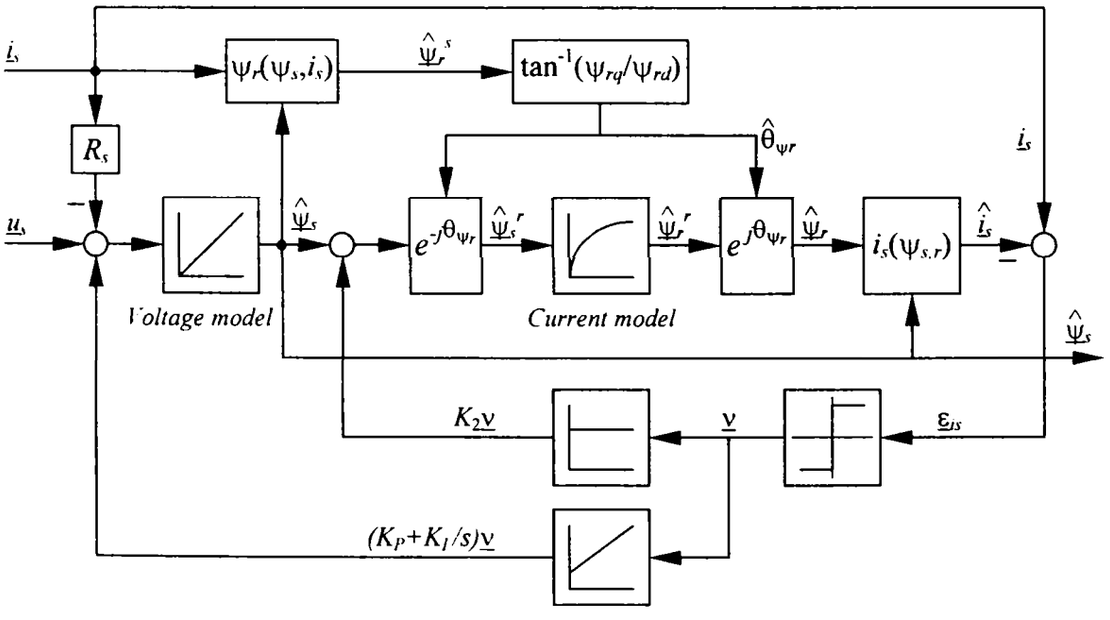

Figure 5.4 Modified SMO with offset compensation – Scheme 1

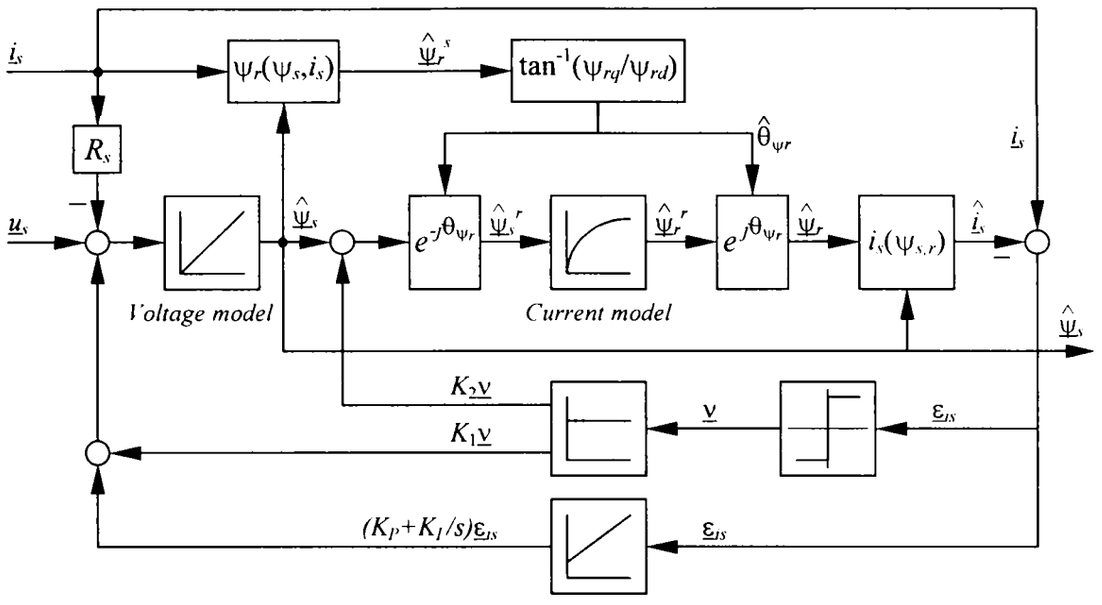

Figure 5.5 Modified SMO with offset compensation – Scheme 2

With reference to observer model (5.43)-(5.44), the gain ***K'*** is

$$K'=\begin{bmatrix} K_P + K_I / s \\ 0 \end{bmatrix} \tag{4.47}$$

This scheme involves more computations, but has the advantage that the PI offset compensator can be tuned independently from the nonlinear mechanism.

Simulation results with the modified SMO from Figure 5.4, with K_P=20, K_I=80 and 0.3 V measurement offset, are presented in Figure 5.6. The flux and torque estimation errors are practically zero for the whole speed range. The estimated speed shows some errors due to chattering. Similar behavior and results have been obtained with the modified observer from Figure 5.5.

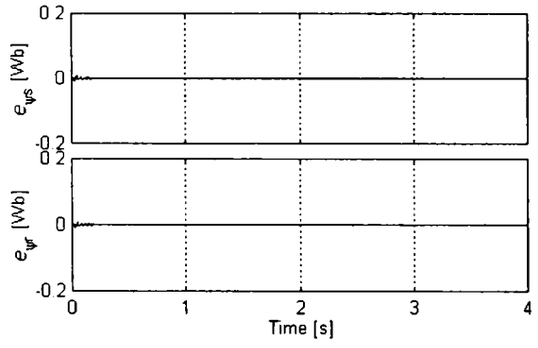

a. Stator and rotor flux estimation errors

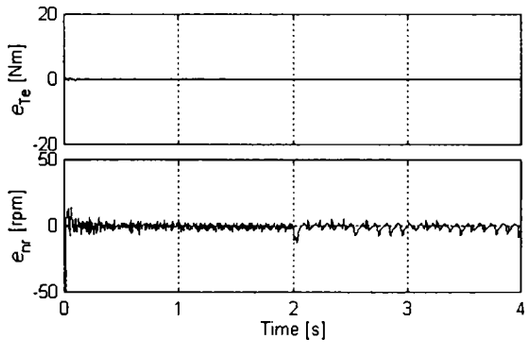

b. Torque and speed estimation errors

Figure 5.6 Estimation errors for modified SMO, with 0.3 V measurement offset

Parameter sensitivity analysis

Simulations with detuned SMO have been carried out in order to determine the system's performance in face of parameter detuning. The estimated stator and rotor flux magnitude errors, $e_{\psi s} = \psi_s - \hat{\psi}_s$ and $e_{\psi r} = \psi_r - \hat{\psi}_r$, for sensorless operation with ±25% stator resistance detuning, are shown in Figure 5.7. Results for two SMO gains, K=0.5 and K=2.5, are presented. With low gain, the SMO behaves like the linear observer, Figure 4.15, exhibiting large estimation errors at low speeds. With high gain the estimation error is decreased, at the price of increasing the chattering.

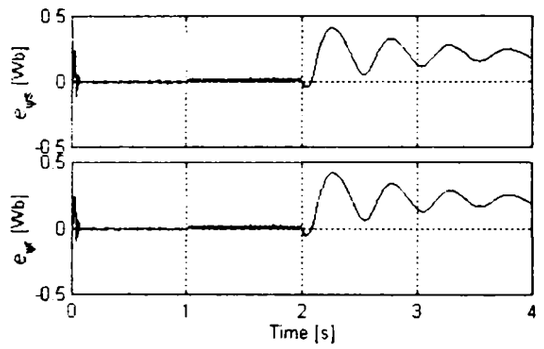

a. +25% R_s detuning, K=0.5

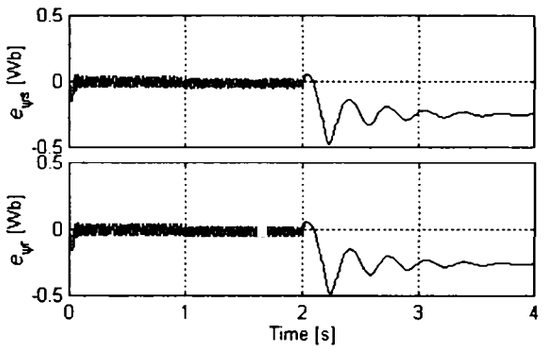

b. -25% R_s detuning, K=0.5

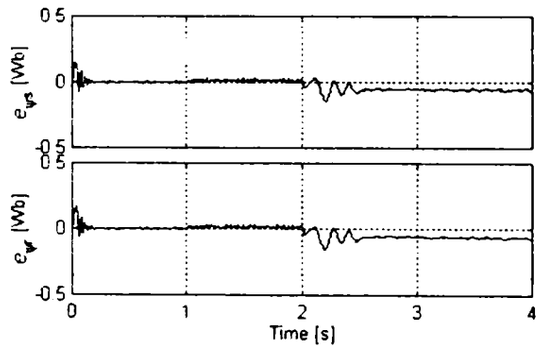

c. +25% R_s detuning, K=2.5

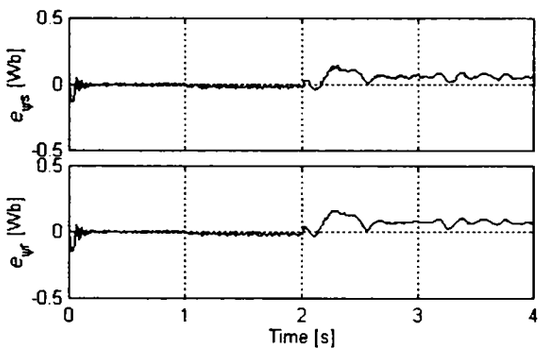

d. -25% R_s detuning, K=2.5

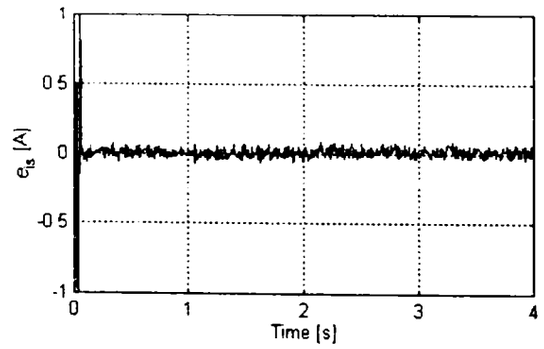

e. +25% R_s detuning, K=0.5

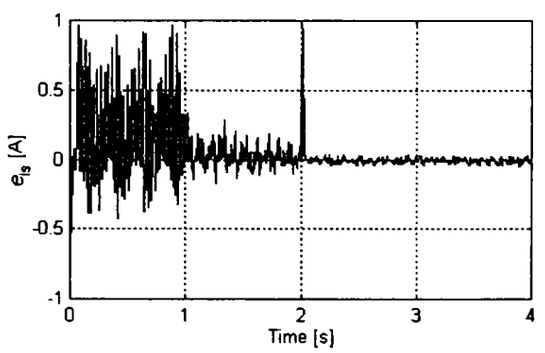

f. -25% R_s detuning, K=0.5

Figure 5.7 Stator and rotor flux magnitude errors and stator current magnitude error for SMO, with ±25% R_s detuning and two different gains, K=0.5 and K=2.5

It is interesting to observe that both, the asymptotical observer and the SMO, are very sensitive to stator resistance detuning. An explanation for that sensitivity is suggested by Figures 5.7.e and f that show the current magnitude estimation errors. At low speed, where the flux estimation error is large, the current estimation error is insignificant. Although not shown, the current phase error is also very small.

At low speed, the SMO maintains very well the sliding mode, since the sliding surface is $S = \underline{i}_s - \hat{\underline{i}}_s = 0$. Despite of that, the SMO is unable to compensate for the R_s detuning. This is an indication that the current and flux errors are uncorrelated for this detuning. It is concluded that the current error based observers must employ a stator resistance adaptation mechanism excited by a nonlinear error that contains a cross-correlation product between the current and flux errors, similar to a torque error.

It is the case of R_s estimator (4.61) that contains the rotor flux - current error product (the active power error). This is superior to (4.60) that is based on reactive power error. The adaptation strategy (4.61) works well for the SMO, as can bee seen in Figure 5.8 that shows R_s estimation with ±50% R_s initial detuning and K_{Rs}=10.

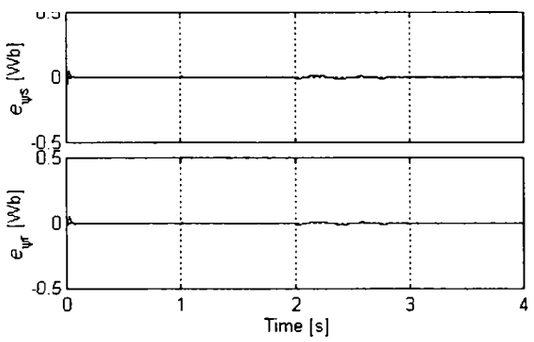

a. Flux errors for +50% R_s detuning

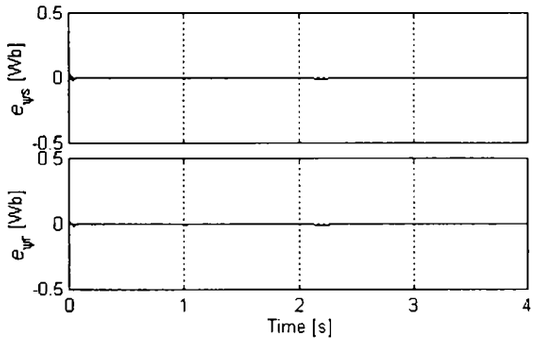

b. Flux errors for -50% R_s detuning

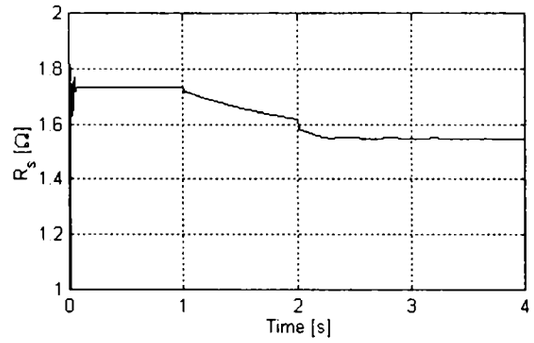

c. Estimated R_s for +50% R_s detuning

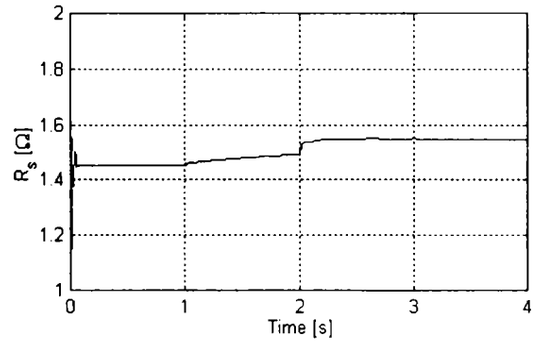

d. Estimated R_s for -50% R_s detuning

Figure 5.8 Stator and rotor flux errors and estimated R_s with ±50% R_s initial detuning

The stator resistance adaptation takes place only when the torque is nonzero. At startup, R_s converges very fast and reaches a value close to the correct one. The rated value, R_s=1.55 Ω, is attained in less than 2 sec. of loaded operation.

The SMO sensitivity to ±50% magnetizing inductance detuning is shown in Figure 5.9.a and b, while the sensitivity to ±50% rotor resistance detuning, in Figure 5.9.c and d. The stator and rotor flux estimation errors are given in all cases.

The SMO is robust to L_m overestimation, at both, high and low speeds. At low speed, the flux magnitude estimation error is driven to zero after a short transient. Unfortunately, the SMO is strongly affected by L_m underestimation. An overestimation of L_m is recommended whenever its value is uncertain.

As the asymptotical observer, the SMO is very robust to rotor resistance detuning, Figure 5.9.c, d. Small errors appear during flux transients, due to rotor time constant detuning. Errors, even larger than ±100% in R_r value have no significant influence on flux estimation, as long as the flux is maintained almost constant or is slowly modified. Fast flux transients are impractical in induction machine drives.

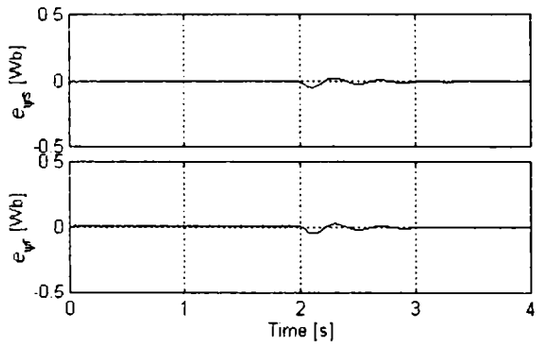

a. +50% L_m detuning

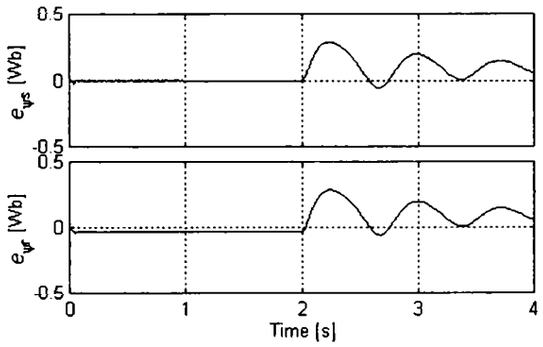

b. -50% L_m detuning

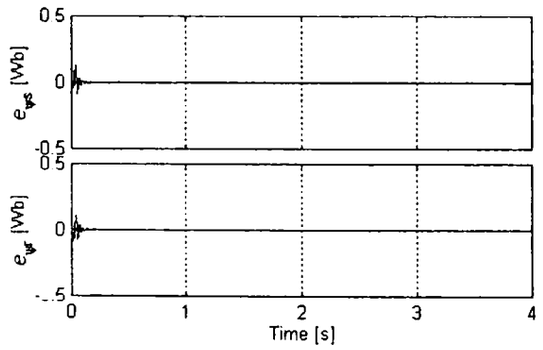

c. +50% R_r detuning

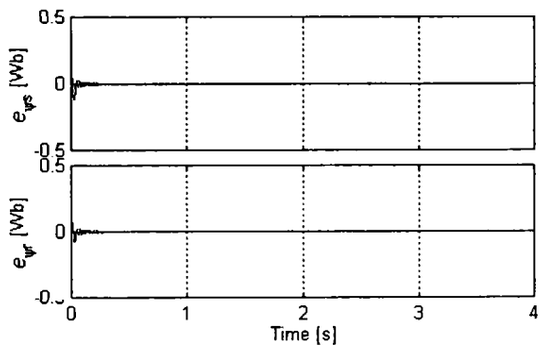

d. -50% R_r detuning

Figure 5.9 Stator and rotor flux estimation errors with L_m, and R_r – simulations

Experimental results with SMO

Extensive experiments have been carried out in order to demonstrate the performance of the SMO, (Figure 5.1), in various speed and load conditions. Very low speed sensorless operation was targeted and the system's ability, to operate stable, under full load, at zero and very low speed, has been confirmed.

Zero speed, full load, sensorless operation, with SMO is presented in Figures 5.10 and 5.11 (estimated and measured speed, estimated torque, stator and rotor flux, estimated stator current and current estimation error). The control strategy is LFSG, with PLL speed estimation and the motor under test is Machine 2 (1.1 kW).

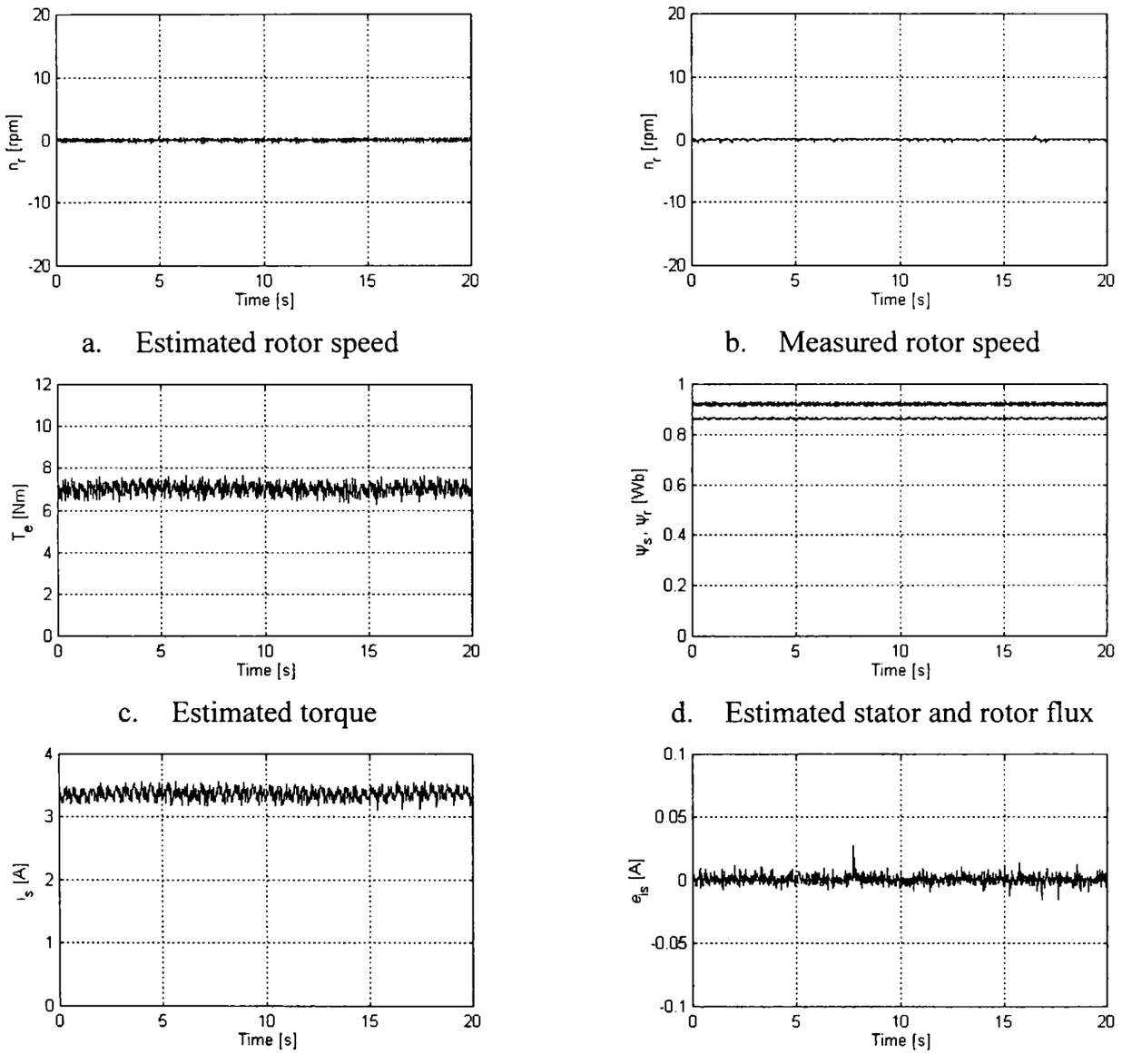

a. Estimated rotor speed

b. Measured rotor speed

c. Estimated torque

d. Estimated stator and rotor flux

e. Estimated stator current magnitude

f. Stator current estimation error

Figure 5.10 Zero speed sensorless operation with LFSG and SMO

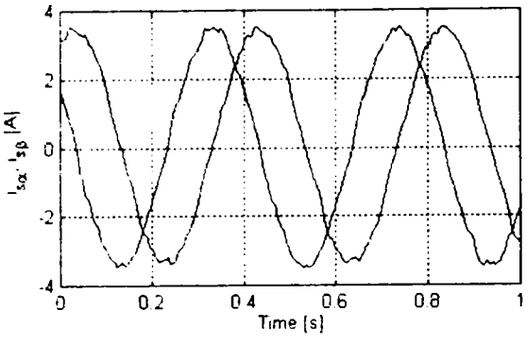

a. Measured (α,β) stator currents

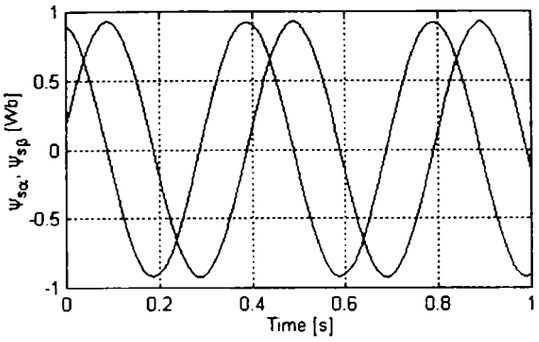

b. Estimated (α,β) stator flux

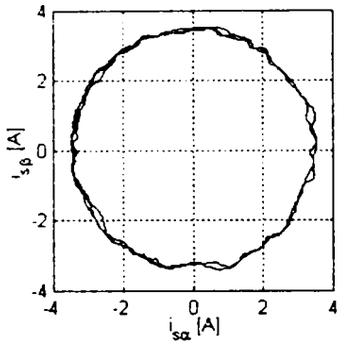

c. Measured current trajectory

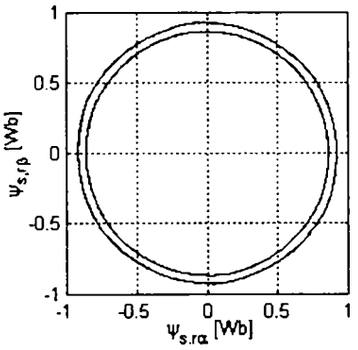

d. Estimated stator and rotor flux trajectory

Figure 5.11 Current and flux during zero speed operation with LFSG and SMO

The SMO performance is illustrated by the current error in Figure 5.10.f that is much smaller than the same error obtained with Luenberger observer, Figure 4.18.f. Although some chattering is present in flux estimates, it has no influence on system's behavior. Details of the instantaneous current and estimated stator flux, on a time span of one second, are shown in Figure 5.11, for the same operating conditions.

Acceleration transients from standstill to 1500 rpm in sensorless operation, with the same system are shown in Figure 5.12. Although the starting torque is 12 Nm, 1.7 times the motor's rated torque 7 Nm, the staring time is quite long for a 1.1 kW motor. This is because the motor was mechanically coupled to a heavy-rotor DC generator.

Although some sensitivity to torque transients is apparent in both fluxes, this is due to control system, not to SMO. The estimation error is not at all affected by torque transients and even decreases at high torque. This indicates that the SMO maintains very well the sliding mode and is very robust, practically invariant with respect to torque and speed perturbations. The estimation error and the flux chattering are larger than those at zero speed, but the system's overall performance is outstanding.

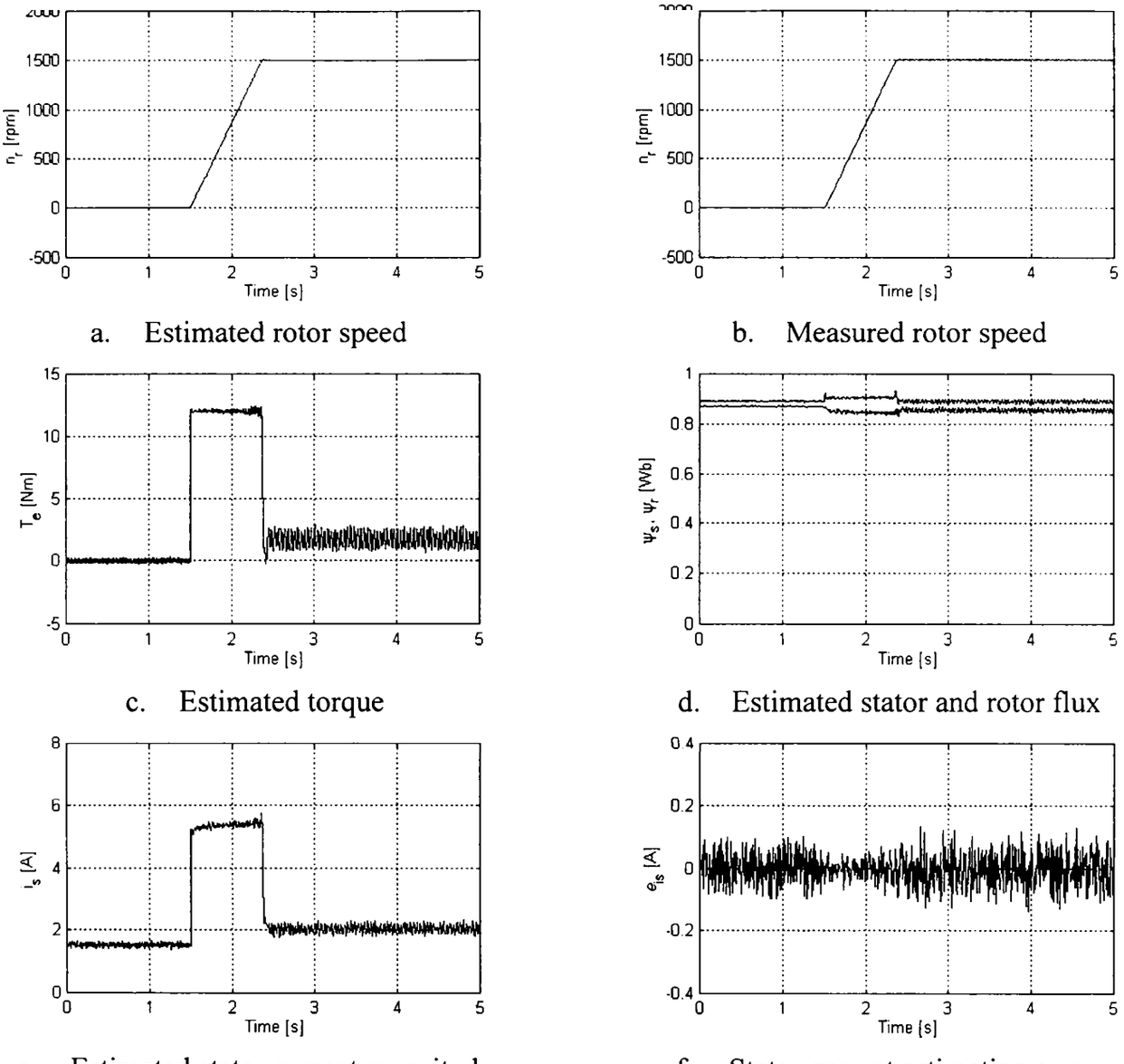

a. Estimated rotor speed

b. Measured rotor speed

c. Estimated torque

d. Estimated stator and rotor flux

e. Estimated stator current magnitude

f. Stator current estimation error

Figure 5.12 Acceleration from standstill to 1500 rpm, with LFSG and SMO

Experimental results with modified SMO

The modified SMO schemes (Figures 5.4 and 5.5) have been also tested, in the same conditions as the basic SMO. Experimental results at zero speed, full load, sensorless operation, with LFSG control, modified SMO (Figure 5.4) and PLL speed estimation are presented in Figures 5.13. The observer exhibits very low estimation errors and, in general, its performance is similar to that of the basic SMO. However, it was noticed that, in some particular situations, especially at low speeds, the modified SMO performs better than the basic SMO, due to its offset compensation properties.

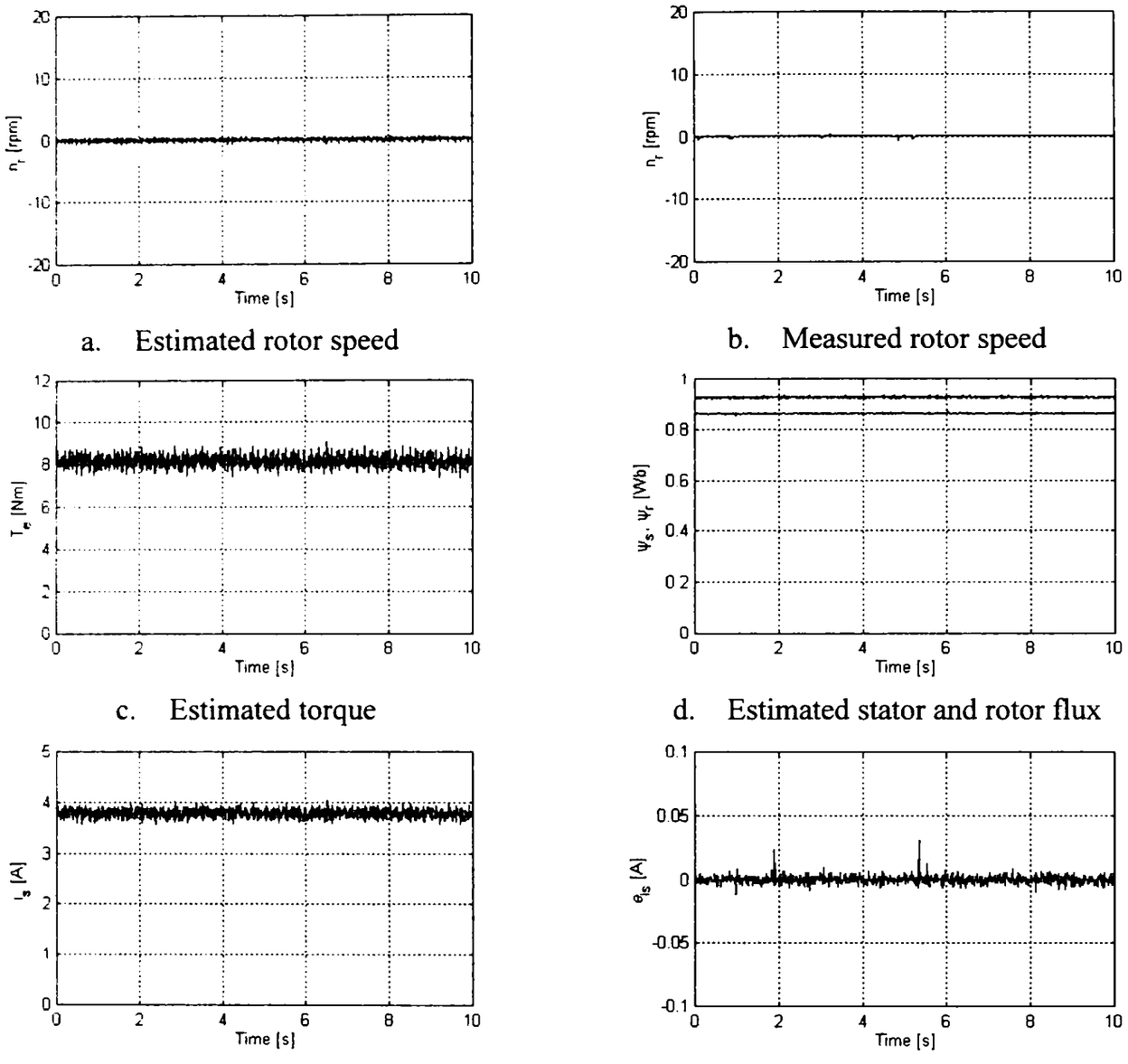

Figure 5.13 Zero speed sensorless operation with LFSG and modified SMO

Very low speed, 3 rpm, full load, sensorless operation with the modified SMO and LFSG control is illustrated in Figure 5.14. The control activity is larger, so are the estimation error, the torque and current ripple, but the overall performance is excellent. Partly, the torque ripple is due to the very noisy (in terms of torque) behavior of the DC generator employed for loading. Despite of that, the system's acoustical noise level was very low. With reference to (4.46), the SMO parameters employed for all experiments are: K=0.5, h=0.03, L=20+0.1ω_r, K_P=20, K_I=40, K_{Rs}=10, almost the same with those used for simulations. For zero speed experiments, h=0.003.

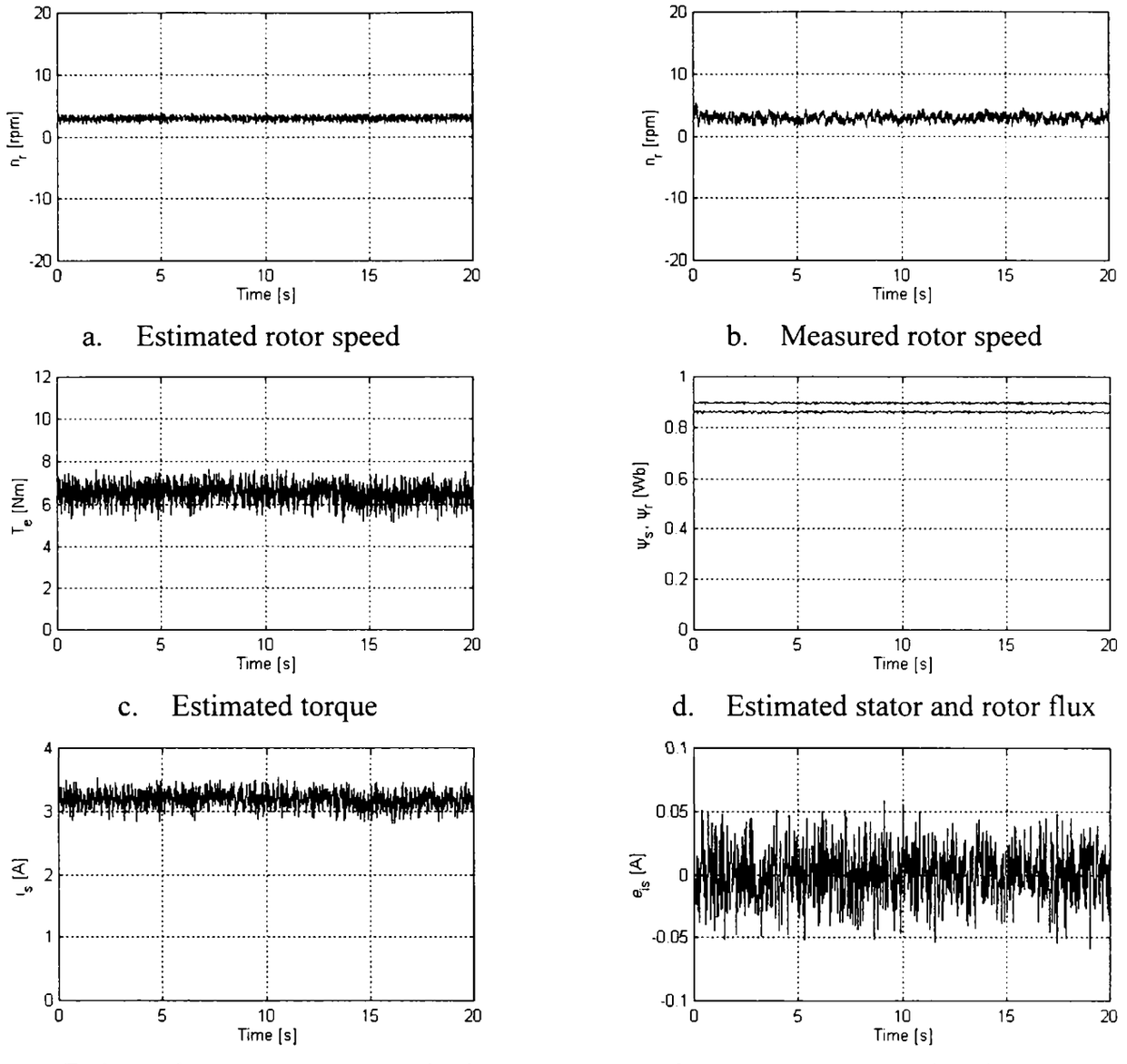

Figure 5.14 Very low speed – 3 rpm – sensorless operation with LFSG and modified SMO

Instantaneous (α,β) components of the current and estimated stator flux, on a time span of one second, are shown in Figure 5.15, for 3 rpm sensorless operation, in the same conditions and with the same SMO parameters as for Figure 5.14. The fact that the current is slightly distorted when compared to the zero speed operation is due to the LFSG controller behavior, rather than to SMO performance.

The startup transients and high speed operation are identical to those shown in Figure 5.12 for the basic SMO case. Similar experimental results have been obtained with the modified SMO topology proposed in Figure 5.5.

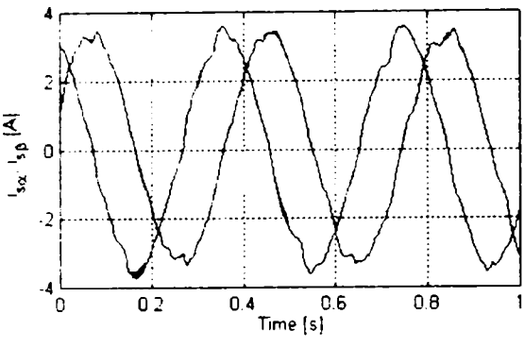

a. Measured (α,β) stator currents

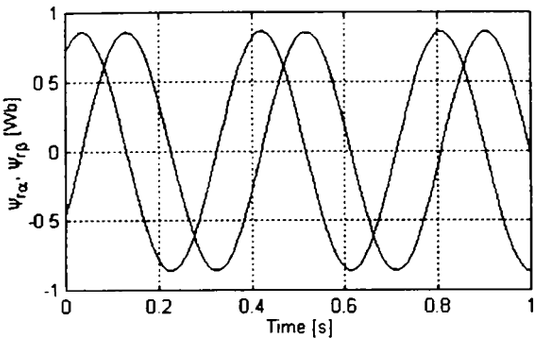

b. Estimated (α,β) rotor flux

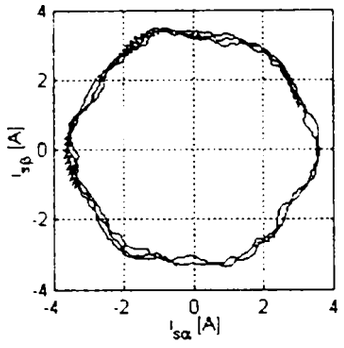

c. Measured current trajectory

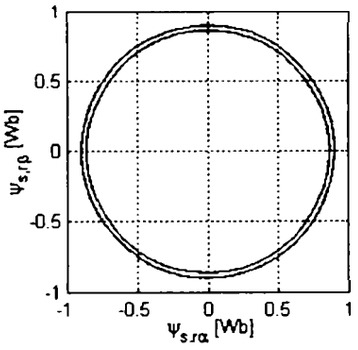

d. Estimated stator and rotor flux trajectory

Figure 5.15 Current and flux at 3 rpm operation with LFSG and modified SMO

Experimental results with generalized observer

The generalized topology, Figure 5.2, allows designing a flexible observer that exploits advantages of both, the asymptotical observer and the SMO. The adequate balance, between these two basic structures, can be found by selecting adequate gains for the linear and the variable structure feedbacks.

Zero speed, full load sensorless operation with the generalized observer, LFSG control and PLL speed estimation is demonstrated in Figure 5.16. The results are comparable to those obtained with SMO, Figures 5.10 and 5.13, since, in this case, the SMO feedback gains were quite large. However, the flux chattering is lower, while the current error is slightly higher, approaching the linear behavior, Figure 4.18.

Instantaneous (α,β) components of the stator current and stator flux, and their complex plane trajectories, during zero speed, full load, sensorless operation, with the same control system, are presented in Figure 5.17. As can be noticed, the flux estimate is sinusoidal, while the current waveform is distorted due to LFSG control.

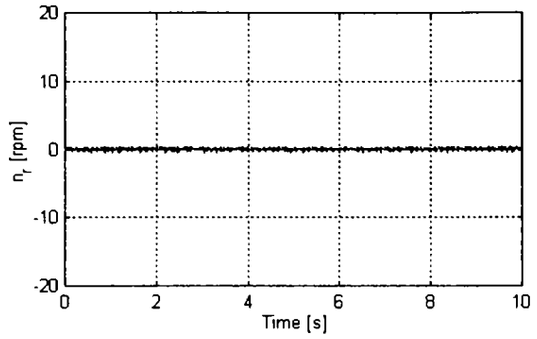

a. Estimated rotor speed

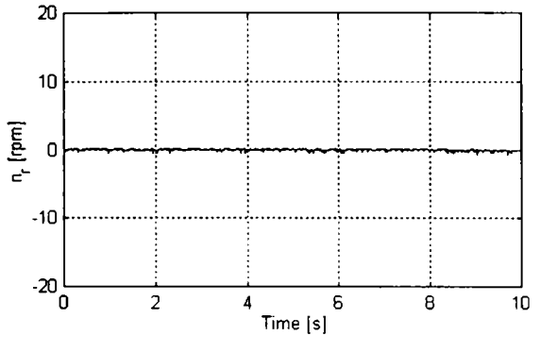

b. Measured rotor speed

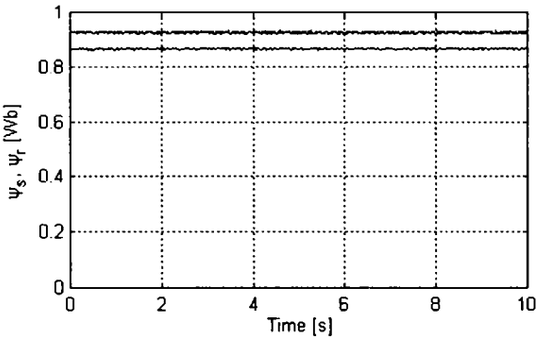

c. Estimated stator and rotor flux

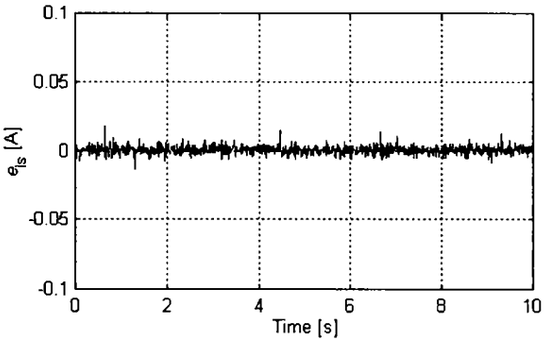

d. Stator current estimation error

Figure 5.16 Zero speed sensorless operation with LFSG and generalized observer

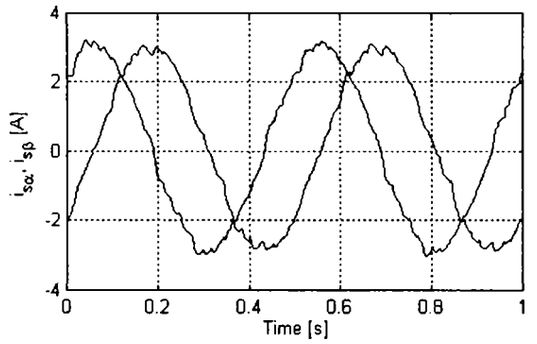

a. Measured (α,β) stator currents

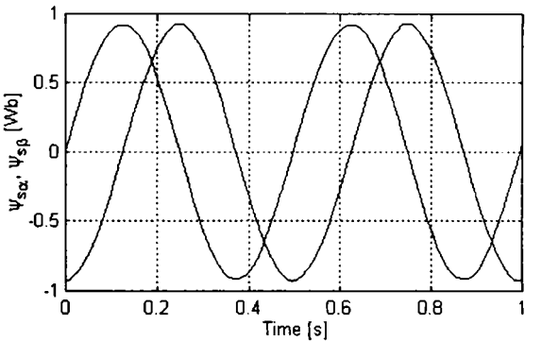

b. Estimated (α,β) stator flux

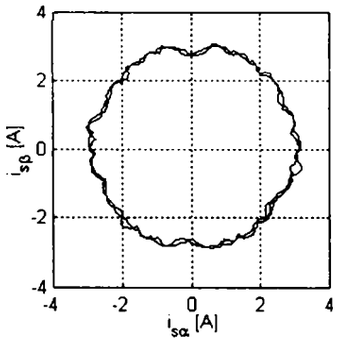

c. Measured current trajectory

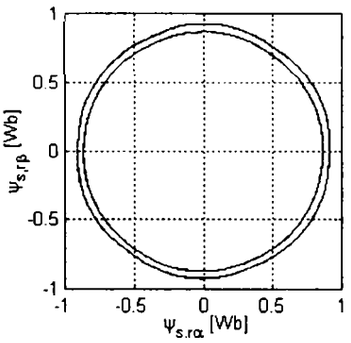

d. Estimated stator and rotor flux trajectory

Figure 5.17 Current and flux at zero speed, with LFSG and generalized observer

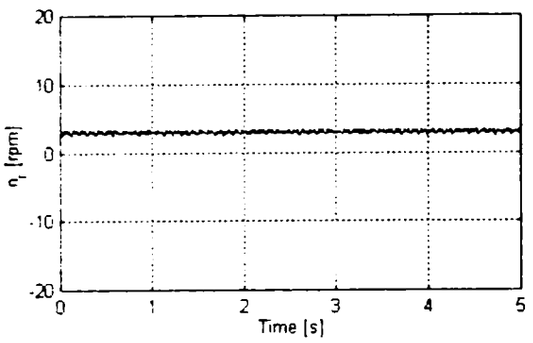

a. Estimated rotor speed

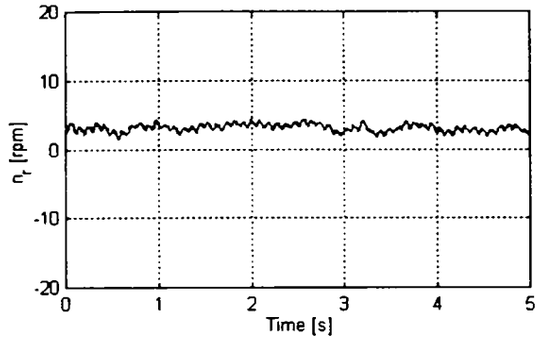

b. Measured rotor speed

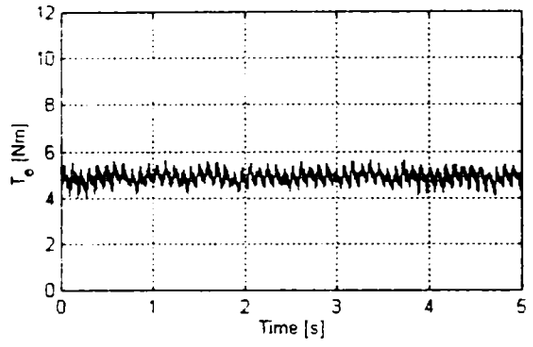

c. Estimated torque

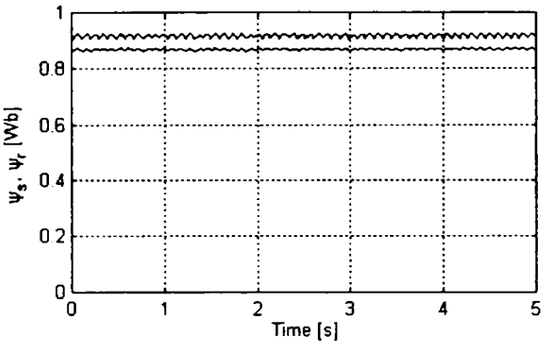

d. Estimated stator and rotor flux

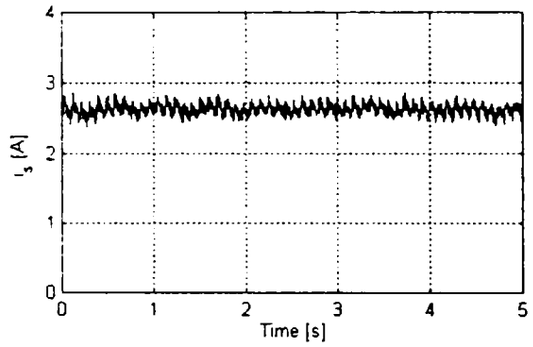

e. Estimated stator current magnitude

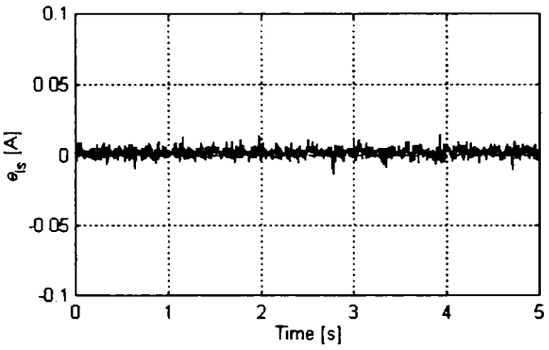

f. Stator current estimation error

Figure 5.18 Sensorless operation at 3 rpm, with LFSG and generalized observer

Sensorless operation at 3 rpm, with the generalized observer, LFSG control and PLL speed estimation is presented in Figure 5.18. The current estimation error is very small, comparable to that obtained for zero speed operation and much smaller than in Figure 5.14. This time, the load is lower than the motor's rated load, but the system's behavior is still good. The estimation is stable, although the flux and speed show larger ripple than before. As the load decreases and the operation approaches the speed unobservability point, i.e. zero Hz stator frequency [19], the system's behavior progressively degrades. It was determined that the lowest stator frequency that still allows stable operation is f_{lim}=0.3 Hz.

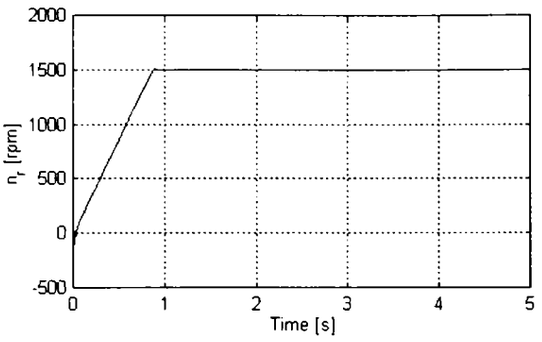

a. Estimated rotor speed

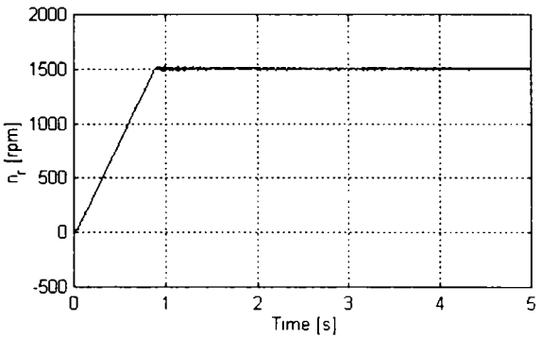

b. Measured rotor speed

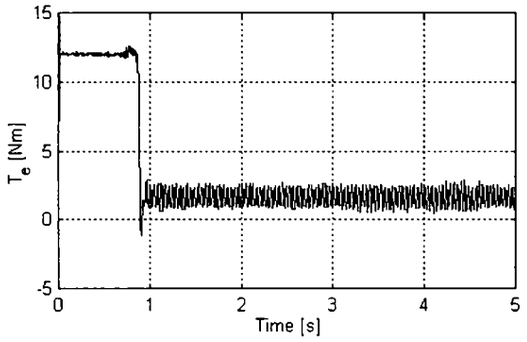

c. Estimated torque

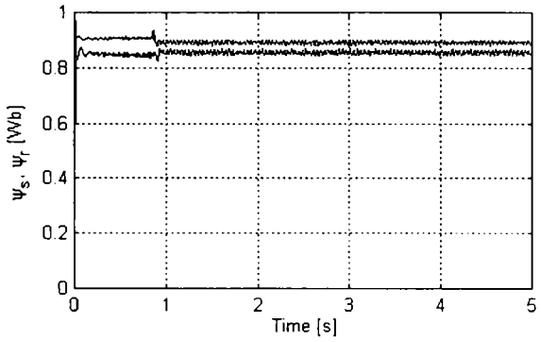

d. Estimated stator and rotor flux

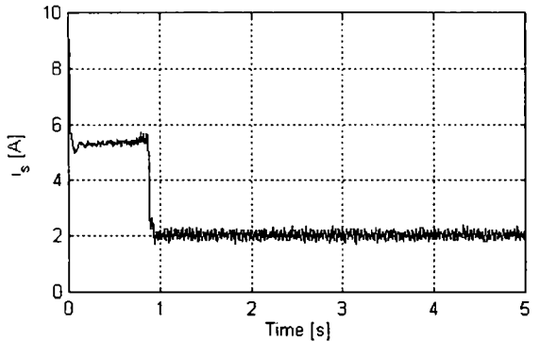

e. Estimated stator current magnitude

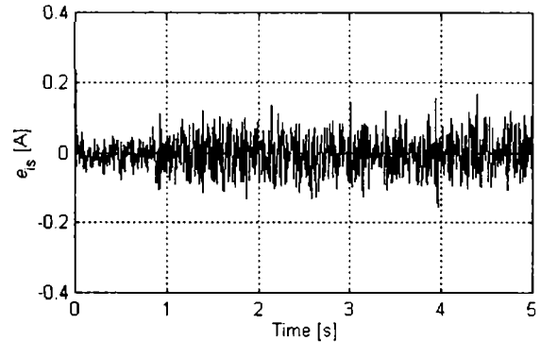

f. Stator current estimation error

Figure 5.19 Starting transients to 1500 rpm, with LFSG and generalized observer

Starting transients to 1500 rpm, in sensorless operation, with the same system is presented in Figure 5.19. The motor is accelerated at 12 Nm constant torque, almost twice its rated torque, but the acceleration time is quite long, since the motor was connected to a DC generator with very large inertia rotor.

At the beginning, until the sliding mode is reached, the estimation error is large. Once the observer reaches the sliding mode, the error remains low, despite of violent torque and speed transients. This is an indication that the SMO maintains very well the sliding mode and is invariant with respect to torque and speed transients. Acceleration transients are similar to those shown for SMO in Figure 5.12.

5.4 Conclusions

A new, inherent sensorless, variable structure observer for induction machines state estimation has been developed and thoroughly analyzed. Several practical methods for observer gain selection have been presented. Two modified topologies, insensitive to measurement offset, have been derived from the basic scheme and a generalization of the inherent sensorless observer concept, that includes the SMO and the Luenberger observers, has been proposed.

The SMO possesses invariant dynamic modes and robustness with respect to modeling uncertainties. It was determined, however, that the SMO is sensitive to model parameters detuning, especially to stator resistance mismatch. For very low speed operation the stator resistance adaptation is mandatory. The stator resistance adaptation mechanism proposed for the asymptotical observer is applicable to SMO and was successfully employed in all experiments.

The SMO performance, including zero speed and 3 rpm, full load, sensorless operation, has been demonstrated by experiments for all proposed schemes. In all situations the current estimation error is smaller than that of the asymptotical observer and estimated quantities contain some negligible high frequency chattering. The system has been proved to be very robust with respect to perturbations and this represents the most important advantage of the sliding mode observer.

Since very low speed operation is the most challenging problem for sensorless drives, only some of the best low speed results, obtained with described systems, have been extensively presented and discussed herewith. Nevertheless that higher speed, steady state and transient operation is absolutely possible and was extensively tested [20]. At higher speeds, all proposed observers perform equally well, with only small, insignificant differences, in the whole speed range, from 3 rpm to 3000 rpm.

References

[1] B.L. Walcott, M.J. Corless, S.H. Żak, *Comparative study of non-linear state-observation techniques.*, International Journal of Control, vol. 45, no. 6, 1987, pp. 2109-2132.

[2] F. Chen, M.W. Dunnigan, *Comparative Study of a Sliding-Mode Observer and Kalman Filters for Full State Estimation in an Induction Machine.*, IEE Proceedings on Electric Power Applications, vol. 149, no. 1, January 2002, pp. 53-64.

[3] E.A. Misawa, J.K. Hedrick, *Nonlinear Observers – A State-of-the-Art Survey.*, Transactions of the ASME Journal of Dynamic Systems, Measurement and Control, vol. 111, Sept. 1989, pp. 344-352.

[4] J.-J.E. Slotine, J.K. Hedrick, E.A. Misawa, *On Sliding Observers for Nonlinear Systems.*, Transactions of the ASME Journal of Dynamic Systems, Measurement and Control, vol. 109, Sept. 1987, pp. 245-252.

[5] Vadim I. Utkin, *Sliding Modes in Control Optimization.*, Springer-Verlag, Berlin, 1992.

[6] Vadim Utkin, Jurgen Guldner, Jingxin Shi, *Sliding Mode Control in Electromechanical Systems.*, Taylor & Francis, 1999.

[7] I. Haskara, U. Ozguner, V.I. Utkin, *On Sliding Mode Observers via Equivalent Control Approach.*, International Journal of Control, vol. 71, no. 6, 1998, pp. 1051-1067.

[8] S.V. Drakunov, V.I. Utkin, *Sliding Mode Observers. Tutorial.*, CDC 1995, The 34th Conference on Decision and Control, New Orleans, LA, 1995, pp. 3376-3378.

[9] S.V. Drakunov, V.I. Utkin, *Discrete Event Sliding Mode Observers for Continuous-Time Systems.*, CDC 1995, The 34th Conference on Decision and Control, New Orleans, LA, 1995, pp. 3403-3405.

[10].C. Aitken, H.M. Schwartz, *Towards Robust Discrete-Time Sliding Mode Observers.*, 1995 American Control Conference, Seattle, WA, 1995, pp. 3730-3734.

[11]Z. Yan, C. Jin, V.I. Utkin, *Sensorless Sliding-Mode Control of Induction Motors.*, IEEE Transactions on Industrial Electronics, vol. 47, no. 6, Dec. 2000, pp. 1286-1297.

[12]A. Benchaib, A. Rachid, E. Audrezet, M. Tadjine, *Real-Time Sliding-Mode Observer and Control of an Induction Motor.*, IEEE Transactions on Industrial Electronics, vol. 46, no. 1, Feb. 1999, pp. 128-137.

[13]M. Tursini, R. Petrella, F. Parasiliti, *Adaptive Sliding Mode Observer for Speed Sensorless Control of Induction Motors.*, IEEE Transactions on Industry Applications, vol. 36, no. 5, Sept./Oct. 2000, pp 1380-1387.

[14]S. Doki, S. Sangwongwanich, S. Okuma, *Implementation of Speed-Sensor-Less Field-Oriented Vector Control using Adaptive Sliding Observer.*, IEEE IECON'92, The 1992 International Conference on Industrial Electronics, 1992, vol. 1, pp. 453-458.

[15]S. Sangwongwanich, S. Doki, T. Yonemoto, S. Okuma, *Adaptive Sliding Observers for Direct Field-Oriented Control of Induction Motor.*, IEEE IECON'90, The 16th Annual Conference of Industrial Electronics Society, 1990, vol. 2, pp. 915-920.

[16]A. Kheloui, K. Aliouane, M. Medjaoui, B. Davat, *Design of a Stator Flux Sliding Mode Observer for Direct Torque Control of Sensorless Induction Machine.*, The 35th IEEE Industry Applications Society Annual Meeting, 2000, Rome, CD-ROM paper 33.7.

[17]V.I. Utkin, D.-S. Chen, S. Zarei, J. Miller, *Sliding Mode Observers for Automotive Alternators.*, Proceedings of the American Control Conference, 1999, CD-ROM paper WA06-3, pp. 165-166.

[18]Jean-Jacques E. Slotine, Weiping Li, *Applied Nonlinear Control.*, Prentice Hall, Englewood Cliffs, New Jersey, 1991

[19]J. Holtz, *Methods for Speed Sensorless Control of AC Drives.*, in K. Rajashekara (Editor) "Sensorless Control of AC Motors", IEEE Press, 1996.

[20]Cristian Lascu, Ion Boldea, *Direct Torque Control of Sensorless Induction Motor Drives. A Sliding Mode Approach.*, Proc. of the International Conference on Optimization of Electrical and Electronic Equipments – OPTIM 2002, Brasov, Romania, 2002, vol. 2, pp. 481-488.

6 SPEED OBSERVERS FOR INDUCTION MACHINE DRIVES

6.1 Introduction

Sensorless control of ADS-s in the very low speed range is a challenging area of research. The basic idea of this approach is to estimate the speed from measured terminal voltages and currents. In induction machine drives, due to the high order and nonlinearity of the machine dynamics, speed estimation is not a trivial task.

The rotor speed estimator is the most important component of the sensorless drive system and the quality of the speed estimator is decisive for the system's overall performance. A variety of different solutions for sensorless speed and torque control have been proposed in the past few years, but only a handful of them have displayed satisfactory performance in the low speed range [1].

There are two categories of rotor speed estimators in ASD-s: estimators based on magnetic saliency and signal injection and estimators based on fundamental excitation. Methods in the former category can operate stable at zero stator frequency, but the high frequency voltage and current components cause torque ripple, loss increasing and acoustical noise. This is a major drawback that makes these methods unattractive, despite of some good results obtained [2].

Methods in the later category employ the fundamental components of stator voltages and currents to extract the speed information. The basic limitation of this method is the inability to provide speed estimation in continuous operation at zero stator frequency.

Indeed, at zero stator frequency the stator flux becomes a DC quantity and the fundamental EMF is zero, that is $\underline{u}_s = R_s \underline{i}_s$, (2.21). It means that the stator current is exclusively governed by the feeding voltage. There is no feedback from rotor and the rotor quantities have no influence on stator current. Since the current is the system's output and the only measurable quantity used for state estimation, it can be concluded that the rotor speed is not observable at zero stator frequency.

Zero stator frequency occurs in regenerating operation at low speeds or at zero speed, no load operation. To reduce at an acceptable level the influence of noise and parameter mismatch, that is strong at low speeds, the stator frequency must be raised from zero to a minimum value [1]. This is possible by considering the speed equation

$$\omega_r = \omega_1 - \omega_s \tag{6.1}$$

At given rotor speed ω_r, the field speed ω_1 can be maintained far from zero by modifying the slip speed ω_s. The slip speed, (2.64) depends on torque and rotor flux magnitude. Since the torque is fixed by load, the slip can be modified by changing the flux magnitude such that to maintain adequate stator excitation [10]. This method is not applicable at no-load, where very low speed operation must be avoided.

Hence, the zero frequency problem does not represent an important limitation and speed estimation methods based on fundamental excitation are viable solutions for sensorless drives. The most important methods in this category are described next.

There are several types of speed estimators based on fundamental excitation:

- Open loop speed estimators based on induction machine equations. Herewith, these are called "Speed estimators".
- Model Reference Adaptive speed estimators.
- Speed adaptive state observers. This category includes asymptotical observers with speed estimators, and SMO-s with sliding mode speed estimators.
- Extended Kalman filters.

6.2 Speed Observers – State of the Art

6.2.1 Open-Loop Speed and Torque Estimation

The simplest and yet one of the best speed estimation methods is based on open-loop rotor speed calculation, using the speed equation (6.1) [3], [4].

$$\hat{\omega}_r = \hat{\omega}_{\psi r} - \hat{\omega}_s \tag{6.2}$$

Using the estimated rotor flux in stator reference frame, the rotor flux speed is

$$\hat{\omega}_{\psi r} = \frac{d}{dt}\hat{\theta}_{\psi r} = \frac{d}{dt}\tan^{-1}\left(\frac{\hat{\psi}_{r\beta}}{\hat{\psi}_{r\alpha}}\right) \tag{6.3}$$

After some manipulations, (6.3) becomes

$$\hat{\omega}_{\psi r} = \frac{1}{\hat{\psi}_r^2}\left(\hat{\psi}_{r\alpha}\frac{d}{dt}\hat{\psi}_{r\beta} - \hat{\psi}_{r\beta}\frac{d}{dt}\hat{\psi}_{r\alpha}\right) \tag{6.4}$$

where $\hat{\psi}_r^2 = \hat{\psi}_{r\alpha}^2 + \hat{\psi}_{r\beta}^2$.

The digital realization of (6.4) approximates the flux derivative in the k-th sampling cycle by finite difference $d\underline{\hat{\psi}}_{r(k)}/dt = (\underline{\hat{\psi}}_{r(k)} - \underline{\hat{\psi}}_{r(k-1)})/T_s$, where $\underline{\hat{\psi}}_{r(k)}$ and $\underline{\hat{\psi}}_{r(k-1)}$ are flux estimates from in two consecutive sampling cycles, k-1 and k, and T_s is the sampling period. The estimated rotor flux speed in the k-th sampling cycle is

$$\hat{\omega}_{\psi r} = \frac{\hat{\psi}_{r\beta(k)}\hat{\psi}_{r\alpha(k-1)} - \hat{\psi}_{r\alpha(k)}\hat{\psi}_{r\beta(k-1)}}{T_s(\hat{\psi}_{r\alpha(k)}^2 + \hat{\psi}_{r\beta(k)}^2)} \tag{6.5}$$

The slip speed is calculated from (2.64) and (2.105) as

$$\hat{\omega}_s = \frac{2R_r}{3p}\frac{\hat{T}_e}{\hat{\psi}_r^2} \tag{6.6}$$

Te electromagnetic torque is estimated by either one of the following equations

$$\hat{T}_e = \frac{3}{2}p(\hat{\psi}_{s\alpha}i_{s\beta} - \hat{\psi}_{s\beta}i_{s\alpha}) \tag{6.7}$$

$$\hat{T}_e = \frac{3}{2}p\frac{L_m}{L_r}(\hat{\psi}_{r\alpha}i_{s\beta} - \hat{\psi}_{r\beta}i_{s\alpha}) \tag{6.8}$$

In spite of simplicity, this method is able to provide accurate estimate during speed transients, allowing fast speed control. However, it suffers from two important limitations. First, the slip speed is sensitive to rotor resistance detuning. This is a common characteristic of all methods that employ (6.6) for slip speed estimation.

Second, equation (6.4) requires evaluation of the flux derivative that acts like a noise amplifier. Since all systems contain a certain amount of noise, (6.5) produces very noisy results. The estimated speed must be filtered in order to remove that noise. This filtering reduces the speed tracking bandwidth and the dynamic stiffness.

Experiments with this estimator are shown in Figure 4.19. The lowest possible speed was 30 rpm, no load (f_1=1 Hz). Continuous sensorless operation at 10 rpm, with a system that employs a speed estimator of this type, is reported in [3]. In this case, (6.2) is implemented using the stator flux speed and the corresponding slip speed.

6.2.2 Model Reference Adaptive Systems

The Model Reference Adaptive System (MRAS) approach makes use of the redundancy of two machine models with different structures that estimate the same state variables on the basis of the same set of input variables, Figure 6.1. The reference model does not involve the speed and is supposed accurate and invariant. It generates the state x. The adaptive model does involve the speed information and generates the inaccurate state x_a. The error ε between x and x_a is used to drive a suitable adaptation mechanism that generates the speed estimate for the adjustable model [4]-[6].

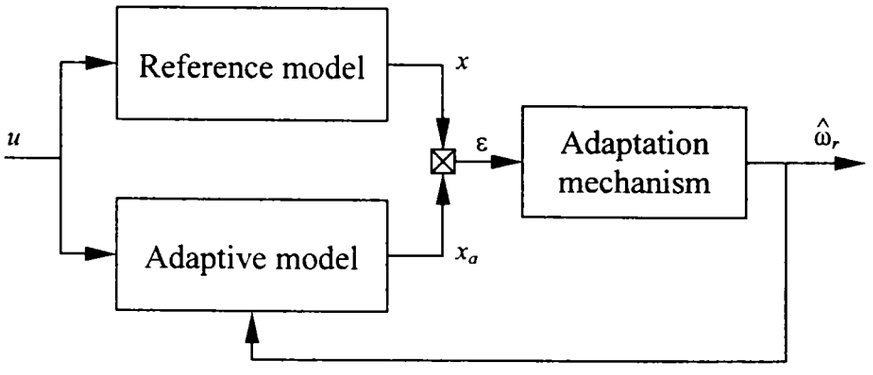

Figure 6.1 Model Reference Adaptive System for speed estimation

Flux error based MRAS estimator

One of the most popular MRAS speed estimators is based on the error between outputs of two rotor flux estimators, the voltage model and the current model, [4], [5].

The reference model is the voltage model in stator reference frame

$$\frac{d}{dt}\underline{\hat{\psi}}_r^u = \frac{L_r}{L_m}(\underline{u}_s - R_s\underline{i}_s) - \frac{L_s L_r \sigma}{L_m}\frac{d}{dt}\underline{i}_s \tag{6.9}$$

The adaptive model is the current model in stator reference frame

$$\frac{d}{dt}\underline{\hat{\psi}}_r^i = \frac{L_m}{T_r}\underline{i}_s + (-\frac{1}{T_r} + j\omega_r)\underline{\hat{\psi}}_r^i \tag{6.10}$$

The adaptation mechanism is a PI controller driven by the error $\varepsilon = \Im m(\underline{\hat{\psi}}_r^u \underline{\hat{\psi}}_r^{i*})$ that is proportional to the angular difference between the two estimated flux vectors.

$$\hat{\omega}_r = (K_P + \frac{K_I}{s})(\hat{\psi}_{r\alpha}^i \hat{\psi}_{r\beta}^u - \hat{\psi}_{r\alpha}^u \hat{\psi}_{r\beta}^i) \tag{6.11}$$

As the error gets minimized, the tuning signal approaches the real speed ω_r.

The MRAS can be interpreted as a vector phase-locked loop (PLL) in which the reference model generates the reference vector and the adjustable model is a vector phase shifter controlled by the estimated speed, as in (6.26)-(6.27).

Accuracy and drift problems that are inherent to the pure integrator are reduced by using a LPF, instead of the integrator in the reference model, as in (4.13).

$$\underline{\hat{\psi}}_r^u = \frac{L_r}{L_m}\frac{1}{s+\omega_0}(\underline{u}_s - R_s\underline{i}_s) - \frac{L_s L_r \sigma}{L_m}\underline{i}_s \tag{6.12}$$

Since the adaptation mechanism is driven by the phase error between the two models and the LPF introduces phase shift, an equivalent filter must be added for the adaptive model. It is recommended to high-pass filter the measured current $\underline{i}_s$, as

$$\underline{i}_s' = \frac{s}{s+\omega_0}\underline{i}_s \tag{6.13}$$

and to employ this value in the current model instead of the measured current.

$$\frac{d}{dt}\underline{\hat{\psi}}_r^i = \frac{L_m}{T_r}\underline{i}_s' + (-\frac{1}{T_r} + j\omega_r)\underline{\hat{\psi}}_r^i \tag{6.14}$$

Below the cutoff frequency ω_0, the speed estimation becomes necessarily inaccurate, as the reference model produces inaccurate flux estimate.

The selection of K_P and K_I gains can be made by pole placement methods, as described in [4] and [5]. Due to noise considerations, these are limited, thereby restraining the dynamic behavior. The dynamic response and stability of MRAS speed estimator are extensively analyzed in [4] and good dynamic performance is reported at 2 Hz stator frequency. Speed reversal is also possible, but, if the drive is operated at zero frequency for more than a few seconds, the estimated speed vanishes and the speed control is lost [4]. In general, at low speed, the estimation is poor.

EMF and power error based MRAS estimators

A MRAS scheme that avoids the drift problem related to the pure integrator and the LPF low speed inaccuracy is based the back EMF error [7]. The reference model is the same voltage model in stator frame and the estimated EMF is calculated as

$$\underline{\hat{e}}_m^u = \frac{L_m}{L_r}\frac{d}{dt}\underline{\hat{\psi}}_r^u = \underline{u}_s - (R_s\underline{i}_s + L_s\sigma\frac{d}{dt}\underline{i}_s) \tag{6.15}$$

The adaptive model is the current model (6.10) that estimates the rotor flux. It is followed by the EMF calculation

$$\underline{\hat{e}}_m^i = \frac{L_m}{L_r}\frac{d}{dt}\underline{\hat{\psi}}_r^i = \frac{L_m}{L_r}(\frac{L_m}{T_r}\underline{i}_s + (-\frac{1}{T_r} + j\omega_r)\underline{\hat{\psi}}_r^i) \tag{6.16}$$

The adaptation mechanism is a PI controller driven by the error $\varepsilon = \Im m(\underline{\hat{e}}_m^u \underline{\hat{e}}_m^{i*})$ that is proportional to the angular difference between the estimated EMF vectors.

$$\hat{\omega}_r = (K_P + \frac{K_I}{s})(\hat{e}_{m\alpha}^i\hat{e}_{m\beta}^u - \hat{e}_{m\alpha}^u\hat{e}_{m\beta}^i) \tag{6.17}$$

In this way, the pure integrator and the LPF have been avoided, but the current derivative has appeared instead. In order to avoid the noise amplification related to current differentiation, the reference current $\underline{i}_s^*$, if available, can replace the measured current $\underline{i}_s$ in the differential term $d\underline{i}_s/dt$ when (6.15) is implemented, [7].

An alternative, very similar scheme is obtained if the instantaneous reactive power $q_m = \Im m(\underline{e}_m\underline{i}_s^*)$ is employed, where $\underline{e}_m$ is estimated either by (6.15), or (6.16).

The reference model calculates the reactive power using $\underline{\hat{e}}_m^u$ from (6.15)

$$\hat{q}_m^u = i_{s\alpha}\hat{e}_{m\beta}^u - i_{s\alpha}\hat{e}_{m\alpha}^u \tag{6.18}$$

The adaptive model calculates the reactive power using $\hat{\underline{e}}_m^i$ from (6.16)

$$\hat{q}_m^i = i_{s\alpha}\hat{e}_{m\beta}^i - i_{s\alpha}\hat{e}_{m\alpha}^i \tag{6.19}$$

The adaptation mechanism is a PI controller driven by the q_m error

$$\hat{\omega}_r = (K_P + \frac{K_I}{s})(\hat{q}_m^u - \hat{q}_m^i) \tag{6.20}$$

This MRAS estimator is robust with respect to stator resistance variations, but the sensitivity to rotor time constant persists. Sensorless operation at 20 rpm, with a system that employs both, EMF and power based estimator, has been reported in [7].

In general, due to noise considerations the PI gains are limited. Therefore, MRAS based systems exhibit rather poor dynamic performance.

6.2.3 Speed Adaptive State Observers

The most important limitation associated to MRAS speed estimators is the poor performance of the reference model that is not accurate and fast enough. In all cases, it is a simple, open loop estimator, sensitive to noise and parameter detuning. A superior approach is to consider as reference model the motor itself and to employ as adaptive model a full-order, speed adaptive state observer.

The most general, speed adaptive, observer based scheme is depicted in Figure 4.6. The adaptation mechanism is driven by the error between the measured and estimated currents. Since state observers have been discussed in previous chapters, only the speed estimation mechanism is presented now.

Speed adaptive Luenberger observers

The adaptive asymptotical observer is shown in Figure 4.4 and is described by (4.35) if rotor flux model is used, or by (4.36)-(4.37) if flux model is used. The model and the compensation gain receive the estimated speed as an adaptive parameter.

The speed estimator is a PI controller driven by the error $\varepsilon = \Im m(\underline{e}_{is}\hat{\underline{\psi}}_r^*)$ that represents the torque error and was derived using Lyapunov stability theory [8]-[10].

$$\hat{\omega}_r = (K_P + \frac{K_I}{s})(\hat{\psi}_{r\alpha} e_{is\beta} - \hat{\psi}_{r\beta} e_{is\alpha}) \tag{6.21}$$

where $\underline{e}_{is} = \underline{i}_s - \underline{\hat{i}}_s$ and K_P and K_I are positive gains.

A variant of this employs the stator flux based torque error $\varepsilon = \Im m(\underline{e}_{is} \underline{\hat{\psi}}_s^*)$ [11]

$$\hat{\omega}_r = (K_P + \frac{K_I}{s})(\hat{\psi}_{s\alpha} e_{is\beta} - \hat{\psi}_{s\beta} e_{is\alpha}) \tag{6.22}$$

The estimation accuracy is higher than that of MRAS (6.11), but the PI gains still have to be limited due to noise considerations. An improvement proposed in [11] is to employ a mechanical model, driven by the nonlinear error ε.

Low speed sensorless operation at 10 rpm, with good dynamic behavior has been reported in [11], with a scheme that uses stator resistance adaptation.

Speed adaptive sliding mode observers

The effective gains of error compensator can be increased by using a sliding mode controller to tune the state observer and to estimate the speed. The state observer is an adaptive SMO and the speed estimator is derived from the nonlinear error, using the equivalent control approach [12]-[14].

The approach in [12] uses (5.12) as adaptive state observer an integrates the error $\varepsilon = \Im m(\mathrm{sgn}(\underline{e}_{is}) \underline{\hat{\psi}}_r^*)$, in order to obtain a sliding mode speed estimator

$$\hat{\omega}_r = \frac{1}{s}(K_1 \hat{\psi}_{r\alpha}\, \mathrm{sgn}(e_{is\beta}) - K_2 \hat{\psi}_{r\beta}\, \mathrm{sgn}(e_{is\alpha})) \tag{6.23}$$

where K_1 and K_2 are positive constants.

The integrator (6.23) plays the role of a LPF for the noisy switching terms. A PI controller may also be used with the price of increasing the noise.

Another simple approach [14] is to employ the same error as in the case of asymptotical state observer and to estimate the speed in the form (6.24)

$$\hat{\omega}_r = n_0\, \mathrm{sgn}(\hat{\psi}_{r\alpha} e_{is\beta} - \hat{\psi}_{r\beta} e_{is\alpha}) \tag{6.24}$$

In fact, the average value of (6.24) is the estimated speed and this is determined by low-pass filtering the very noisy estimate given by (6.24). In this case, the adaptive observer is the SMO (5.22).

An approach similar to (6.23) is proposed in [13], with the difference that the switching component sgn($\underline{e}_{is}$) is low-pass filtered before the estimation algorithm. Very good dynamic behavior and low speed sensorless operation at 50 rpm is reported in both [12] and [13].

Speed estimators based on adaptive observers are superior to MRAS estimators. mainly because the machine is employed as reference model. However, their dynamic performance is still somewhat limited due to noise considerations.

6.2.4 Extended Kalman Filters

The Kalman Filter is a variable gain asymptotical observer in which the gain is on-line adapted to give optimal mean square estimation error when the system perturbation is modeled as a white noise process. The Extended Kalman Filter (EKF) is the extension of Kalman Filter to nonlinear systems. Both are stochastic observers and require information about the measurement noise statistics.

The EKF appeared to be the ultimate solution for sensorless drives. It has the advantage that is able to handle nonlinear systems and copes well with the fifth order complete model (2.15)-(2.20) of the induction machine. Thus, EKF is able to estimate all electromagnetic quantities and the speed in the same time [15].

However, it has several limitations. It suffers from lack of inherent robustness against modeling errors and disturbances. Perfect knowledge of the system model and noise characteristics are assumed. There is no a priori performance and stability guarantied. Since in ASD-s disturbances are far from white noise, it does not guarantee adequate bandwidth for disturbance rejection. The EKF implementation involves significant computation complexity and requires powerful processors. Recent studies have demonstrated the superiority of other observers, like SMO, over EKF, [16].

Since the EKF theory is extensively presented in literature, it is not discussed here anymore. Examples of its application in induction motors sensorless drives are [15], [16] and many others. The best low speed sensorless performance is 20 rpm [15].

6.3 Speed Observers – Proposed Solutions

6.3.1 Phase-Locked Loop Speed Observers

Theoretical background

Phase-Locked Loop (PLL) is a very powerful concept employed for phase angle and frequency detection in various power applications such as line converters, active filters, high-precision servomechanisms, etc. In motion control, PLL systems have been exclusively used for rotor speed and position detection from resolver or encoder signals, as a part of high precision positioning systems [17]-[20].

A PLL system contains three components: a phase detector, a loop filter and a voltage controlled oscillator (VCO). Figure 6.2 shows a two-phase type PLL system employed for speed and position angle detection [17].

The phase detector plays the role of a comparator. It receives as reference two harmonic signals, $x^* = \cos(\alpha)$ and $y^* = \sin(\alpha)$, and as feedback other two estimated signals $\hat{x} = \cos(\hat{\alpha})$ and $\hat{y} = \sin(\hat{\alpha})$. It produces the estimation error

$$\varepsilon = \sin(\alpha)\cos(\hat{\alpha}) - \cos(\alpha)\sin(\hat{\alpha}) = \sin(\alpha - \hat{\alpha}) \tag{6.25}$$

The loop filter is of PI type and produces the estimated pulsation (speed) at the output of its integral component. The VCO is an integrator that generates the estimated position angle, followed by a harmonic generator that constructs $\hat{x}$ and $\hat{y}$.

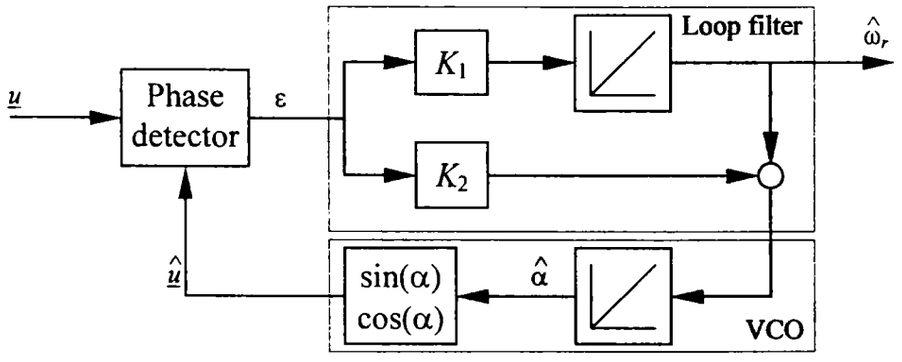

Figure 6.2 Two phase PLL system for speed estimation

The loop filter structure and the VCO have been selected such that the PLL speed estimator mathematical model is described by the following nonlinear observer

$$\frac{d}{dt}\begin{bmatrix}\hat{\alpha}\\ \hat{\omega}_r\end{bmatrix}=\begin{bmatrix}0 & 1\\ 0 & 0\end{bmatrix}\begin{bmatrix}\hat{\alpha}\\ \hat{\omega}_r\end{bmatrix}+\begin{bmatrix}K_1\\ K_2\end{bmatrix}\varepsilon \tag{6.26}$$

where $\boldsymbol{K}=[K_1\ K_2]^T$ is the observer gain.

This model is, precisely, a nonlinear observer for constant frequency systems. The scheme is proposed in [18] for speed detection from resolver signals and for speed estimation in sensorless synchronous machine drives.

The reference signals may be formally regarded as a reference vector $\underline{z}^*=x^*+jy^*$, and the estimated signals into as an estimated vector $\hat{\underline{z}}=\hat{x}+j\hat{y}$. It is evident that the MRAS estimator is based on this scheme, where the reference model provides reference $\underline{z}^*$ and the adaptive model is the VCO, [4]. Similarly for adaptive observers, where the reference is $\underline{z}^*=\underline{i}_s$ and the observer, produces $\hat{\underline{z}}=\hat{\underline{i}}_s$.

Since the constant speed assumption is not always correct, the estimator can be enhanced with the acceleration equation (γ is the acceleration), in the form

$$\frac{d}{dt}\begin{bmatrix}\hat{\alpha}\\ \hat{\omega}_r\\ \hat{\gamma}\end{bmatrix}=\begin{bmatrix}0 & 1 & 0\\ 0 & 0 & 1\\ 0 & 0 & 0\end{bmatrix}\begin{bmatrix}\hat{\alpha}\\ \hat{\omega}_r\\ \hat{\gamma}\end{bmatrix}+\begin{bmatrix}K_1\\ K_2\\ K_3\end{bmatrix}\varepsilon \tag{6.27}$$

This PLL model, derived from EKF theory in [19], is proposed for speed detection from noisy resolver signals.

The only known application for induction machine sensorless drives is an enhancement of (6.22) with (6.27), described in [11]. In this case, instead of the PI based estimator (6.22), which corresponds to (6.26), the model (6.27) is used.

Observer synthesis

Obviously, the above models are not suitable for induction machine sensorless drives, since the rotor position α, which enters in (6.25) is unknown. It is also clear that the rather poor dynamic performance of the MRAS estimators and of the speed adaptive schemes is due to the constant speed assumption that is implicitly assumed in the model (6.26). From this point of view, (6.27) is a superior solution.

Based on (2.20) and (6.1), the mechanical model of the drive is approximated as

$$\frac{d}{dt}\begin{bmatrix}\alpha\\ \omega_r\\ T_L\end{bmatrix}=\begin{bmatrix}0 & 1 & 0\\ 0 & 0 & -p/J\\ 0 & 0 & 0\end{bmatrix}\begin{bmatrix}\alpha\\ \omega_r\\ T_L\end{bmatrix}+\begin{bmatrix}1 & 0\\ 0 & p/J\\ 0 & 0\end{bmatrix}\begin{bmatrix}\omega_s\\ T_e\end{bmatrix} \tag{6.28}$$

where α is the revolving field position and the load torque T_L was assumed constant. The slip speed ω_s and the electromagnetic torque T_e are regarded as known inputs.

An observer for this model can be constructed as in (4.2)

$$\frac{d}{dt}\begin{bmatrix}\alpha\\ \omega_r\\ T_L\end{bmatrix}=\begin{bmatrix}0 & 1 & 0\\ 0 & 0 & -p/J\\ 0 & 0 & 0\end{bmatrix}\begin{bmatrix}\alpha\\ \omega_r\\ T_L\end{bmatrix}+\begin{bmatrix}1 & 0\\ 0 & p/J\\ 0 & 0\end{bmatrix}\begin{bmatrix}\omega_s\\ T_e\end{bmatrix}+\begin{bmatrix}K_1\\ K_2\\ K_3\end{bmatrix}\varepsilon \tag{6.29}$$

where the slip speed is given by (6.6) and the torque by (6.7).

The PLL observer error is obtained from (6.25) where the reference $\underline{z}^*$ is the rotor flux estimated by the flux observer (any of them) and α is its position.

$$\varepsilon=\sin(\hat{\theta}_{\psi r})\cos(\hat{\alpha})-\cos(\hat{\theta}_{\psi r})\sin(\hat{\alpha})=\sin(\hat{\theta}_{\psi r}-\hat{\alpha}) \tag{6.30}$$

The PLL speed observer block diagram is shown in Figure 6.3. This observer estimates the rotor speed and the load torque. However, the load torque estimate is poor. The estimated speed is extracted from the input of the last integrator, not by mistake. The speed estimation dynamic response is improved in this way.

Alternatively, an asymptotical Luenberger observer is obtained by taking simply

$$\varepsilon=\hat{\theta}_{\psi r}-\hat{\alpha} \tag{6.31}$$

The observer block diagram is shown in Figure 6.4. The two observers are equivalent, since, in phase-locked operation, (6.37) approximates (6.38).

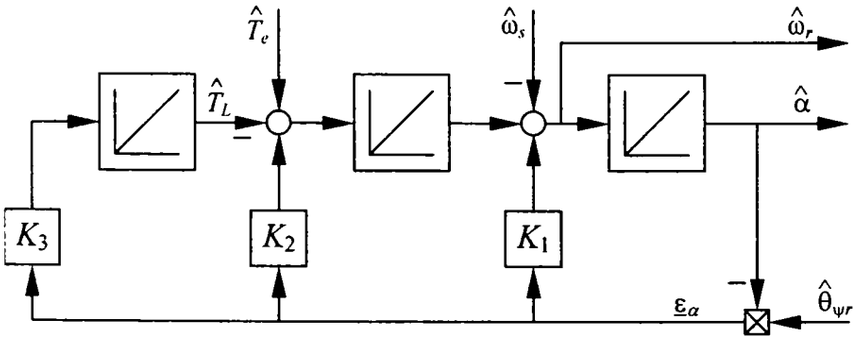

Figure 6.3 Phase-Locked Loop speed observer

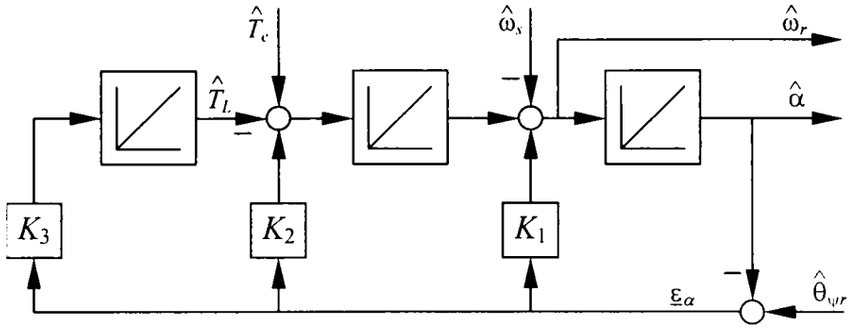

Figure 6.4 Asymptotical Luenberger speed observer

According to (4.3), the asymptotical observer error dynamics is

$$de/dt = (A - KC)e \tag{6.32}$$

where $e=[\varepsilon\ 0\ 0]^T$, $\boldsymbol{K}=[K_1\ K_2\ K_3]^T$, $\boldsymbol{C}=[1\ 0\ 0]^T$ and $\boldsymbol{A}$ is the system's matrix, from (6.28).

The observer gain is determined by pole placement method. Let p_1, p_2, p_3 be the observer poles (eigenvalues of $\boldsymbol{E}=\boldsymbol{A}-\boldsymbol{KC}$), allocated such that the observer is fast and stable. In this case, the observer gains are

$$K_1 = -S \qquad K_2 = SP_2 \qquad K_3 = JP \tag{6.33}$$

where $S = p_1 + p_2 + p_3$, $SP_2 = p_1p_2 + p_2p_3 + p_3p_1$, $P = p_1p_2p_3$.

Gain values are limited only by noise considerations. If the noise level is small it is possible to select all three poles real, negative. However, for better dynamics, two of them can be selected complex conjugates with not too large imaginary components.

Parameter sensitivity analysis

Simulations have been performed in order to determine the speed observer's dynamic and static performance. Figure 6.5 shows simulation results (startup, loading, deceleration, unloading, and acceleration) under perfect tuning of flux and speed observers. The speed and torque estimation errors are very small in all situations. The system employs Linear-DTC, SMO, PLL observer and Machine 1 (Appendix B).

It can be seen from (6.29) that the observer depends on estimated slip, estimated torque and motor's inertia. Since the slip speed is a function of torque, rotor resistance and flux, and the torque depends on current and flux, it follows that the observer is sensitive to flux errors, rotor resistance and inertia.

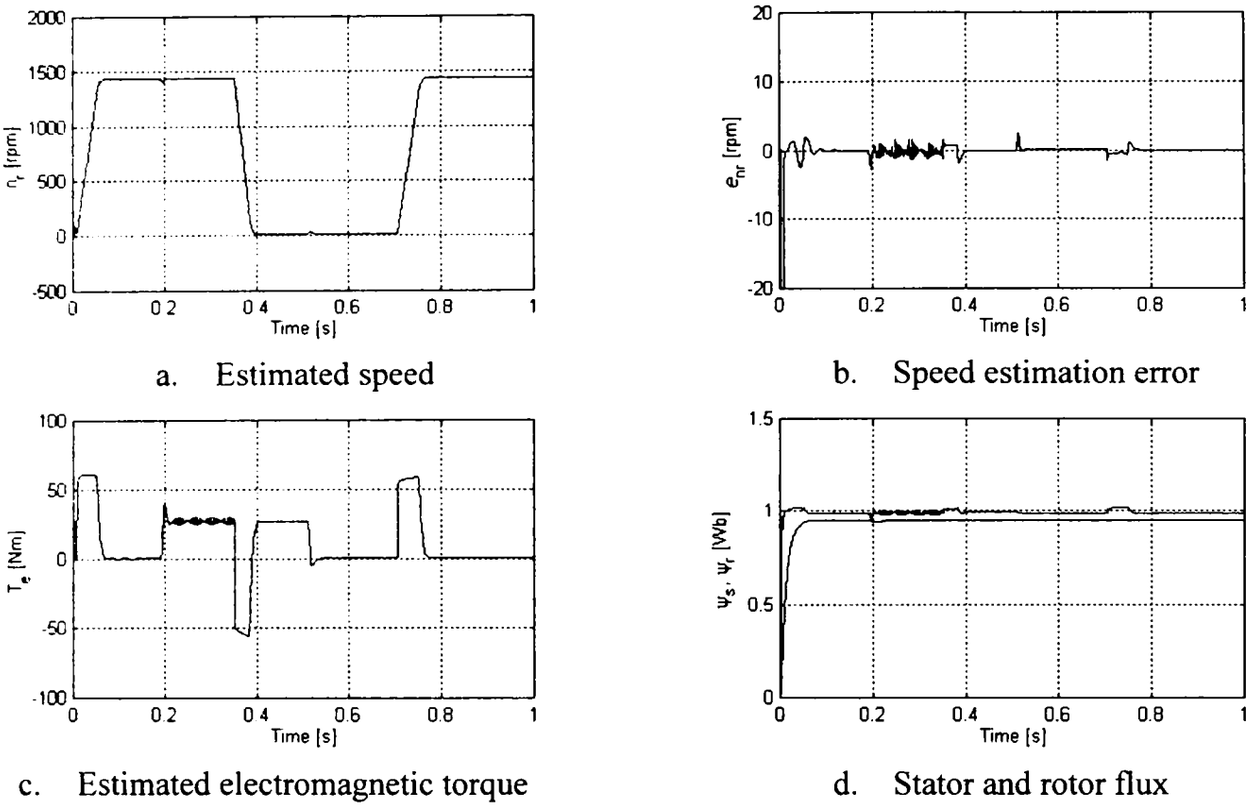

a. Estimated speed

b. Speed estimation error

c. Estimated electromagnetic torque

d. Stator and rotor flux

Figure 6.5 Sensorless operation of Linear-DTC with PLL speed observer - simulations

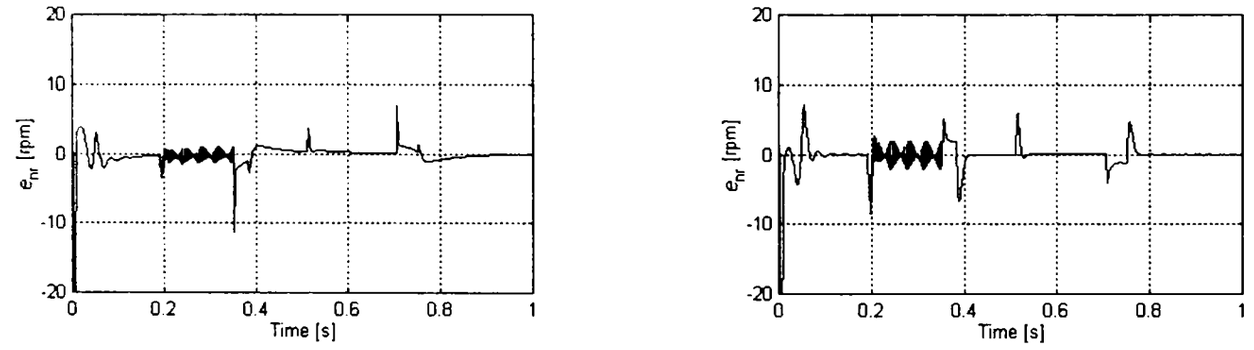

Figure 6.6 Speed estimation errors with J_{obs}=10J (left) and J_{obs}=0.1J (right) - simulations

In ASD-s, the equivalent inertia changes in a wide range. Fortunately, the speed observer is very robust, with respect to inertia mismatch. Figure 6.6 shows estimation errors with observer inertia, J_{obs} ten times larger and ten times smaller than motor's inertia. Only small errors appear and the drive's behavior is not affected.

Figure 6.7 shows speed estimation errors with ±50% rotor resistance detuning, in the same conditions as for Figure 4.15. At this time, there are large errors that have strong influence at low speed and an adaptation mechanism is mandatory.

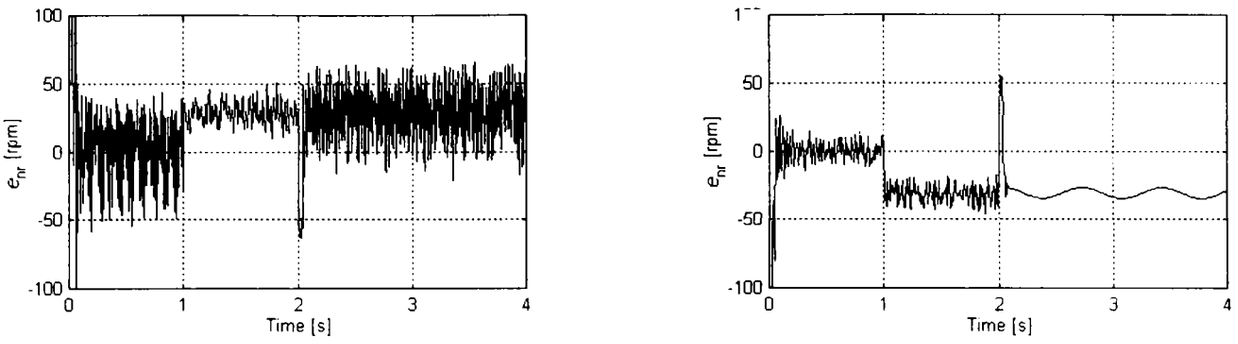

Figure 6.7 Speed estimation errors with +50% (left) and –50% (right) R_r detuning

It is known that simultaneous identification of rotor resistance and rotor speed, by means of adaptive observers is possible only when the rotor flux is not constant [6]. It is not the case of vector control, where the flux is kept constant most of the time.

However, it is possible to estimate R_r indirectly and a very simple method derived from thermal considerations has been used here. Neglecting the of skin effects, the stator and rotor resistances vary linearly with temperature

$$R_s = R_{s0}(1+\alpha_{Cu}(T_1 - T_0)) \tag{6.34}$$

$$R_r = R_{r0}(1+\alpha_{Al}(T_2 - T_0)) \tag{6.35}$$

where R_{s0} and R_{r0} are nameplate (cold) resistances, at temperature T_0=25°C, T_1 and T_2 are actual (average) temperatures of stator and rotor, and α_{Cu} and α_{Al} are the resistance temperature coefficients of copper and aluminum, respectively.

Since the stator resistance is estimated, the rotor resistance may be estimated as

$$\hat{R}_r = \hat{R}_s \frac{R_{r0}(1+\alpha_{Al}(T_2 - T_0))}{R_{s0}(1+\alpha_{Cu}(T_1 - T_0))} \tag{6.36}$$

However, since T_1 and T_2 are unknown, R_r is estimated in proportion to R_s

$$\hat{R}_r = \hat{R}_s \frac{R_{r0}}{R_{s0}} k_{sr} = \hat{R}_s k_{sr0} k_{sr} \tag{6.37}$$

where k_{sr} is an empirical coefficient that takes into account that $T_1 < T_2$.

Very low speed operation without stator and rotor resistance adaptation is possible, but inaccurate. In all experiments that employ the PLL observer, the stator resistance estimation was (4.61), with K_{Rs}=10 and the rotor resistance estimation was (6.37), with k_{sr}=1.12. Resistances R_{s0} and R_{r0} were a priori measured.

Experimental results

Experimental results with the PLL speed observer, LFSG Control and SMO are also presented in chapter 5, while experiments with Linear-VSC, improved voltage model flux estimator and PLL speed estimation are given in chapter 4.

Regenerating and motoring sensorless operation at ±6 rpm, with a system that employs the RCG control strategy, modified SMO, PLL speed observer and Machine 2 is shown in Figure 6.8. The speed estimation is relatively accurate, although, at such low speeds it is affected by some oscillations. Estimated speed, current and stator flux transients during a similar speed reversal are shown in Figure 6.9.

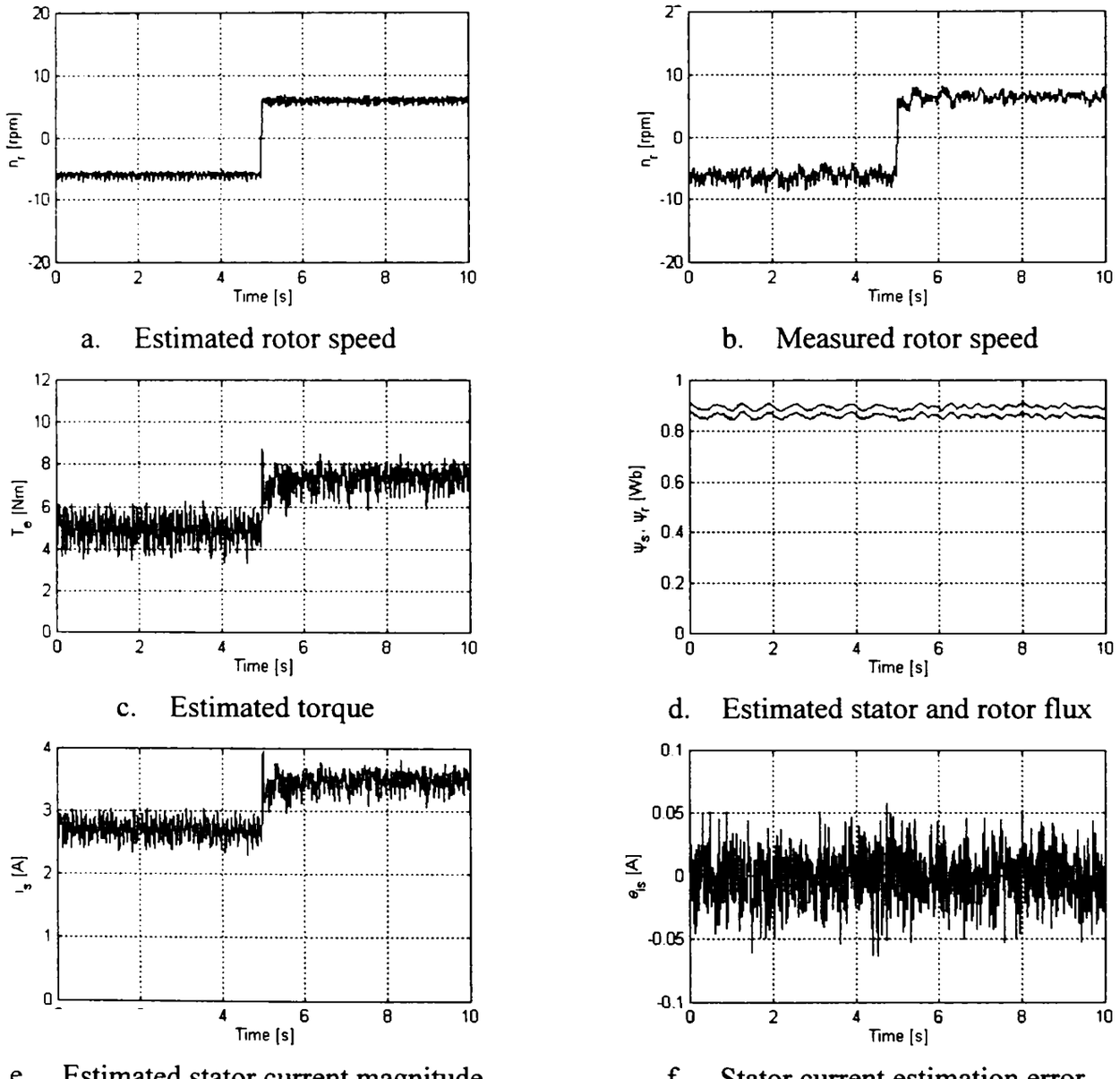

a. Estimated rotor speed

b. Measured rotor speed

c. Estimated torque

d. Estimated stator and rotor flux

e. Estimated stator current magnitude

f. Stator current estimation error

Figure 6.8 Low speed reversal, with RCG Control, modified SMO and PLL observer

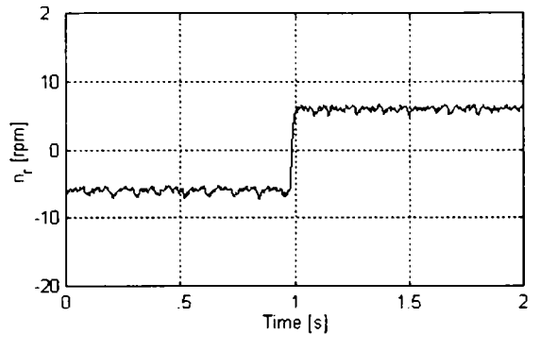

a. Estimated rotor speed

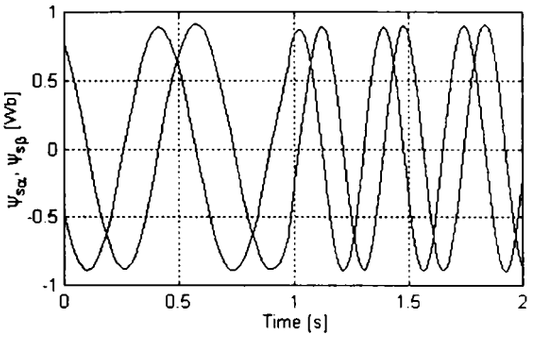

b. Estimated (α,β) stator flux

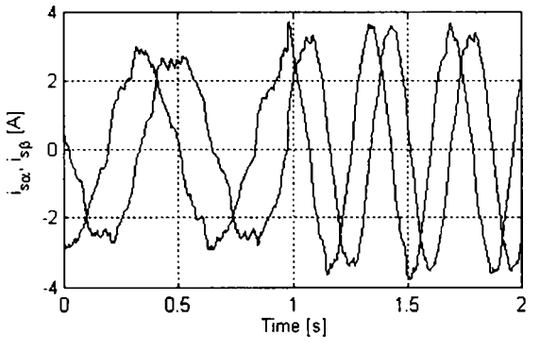

c. Estimated (α,β) stator current

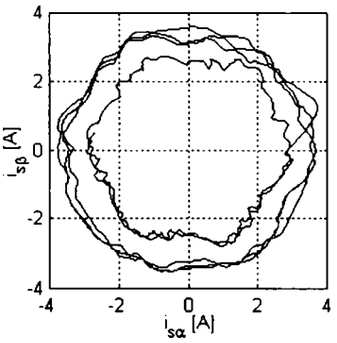

d. Estimated current trajectory

Figure 6.9 Low speed reversal, with RCG Control, modified SMO and PLL observer

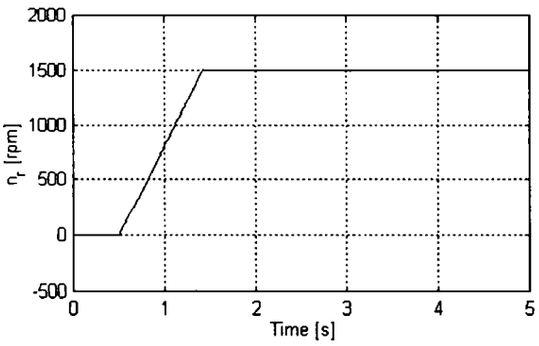

a. Estimated rotor speed

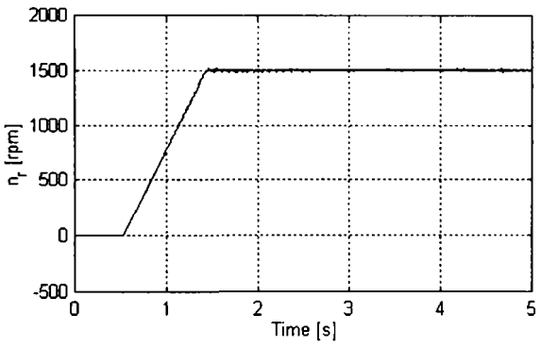

b. Measured rotor speed

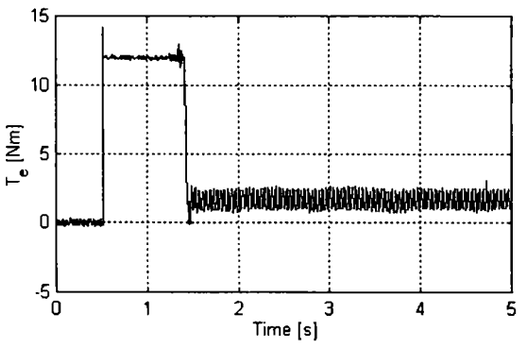

c. Estimated torque

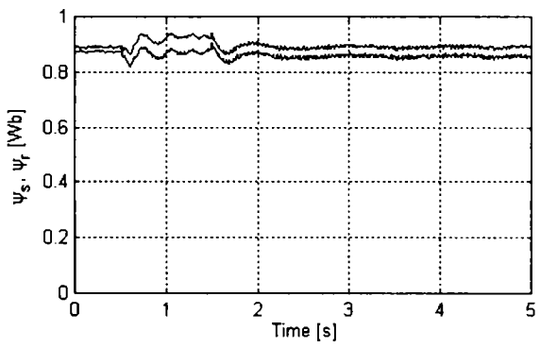

d. Estimated stator and rotor flux

Figure 6.10 Acceleration from standstill to 1500 rpm, with RCG Control, generalized observer and PLL speed observer

Acceleration transients, from standstill to 1500 rpm, with a system that employs the RCG Control, generalized flux observer, PLL speed observer and Machine 2 (Appendix B), are shown in Figure 6.10. The quality of speed estimation during transients is very good, in spite of some oscillations that are present in the estimated flux. These oscillations are due to very high gains employed in RCG Control.

Although only experiments with the PLL observer are shown, the Luenberger observer has identical behavior. This was confirmed by simulations and experiments.

Conclusions

Speed observers, based on the mechanical model of the drive and on the PLL theory, are described. So far, PLL based observers have been widely used for speed estimation from resolver and encoder signals, in high performance servo-drives, but no solutions for induction machine sensorless drives are known, excepting [11].

Two new speed observers for induction machine sensorless drives, based on the PLL concept have been developed and analyzed. Both employ the drive's mechanical model that was manipulated such that to allow the speed estimation from the estimated rotor flux and torque only. The first topology uses a nonlinear correction term, similar to a PLL system, while the second observer uses a linear correction term and has the structure of a linear Luenberger observer.

Although the proposed solution resembles the one in [11], since both are based on the same mechanical model, a major difference exists: the solution in [11] is based on an adaptive state observer, while the present solution is designed so that to be employed together with the inherent sensorless state observer.

Simulation and experimental results with the PLL observer are presented. Full load sensorless operation at zero and very low speed in motoring and regenerating regimes is demonstrated. High speed transients and steady state operation is also shown. Overall, the drive with PLL observer exhibits excellent dynamic performance and accurate low speed behavior.

6.3.2 Modified MRAS Speed Estimators

Model Reference Adaptive speed estimators have been very popular in the past years. They exhibit fairy good performance and have simple structure that makes them very attractive for low cost digital implementations. However, they exhibit moderate dynamic performance and suffer from parameter and noise sensitivity.

Recalling the basic MRAS estimator (6.9)-(6.11), one of its most important limitations is represented by the precision of the reference model that is open loop operated. Its accuracy has important influence on the overall estimation performance. So far, the reference model has been based on the voltage model (6.9) that is unable to operate correctly due to drift problem. Its practical realization, based on LPF, (6.12), is inaccurate at low speeds, while the EMF based solution (6.15) is noise sensitive.

A simple solution to this problem is to implement the reference model as a state observer that realizes accurate flux estimation in a wide speed range. Nevertheless that the state observer is not allowed to be explicitly speed adaptive, that is, it must be an inherent sensorless observer. Such an observer contains an internal correction loop and provides an accurate estimate, as reference for MRAS.

The block diagram of the proposed MRAS topology for speed estimation is illustrated in Figure 6.11. This scheme was developed in the same time with the modified Jansen-Lorenz observer and, therefore, the reference model is the inherent sensorless Jansen-Lorenz observer shown in Figure 4.20.

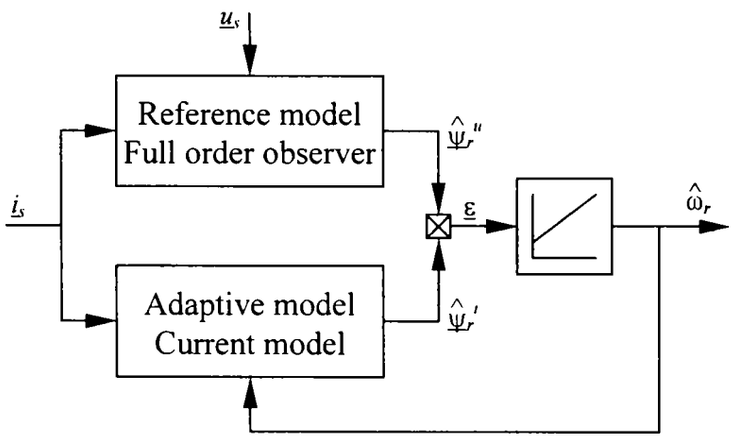

Figure 6.11 Modified MRAS speed estimator

The adaptive model remains the same current model in stator frame, (6.10), and the adaptation mechanism is the PI controller (6.11). In this topology, the current model appears twice, but these two occurrences do not overlap. The reference model operates the current model in rotor flux frame using only the estimated rotor flux position for coordinate transformations, while the speed adaptive current model is implemented in stator frame and employs the estimated speed.

The system's complexity has apparently increased. In fact, a flux observer is present in most sensorless systems and its output can be directly employed as reference for the MRAS estimator. An attractive alternative, due to its simplicity, is to use, as reference model, the modified voltage model shown in Figure 4.25.

Experimental results

Several experiments with the modified MRAS speed estimator are presented in chapter 4. The lowest speed obtained in sensorless operation was 15 rpm, shown in Figure 6.12. This represents the best theoretical performance, since the real speed is oscillating with amplitude of 5 rpm and the acoustical noise is increased.

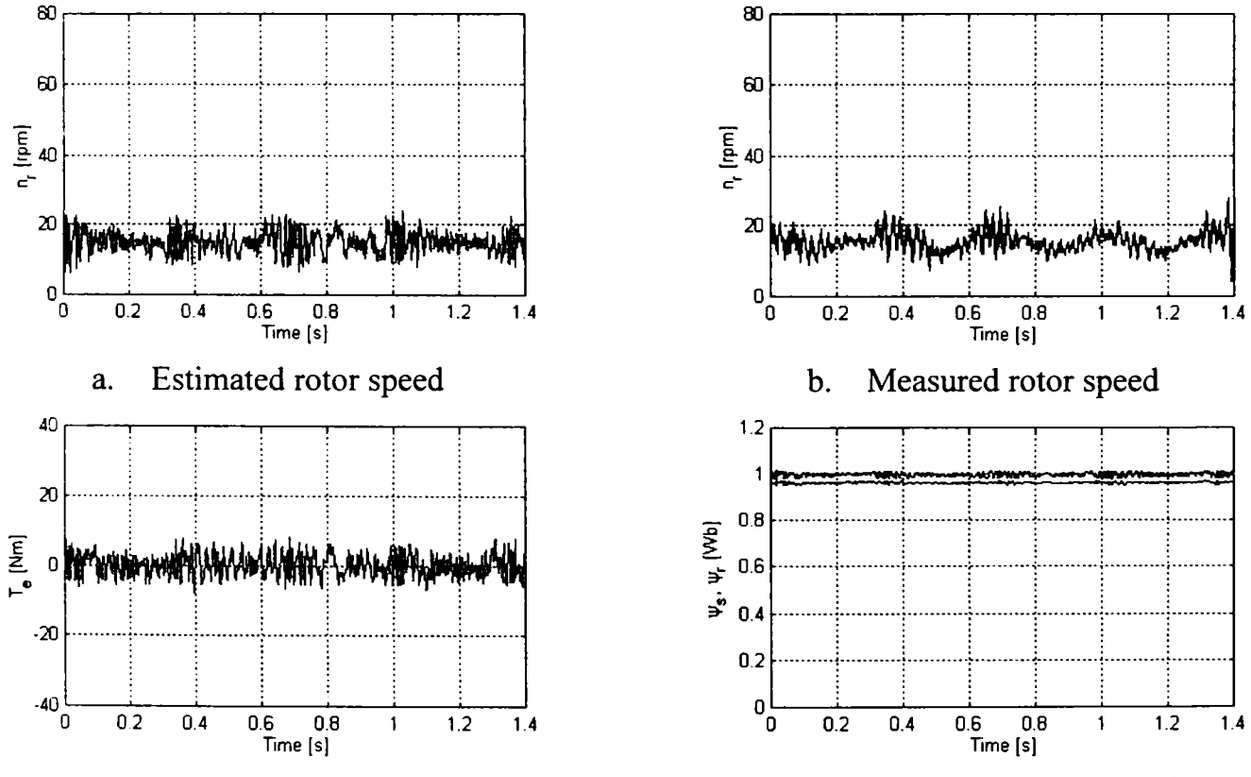

a. Estimated rotor speed

b. Measured rotor speed

c. Estimated torque

d. Estimated stator and rotor flux

Figure 6.12 Low speed sensorless operation with DTC and modified MRAS estimator

The best practical low speed performance is 30 rpm, presented in Figure 4.23 in the same conditions. In both cases, the control system is classical DTC, with modified Jansen-Lorenz flux observer, modified MRAS speed estimator and the motor under test is Machine 1 (Appendix B). In both cases the operation is stable.

Sensorless speed reversal from –750 rpm to 750 rpm (±25 Hz) in no load operation is shown in Figure 6.13. The control system is Linear-DTC, with the same estimation system and motor as before. The system's response is good and fast. During fast transients, however, the speed exhibits some oscillations. Since the estimated flux is quite good (subfigures c, d), these oscillations reflect the quality of the torque control and the speed estimation dynamic performance.

This modest dynamic performance of the speed estimator was expected, since the adaptation mechanism and the adaptive model are equivalent to PLL estimator model (6.26) that assumes constant rotor speed. More experimental results with the Linear-DTC and modifier MRAS estimator, including sensorless operation at 30 rpm, have been presented in Figure 4.24 and in [21].

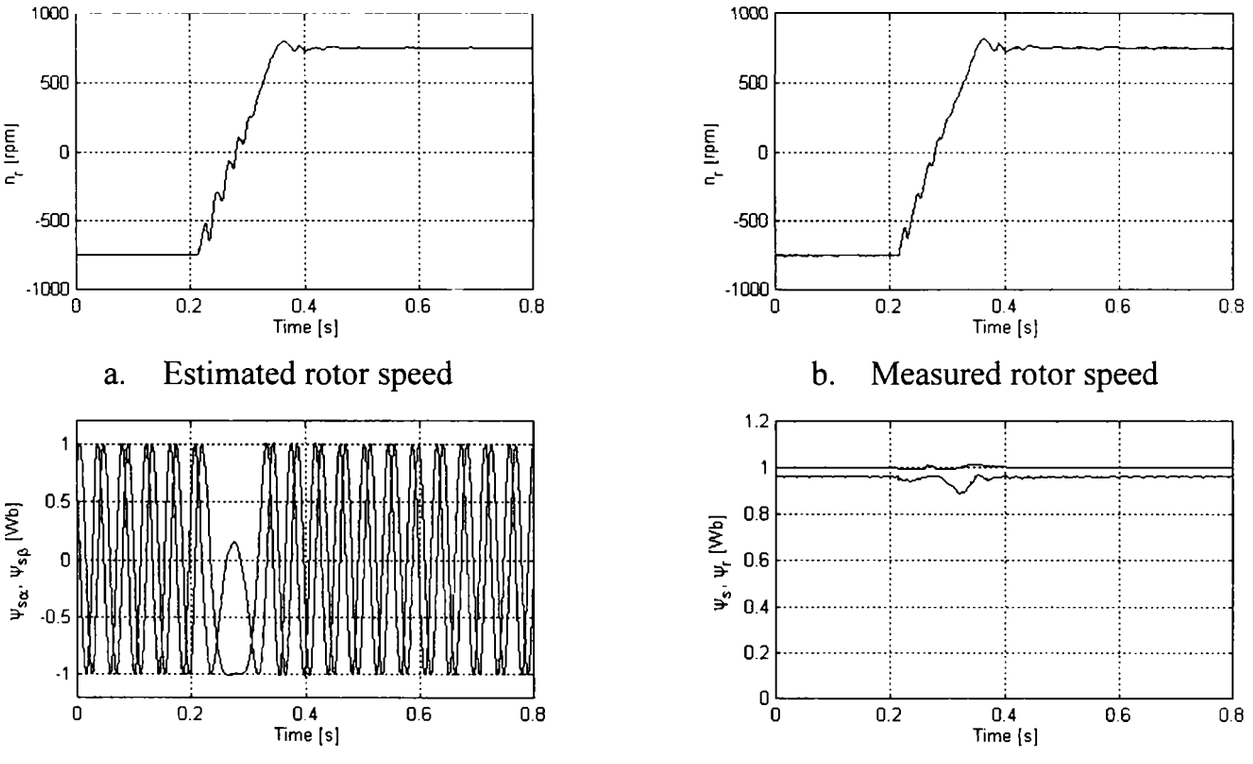

a. Estimated rotor speed

b. Measured rotor speed

c. Estimated stator flux (α,β) components

d. Estimated stator and rotor flux

Figure 6.13 Sensorless speed reversal with Linear-DTC and modified MRAS estimator

6.4 Conclusions

The most important speed estimation methods for sensorless induction machine drives are described in this chapter. Existing solutions, including open loop estimators, MRAS estimators and observer based speed estimators are discussed.

Two new speed observers for induction machine sensorless drives, based on mechanical model have been developed and analyzed. The first one uses a nonlinear correction error similar to a PLL estimator, while the second one is a Luenberger speed observer. Simulations have demonstrated that both topologies are extremely robust with respect to the moment of inertia detuning, but are sensitive to rotor resistance detuning. A simple and practical method for rotor resistance adaptation is also described and implemented.

Experiments with proposed observers have demonstrated very good low speed performance. Full load, sensorless operation, at zero speed and 3 rpm, with a variety of control strategies and state observers is presented. Low and high speed transients, also shown here, prove the excellent dynamic behavior of the two proposed schemes. It was determined that these observers are superior to MRAS estimators in both, low speed and dynamic performance.

A novel, improved MRAS estimator is described in the last section. This is only an enhancement, with a full order observer, of a standard MRAS scheme. This topology allows running the drive at relatively low speeds in sensorless operation. Different experiments demonstrated that this topology exhibits moderate dynamic performance and is inferior to PLL type observers.

References

[1] J. Holtz, *Methods for Speed Sensorless Control of AC Drives.*, in K. Rajashekara (Editor) "Sensorless Control of AC Motors", IEEE Press, 1996.

[2] J. Holtz, *Sensorless Position Control of Induction Motors – An Emerging Technology.* IEEE Transactions on Industrial Electronics, vol. 45, no. 6, Dec. 1998, pp. 840-852.

[3] J. Holtz, J. Quan, *Sensorless Vector Control of Induction Motors at Very Low Speed Using a Nonlinear Inverter Model and Parameter Identification.*, The 36th IEEE Industry Applications Society Annual Meeting, 2001, CD-ROM paper 62.3.

[4] C. Schauder, *Adaptive Speed Identification for Vector Control of Induction Motors without Rotational Transducers.*, IEEE Transactions on Industry Applications, vol. 28, no. 5, Sept./Oct. 1992, pp. 1054-1061.

[5] H. Tajima,Y. Hori, *Speed Sensorless Field-Oriented Control of the Induction Machine.*, IEEE Transactions on Industry Applications, vol. 29, no.1, Jan./Feb. 1993, pp. 175-180.

[6] K. Ohnishi, N. Matsui, Y. Hori, *Estimation, Identification and Sensorless Control in Motion Control Systems.*, Proc. of IEEE, vol. 82, no. 8, August 1994, pp. 1253-1265.

[7] F.Z. Peng, T. Fukao, J.-S. Lai, *Low-Speed Performance of Robust Speed Identification Using Instantaneous Reactive Power for Tacholess Vector Control of Induction Motors.*, The IEEE Industry Applications Society Annual Meeting 1994, pp. 509-514.

[8] H. Kubota, K. Matsuse, T. Nakano, *DSP Based Speed Adaptive Flux Observer for Induction Motor Applications.*, IEEE Transactions on Industry Applications, vol. 29, no. 2, Mar./Apr. 1993, pp. 344-348.

[9] H. Kubota, K. Matsuse, *Speed Sensorless Field-Oriented Control of Induction Motor with Rotor Resistance Adaptation.*, IEEE Transactions on Industry Applications, vol. 30, no. 5, Sept./Oct. 1994, pp. 1219-1224.

[10]H. Kubota, I. Sato, Y. Tamura, K. Matsuse, H. Ohta, Y. Hori, *Regenerating-Mode Low-Speed Operation of Sensorless Induction Motor Drive with Adaptive Observer.*, IEEE Transactions on Industry Applications, vol. 38, no. 4, July/August 2002, pp. 1081-1086.

[11]J. Maes, J. Melkebeek, *Speed Sensorless Direct Torque Control of Induction Motors using an Adaptive Flux Observer.*, IEEE Transactions on Industry Applications, vol. 36, no. 3, May/June 2000, pp. 778-785.

[12]M. Tursini, R. Petrella, F. Parasiliti, *Adaptive Sliding Mode Observer for Speed Sensorless Control of Induction Motors.*, IEEE Transactions on Industry Applications, vol. 36, no. 5, Sept./Oct. 2000, pp 1380-1387.

[13]S. Doki, S. Sangwongwanich, S. Okuma, *Implementation of Speed-Sensor-Less Field-Oriented Vector Control using Adaptive Sliding Observer.*, IEEE IECON'92, The 1992 International Conference on Industrial Electronics, 1992, vol. 1, pp. 453-458.

[14]Z. Yan, C. Jin, V.I. Utkin, *Sensorless Sliding-Mode Control of Induction Motors.*, IEEE Transactions on Industrial Electronics, vol. 47, no. 6, Dec. 2000, pp. 1286-1297.

[15]Y.-R. Kim, S.-K. Sul, M.-H. Park, *Speed Sensorless Vector Control of Induction Motor Using Extended Kalman Filter.*, IEEE Transactions on Industry Applications, vol. 30, no. 5, Sept./Oct. 1994, pp. 1225-1233.

[16]F. Chen, M.W. Dunnigan, *Comparative Study of a Sliding-Mode Observer and Kalman Filters for Full State Estimation in an Induction Machine.*, IEE Proceedings on Electric Power Applications, vol. 149, no. 1, January 2002, pp. 53-64.

[17]T. Emura, L. Wang, M. Yamanaka, H. Nakamura, *A High-Precision Positioning Servo Controller Based on Phase/Frequency Detecting Technique of Two-Phase-Type PLL.*, IEEE Transactions on Industrial Electronics, vol. 47, no. 6, Dec. 2000, pp. 1298-1306.

[18]L. Harnefors, H.-P. Nee, *A General Algorithm for Speed and Position Estimation of AC Motors.*, IEEE Transactions on Industrial Electronics, vol. 47, no. 1, Feb. 2000, pp. 77-83.

[19]L. Harnefors, *Speed Estimation from Noisy Resolver Signals.*, IEE Power Electronics and Variable Speed Drives, Conference Publication No. 429, 1996, pp. 279-282.

[20]R.D. Lorenz, K.W. Van Patten, *High-Resolution Estimation for All-Digital, ac Servo Drives.*, IEEE Trans. Industry Applications, vol. 27, no. 4, July/Aug. 1991, pp. 701-705.

[21]T. Pana, Y. Hori, *Simultaneous speed estimation and rotor resistance identification for sensorless induction motor drives.*, Proceedings of Japan Industry Applications Society Conference, Ehime, Japan, 1994, pp. 135-140.

[22]C. Lascu, I. Boldea, F. Blaabjerg, *A Modified Direct Torque Control (DTC) for Induction Motor Sensorless Drive.*, The 33rd IEEE Industry Applications Society Annual Meeting 1998, St. Louis, MO, USA, vol. 1, pp. 415-422.

7 DIRECT TORQUE CONTROL OF INDUCTION MACHINE DRIVES

7.1 Introduction

The *Direct Torque (and Flux) Control* (DTC) was developed sixteen years ago as a high performance strategy for dead-beat torque and flux control of induction machine drives [1], [2]. Since then, this technique has been generalized, as Torque Vector Control (TVC), to all AC machine drives [3] and was recognized as a viable alternative to Field Oriented Control (FOC) [4]-[6]. Today, industrial ASD-s based on DTC are present on the market [7].

DTC abandons the analogy to DC motor current control, characteristic to FOC, and achieves fast and robust flux and torque control by means of bang-bang control, which matches very well the switching operation of VSI. The name DTC is derived from the fact that, on the basis of torque and flux errors, it is possible to directly determine the next inverter state, so that to maintain these errors within prefixed limits. No current control or PWM are employed.

The fundamental principle of DTC can be stated as: Simultaneous control of torque and flux is achieved by exclusive use of the available VSI voltage vectors, without intermediate current control and/or decoupling network.

The most important advantages of DTC are:

- It provides very good (fast) dynamic response for torque and flux control.
- It is robust with respect to motor parameter detuning, if compared to FOC.
- It does not require current controllers and coordinate transformations.

- It is simple and well matched to the discrete nature of VSI.
- It is inherently sensorless control since it does not require any mechanical information from motor's shaft.

The fact that DTC does not require PWM and, therefore, no timers in digital systems is not regarded as a particular advantage [4], since, in any digital controlled drive system, at least one timer is present for sampling period generation.

The classical DTC presents also several disadvantages:

- In steady state operation it exhibits high torque, flux and current ripple.
- The VSI switching frequency is variable and much lower than the sampling frequency.
- It operates with nonzero stead-state torque error.
- It produces high acoustical noise, especially at low speeds.
- There are difficulties to control the torque and flux at very low speeds.
- It is not capable to directly control and limit the current.

To some extent, the first three problems are related to each other, and solving one of them has the effect of improving behavior with respect to all of them. Many researchers have tried to improve the DTC behavior and the most important solutions will be presented in the next section.

Recent studies have demonstrated that DTC and FOC offer comparable levels of performance, each with particular advantages and disadvantages [4]-[6]. DTC is robust and might be preferable for high dynamic applications, but shows higher torque, flux and current ripple. FOC is capable to achieve fast and accurate current control, but is sensitive to motor parameter detuning and is more complex.

The DTC strategy and the basic DTC drive are presented in the next section. Variable Structure DTC schemes are developed and analyzed in the following sections. Simulations and experimental results are provided and discussed.

7.2 Classical Direct Torque Control

Direct Torque Control Principle

The block diagram of a DTC sensorless drive is shown in Figure 7.1. It contains two flux and torque comparators, a switching strategy that generates the switching signals for VSI and a torque and stator flux observer.

In principle, the DTC strategy can be described as: in each sampling period, the most appropriate voltage vector is selected so that to rapidly decrease the torque and flux magnitude errors. The right application of this principle allows fast, decoupled control of torque and flux, without PWM or current control.

The torque production and control in induction machines is based on torque equation (2.19). In stator flux reference frame, $\psi_s = \psi_{sd}$ and (2.19) is

$$T_e = \frac{3}{2} p \psi_s i_{sq} \tag{7.1}$$

In FOC, the control quantity is the torque current i_{sq}, which linearly controls the toque T_e, provided that the stator flux magnitude ψ_s is constant. In DTC, the torque control quantity is the stator flux vector and no current control is involved.

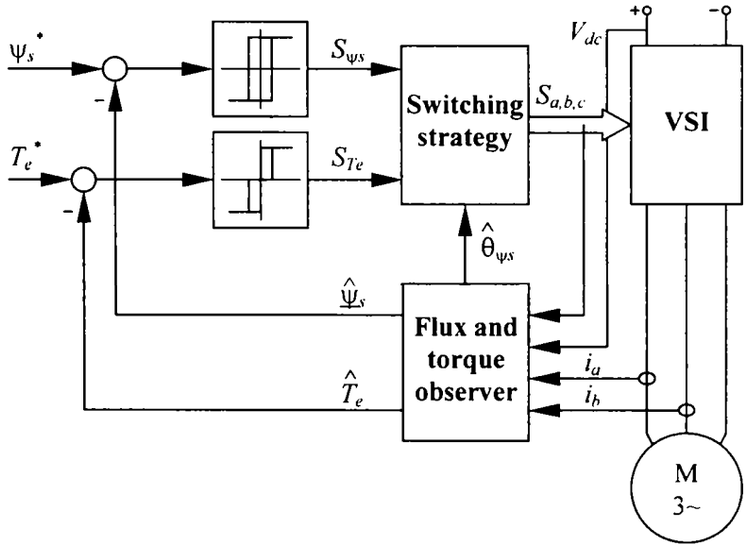

Figure 7.1 Basic Direct Torque Control sensorless drive

From (7.1) and (2.32), using the rotor flux magnitude ψ_r, the torque is

$$T_e = \frac{3}{2} p \frac{L_m}{L_s L_r \sigma} \psi_r \psi_s \sin(\theta_{sr}) \tag{7.2}$$

where θ_{sr} is the stator flux vector position with respect to rotor flux vector.

The torque can be controlled by modifying the stator flux vector (magnitude ψ_s and position θ_{sr}). The stator flux vector is a state variable that can be adjusted by means of stator voltage. The stator equation (2.15) in stator flux reference frame is

$$\underline{u}_s = R_s \underline{i}_s + \frac{d\underline{\psi}_s}{dt} + j\omega_{\psi s} \underline{\psi}_s \tag{7.3}$$

$$u_{sd} = R_s i_{sd} + \frac{d\psi_s}{dt} \tag{7.4a}$$

$$u_{sq} = R_s i_{sq} + \omega_{\psi s} \psi_s \tag{7.4b}$$

where $\omega_{\psi s}$ is the stator flux vector angular speed.

The stator flux magnitude is controlled according to (7.4a). Assuming that the stator voltage drop $R_s i_{sd}$ is small, the variation of ψ_s is proportional to u_{sd}. A positive value of u_{sd} determines the increase of ψ_s, while a negative value will decrease it.

From (7.1) and (7.4b), the torque is

$$T_e = \frac{3p}{2R_s} \psi_s (u_{sq} - \omega_{\psi s} \psi_s) \tag{7.5}$$

It is evident that the imaginary component of the stator voltage, u_{sq} is qualified to control the torque. The stator flux vector moves in the direction of the applied voltage vector. Thus, selecting the adequate sequence of voltage vectors, it is possible to drive the stator flux along a desired trajectory and to control the torque.

The rotor flux dynamics with respect to stator flux is given by (2.38). This indicates that the rotor flux follows the stator flux with a time delay given by the time constant $T_r\sigma$. When a new voltage vector is applied, the stator flux moves faster than the rotor flux, the angle θ_{sr} is modified and so is the torque.

The principle of the classical DTC strategy is illustrated in Figure 7.2. The complex plane is divided into six sectors, S1 to S6, such that, each of the VSI active voltage vectors is the symmetry axis of one sector. Then, the position of the stator flux vector, with respect to these sectors is found.

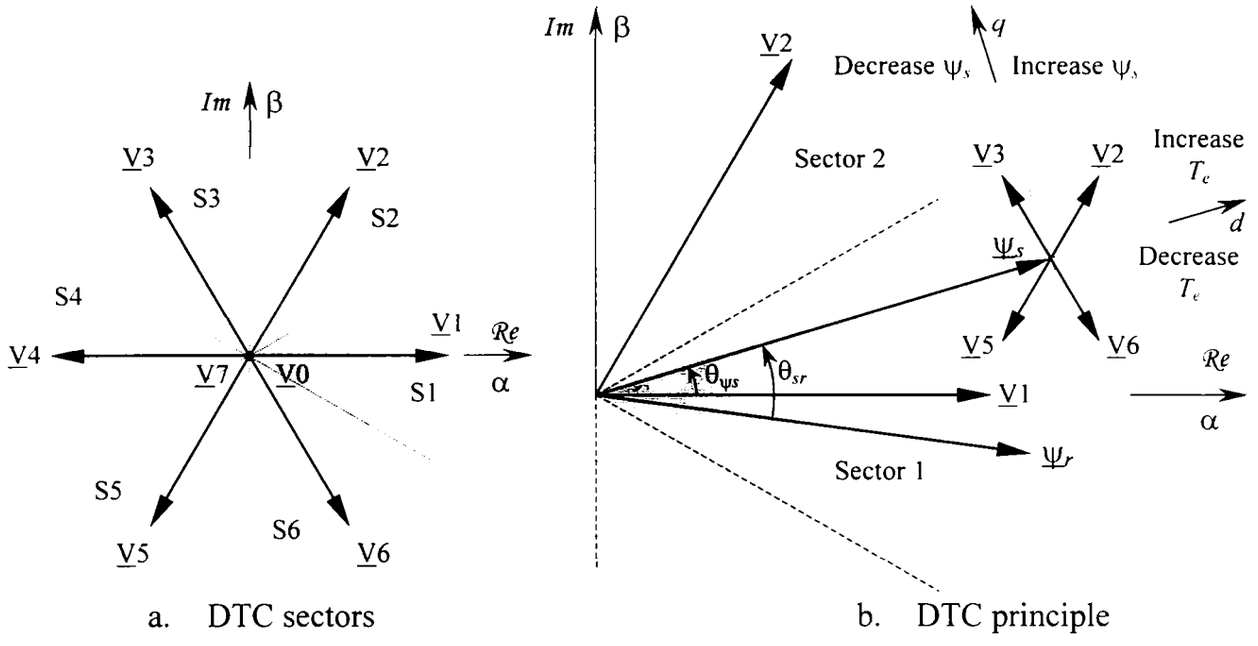

Figure 7.2 The Direct Torque Control sectors and principle

In Figure 7.2.b the stator flux vector is located in sector S1. In this case, the stator flux magnitude is increased if $\underline{V_2}$ or $\underline{V_6}$ are applied and is decreased if $\underline{V_3}$ or $\underline{V_5}$ are applied. The stator flux is moved away from the rotor flux, increasing θ_{sr} and the torque if $\underline{V_2}$ or $\underline{V_3}$ are applied and is approaching the rotor flux, decreasing θ_{sr} and the torque if $\underline{V_5}$ or $\underline{V_6}$ are applied. Similar reasoning applies to all six sectors.

The voltage vector selection is made on the basis of torque and flux errors, as shown in Figure 7.3. The torque error $e_{Te} = T_e^* - \hat{T}_e$ is applied to a three-level hysteresis bang-bang controller that produces the discrete signal S_{Te} as follows:

$S_{Te} = 1$ if $e_{Te} > h$, or if $0 < e_{Te} < h$ and $de_{Te}/dt < 0$

$S_{Te} = 0$ if $0 < e_{Te} < h$ and $de_{Te}/dt > 0$, or if $-h < e_{Te} < 0$ and $de_{Te}/dt < 0$

$S_{Te} = -1$ if $e_{Te} < -h$, or if $-h < e_{Te} < 0$ and $de_{Te}/dt > 0$

The flux error $e_{\psi s} = \psi_s^* - \hat{\psi}_s$ is applied to a two-level hysteresis bang-bang controller that produces the discrete signal $S_{\psi s}$ as follows:

$S_{\psi s} = 1$ if $e_{\psi s} > g$, or if $|e_{\psi s}| < g$ and $de_{\psi s}/dt < 0$

$S_{\psi s} = -1$ if $e_{\psi s} < -g$, or if $|e_{\psi s}| < g$ and $de_{\psi s}/dt > 0$

where g and h are the flux and torque comparator hysteresis bands, respectively. These can be implemented as constants or as speed and load dependent quantities [7].

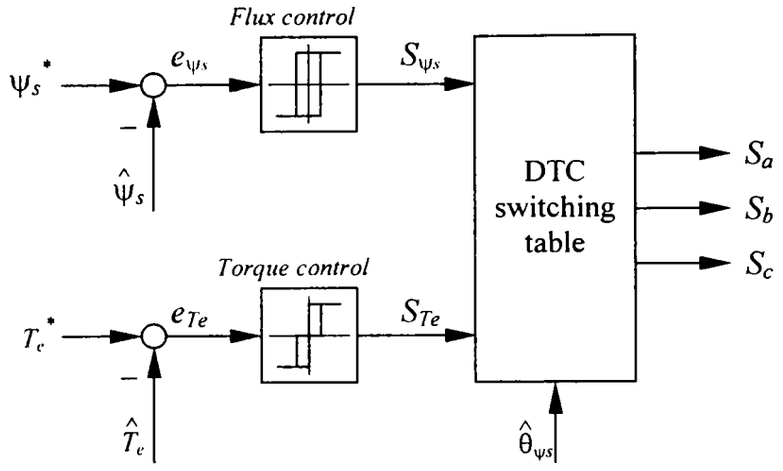

Figure 7.3 The Direct Torque Control block diagram

The voltage vector is selected from a switching table that receives as entries S_{Te}, $S_{\psi s}$ and the sector in which the stator flux is located. Table 7.1 generalizes, for all six sectors, the DTC switching strategy, illustrated in Figure 7.2.b for the first sector. In this table, zero voltage vectors, V_0 or V_7, are used to decrease the torque whenever the torque error is negative, small. At each instant, the voltage vector $\underline{V}_k$ (3.10), given by Table 7.1, is directly applied to motor by the VSI, Figure 7.3.

This very simple strategy produces fast dynamic torque response. However, in steady state the torque and flux ripple are high. The VSI switching frequency is variable and its value depends on hysteresis bands g and h, [8]. In digital implementation, the switching frequency cannot be higher than the sampling frequency, that is, the voltage vector and the VSI state are updated with the sampling frequency.

Table 7.1 The Direct Torque Control switching table

Sector		1	2	3	4	5	6
$S_{\psi s} = 1$	$S_{Te} = 1$	$\underline{V}_2$	$\underline{V}_3$	$\underline{V}_4$	$\underline{V}_5$	$\underline{V}_6$	$\underline{V}_1$
	$S_{Te} = 0$	$\underline{V}_7$	$\underline{V}_0$	$\underline{V}_7$	$\underline{V}_0$	$\underline{V}_7$	$\underline{V}_0$
	$S_{Te} = -1$	$\underline{V}_6$	$\underline{V}_1$	$\underline{V}_2$	$\underline{V}_3$	$\underline{V}_4$	$\underline{V}_5$
$S_{\psi s} = -1$	$S_{Te} = 1$	$\underline{V}_3$	$\underline{V}_4$	$\underline{V}_5$	$\underline{V}_6$	$\underline{V}_1$	$\underline{V}_2$
	$S_{Te} = 0$	$\underline{V}_0$	$\underline{V}_7$	$\underline{V}_0$	$\underline{V}_7$	$\underline{V}_0$	$\underline{V}_7$
	$S_{Te} = -1$	$\underline{V}_5$	$\underline{V}_6$	$\underline{V}_1$	$\underline{V}_2$	$\underline{V}_3$	$\underline{V}_4$

Torque and flux ripple analysis

In digital systems, the hysteresis bands can be set to zero in order to reduce the ripple. The torque controller becomes a three-level asymmetric comparator:

$$S_{Te} = \begin{cases} 1 & if\ e_{Te} > h_p \\ 0 & if\ h_n < e_{Te} < h_p \\ -1 & if\ e_{Te} < h_n \end{cases} \tag{7.6}$$

A good choice is $h_p = 0$ at positive field speed and $h_n = 0$ at negative field speed.

Similarly, the flux controller becomes a two level comparator

$$S_{\psi s} = \text{sgn}(e_{\psi s}) \tag{7.7}$$

The torque slope can be determined by differentiating (7.2). Using the flux model in stator frame, (2.44)-(2.45), the torque slope is

$$\begin{aligned} \frac{d}{dt}T_e &= -(\frac{1}{T_s\sigma} + \frac{1}{T_r\sigma})T_e - k_{Te}\omega_r(\psi_{sd}\psi_{rd} + \psi_{sq}\psi_{rq}) + k_{Te}(\psi_{rd}u_{sq} - \psi_{rq}u_{sd}) \\ &= a - b + c \end{aligned} \tag{7.8}$$

where $k_{Te} = 3pL_m/(2L_sL_r\sigma)$, ω_r is the rotor speed and a, b, c are symbolic names.

The first term in (7.8), a, is due to stator and rotor resistances and is very small compared to b and c. The second term, b, is rotor speed dependent and c represents the effect of the applied voltage. During a switching period, T_{sw}, only one voltage vector is applied and, therefore, u_{sd} and u_{sd} are constant. Since fluxes are slowly variable and T_{sw} is small, it can be assumed that fluxes are also constant.

At high speeds, b is large. If an active voltage is applied, c is large, comparable to b, which partly cancels the action of c, and the torque increases slowly. If a zero voltage is applied, c=0 and $-b$ alone indicates a fast (violent) torque decrease.

At low speeds b is a small quantity. An active vector determines a large value of c that dominates b and the torque increases fast. A zero vector makes c=0 and the torque decreases slowly, as b is a small quantity now. At medium speeds, the torque rising and falling slopes are comparable.

Simulation results with a DTC drive are presented in Figure 7.4. Torque and flux behavior at high speed (1500 rpm) and low speed (30 rpm) are shown. The torque decreases fast at high speed and increases fast at low speed, as explained above. The sampling frequency is f_s=10 kHz and the motor is Machine 1 (4 kW, Appendix A).

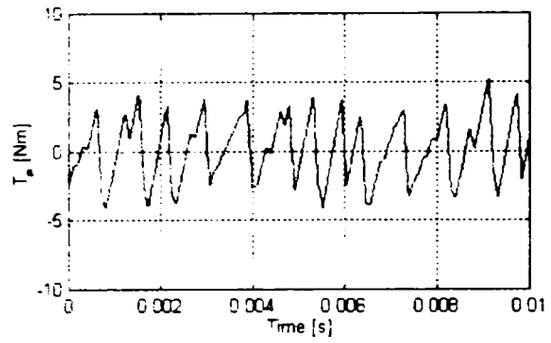

a. Torque at 1500 rpm

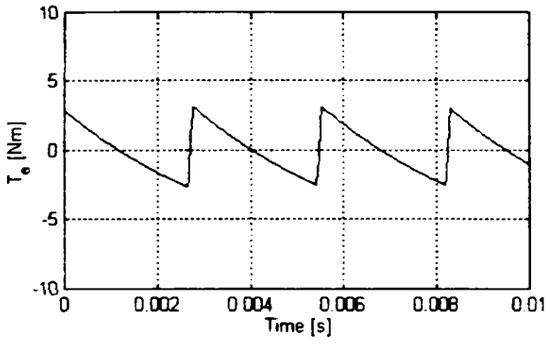

b. Torque at 30 rpm

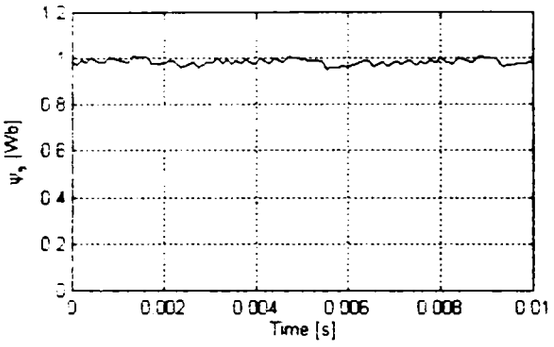

c. Stator flux at 1500 rpm

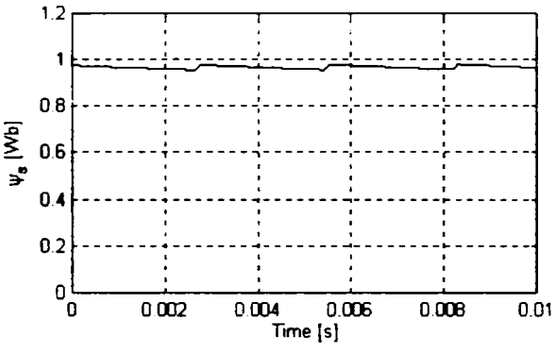

d. Stator flux at 30 rpm

Figure 7.4 Torque and stator flux magnitude for DTC at high and low speeds at f_s=10 kHz

The torque ripple in one switching period can be approximated as

$$\Delta T_e = T_{e(k)} - T_{e(k-1)} \cong (a - b + c)T_{sw} \tag{7.9}$$

Similar analysis can be carried out for the stator flux. The flux magnitude slope is given by (7.4) and the flux magnitude ripple can be approximated as

$$\Delta\psi_s = \psi_{s(k)} - \psi_{s(k-1)} \cong (u_{sd} - R_s i_{sd})T_{sw} \tag{7.10}$$

The slope and the ripple are determined by the voltage u_{sd}, which is the projection of the commanded vector on the stator flux direction. Since the voltage vectors are fixed and the flux vector is rotating, u_{sd} is variable along a sector. Hence, the flux slope changes as the flux moves within the sector, Figure 7.4.c.

Since the motor parameters cannot be modified and fluxes are also fixed by other constraints, it is evident from (7.9) and (7.10) that the most effective way to decrease the torque and flux ripple is to *increase the vector switching frequency*.

A close look to Figure 7.4.b reveals that the violent torque increase takes place in one sampling period (T_s=100 μs) because the zero vector was applied for the entire period. The sampling time delay has the effect of a (time) hysteresis band.

Improved DTC strategies

There are two approaches to increase the vector switching frequency T_{sw}:

1. Maintaining the classical strategy that applies only one vector in each sampling period and drastically increasing the sampling frequency [7], [8].
2. Maintaining the sampling time unchanged and increasing the vector frequency by applying several vectors in the same sampling period [9]-[15].

The sampling frequency f_s is the frequency of the main control loop that realizes the voltage and current measurement, the flux and torque estimation and the DTC. In the first approach (the brute force approach), this frequency is increased.

Simulation results (torque only) with DTC, in the same conditions as for Figure 7.4, with sampling frequency f_s=40 kHz, are presented in Figure 7.5. Increasing four times the f_s has resulted in reduction of torque and flux ripple in the same proportion.

This approach entirely preserves the classical DTC strategy and its fast dynamic response but requires powerful (and expensive) DSP-s. The commercial drive described in [7] uses a dedicated DSP (ASIC) in a multiprocessor architecture and adaptive switching thresholds, h_p and h_n, In [8], a powerful 32 bit floating-point DSP is employed. In both cases, the fastest (DTC) sampling frequency is 40 kHz.

The second approach assumes that several vectors are applied in the same cycle. In order to compensate for the torque and flux errors, the control system should be able to generate any vector, as a combination of basic vectors, by using some form of PWM.

This ideal behavior can be approximated by applying in each period different vectors, for prefixed time intervals, strategy called *Discrete SVM* (DSVM) in [9], [10]. A higher number of vectors determines lower torque and current ripple.

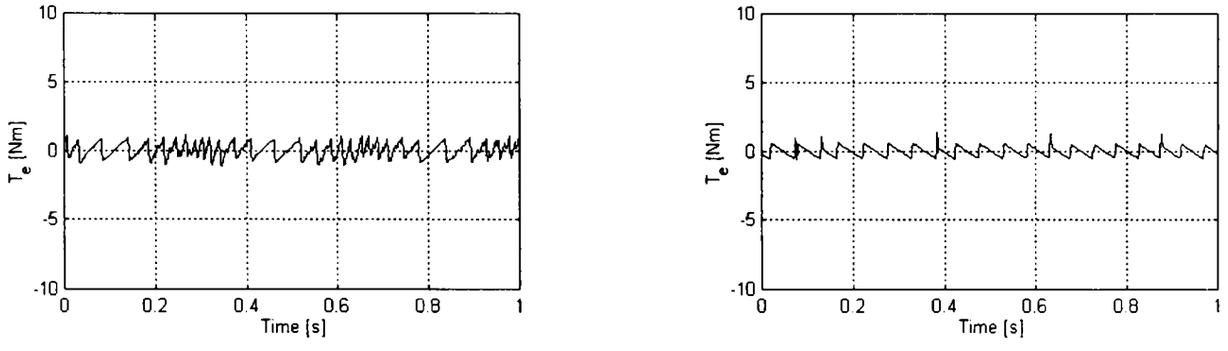

Figure 7.5 Simulated torque for DTC at 300 rad/s (left) and 10 rad/s (right), at f_s=40 kHz

In [9], the switching cycle is subdivided in three equal intervals. For each sector, there are 19 interesting combinations of three basic vectors that can control the flux and torque simultaneously, in the same forward-backward manner as DTC does. For each sector, there are four switching tables, one for small EMF range, one for medium EMF range and two for large EMF range, for one direction of rotation.

Each sector is divided into two sub-sectors, the torque controller is a five-level hysteresis comparator and the flux controller is two-level. The torque comparator output, S_{Te} assumes five values: –2, -1, 0, 1, 2. The comparison thresholds are selected so that in steady state S_{Te} is –1, 0, 1, while –2 and 2 are generated only in high dynamic transients and the switching tables are designed accordingly.

In this way, it is possible to choose among 19 voltage vectors instead of five, as in classical DTC, without significant increase of the computation time. Results reported in [9] and [10] show a certain reduction of the torque, flux and current ripple.

A different, more elaborate approach, which performs dead-beat torque and flux control has been described in [11] and [12]. In this case, the torque error represents the desired change in torque, ΔT_e^* over one sampling period, T_s. From (7.8), an equation similar to (7.9), in stator frame, can be written in terms of desired torque change

$$\Delta T_e = T_e^* - T_e = (a - b + k_{Te}(\psi_{rd} u_{s\beta}^* - \psi_{rq} u_{s\alpha}^*))T_s \tag{7.11}$$

where $\underline{u}_s^* = u_{s\alpha}^* + j u_{s\beta}^*$ is the reference voltage vector and a can be neglected.

Similarly, the flux error represents the desired change in flux and, if the $R_s \underline{i}_s$ voltage drop is neglected, the reference stator flux magnitude squared is

$$\psi_s^{*2} = (u_{s\alpha}^* T_s + \psi_{s\alpha})^2 - (u_{s\beta}^* T_s + \psi_{s\beta})^2 \tag{7.12}$$

Equations (7.11) and (7.12) are solved for $\underline{u}_s^* = u_{s\alpha}^* + j u_{s\beta}^*$ using the estimated stator and rotor flux. The reference vector commanded to VSI is constructed as

$$\underline{v}_s^* = \underline{u}_s^* + R_s \underline{i}_s \tag{7.13}$$

Finally, the standard SVM technique is employed to realize the reference vector (7.13). In this way, the torque and current pulsations result low.

Finding the solution of (7.11)-(7.12) requires solving of a quadratic equation. This is computation intensive and gives two solutions from which only one is selected. Improvements of this technique in transient conditions and in overmodulation region,

where dead-beat control is not possible, are described in [12]. A very similar, dead-beat DTC scheme is also presented in [13].

Another development of the DTC scheme, based on classical SVM is the so-called Stator Flux Vector Control [14], [15]. The principle of operation relies on driving the stator flux vector towards its reference, defined by the input commands. In this case, the input commands are the reference torque and rotor flux magnitude.

The voltage vector reference calculation is performed in two distinct steps. First, the reference stator flux vector, $\underline{\psi}_s^{r*}$, in rotor flux reference frame, is computed from the flux model (2.38), using the reference torque, T_e^* and rotor flux magnitude, ψ_r^*

$$\psi_{sd}^{r*} = \frac{L_s}{L_m}\psi_r^* + \frac{L_s T_r \sigma}{L_m}\frac{d}{dt}\psi_r^* \tag{7.14}$$

$$\psi_{sq}^{r*} = \frac{2}{3p}\frac{L_s L_r \sigma}{L_m}\frac{T_e^*}{\psi_r^*} \tag{7.15}$$

Next, a stator flux P-type controller is implemented in stator reference frame

$$\underline{u}_s^* = R_s \underline{i}_s + K_P(\underline{\psi}_s^* - \underline{\hat{\psi}}_s) \tag{7.16}$$

where $\underline{\psi}_s^* = \underline{\psi}_s^{r*} e^{j\hat{\theta}_{\psi r}}$ is the reference stator flux in stator frame and K_P is the controller gain. If $K_P = 1/T_s$, a dead-beat controller is obtained, [14].

As before, the reference voltage is realized by means of SVM. In this way, the switching frequency is constant and the torque and current ripples are small.

Apart from the SVM based solutions that give, by far, the best results in terms of torque and current ripple, many other DTC schemes have been developed. The presence of the switching table that can be designed based on engineering insight suggests that an approach based on artificial intelligence methods is realistic. An early DTC solution implemented as a fuzzy logic controller is described in [16].

Recently, solutions that implement the DTC controller as a neural network have been developed [17]. The solution described in [18] must be noted for its originality: it implements the entire sensorless algorithm (state estimation and DTC) within a single, large neural network that receives as inputs the measured currents and voltages and produces the VSI switching signals.

7.3 Linear Direct Torque Control

Linear DTC synthesis

The most efficient way to reduce the torque, current and flux ripple is to increase the vector switching frequency and, from this perspective, solutions based on SVM are very attractive. In this section a new Linear Direct Torque and Flux Control scheme, called *Linear-DTC* is developed.

The philosophy behind this approach is: the classical DTC strategy applies one vector in each sampling period; a reduction of torque ripple is obtained if the interval is divided in three, and three vectors are applied in one cycle [9], [10]. The interval can be further divided in 10, 100, 1000, ... subintervals, and the torque ripple will continue to decrease. At the limit, a linear space is obtained and the torque and flux will exhibit an asymptotical behavior. A linear controller has to be designed for this space.

In this case, the switching table approach is not feasible anymore and is replaced with the SVM algorithm, which converts a linear reference vector into a digital, three-bit word. In each switching period, the standard SVM scheme, Figure 3.8, applies six voltage vectors with variable duration and guaranties constant switching frequency. Due to the fact that vectors duration is variable, with a high resolution given by the DSP's timer resolution, the SVM achieves very high resolution of voltage control.

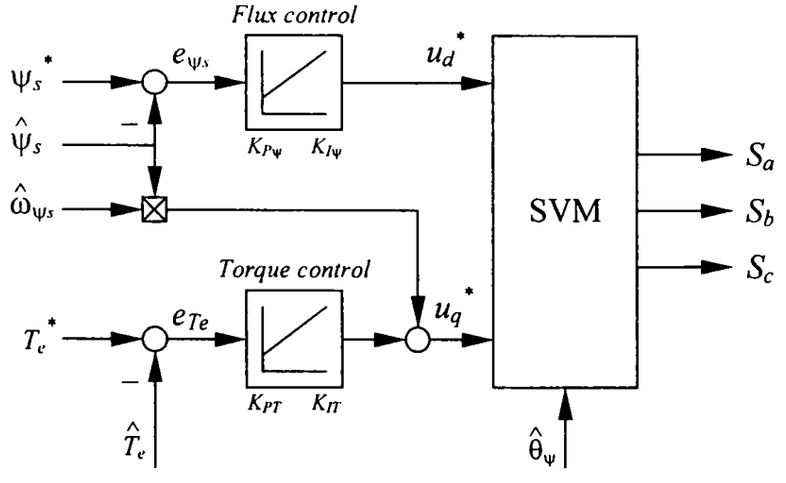

Figure 7.6 The Linear Direct Torque Control block diagram

The block diagram of the Linear-DTC is represented in Figure 7.6. The nonlinear, bang-bang torque and flux controllers have been replaced with linear PI controllers and the VSI switching signals are generated by the SVM block.

A reference voltage vector, $\underline{u}_s^* = u_{sd}^* + ju_{sq}^*$, in stator flux reference frame, is obtained as the output of torque and flux controllers

$$u_{sd}^* = (K_{P\psi} + K_{I\psi}\frac{1}{s})(\psi_s^* - \hat{\psi}_s) \tag{7.17}$$

$$u_{sq}^* = (K_{PT} + K_{IT}\frac{1}{s})(T_e^* - \hat{T}_e) + \hat{\omega}_{\psi s}\hat{\psi}_s \tag{7.18}$$

where "*" denotes reference quantities and $\hat{\omega}_{\psi s} = d\hat{\theta}_{\psi s}/dt$ is the stator flux speed.

The reference voltage is transformed to stator frame using the estimated stator flux position, $\underline{u}_s^{s*} = \underline{u}_s^* e^{j\hat{\theta}_{\psi s}}$ and $\underline{u}_s^{s*}$ is applied to the SVM unit that produces the VSI switching signals S_a, S_b, S_c.

The reason for the PI controllers presence can be seen from (7.4) and (7.5) that give the flux and torque in induction machines. Replacing, formally, (7.17) in (7.4), neglecting the small IR voltage drop and assuming that the estimated flux is the same as the real flux, the stator flux control loop transfer function results as

$$H_{\psi s}(s) = \frac{\psi_s}{\psi_s^*} = \frac{K_{P\psi}s + K_{I\psi}}{s^2 + K_{P\psi}s + K_{I\psi}} \tag{7.19}$$

It is evident that a proportional controller would have been enough. In this case, a first order (LPF) transfer function is obtained from (7.19), with $K_{I\psi}$=0. The PI controller was chosen in order to speed up the flux control.

The torque control loop transfer function is obtained by formally replacing (7.18) in (7.5) and assuming that estimated quantities are the same as real ones

$$H_{Te}(s) = \frac{T_e}{T_e^*} = \frac{k_T(K_{PT}s + K_{IT})}{(1 + k_T K_{PT})s + k_T K_{IT}} \tag{7.20}$$

where $k_T = 3pL_m\psi_s/(2L_sL_r\sigma)$.

The open loop transfer function is $H_{Te0}(s) = k_T(K_{PT} + K_{IT}/s)$ and this indicates that the PI controller is required in order to obtain zero steady-state torque error. This is an important advantage over classical DTC that operates with steady-state torque error.

In order for the torque loop to behave linearly, the stator flux must be constant, or slowly variable. This is the reason for which the flux control loop must be fast and robust enough. In this way, decoupled torque and flux control has been obtained without employing any explicit decoupling network.

If speed control is desired, the reference torque is produced by a speed controller. A PI controller, cascaded with the torque control loop, is fully qualified for this task

$$T_e^* = (K_{P\omega} + K_{I\omega}\frac{1}{s})(\omega_r^* - \hat{\omega}_e) \tag{7.21}$$

Assuming once more that the estimated and real speed are the same, the block diagram of the equivalent mechanical control system of induction machine is represented in Figure 7.7. If the stator flux is constant, this represents a linear dynamic system.

In (7.17), an additional term, representing the $R_s\underline{i}_s$ drop can bee added, in the same way as in (7.13). This can increase the robustness during large torque transients. Since the $R_s\underline{i}_s$ drop is relatively small, its absence is preferred, for simplicity.

The Linear-DTC is stator flux oriented, stator flux regulating control. For constant stator flux operation, the flux is constant below base speed and inverse proportional to the rotor speed, above base speed. In high performance drives, the flux reference can be modified using a field weakening strategy that maximizes the system's torque capability.

If constant rotor flux operation is desired, then the rotor flux reference is constant and the stator flux reference is calculated from (7.14)-(7.15), in steady state, as

$$\psi_s^* = \sqrt{\left(\frac{L_s}{L_m}\psi_r^*\right)^2 + \left(\frac{2}{3p}\frac{L_s L_r \sigma}{L_m}\frac{T_e^*}{\psi_r^*}\right)^2} \tag{7.22}$$

In this case, however, the stator flux will be variable during torque transients.

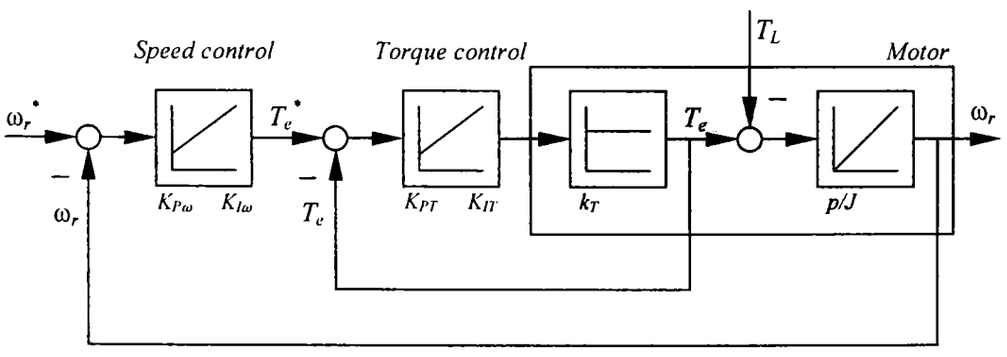

Figure 7.7 Speed and torque equivalent control with Linear-DTC

Experimental results

At this point, enough pieces of information are available, to construct the first sensorless Linear-DTC drive. Its scheme, represented in Figure 7.8, contains the Linear-DTC from Figure 7.5, the PI speed controller (7.21), the modified Jansen-Lorenz observer from Figure 4.20, the modified MRAS speed estimator from Figure 6.11, and the torque estimator (6.7). The Linear-DTC uses the standard SVM scheme, Table 3.1, with DTC dynamic OVM from Figure 3.11 and dead time compensation strategy (3.46). The motor is Machine 1 (P_N=4 kW, T_{eN}=27 Nm, Appendix B). The system operates with constant stator flux and no resistance adaptation was employed.

This was the very first sensorless DTC drive implemented. Experiments reported in Figures 4.24 and 6.13 were obtained with this. Experimental results shown in Figure 4.19 have been realized with a very similar system that employs the inherent sensorless Luenberger observer, Figure 4.7 and the speed estimator (6.2)-(6.6). All these results demonstrate the speed sensorless control performance.

A comparison between Linear-DTC, Figure 7.5 and classical DTC, Figure 7.3, implemented in the system described above, is presented in Figures 7.9 to 7.11. Speed, torque and flux transients during acceleration from 150 rpm to 1500 rpm are shown comparatively for both strategies in Figure 7.9. Figure 7.10 shows the instantaneous stator current at 1500 rpm (50 Hz stator frequency). All experiments have been carried out with both systems running at the same sampling frequency, f_s=8 kHz.

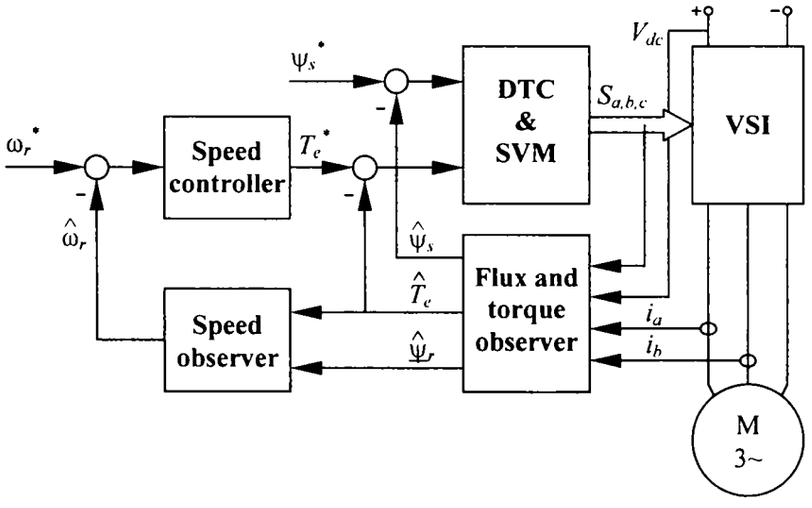

Figure 7.8 The Linear-DTC sensorless drive

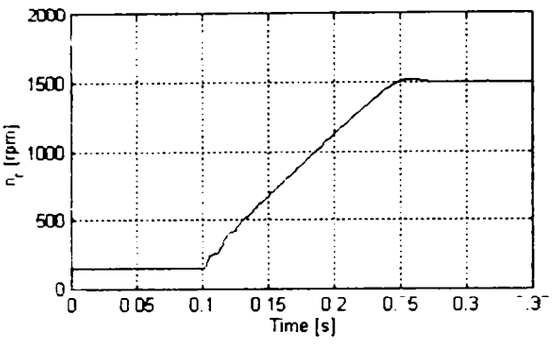

a. Estimated rotor speed – Linear-DTC

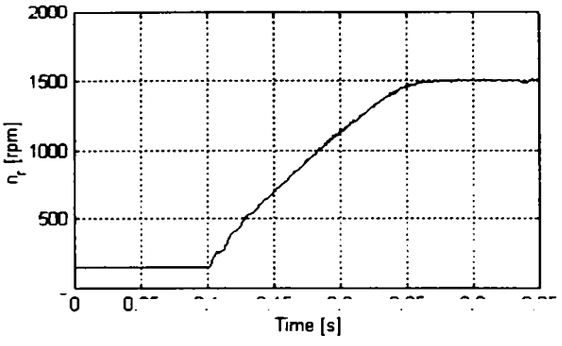

b. Estimated rotor speed - DTC

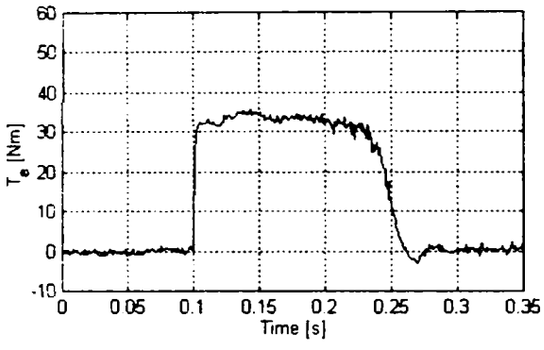

c. Estimated torque – Linear-DTC

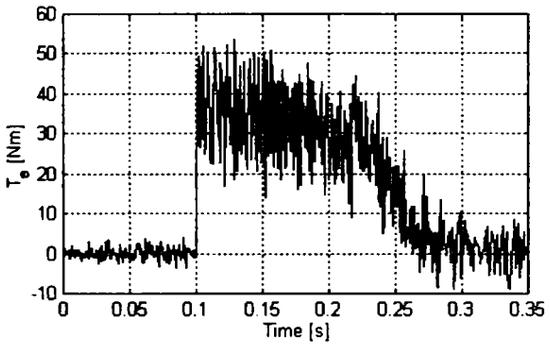

d. Estimated torque - DTC

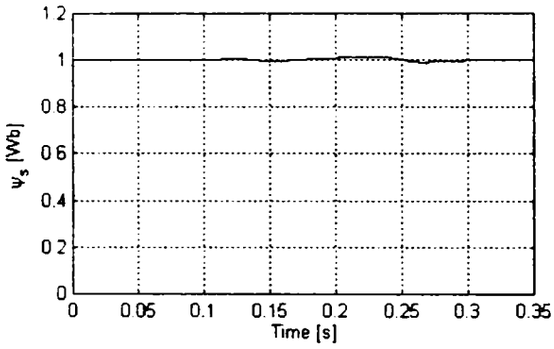

e. Estimated stator flux – Linear-DTC

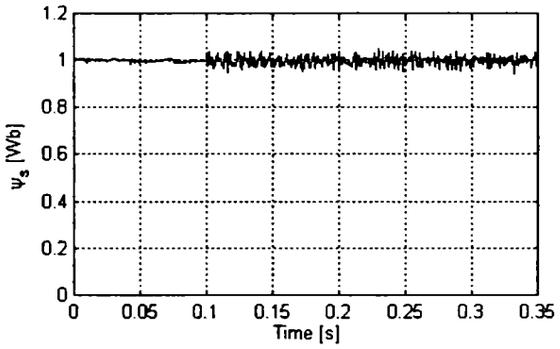

f. Estimated stator flux - DTC

Figure 7.9 Acceleration from 150 rpm to 1500 rpm with Linear-DTC and Classical DTC, using Modified Jansen-Lorenz observer and modified MRAS speed estimator.

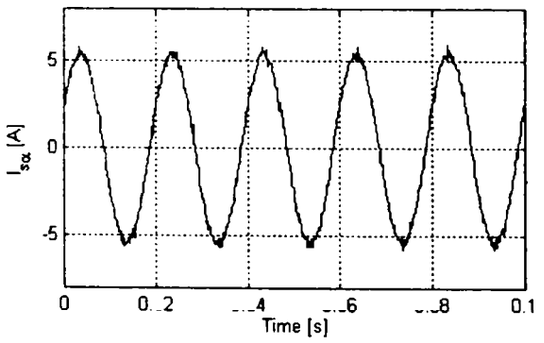

a. Stator current – Linear-DTC

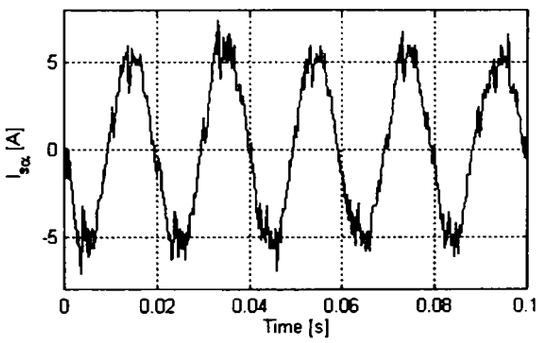

b. Stator current - DTC

Figure 7.10 Stator current at 50 Hz steady state, with Linear-DTC and Classical DTC

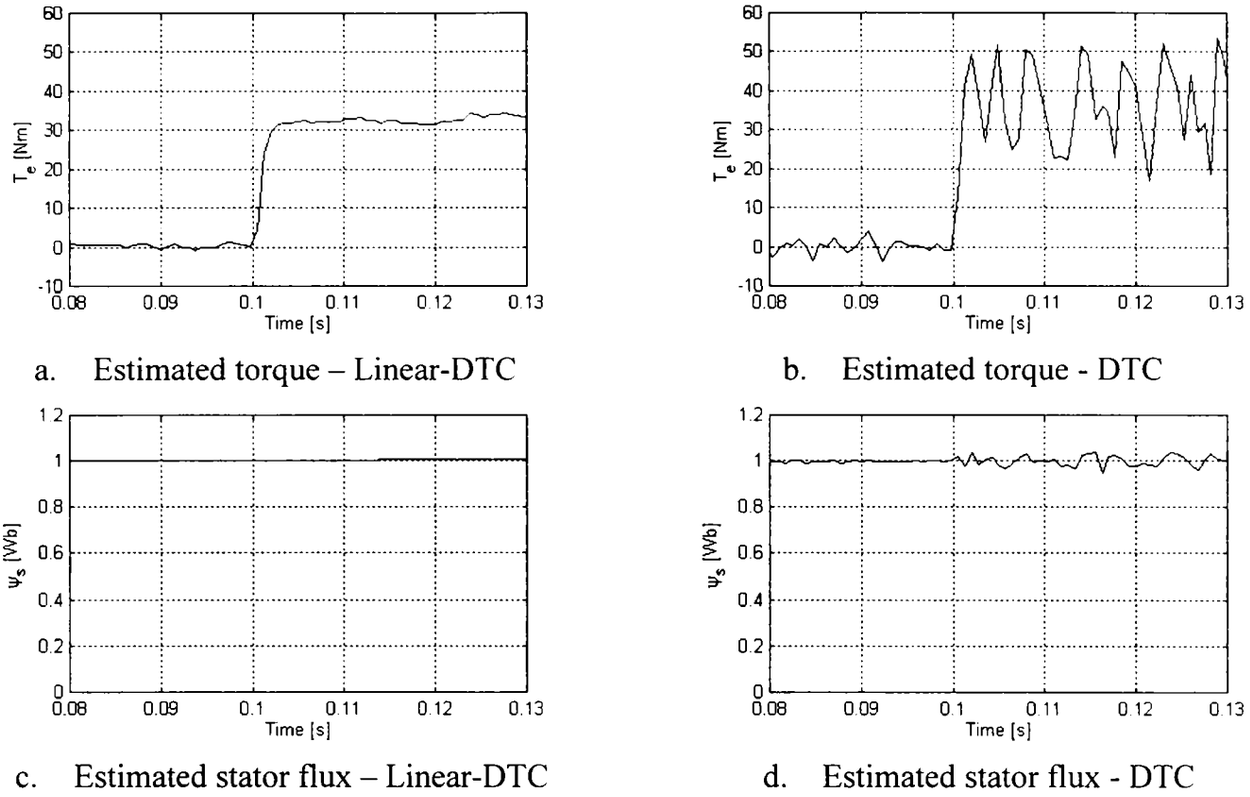

a. Estimated torque – Linear-DTC

b. Estimated torque - DTC

c. Estimated stator flux – Linear-DTC

d. Estimated stator flux - DTC

Figure 7.11 Torque and flux dynamic behavior with Linear-DTC and Classical DTC

The torque, current and flux ripple and the acoustical noise are considerably reduced when Linear-DTC is employed. Its superiority over DTC is evident in steady state. The flux controller is robust with respect to torque and speed transients.

One of the most important advantages of DTC is the fast torque response, usually in the range of 1-2 ms ("below 2 ms", [7]). Figure 7.11 shows a time-zoom on the torque and flux waveforms from Figure 7.9. A reference torque step of 32 Nm (motor's rated torque is T_{eN}=27 Nm) is applied at t=0.1 s. The DTC reaches 30 Nm in 1 ms, while the Linear-DTC needs 2 ms to reach 30 Nm. Although the Linear-DTC is slightly slower than DTC, its performance is very good and is comparable to that of DTC.

Better results have been obtained with drives that employ SMO-s. Figure 7.12 shows torque and flux transients during acceleration from standstill, with a drive that uses Linear-DTC, the generalized SMO from Figure 5.2 with resistances adaptation, the PLL speed observer Figure 6.3 and Machine 2 (P_N=1.1 kW, T_{eN}=7 Nm). A torque step of 12 Nm is applied at t=10 ms. Excellent dynamic performance is displayed: the value of 14 Nm is reached in 1 ms and the set value is firmly maintained after transients. The low current estimation error demonstrates the observer's robustness.

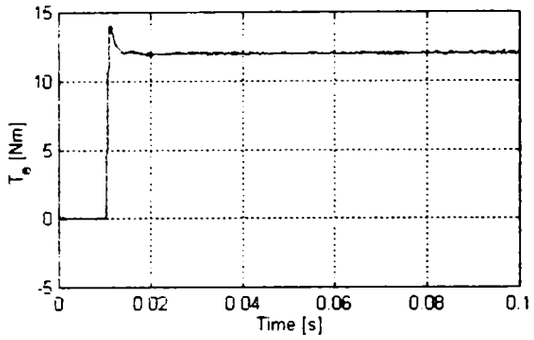

a. Estimated torque – Linear-DTC

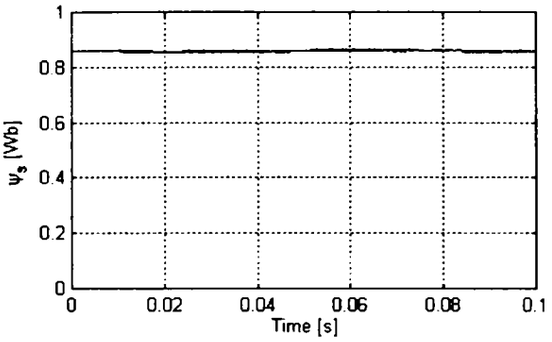

b. Estimated stator flux – Linear-DTC

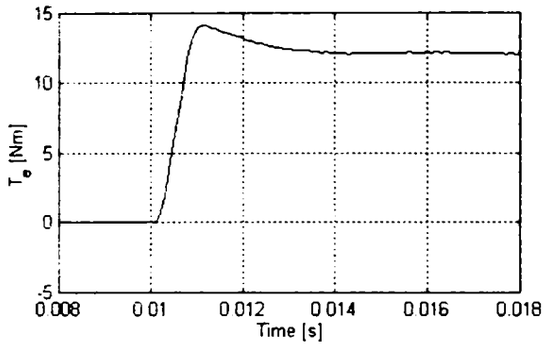

c. Estimated torque – time zoom

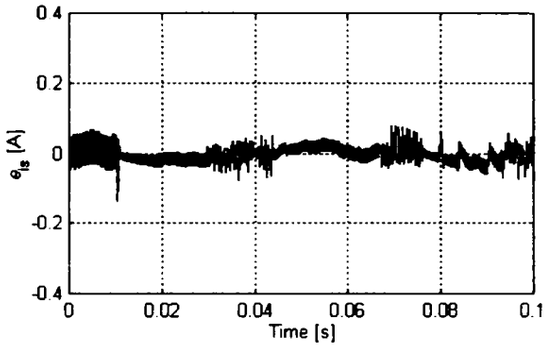

d. Current estimation error – SMO

Figure 7.12 Torque and flux dynamic behavior with Linear-DTC and generalized SMO

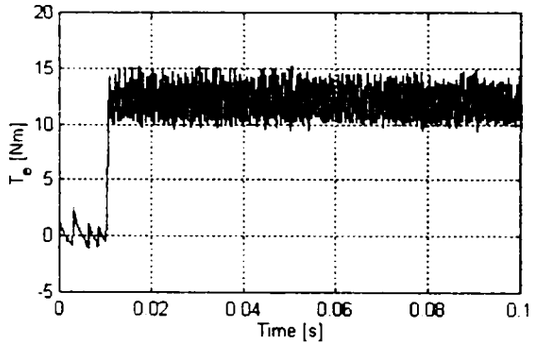

a. Estimated torque – DTC

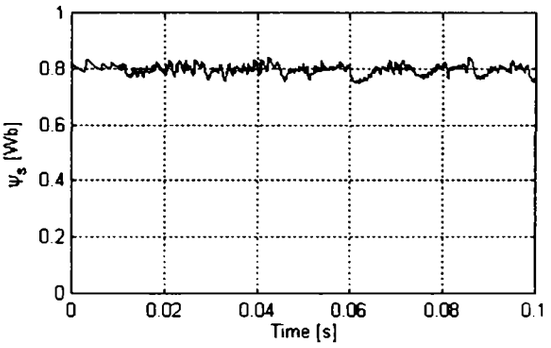

b. Estimated stator flux – DTC

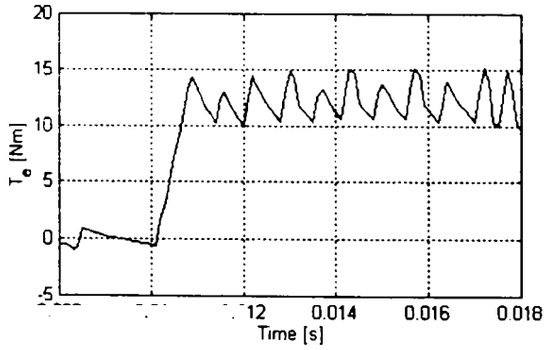

c. Estimated torque – time zoom

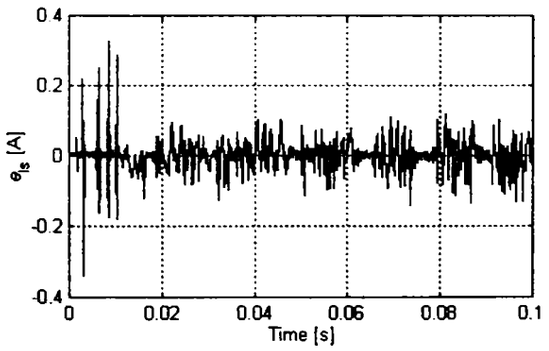

d. Current estimation error – SMO

Figure 7.13 Torque and flux dynamic behavior with classical DTC, generalized SMO, PLL speed observer and Machine 2; sampling frequency f_s = 10 kHz.

Similar torque transients, with the same system, controlled by classical DTC are presented in Figure 7.13. The motor is accelerated from standstill with a torque step of 12 Nm applied at t=10 ms. The torque reaches 15 Nm in 1 ms, but the torque and flux ripple is very big. Despite of violent switching, the current estimation error remains low, an indication of the generalized SMO performance.

Compared to Figure 7.13, Figure 7.12 clearly demonstrates the performance of the Linear-DTC. The torque dynamic response is the same, while the steady state ripple is practically inexistent. In both cases, the sampling frequency was f_s = 10 kHz. For Linear-DTC, the VSI switching frequency is also 10 kHz, while for classical DTC, the VSI switching frequency is lower. It can be estimated from Figure 7.13.c that the voltage vectors switching frequency is about 3.5 kHz. It is considered that comparison with both systems running at f_s = 10 kHz is realistic, since this is a measure of the DSP's performance to price ratio.

Conclusions

The Linear-DTC strategy is capable to realize the direct torque and flux control without decoupling network and/or intermediate current control. It approaches the DTC philosophy from the linear control perspective, replacing the bang-bang controllers with linear PI controllers and the switching table with the high resolution SVM.

This solution achieves high dynamic torque response, comparable to that obtained with classical DTC. In steady-state, the Linear-DTC exhibits significantly lower torque, current and flux ripple. This strategy is simple; it does not require rotor speed or position information and operates the VSI at constant switching frequency.

Overall, the Linear-DTC preserves the DTC dynamic performance and offers superior steady state behavior. The robustness is not guarantied by the linear torque and flux controllers, but is demonstrated by experiments. The excellent dynamic and static performance is also demonstrated by various experimental results. More results with Linear-DTC have been reported in [19] and [20].

7.4 Variable Structure Direct Torque Control

7.4.1 Variable Structure Control

Variable Structure Control (VSC) or *Sliding Mode Control* is a general design approach for a wide spectrum of control problems and dynamic systems, including nonlinear and uncertain systems. It has its roots in relay and bang-bang control theory and its most important feature is its ability to result in very robust, in many cases, invariant control systems. The advances in digital signal processing have made the practical application of VSC a viable alternative to other control methods [21]-[25].

Essentially, VSC utilizes high speed switching control laws to drive the state trajectory of a nonlinear system onto a specified surface in the state space, called sliding surface, and to maintain the system's trajectory on this surface for all subsequent time. The system's evolution, restricted to this surface, represents the desired system dynamics and is called *sliding mode*. The system's structure is intentionally changed each time the system's trajectory intersects the sliding surface.

Variable structure control provides a systematic approach to the problem of maintaining stability and consistent performance in face of modeling imprecisions, unmodeled dynamics and disturbances. By proper design of the sliding controller and surface, this is reached in finite time and VSC attains conventional control goals, such as stabilization, tracking and regulation.

Implementation of VSC involves high frequency switching. This is convenient for ASD-s, since the power inverters are, by nature, switching devices. Due to high frequency switching the system's states exhibit oscillations, known as chattering. This can excite unmodeled dynamics and represents the drawback of VSC. However, several methods to reduce the negative effects of chattering are available [25]-[27].

Despite of VSC popularity, few applications to induction machine sensorless drives have been reported [26]-[31]. Even fewer are directly related to DTC [32]-[33].

VSC principles

Let, a nonlinear and/or uncertain dynamic system, be described by the linear in the output model (7.23) that is convenient for induction machine control.

$$dx/dt = f(x,t) + B(x,t)u \tag{7.23}$$

where $x \in \Re^n$ is a $n \times 1$ state vector and $u \in \Re^r$ is a $r \times 1$ input vector and $\boldsymbol{B} \in \Re^{n \times r}$.

The design of VSC for this model consists of the following steps:

1. Determine a r-dimensional switching function $S(x)$, such that the system's trajectory (sliding mode) on the *switching surface*, $S(x) = 0$, is stable.
2. Determine a discontinuous control law

$$u(x) = \begin{cases} u^+(x) & when\ S(x) > 0 \\ u^-(x) & when\ S(x) < 0 \end{cases} \tag{7.24}$$

componentwise, such that the reaching condition $S \cdot dS/dt < 0$ is satisfied.

As a result, the closed loop system is globally stable. The system's response consists in 3 modes: the reaching mode, until the surface is reached, the sliding mode on the surface and the steady-state mode at the equilibrium point.

The state trajectory has the following attributes: Starting from any initial point x_0, the state x will move monotonically toward the surface and will reach it in finite time. Once the trajectory has crossed the switching surface for the first time, it will cross the surface regularly, resulting in zigzag motion about the surface. The size of each successive step is not increasing and the trajectory stays within a specified band.

The switching function design means finding a function that will give the desired dynamics. The most common choice for S is a linear, r-dimensional function

$$S = C^T x \tag{7.25}$$

The system's trajectory on the switching surface $S = 0$ can be determined using the equivalent control method [26]. The equivalent control, u_{eq}, is that linear control which determines the state trajectory to move along the switching surface S. This is found by recognizing that the sliding mode existence implies $S = 0$ and $dS/dt = 0$. Replacing in (7.23) and solving for u, that becomes u_{eq}, one gets

$$u_{eq} = -(C^T B(x,t))^{-1} C^T f(x,t) \tag{7.26}$$

where $C^T B(x,t)$ is assumed nonsingular for all x and t.

The system's dynamics on the sliding surface (in sliding mode) is given by

$$dx/dt = f_{sm}(x,t) = (I - B(x,t)(c^T B(x,t))^{-1} c^T) f(x,t) \tag{7.27}$$

The matrix c is designed such that (7.27) has the desired dynamics.

The motion on the surface is governed by a reduced order set of equations because of constrain $S(x) = 0$. This represents a system of r algebraic equations that can be solved with respect to r components of the state vector, in the form

$$x_2 = s_0(x_1) \tag{7.28}$$

where $x^T = [x_1^T \; x_2^T]$, and $x_1 \in \Re^{n-r}$, $x_2 \in \Re^r$ are subvectors of x.

Replacing x_2 by $s_0(x_1)$ in the first n-r equations of (7.27) gives a reduced order sliding mode equation with state x_1

$$dx_1/dt = f_{1sm}(x_1, s_0(x_1), t) \tag{7.29}$$

where $f_{sm}^T(x,t) = f_{sm}^T(x_1, x_2, t) = [f_{1sm}^T(x_1, x_2, t) \; f_{2sm}^T(x_1, x_2, t)]$

The motion equation (7.29) depends on function s_0, i.e. on the sliding surface equation. This function can be handled as r-dimensional control for the system (7.29).

The function S must be selected such that the sliding surface can be reached and the sliding mode evolution is stable. The condition under which the state will move toward the surface is the reaching condition. This is determined from Lyapunov stability theory (Appendix A). If $V = S \cdot dS/dt$ is a Lyapunov function candidate, then a global reaching condition is $dV/dt < 0$ when $S \neq 0$. If S is given by (7.25) with $\boldsymbol{C}$ constant, the reaching condition reduces to $S \cdot dS/dt < 0$. Finite reaching time is guarantied if the reaching condition is modified as $dV/dt < -\varepsilon$ when $S \neq 0$, $\varepsilon > 0$.

There are many other possibilities to select S. One of the most intersting is the reaching law method that specifies the dynamics of S in the form [23]

$$dS/dt = -Q\,\mathrm{sgn}(S) - KS \tag{7.30}$$

where $\boldsymbol{Q}$ and $\boldsymbol{K}$ are diagonal matrices with positive elements.

The reaching law (7.30) not only establishes the reaching condition, but also specifies the dynamic behavior of the system during the reaching phase [23].

The second phase in VSC design is the control law design. Here, the goal is to determine the switched feedback gains that will drive the state trajectory on the sliding surface and will maintain the sliding mode condition.

In many cases, it is convenient to predefine the structure of VSC and then to determine the controller gains, such that the desired reaching law is satisfied.

The most popular predefined VSC laws are [22], [23]:

1. Relays with Constant Gains - RCG

$$u_i(x) = K_i \operatorname{sgn}(s_i(x)) \tag{7.31}$$

2. Linear Feedback with Switched Gains - LFSG

$$u_i(x) = K_i x \operatorname{sgn}(s_i(x) \cdot x) \tag{7.32}$$

3. Linear and discontinuous feedback

$$u_i(x) = u_{eq} + K_i \operatorname{sgn}(s_i(x)) \tag{7.33}$$

4. Linear continuous feedback

$$u_i(x) = K_i s_i(x) \tag{7.34}$$

where, in all cases, s_i, $i = 1, 2, ..., r$ are components of $S = [s_1(x)\ s_2(x) \dots s_r(x)]^T$ and $K_i < 0$ is determined from the reaching condition.

Other methods to select the control law, which do not employ a predefined VSC scheme, described in literature are: diagonalization method, control hierarchy method, integral sliding mode, [22]-[26].

In order to reduce the chattering, a boundary layer can be introduced by replacing the sign function with the saturation function (5.45). Outside the layer the control is VSC, while within the layer, the control is a high gain linear control.

Robustness is one of the most distinguishing properties of variable structure systems. For a system in sliding mode, the equation (7.27) can be entirely independent of modeling errors and external disturbances. In this case, the VSC is *invariant* to modeling uncertainties and disturbances. The invariance property requires certain matching conditions to be satisfied. Consider the system (7.35) in the form

$$dx / dt = f(x,t) + B(x,t)u + \Delta f(x,t) \tag{7.35}$$

where Δf represents the cumulated effects of all modeling errors and disturbances.

The sliding mode is invariant if there exist $g(x,t)$, such that (7.36) is satisfied.

$$\Delta f(x,t) = B(x,t)g(x,t) \tag{7.36}$$

The physical meaning of this condition is that all uncertainties and disturbances must enter the system through the control channel [23].

VSC and DTC – Existing solutions

Recognizing that the VSI is a device that changes the structure of its electrical circuit with high switching frequency, it appears natural to regard the drive control from a VSC perspective. The best example is represented by the classical DTC itself that is, precisely, a VSC system, excellently designed to cope with the eight-state discrete nature of the VSI [32], [33].

In DTC, the sliding surface is $S = [e_{Te}\ e_{\psi s}]^T$ and the control quantities are the eight available voltage vectors. Another solution, proposed in [26]-[27], employs the flux and speed errors to construct the sliding surface

$$S = [e_{\psi s} + s e_{\psi s} \quad e_{\omega r} + s e_{\omega r} \quad (u_a + u_b + u_c)/s]^T \tag{7.37}$$

where $e_{\omega r} = \omega_r^* - \hat{\omega}_r$, u_a, u_b, u_c are motor phase voltages and s is the Laplace operator.

The motor is directly controlled, without PWM, by using the control law

$$u_{si} = u_0 \operatorname{sgn}(s_i^*) \qquad i = a, b, c \tag{7.38}$$

where $S^* = [s_a^*\ s_b^*\ s_c^*]^T = DS$, with matrix $\boldsymbol{D}$ adequately designed to drive the motor states onto S and $u_0 = 2V_{dc}/3$. The implementation of this scheme is presented in [29] where low speed steady-state sensorless operation at 19 rpm is reported.

A very similar solution, which also resembles much to DTC, employs the same control law (7.38) and a sliding surface based on torque and flux errors [28]

$$S = [e_{Te} \quad e_{\psi s} + s e_{\psi s} \quad (u_a + u_b + u_c)/s]^T \tag{7.39}$$

Sensorless speed control at 300rpm, continuous operation is reported in [28]. The torque control and dynamic response is good, but the torque ripple is quite large, because voltage vectors are applied without PWM, as in DTC.

A complete VSC solution is presented in [33] where the classical DTC is employed for torque and flux control and VSC is used for speed control. Low speed performance was obtained, but the speed exhibits rather large chattering.

Several new Variable Structure DTC (VSC-DTC) solutions are presented in the following sections. These schemes are VSC realizations of the Linear-DTC.

7.4.2 Relays with Constant Gains

The Linear-DTC achieves good torque and flux control with very low torque and current ripple. It preserves the DTC fast torque response and implementation simplicity. However, the robustness in face of perturbations and model uncertainties is not implicitly guarantied, due to linear controllers.

A class of Variable Structure Controllers that follow the Linear-DTC principles has been developed. It is based on predefined control laws, enhanced with PI control and SVM, in order to obtain low torque ripple and constant switching frequency.

The first control law is *Relays with Constant Gains - Direct Torque Control* (RCG Control). Its block diagram is depicted in Figure 7.14.

The sliding surface is defined as $S = s_{\psi s} + j s_{Te}$ where

$$s_{\psi s} = e_{\psi s} + c_{\psi s} de_{\psi s} / dt \tag{7.40a}$$

$$s_{Te} = e_{Te} + c_{Te} de_{Te} / dt \tag{7.40b}$$

where $c_{\psi s}$ and c_{Te} are design constants and $e_{\psi s}$ and e_{Te} are the flux and torque errors.

The control law produces the reference voltage vector $\underline{u}_s^* = u_{sd}^* + j u_{sq}^*$

$$u_{sd}^* = (K_{P\psi} + K_{I\psi} \frac{1}{s}) \operatorname{sgn}(s_{\psi s}) \tag{7.41}$$

$$u_{sq}^* = (K_{PT} + K_{IT} \frac{1}{s}) \operatorname{sgn}(s_{Te}) + \hat{\omega}_{\psi s} \hat{\psi}_s \tag{7.42}$$

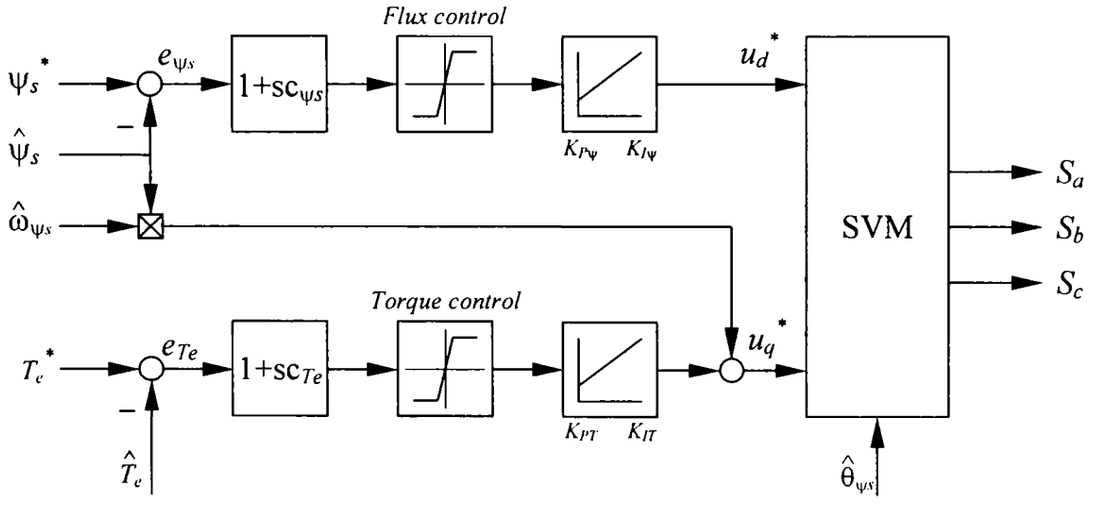

Figure 7.14 Relays with Constant Gains - Direct Torque Control block diagram

The reference voltage vector is applied to SVM, in the same way as for Linear–DTC. Since u_s^*, given by (7.41)-(7.42), is in stator flux reference frame, it is transformed to stator frame, $\underline{u}_s^{s*} = \underline{u}_s^* e^{j\hat{\theta}_{ws}}$. Next, the SVM unit receives $\underline{u}_s^{s*}$ and generates the VSI switching signals S_a, S_b and S_c.

The control law contains a discontinuous part followed by a linear PI controller. This combination allows obtaining a good balance between linear behavior, specific to Linear-DTC and switching behavior, specific to DTC. In particular, by proper choice of parameters K_P and K_I, the torque ripple can be maintained low, while the dynamic performance is not compromised. It was determined from experiments that the best approach is to increase K_P until the torque ripple attains an upper limit and, then, to modify K_I such that the desired dynamic response is obtained.

In order to further reduce the chattering, a boundary layer was implemented by replacing the sign function with the saturation function (5.45). Inside the layer the controller becomes high gain Linear-DTC and the error is driven toward zero by the PI controllers. Outside the layer, the system exhibits discontinuous behavior.

The system's robustness is improved by increasing the PI gains. Once more, an adequate tradeoff between low torque ripple and high gain requirement must be found. The presence of SVM offers a certain degree of flexibility from this point of view.

Experimental results

The generic *Variable Structure Direct Torque Control* (VSC-DTC) sensorless drive block diagram is represented in Figure 7.15. Similarly to Linear-DTC scheme, the VSC&SVM block may incorporate any of the VSC strategies presented in this section. The flux observer can be either the inherent sensorless Luenberger observer described in Figure 4.7, or the SMO from Figure 5.1. All sub-variants of the basic observer schemes are also valid. The speed observer is the PLL observer from Figure 6.3 and the torque is calculated with (6.7).

The VSC-DTC uses the standard SVM scheme, Table 3.1, with DTC dynamic OVM from Figures 3.12 and 3.13, and dead time compensation strategy (3.46). The motor is Machine 2 (P_N=1.1 kW, T_{eN}=7 Nm, Appendix B). The system employs stator and rotor resistances estimation and adaptation, (4.61) and (6.37).

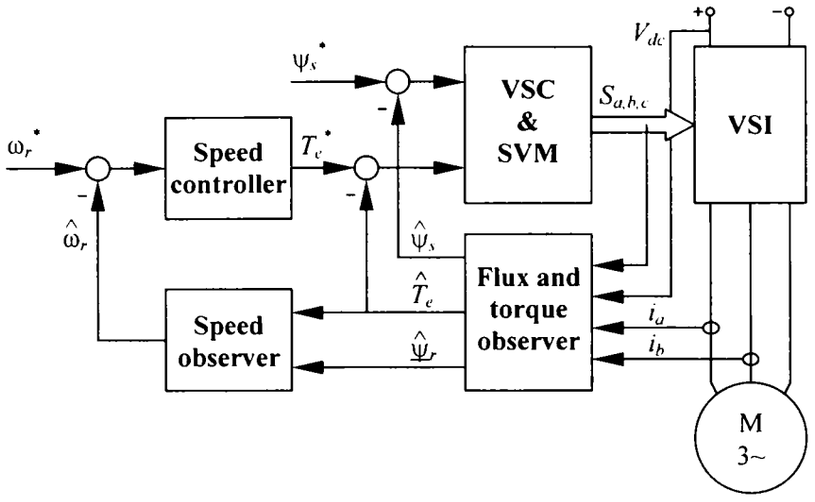

Figure 7.15 Variable Structure Direct Torque Control sensorless drive

Zero speed, full load, sensorless operation with RCG Control and modified SMO (SMO with offset compensation) is presented in Figures 7.16 and 7.17. Figure 7.16 shows the speed, torque and flux magnitude, while Figure 7.17 shows the instantaneous waveforms of current and stator flux. Similar operation at zero speed, with Luenberger observer, was shown in Figure 4.18. In both cases the speed control is very good and the torque and current ripple is small.

Sensorless operation at 3 rpm, full load, with the same system, is demonstrated in Figure 7.18. At this time the torque and current ripple is higher, but the low speed performance is excellent. Partly, the torque ripple is due to parasitic torques introduced by the DC generator used to load the induction machine.

Low speed reversal with RCG Control was presented in Figures 6.8 and 6.9. In this case, the machine was operated as motor and generator at 6 rpm, under full load. The system's behavior is also very good, although the speed and torque ripple increases as much as the stator frequency decreases.

A problem, associated to RCG, is the flux ripple. Compared to other VSC-DTC strategies proposed herewith, this method produces the highest flux ripple. However, this torque ripple is much smaller than that obtained with classical DTC. Oscillations and a certain lack of robustness on the flux channel have been observed during torque and speed transients, for example, in Figure 6.10 that shows acceleration transients with RCG Control. On the other hand, the dynamic torque behavior is very good.

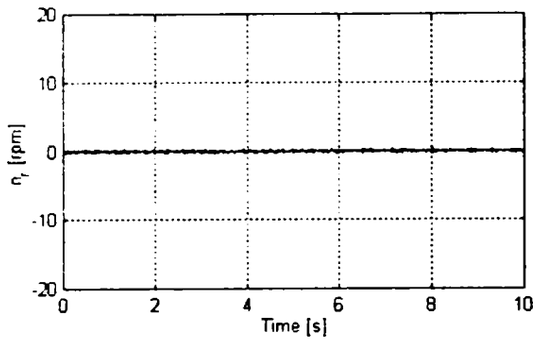

a. Estimated rotor speed

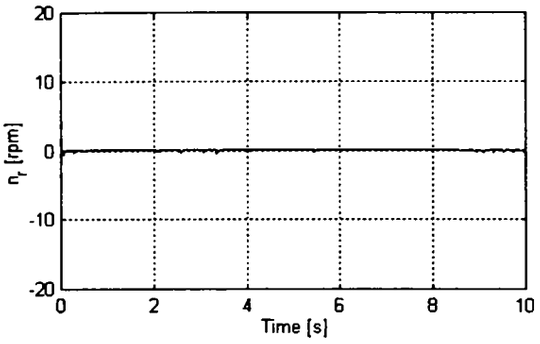

b. Measured rotor speed

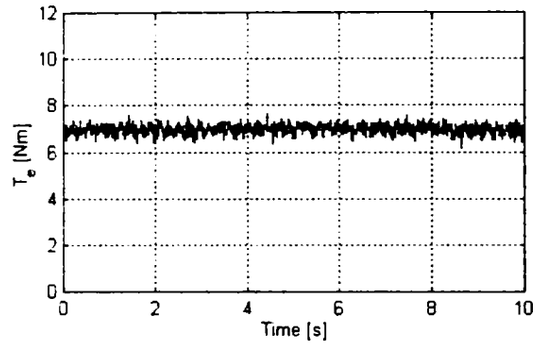

c. Estimated torque

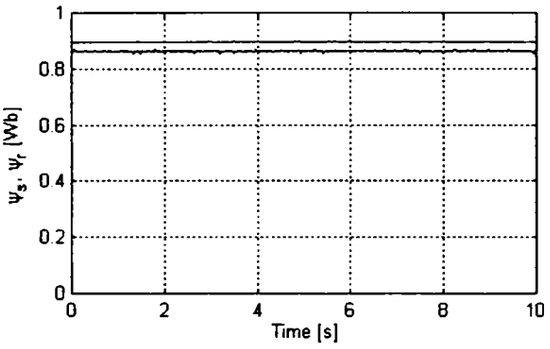

d. Estimated stator and rotor flux

Figure 7.16 Zero speed sensorless operation with RCG Control and modified SMO

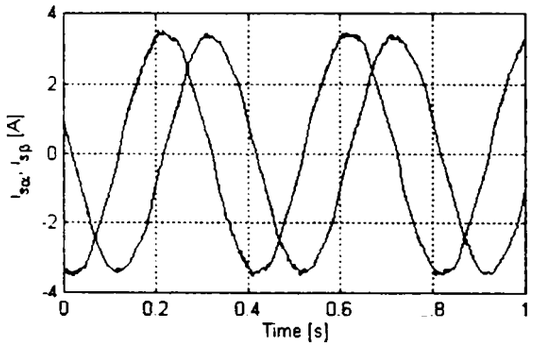

a. Measured (α,β) stator currents

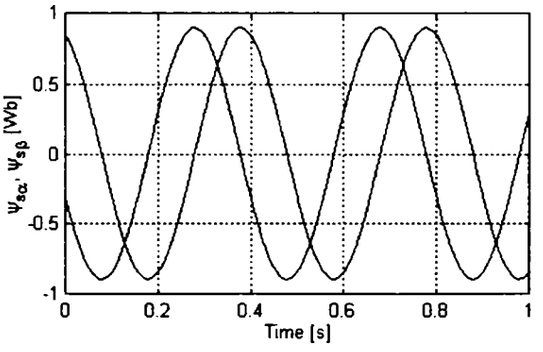

b. Estimated (α,β) stator flux

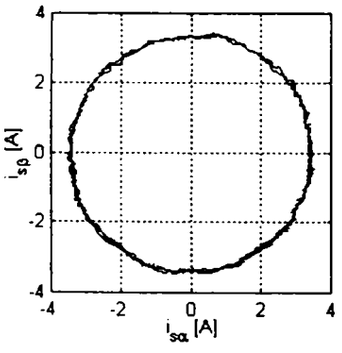

c. Measured current trajectory

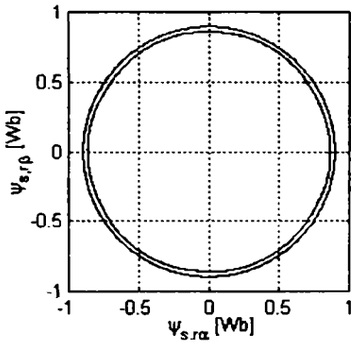

d. Estimated stator and rotor flux trajectory

Figure 7.17 Current and flux during zero speed operation with RCG and modified SMO

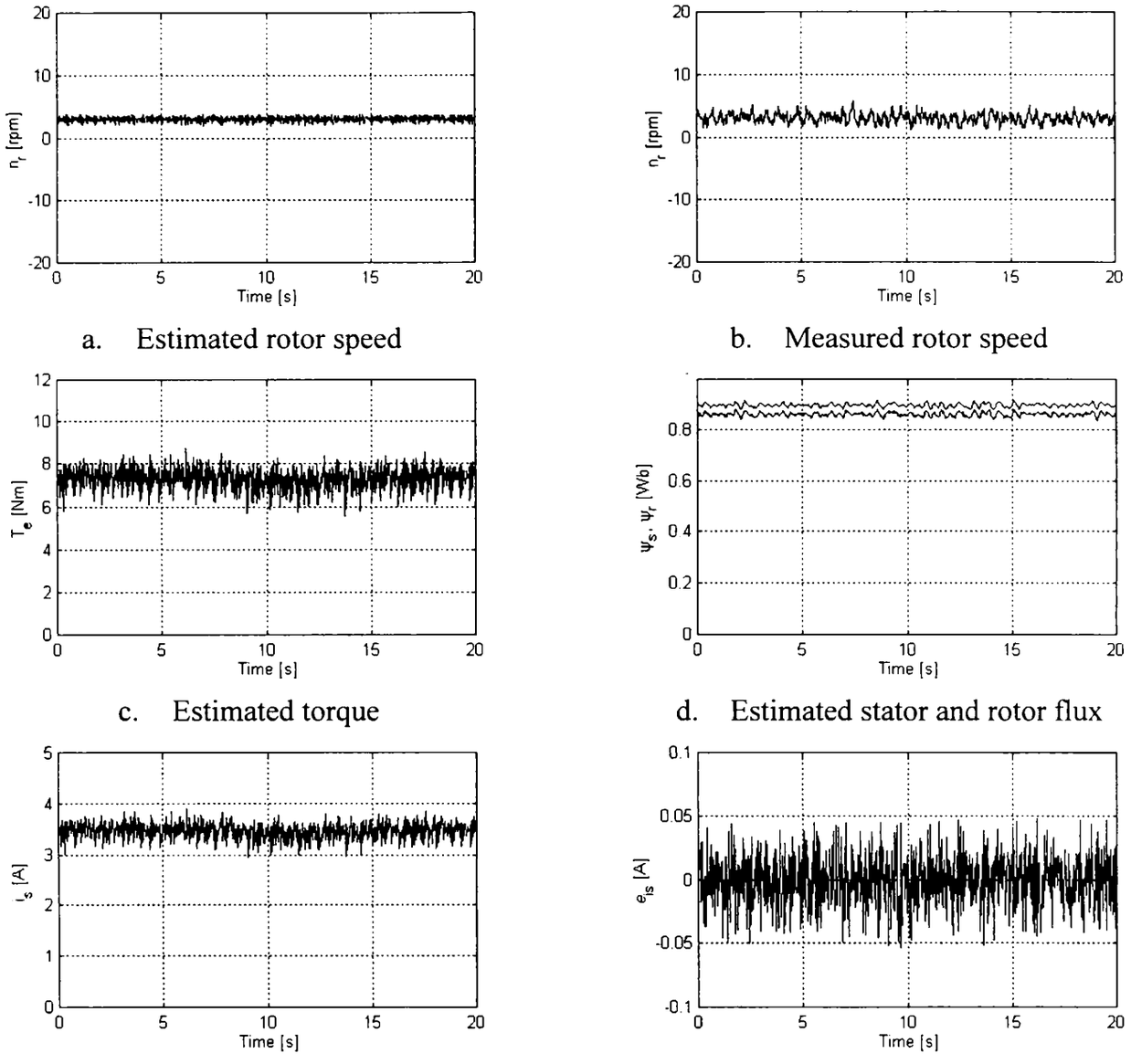

Figure 7.18 Very low speed sensorless operation with RCG Control and modified SMO

Torque transients with RCG Control, during acceleration from standstill, are presented in Figure 7.19 for larger PI gains and in Figure 7.20 for smaller PI gains. In both cases, the flux observer is the generalized SMO from Figure 5.2. A reference torque step of 12 Nm (T_{eN}=7 Nm) is applied at t=10 ms.

With high gains, the reference torque is reached in more than 2 ms and the torque ripple is large. With low gains the reference is reached in more than 4 ms and the torque ripple is small. These times are longer than those obtained with DTC or Linear-DTC and there is no torque overshot. In both cases, the stator flux shows low sensitivity to torque transients and the rotor flux exhibits some oscillations.

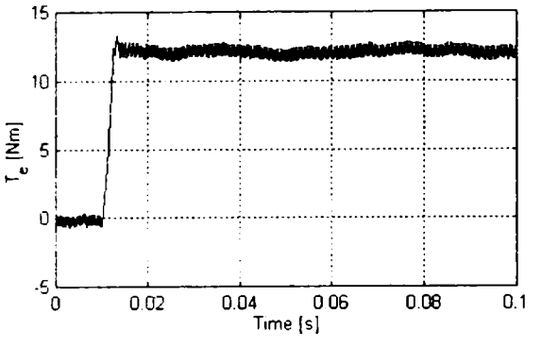

a. Estimated torque – RCG

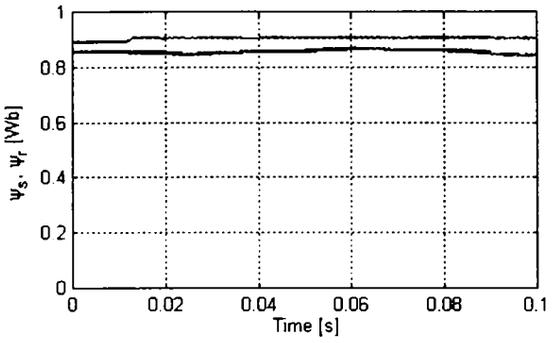

b. Estimated stator and rotor flux

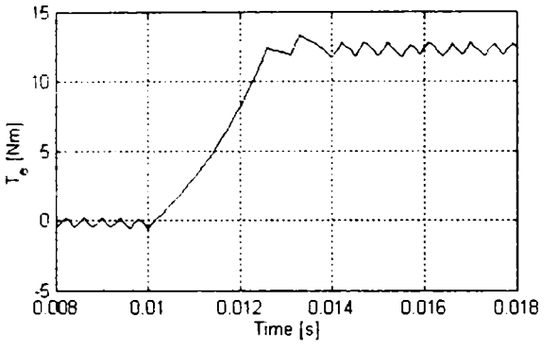

c. Estimated torque – time zoom

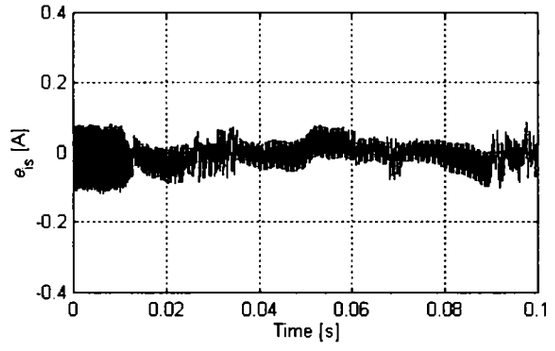

d. Current estimation error

Figure 7.19 Torque transients with RCG Control and generalized SMO – high gains

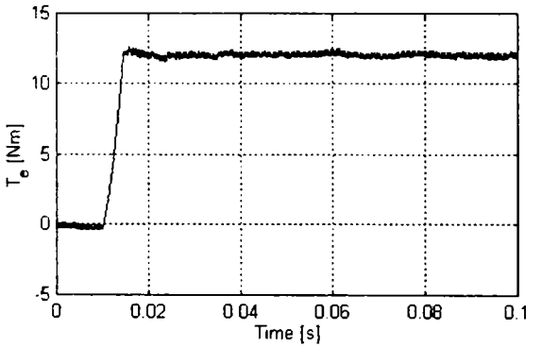

a. Estimated torque – RCG

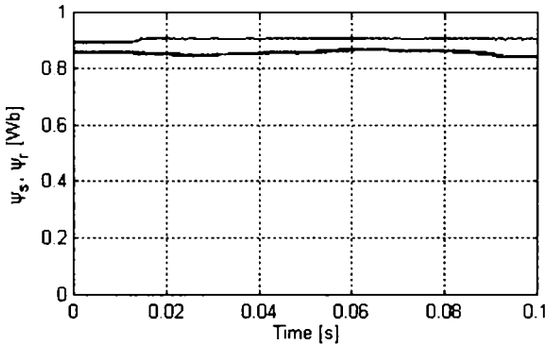

b. Estimated stator and rotor flux

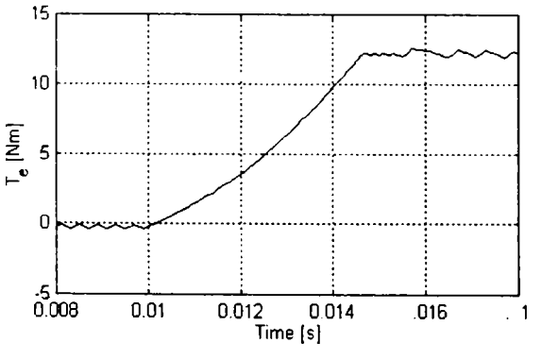

c. Estimated torque – time zoom

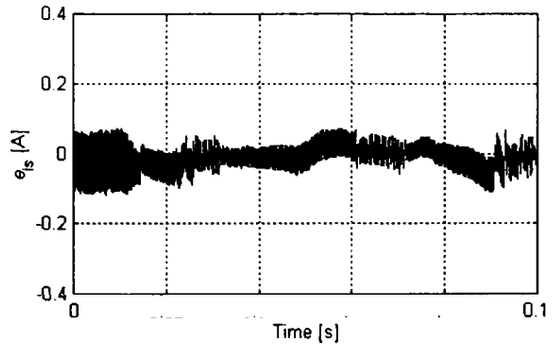

d. Current estimation error

Figure 7.20 Torque transients with RCG Control and generalized SMO – low gains

7.4.3 Linear Feedback with Switched Gains

The RCG Control exhibits the characteristic behavior of a VSC system. The torque chattering is moderate, but the torque response is not as fast as in the case of DTC. It is of interest to find a control strategy that operates with lower chattering.

The *Linear Feedback with Switched Gains Direct Torque Control* (LFSG) is the second VSC-DTC strategy proposed. Its block diagram is represented in Figure 7.21.

The sliding surface $S = s_{\psi s} + j s_{Te}$ is the same as for RCG Control, defined in (7.40). The design constants $c_{\psi s}$ and c_{Te} are selected relatively small, not to amplify the high frequency noise content of flux and torque.

The LFSG control law produces the reference voltage vector $\underline{u}_s^* = u_{sd}^* + j u_{sq}^*$ in stator flux reference frame

$$u_{sd}^* = (K_{P\psi} + K_{I\psi}\frac{1}{s}) e_{\psi s}\,\mathrm{sgn}(e_{\psi s} s_{\psi s}) \tag{7.43}$$

$$u_{sq}^* = (K_{PT} + K_{IT}\frac{1}{s}) e_{Te}\,\mathrm{sgn}(e_{Te} s_{Te}) + \hat{\omega}_{\psi s}\hat{\psi}_s \tag{7.44}$$

where gains K_P and K_I of both controllers are selected such that the system is stable. In this case, a large enough K_P will accomplish that.

The reference voltage is transformed to stator frame, $\underline{u}_s^{s*} = \underline{u}_s^* e^{j\hat{\theta}_{\psi s}}$ and $\underline{u}_s^{s*}$ is realized by SVM that produces the VSI switching signals S_a, S_b, S_c.

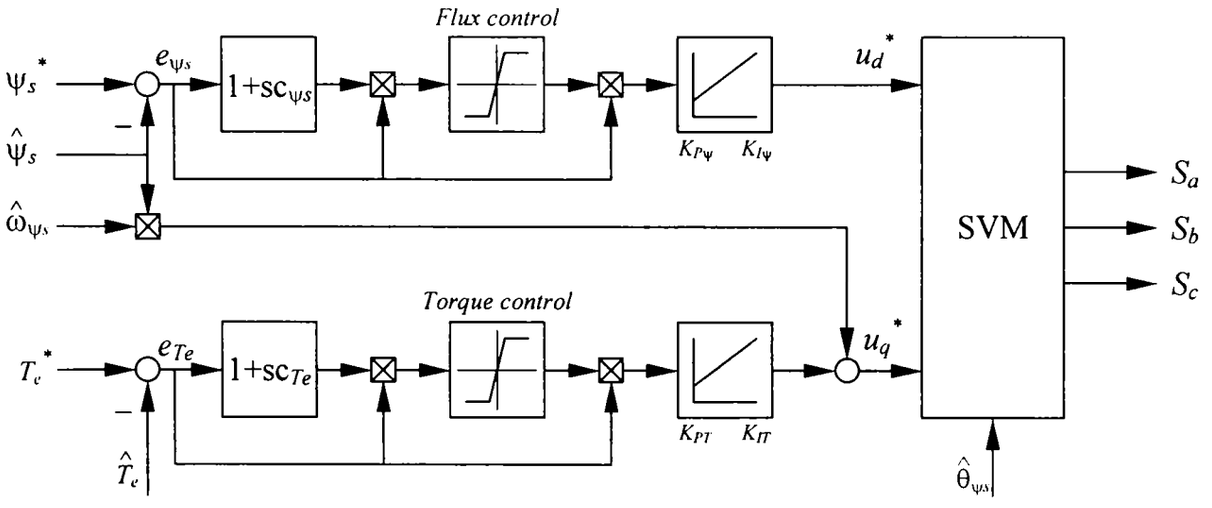

Figure 7.21 Linear Feedback with Switched Gains - Direct Torque Control block diagram

The LFSG controller resembles very much to Linear-DTC. The flux and torque errors can be regarded as inputs, while the sign functions only control the PI gains signs. Hence, the "switched gains" attribute has an explanation. The LFSG controller is expected to behave similar to a linear controller when the torque and flux errors are small and to exhibit switching behavior for large errors.

Similarly to RCG Control, in order to reduce the chattering, a boundary layer was implemented by replacing the sign function with the saturation function (5.45). Inside the layer the controller becomes high gain Linear-DTC and the error is driven toward zero by the PI controllers. Outside the layer, the control system has discontinuous behavior.

Experimental results

The LFSG sensorless drive implementation is based on the generic block diagram from Figure 7.15. The "VSC&SVM" block includes the LFSG control from Figure 7.21, while the state observer is one of the SMO-s presented in Chapter 5. The motor under test is Machine 2 (P_N=1.1 kW, T_{eN}=7 Nm, Appendix B).

Extensive experiments have been carried out at low and high speeds in order to demonstrate the validity of this sensorless scheme. Simulations have been also carried out. Since simulations and experiments are very similar, only the most important experimental results are presented herewith.

All experiments presented in Chapter 5 have been obtained with LFSG and various SMO-s. Most of those results show the low speed steady state performance. Figures 5.10, 5.11, 5.13, 5.16 and 5.17 show zero speed sensorless operation, while Figures 5.14, 5.15 and 5.18 demonstrate sensorless operation at 3 rpm, full load, all with LFSG control. In all cases, the low speed performance is evident.

Startup transients to 1500 rpm, sensorless operation, with LFSG and SMO are presented in Figure 7.22. The motor is accelerated at 12 Nm constant torque, almost twice its rated torque, but the acceleration time is quite long, since the motor was connected to a DC generator with very large inertia rotor. The steady state torque oscillations at high speeds are due to DC generator parasitic torques. The torque controller produces very small oscillations, as can be seen when the torque is 12 Nm.

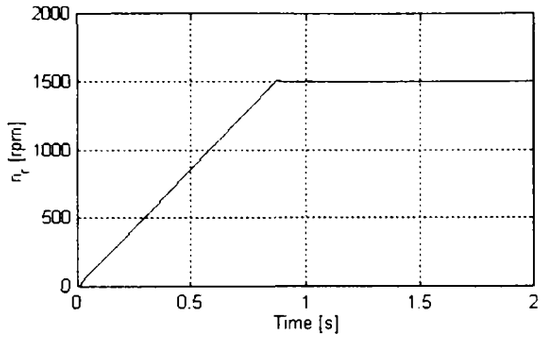

a. Estimated rotor speed

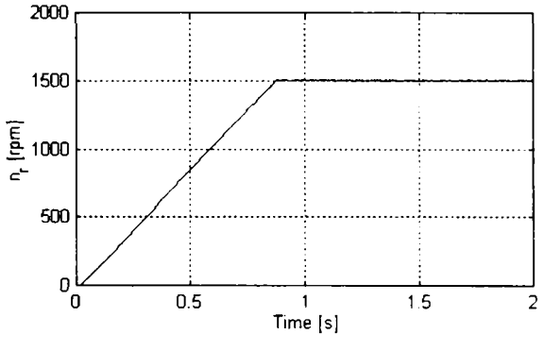

b. Measured rotor speed

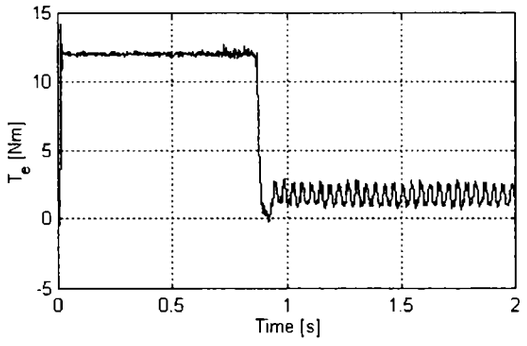

c. Estimated torque

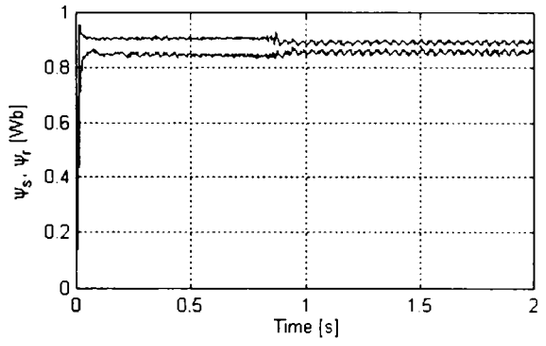

d. Estimated stator and rotor flux

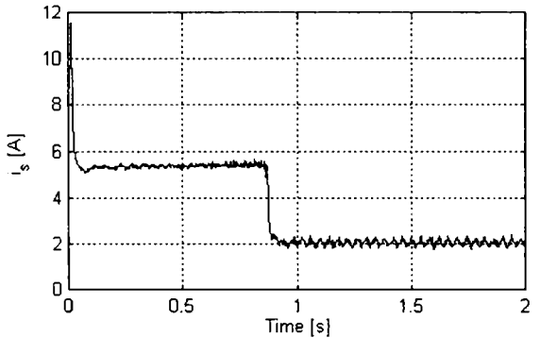

e. Estimated stator current magnitude

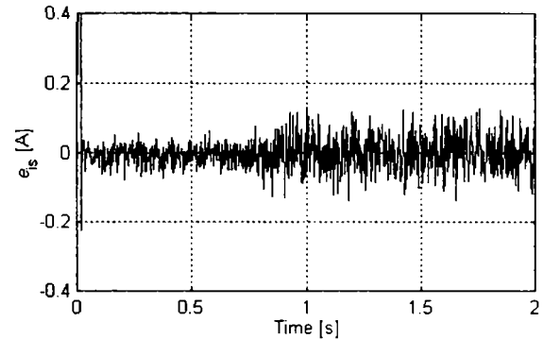

f. Stator current estimation error

Figure 7.22 Starting transients to 1500 rpm, with LFSG and SMO

At high speed, the flux exhibits small ripple. The same problem is noticeable in Figure 5.19 that shows a similar startup, with generalized observer instead of SMO. In both cases, however, the torque and flux control is excellent.

If compared to RCG Control, the LFSG flux control is more robust. For example, similar acceleration transients, from standstill to 1500 rpm, are shown in Figure 5.12 with LFSG and in Figure 6.10 with RCG Control. The flux control is fast and robust in the former case and rather sensitive to torque and speed transients in the later.

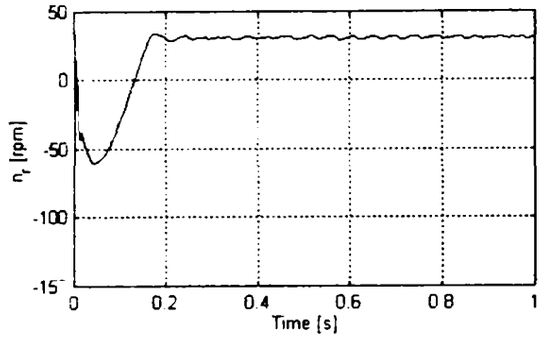

a. Estimated rotor speed

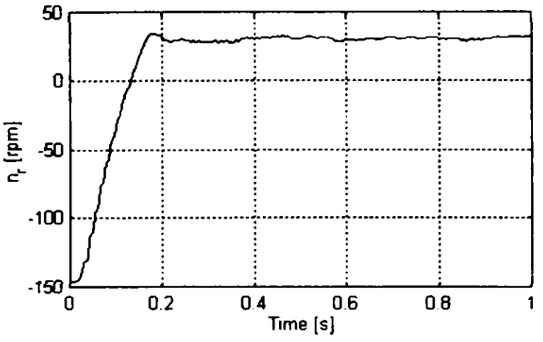

b. Measured rotor speed

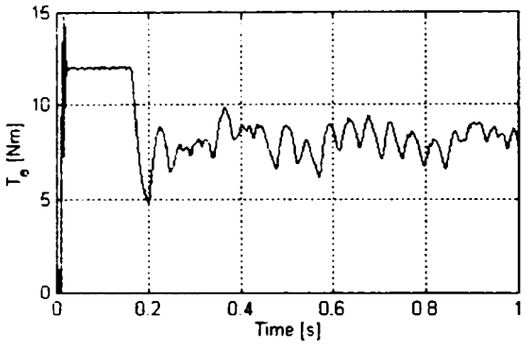

c. Estimated torque

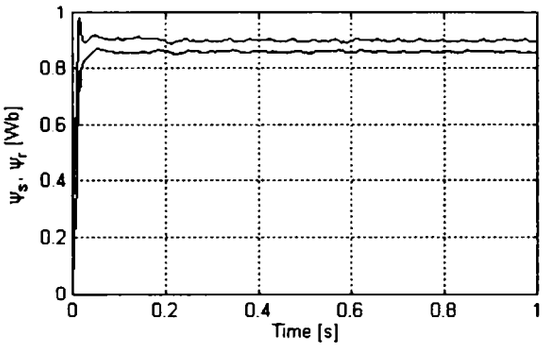

d. Estimated stator and rotor flux

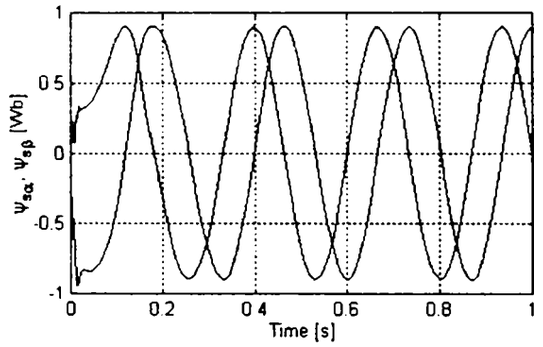

e. Estimated stator flux

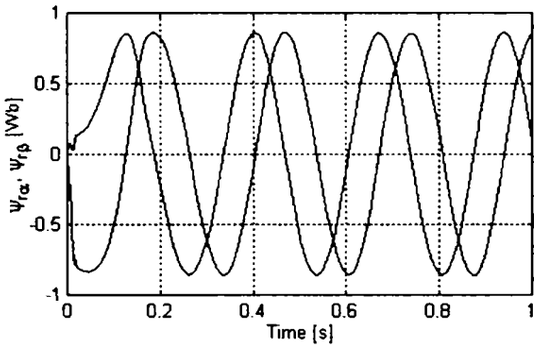

f. Estimated rotor flux

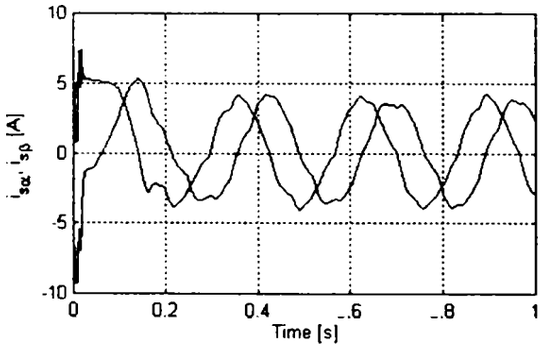

g. Measured stator current magnitude

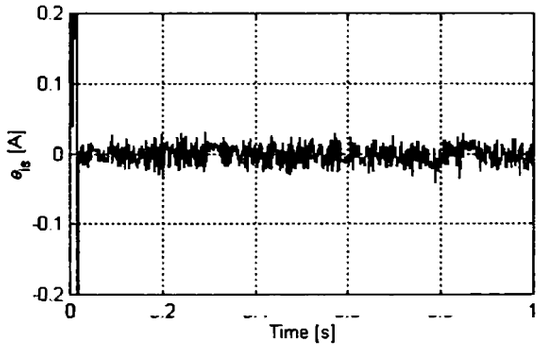

h. Stator current estimation error

Figure 7.23 Startup on-the-fly transients to 30 rpm, with LFSG and generalized observer

Figure 7.23 demonstrates the startup on-the-fly capability of the drive. Initially, the DC machine rotates the motor at negative speed. At t=0 s, the drive control system

is started, with 30 rpm speed reference. The flux and torque are fast installed and the PLL speed observer "captures" the rotor speed in 0.1s. In less than 0.2 s the induction machine runs at 30 rpm, full load. The current error indicates that the generalized state observer reaches sliding mode in about 10 ms. Thus, the stator frequency and all electromagnetic quantities are correctly detected after this time. Flux transients shown in Figure 7.23.d,e,f demonstrate the flux controller capability. The flux is fast installed and firmly maintained. The torque pulsations are due to parasitic torque produced by the DC machine.

Torque transients with LFSG, during acceleration from standstill, are presented in Figure 7.24 A reference torque step of 12 Nm (T_{eN}=7 Nm) is applied at t=10 ms. The first torque peak reaches 12 Nm in less than 1 ms. In the next millisecond the torque pulsations attenuate and the steady state operation is without torque ripple. It is evident that for large torque errors the controller has switching behavior, like DTC, while in steady state it exhibits ripple free behavior, like Linear-DTC. The flux control is also good and the stator flux shows low sensitivity to torque transients, comparable to that of the Linear-DTC. The state observer is also very robust to torque transients.

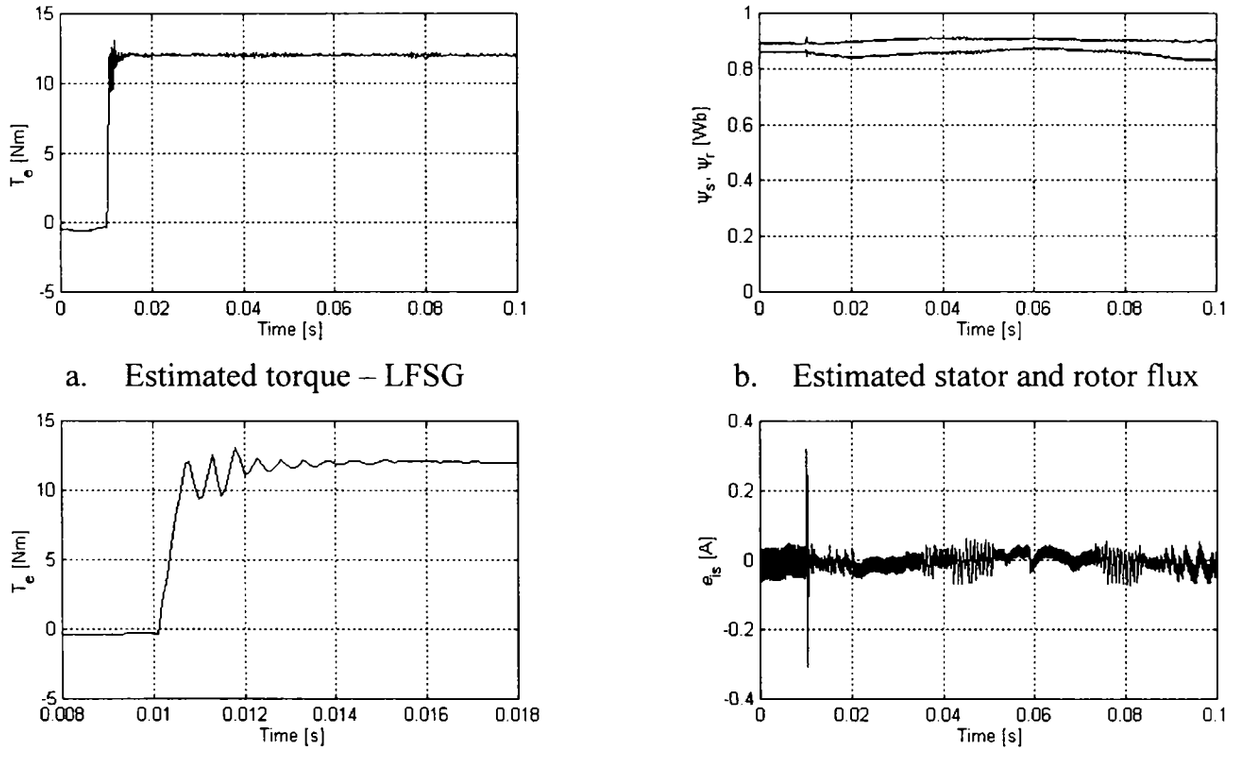

a. Estimated torque – LFSG

b. Estimated stator and rotor flux

c. Estimated torque – time zoom

d. Current estimation error

Figure 7.24 Torque transients with LFSG control and generalized observer

7.4.4 Linear and Discontinuous Feedback

The third VSC-DTC strategy is *Linear and Discontinuous Feedback Direct Torque Control* (Linear-VSC). Like LFSG, this is a combination between Linear-DTC and VSC that attempts to take advantage of the best features of these two strategies. Its block diagram is represented in Figure 7.25.

The sliding surface $S = s_{\psi s} + j s_{Te}$ is the same as for RCG Control and LFSG, as defined by (7.40). The design constants $c_{\psi s}$ and c_{Te} are selected relatively small.

The Linear-VSC control law produces the reference stator voltage vector $\underline{u}_s^* = u_{sd}^* + j u_{sq}^*$, in stator flux reference frame

$$u_{sd}^* = (K_{P\psi} + K_{I\psi}\frac{1}{s})(e_{\psi s} + K_{VSC\psi}\,\mathrm{sgn}(s_{\psi s})) \tag{7.45}$$

$$u_{sq}^* = (K_{PT} + K_{IT}\frac{1}{s})(e_{Te} + K_{VSCT}\,\mathrm{sgn}(s_{Te})) + \hat{\omega}_{\psi s}\hat{\psi}_s \tag{7.46}$$

where gains K_P and K_I are selected in the same way as for Linear-DTC.

In particular, K_P and K_I of both controllers are selected such that the linear part of the controller gives adequate dynamic response. An additional gain, K_{VSC}, has been used for the discontinuous part of both controllers. Modifying K_{VSC} allows finding a good balance between linear behavior and VSC behavior. With K_{VSC} large enough, the system works as a VSC, while small or zero K_{VSC} leads to linear behavior.

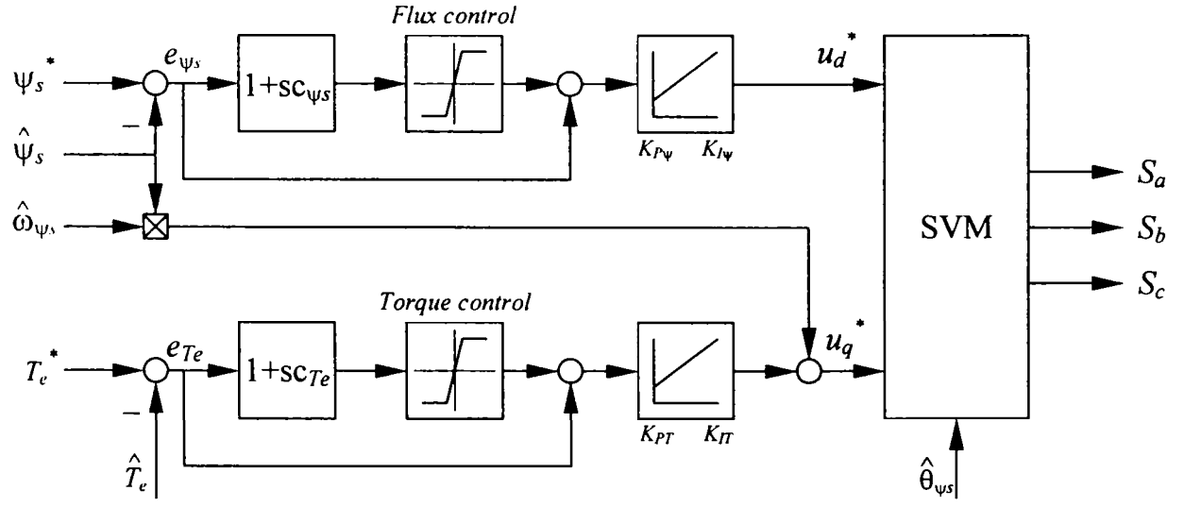

Figure 7.25 Linear and Discontinuous Feedback - Direct Torque Control block diagram

The separation between these two modes, linear and discontinuous, is evident from (7.45)-(7.46). During transient operation, the torque and flux errors are large and the linear PI component action is strong. In steady state, the discontinuous mode is dominant and switching behavior is obtained. This situation is the opposite of the one in the LFSG case. This scheme has the advantage that the two modes can be easily balanced by modifying the PI and VSC gains.

The reference voltage is transformed to stator frame, $\underline{u}_s^{s*} = \underline{u}_s^* e^{j\hat{\theta}_{\psi_s}}$, and $\underline{u}_s^{s*}$ is realized by means of SVM, which produces the VSI switching signals S_a, S_b, S_c. The DTC enhanced overomodulation from Figure 3.13, is employed whenever the reference voltage is too large to be realized by linear modulation.

Similarly to LFSG, in order to reduce the chattering, a boundary layer was introduced, by replacing the sign function with the saturation function (5.45). Inside the layer the VSC becomes high gain Linear-DTC and the error is driven toward zero by the PI controllers. Outside the layer, the system exhibits discontinuous behavior.

Experimental results

The Linear-VSC sensorless drive realization is based on the generic block diagram from Figure 7.15. The "VSC&SVM" block includes the Linear-VSC control from Figure 7.25, while the state observer is one of the SMO-s presented in Chapter 5. The motor under test is Machine 2 (P_N=1.1 kW, T_{eN}=7 Nm, Appendix B).

Experimental results with Linear-VSC are presented in Figures 4.26 to 4.28. These figures show steady state operation at zero speed, reversal at 6 rpm and startup transients, all obtained with modified voltage model flux estimator. The Linear-VSC is able to sustain zero speed, full load operation with any linear or nonlinear state observer, presented in Chapters 4 and 5.

Very low speed sensorless operation at 3 rpm, full load, with Linear-VSC and modified SMO are presented in Figures 7.26 and 7.27. Compared to all other methods, Linear-VSC exhibits the best low speed behavior. However, only minor differences exist. As demonstrated, all control methods are capable to run at 0 rpm and 3 rpm, under full load, for an undetermined period. The current estimation error is very low and the instantaneous current is not too much distorted, Figure 7.27.

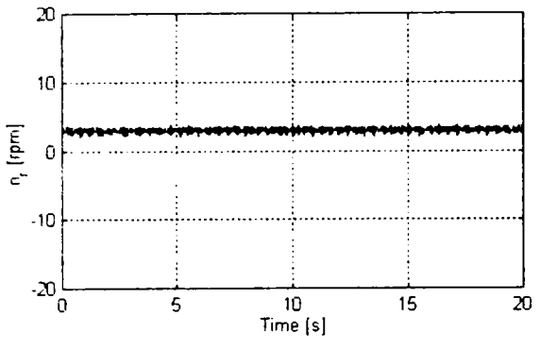

a. Estimated rotor speed

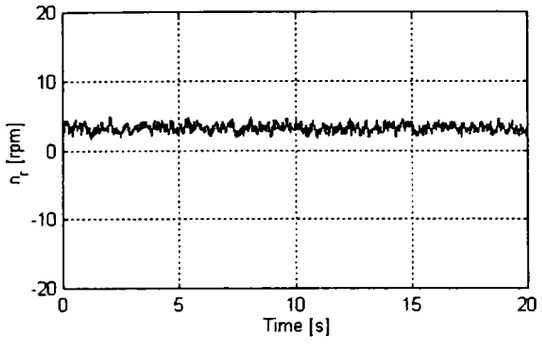

b. Measured rotor speed

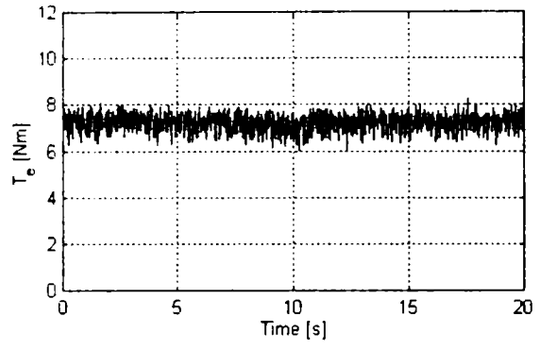

c. Estimated torque

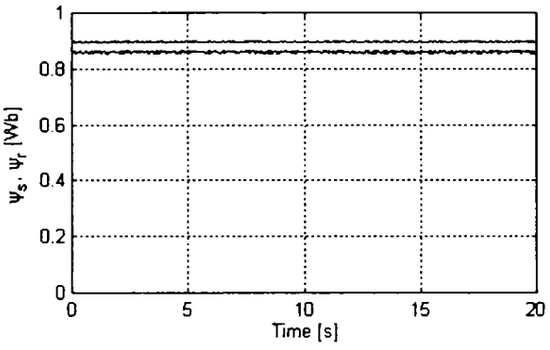

d. Estimated stator and rotor flux

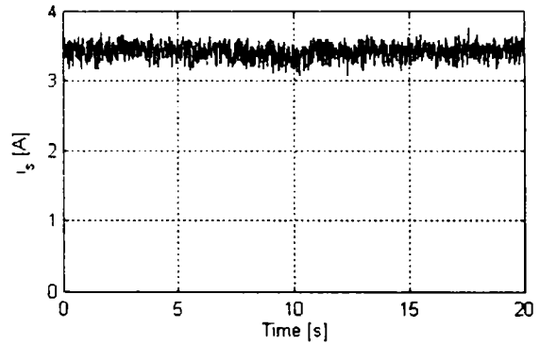

e. Estimated stator current magnitude

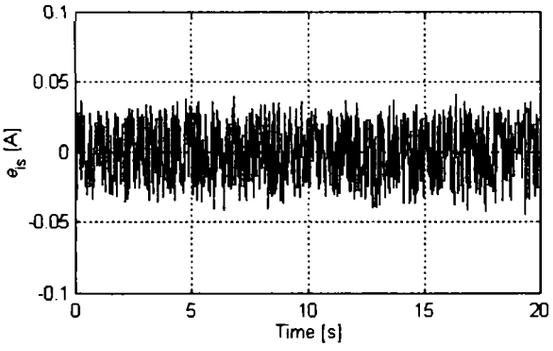

f. Stator current estimation error

Figure 7.26 Very low speed sensorless operation with Linear-VSC and modified SMO

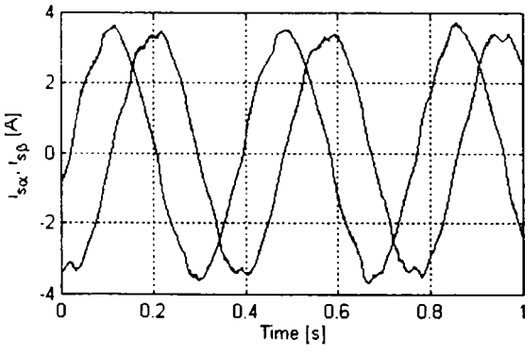

a. Estimated (α,β) stator current

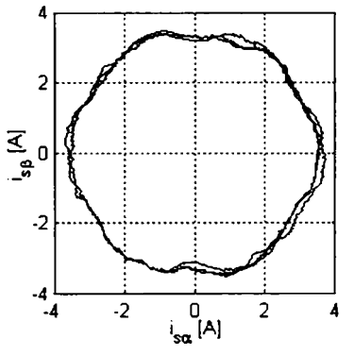

b. Estimated current trajectory

Figure 7.27 Estimated instantaneous stator current during 3 rpm sensorless operation with Linear-VSC and modified SMO

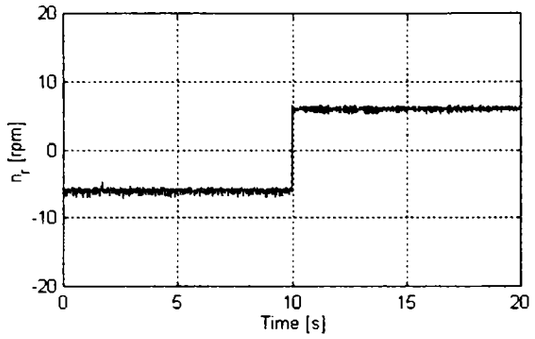

a. Estimated rotor speed

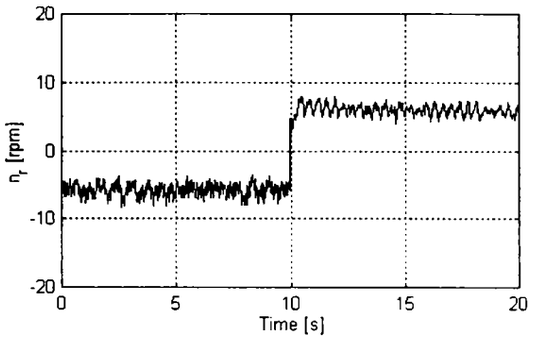

b. Measured rotor speed

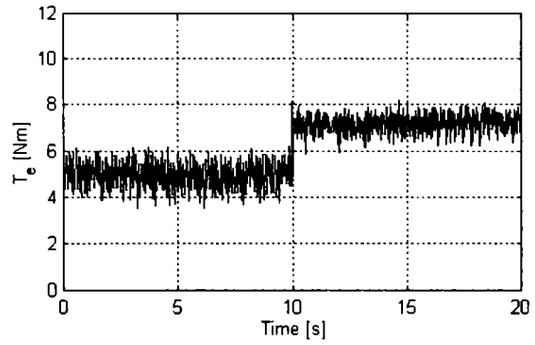

c. Estimated torque

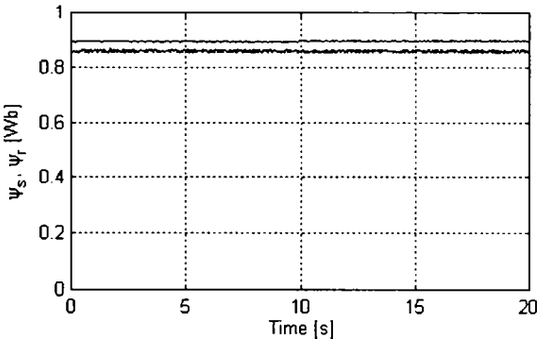

d. Estimated stator and rotor flux

Figure 7.28 Sensorless operation at ±6rpm and reversal under full load, with Linear-VSC

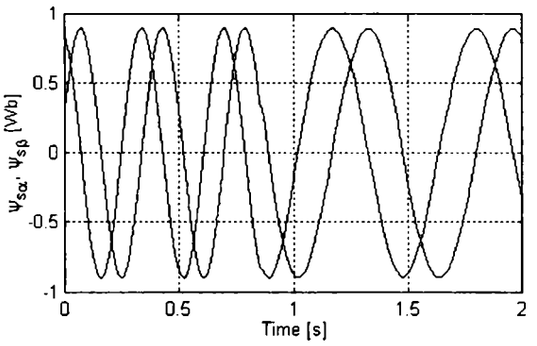

a. Estimated (α,β) stator flux

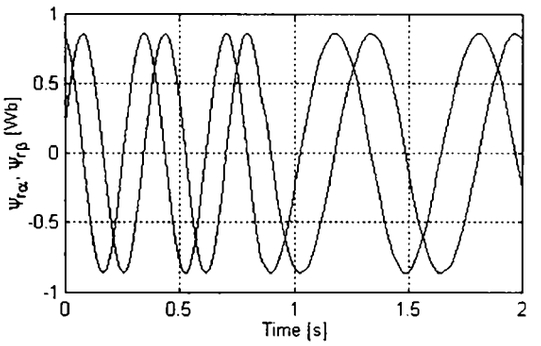

b. Estimated (α,β) rotor flux

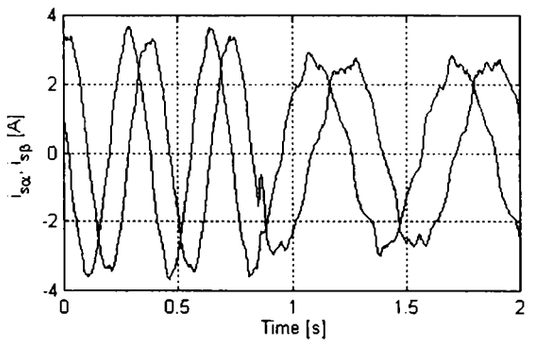

a. Estimated (α,β) stator current

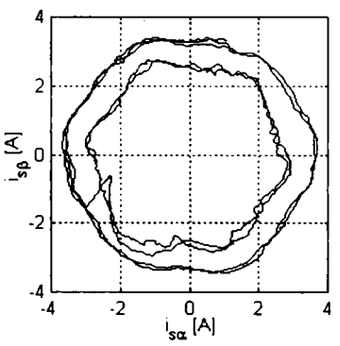

b. Estimated current trajectory

Figure 7.29 Estimated stator flux, rotor flux and current during reversal from +6rpm to –6 rpm, in full load sensorless operation, with Linear-VSC

Very low speed reversal, with the same control system, is presented in Figure 7.28. In this case, regenerative and motoring sensorless operation at 6 rpm, full load is demonstrated. The speed control is fast and stable.

The instantaneous stator flux, rotor flux and stator current and the current vector trajectory, during speed reversal from +6 rpm to –6 rpm, are shown in Figure 7.29. This illustrates the performance of the flux controller.

Acceleration transients from standstill to 1500 rpm, with Linear-VSC sensorless drive are presented in Figure 7.30. The torque response and the speed control are excellent, despite of some flux oscillations.

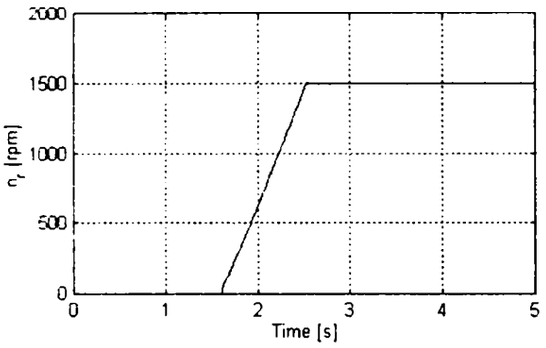

a. Estimated rotor speed

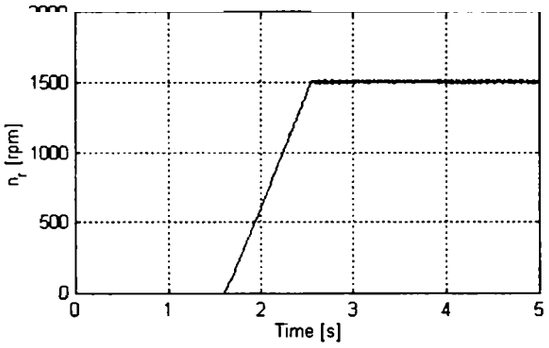

b. Measured rotor speed

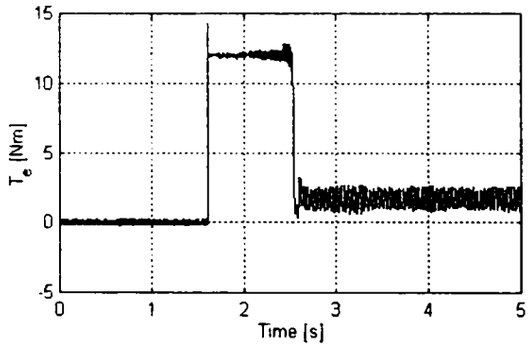

c. Estimated torque

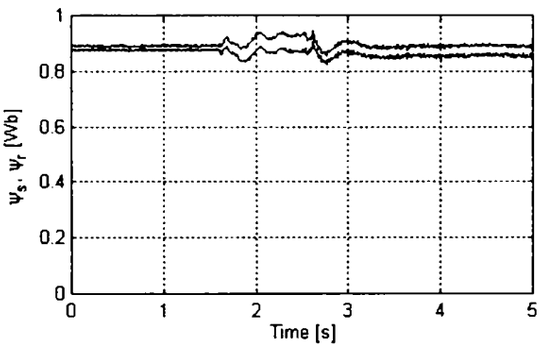

d. Estimated stator and rotor flux

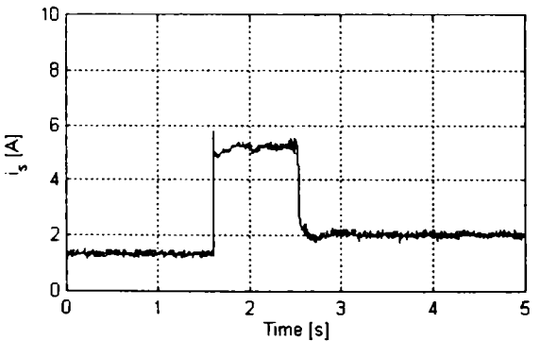

e. Estimated stator current magnitude

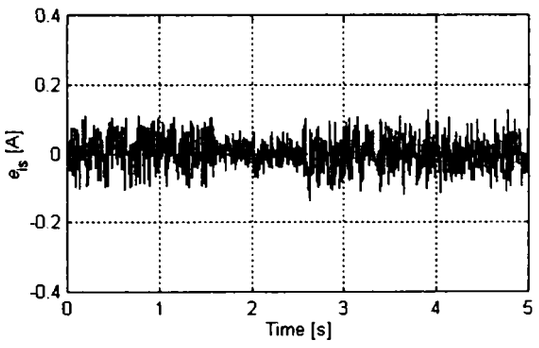

f. Stator current estimation error

Figure 7.30 Acceleration from 0 rpm to 1500 rpm with Linear-VSC and generalized SMO

The flux shows certain sensitivity to torque and speed transients. This resembles very much to the sensitivity of the RCG Control, shown in Figure 6.10, and is due to the flux controller. The current estimation error is low, an indication that the state observer is robust and behaves very well.

Torque transients with Linear-VSC, during acceleration from standstill, are presented in Figure 7.31 A reference torque step of 12 Nm (T_{eN}=7 Nm) is applied at t=10 ms. The torque reaches 12 Nm in one millisecond. As expected, the behavior of Linear-VSC is the opposite of the LFSG behavior. During torque transients it exhibits linear behavior, without ripple, while in steady state it shows very small chattering, like VSC. This behavior is convenient because the presence of VSC increases the robustness. The chattering level can be controlled by the K_{VSC} gain.

The flux control is also very good. Figure 7.31.b resembles to Figure 7.20.b for RCG Control and both are slightly better than Figure 7.24.b for LFSG. However, the Linear-VSC torque response is better than that of the RCG-Control The current estimation error is low, indicating the excellent robustness of the SMO.

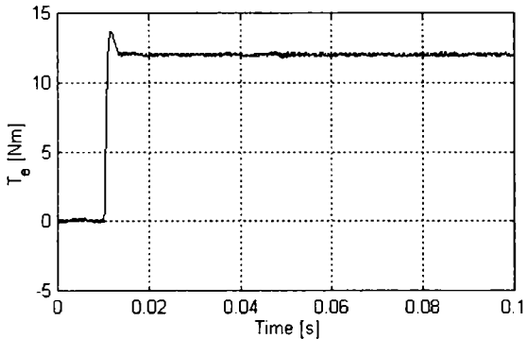

a. Estimated torque – Linear-VSC

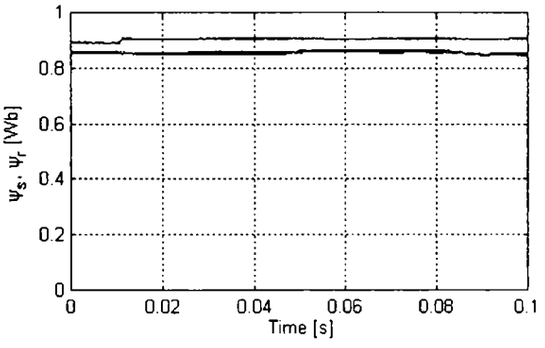

b. Estimated stator and rotor flux

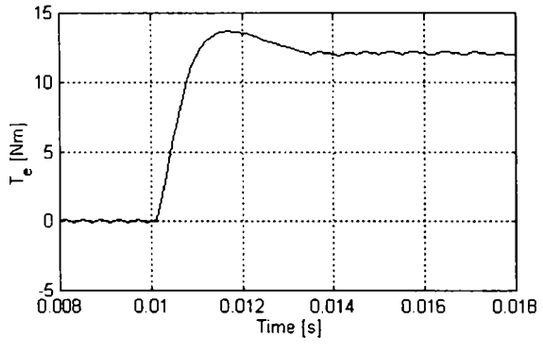

c. Estimated torque – time zoom

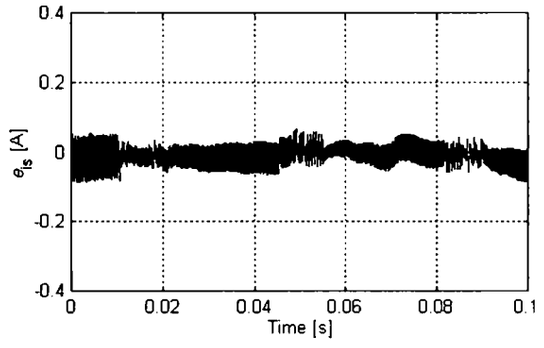

d. Current estimation error

Figure 7.31 Torque transients with Linear-VSC control and generalized observer

7.5 Conclusions

Direct torque and flux control (DTC) strategies for sensorless induction machine drives are presented in this chapter. The classical DTC strategy and its advantages and limitations are presented in the first part. Existing and new DTC solutions based on variable structure control are described in the second part.

Four new schemes for direct torque and flux control of sensorless induction machine drives are introduced and analyzed. Extensive experimental results are provided. It is of interest to compare the performance of the proposed DTC schemes and to provide recommendations for future use. This is not easy, since all proposed schemes show very good static and dynamic performance and only minor differences exist.

All proposed schemes, Linear-DTC, RCG Control, LFSG and Linear-VSC have been tested at zero speed under full load and all behave satisfactorily. The lowest nonzero speed tested was 3 rpm, and all schemes were able to sustain stable, continuous sensorless operation at 3 rpm, full load. The highest speed tested with all schemes was 3000 rpm, corresponding to twice the motor's rated frequency. Thus, the speed range of all strategies is 1:1000 in sensorless operation.

In terms of torque control, all strategies were able to achieve torque response of one millisecond, excepting for the RCG Control that realizes two or more milliseconds. This performance is obtained at zero speed and is the same as the DTC performance. All strategies exhibit very low torque and current ripple, far better than classical DTC. From this point of view, all strategies accomplish the most important requirement: fast torque response and low torque ripple. The acoustical noise associated to these is practically inexistent, while the acoustical noise produced by DTC is annoying.

In terms of flux control there are some small differences. The Linear-DTC and LFSG exhibit better flux control during torque and speed transients. The RCG Control and Linear-VSC show some sensitivity and the estimated flux oscillates. However, in all situations, the speed and torque control are insensitive to these flux oscillations. In all situations, the estimated stator and rotor flux have lower ripple than in a DTC drive.

Overall, the torque and flux control performance of all proposed schemes is excellent. Compared to classical DTC, they exhibit equally fast torque and flux control with very low ripple. Linear-DTC has standard linear behavior, while RCG Control has typical sliding mode behavior. LFSG has switching behavior during transients and linear behavior in steady state. Linear-VSC has linear behavior during transients and VSC behavior in steady state. In all cases, the flux and torque control is achieved directly, without current control and Space Vector Modulation is employed.

Nevertheless that all proposed methods are more complex than DTC. Time measurements have shown that, with the available hardware (Appendix C), the classical DTC algorithm, including state estimation, takes less than 50 μs, while the proposed algorithms take 60 μs to 70 μs. These times are for C language based implementation on floating point, 32-bit DSP. It is considered that the advantages of the new methods pay off for the small time difference.

All proposed schemes are stator flux oriented, stator flux controlled schemes. These strategies are DTC strategies because there is no current control. The torque and flux are directly controlled by means of linear or nonlinear controllers, as in DTC.

Extensive experimental results support the above statements. Only the most significant results have been presented herewith. Most of the results have been obtained with the same physical setup (Appendix C) and only the control strategy and/or the state observer were changed. In this way, comparing different results is meaningful. For example, for all strategies (DTC, Linear-DTC, RCG, LFSG, Linear-VSC) the sampling frequency was f_s=10 kHz (Figures 7.12 to 7.31). Another set of experiments that compare Linear-DTC to classical DTC (Figures 7.9 to 7.11), the sampling frequency was f_s=8 kHz, for both strategies.

More experimental results with Linear-DTC and classical DTC have been reported in [34], while results with VSC-DTC strategies were reported in [35].

References

DTC

[1] I. Takahashi, T. Noguchi, *A New Quick Response and High Efficiency Strategy of an Induction Motor.*, Record of IEEE IAS, 1985 Annual Meeting, 1985, pp. 495-502.

[2] M. Depenbrock, *Direct Self Control for High Dynamics Performance of Inverter Feed a.c. Machines.*, ETZ Archive, vol. 7, no. 7, 1985, pp. 211-218.

[3] I. Boldea, S.A. Nasar, *Torque Vector Control (TVC) - A Class of Fast and Robust Torque, Speed and Position Digital Controllers for Electric Drives.*, Proceedings of EMPS, vol. 15, 1988, pp. 135-148.

[4] D. Casadei, F. Profumo, G. Serra, A. Tani, *FOC and DTC: Two Viable Schemes for Induction Motors Torque Control.*, Proc. of EPE-PEMC 2000, 2000, pp. 1-128 - 1-135.

[5] D.Telford M.W.Dunnigan B.W.Williams, *A Comparison of Vector Control and Direct Torque Control of an Induction Machine.*, IEEE PESC 2000 Conf., CD-ROM paper 14.1.

[6] Hoang Le-Huy, *Comparison of Field-Oriented Control and Direct Torque control for Induction Motor Drives.*, The 34th IEEE IAS Annual Meeting, 1999, CD-ROM paper 28.1.

[7] P. Pohjalainen, P. Tiitinen, J. Lalu, *The Next-Generation Motor Control Method – Direct Torque Control, DTC.*, EPE Chapter Symp., Lausanne, Switzerland, 1994, pp. 115-120.

[8] J.-K. Kang, S.-K. Sul, *Analysis and Prediction of Inverter Switching Frequency in Direct Torque Control of Induction Machine Based on Hysteresis Bands and Machine Parameters.*, IEEE Trans. Industrial Electronics, vol. 48, no. 3, June 2001, pp. 545-553.

[9] D. Casadei, G. Serra, A. Tani, *Implementation of a Direct Torque Control Algorithm for Induction Motors Based on Discrete Space Vector Modulation.*, IEEE Transactions on Power Electronics, vol. 15, no. 4, July 2000, pp. 769-777.

[10]D. Casadei, G. Serra, A. Tani, *Improvement of Direct Torque Control Performance by Using a Discrete SVM Technique.*, The 29th IEEE PESC98, 1998, vol. 2, pp. 997-1003.

[11]T.G. Habetler, F. Profumo, M. Pastorelli, L.M. Tolbert, *Direct Torque Control of Induction Machines Using Space Vector Modulation.*, IEEE Transactions on Industry Applications, vol. 28, no. 5, Sept./Oct. 1992, pp. 1045-1053.

[12]G. Griva, T.G. Habetler, F. Profumo, M. Pastorelli, *Performance Evaluation of a Direct Torque Controlled Drive in the Continuous PWM-Square Wave Transition Region.*, IEEE Transactions on Power Electronics, vol. 10, no. 4, July 1995, pp. 464-471.

[13]B.H. Kenny, R.D. Lorenz, *Stator and Rotor Flux Based Deadbeat Direct Torque Control of Induction Machines.*, The 36th IEEE IAS Annual Meeting, 2001, CD-ROM paper 3.5.

[14]D. Casadei, G. Serra, A. Tani, *Stator Flux Vector Control for High Performance Induction Motor Drives using Space Vector Modulation.*, Proceedings of OPTIM'96, Brasov, Romania, 1996, pp. 1413-1422.

[15]D. Casadei, G. Serra, A. Tani, L. Zarri, F. Profumo, *Performance Analysis of a Speed Sensorless Induction Motor Drive Based on a Constant Switching Frequency DTC Scheme.*, The 35th IEEE IAS Annual Meeting, 2000, Rome, CD-ROM paper 33.3.

[16]A. Mir, M.E. Elbuluk, D.S. Zinger, *Fuzzy Implementation of Direct Self Control of Induction Motors.*, IEEE Transactions on Industry Applications, vol. 30, no. 3, May/June 1994, pp. 729-735.

[17]P.Z. Grabowski, M.P. Kazmierkowski, B.K. Bose, F. Blaabjerg, *A Simple Direct-Torque Neuro-Fuzzy Control of PWM-Inverter-Fed Induction Motor Drive.*, IEEE Transactions on Industrial Electronics, vol. 47, no. 4, August 2000, pp. 863-870.

[18]K.L. Shi, T.F. Chan, Y.K. Wong, S.L. Ho, *Direct Self Control of Induction Motor Based on Neural Network.*, IEEE Transactions on Industry Applications, vol. 37, no. 5, Sept./Oct. 2001, pp. 1290-1298.

[19]Cristian Lascu, Andrzej M. Trzynadlowski, *A Sensorless Hybrid DTC Drive for High-Volume Applications Using the TMS320F243 DSP Controller.*, The 36th IEEE Industry Applications Society Annual Meeting 2001, Chicago, IL, USA, vol. 1, pp. 482-489.

[20]Cristian Lascu, Ion Boldea, Frede Blaabjerg, *A Modified Direct Torque Control for Induction Motor Sensorless Drive.*, IEEE Transactions on Industry Applications, vol. 36, no. 1, Jan./Feb. 2000, pp. 122-130.

VSC

[21]Jean-Jacques E. Slotine, Weiping Li, *Applied Nonlinear Control.*, Prentice Hall, Englewood Cliffs, New Jersey, 1991

[22]R.A. DeCarlo, S.H. Zak, G.P.Matthews, *Variable Structure Control of Nonlinear Multivariable Systems: A Tutorial.*, Proc. of IEEE, vol. 76, no. 3, March 1988, pp. 212-232.

[23]J.Y. Hung, W. Gao, J.C. Hung, *Variable Structure Control. A Survey.*, IEEE Transactions on Industrial Electronics, vol. 40, no. 1, Feb. 1993, pp. 2-22.

[24]S.V. Drakunov, V.I. Utkin, *Sliding Mode Control in Dynamic Systems.*, International Journal of Control, vol. 55, no. 4, 1992, pp. 1029-1037.

[25]K.D. Young, V.I. Utkin, U. Ozguner, *A Control Engineer's Guide to Sliding Mode Control.*, IEEE Transactions on Control Systems Technology, vol. 7, no. 3, May 1999, pp. 328-342.

[26]V.I. Utkin, *Sliding Mode Control Design Principles and Applications to Electric Drives.*, IEEE Transactions on Industrial Electronics, vol. 40, no. 1, Feb. 1993, pp. 23-36.

[27]Vadim Utkin, Jurgen Guldner, Jingxin Shi, *Sliding Mode Control in Electromechanical Systems.*, Taylor & Francis, 1999.

[28]Z. Yan, C. Jin, V.I. Utkin, *Sensorless Sliding-Mode Control of Induction Motors.*, IEEE Transactions on Industrial Electronics, vol. 47, no. 6, Dec. 2000, pp. 1286-1297.

[29]A. Benchaib, A. Rachid, E. Audrezet, M. Tadjine, *Real-Time Sliding-Mode Observer and Control of an Induction Motor.*, IEEE Transactions on Industrial Electronics, vol. 46, no. 1, Feb. 1999, pp. 128-137.

[30]H.-J. Shieh, K.-K. Shyu, *Nonlinear Sliding-Mode Torque Control with Adaptive Backstepping Approach for Induction Motor Drive.*, IEEE Transactions on Industrial Electronics, vol. 46, no. 2, April 1999, pp. 380-389.

[31]M. Rodič, K. Jezernik, *Speed-Sensorless Sliding-Mode Torque Control of an Induction Motor.*, IEEE Transactions on Industrial Electronics, vol. 49, no. 1, Feb. 2002, pp. 87-95.

[32]F. Moldoveanu, V. Comnac, M. Cernat, I. Draghici, L. Cazac, R. Ungar, *Torque and Stator Flux Control of PWM Inverter-Feed Asynchronous Machine: A Sliding Mode Approach*, Proceedings of PCIM 2000 Europe, 2000, CD-ROM paper imd10.

[33]I. Boldea, A. Trica, *Torque vector control (TVC) voltage fed induction motor drives-very low performance via sliding mode.*, Proceedings of ICEM-1990, vol. 3, pp. 1212-1217.

[34]Cristian Lascu, Ion Boldea, Frede Blaabjerg, *A Modified Direct Torque Control for Induction Motor Sensorless Drive.*, IEEE Transactions on Industry Applications, vol. 36, no. 1, Jan./Feb. 2000, pp. 122-130.

[35]Cristian Lascu, Ion Boldea, *Direct Torque Control of Sensorless Induction Motor Drives. A Sliding Mode Approach.*, Proc. of the International Conference on Optimization of Electrical and Electronic Equipments – OPTIM 2002, Brasov, Romania, 2002, vol. 2, pp. 481-488.

8 CONCLUSIONS

The present thesis is devoted to high performance direct torque and flux control of sensorless induction machine drives. It approaches the most important features of sensorless drives, the state estimation and the torque and flux control. The most important existing solutions for DTC sensorless drives are analyzed and several novel or entirely new solutions are proposed.

The thesis is structured on eight chapters. Chapter one makes a short introduction to adjustable speed drives with induction machines. Several basic definitions and classifications are provided here. The basic schemes for induction machine vector control are presented.

Chapter two is devoted to induction machine modeling. The induction machine general model based on space vectors is discussed. The most important state space models are described. Induction machine models including saturation and iron looses are also presented.

Chapter three is devoted to Voltage Source Inverter modeling. The basic topology of the VSI is presented and the space vectors based model of the VSI is given. The most important nonlinearities of the VSI are described and methods to compensate for those are presented. The Space Vector Modulation strategy is described in detail, including overmodulation strategies.

Chapter four approaches the state estimation for induction machine sensorless drives. The most important existing asymptotical observers and estimators are described. A new concept of inherent sensorless observer is introduced and several new or improved schemes of state observers and estimators are proposed and analyzed. Simulations and experimental results are provided.

Chapter five approaches the induction machine state estimation by means of sliding mode observers. The most important sliding mode observers are described. The inherent sensorless observer concept is extended to sliding mode observers and a new sliding mode observer is developed and analyzed. Simulations and experimental results are provided.

Chapter six presents speed observers for induction machine sensorless drives. The existing solutions based on fundamental excitation are discussed. A new speed observer based on mechanical model is introduced. Simulations and experimental results are provided.

Chapter seven presents the direct torque and flux control for induction machines. The classical DTC strategy is presented first. In the second part, four new DTC solutions that offer improved behavior and similar dynamic performance as DTC are proposed and analyzed. Simulations and experimental results are provided.

The following contributions are believed to be new:

- The DTC enhanced overmodulation concept has been proposed in chapter three. Two practical solutions, which enhance with DTC, two existing OVM schemes, have been proposed.
- The inherent sensorless observer concept for induction machine state estimation has been developed in chapter four. Three new inherent sensorless schemes have been proposed, analyzed, simulated and experimentally tested. This observer is very useful in sensorless drives.
- A new scheme for stator resistance estimation was proposed and tested.
- A modified scheme for an existing Jansen-Lorenz flux observer has been proposed in chapter four. Simulation and experiments are provided.
- Experimental results with a modified voltage model estimator have been carried out for the first time. The results are presented in chapter four, also.
- The inherent sensorless observer concept has been extended to sliding mode state observers, in chapter five. Four new inherent sensorless sliding mode observers have been proposed, analyzed, simulated and experimentally tested.

This observer provides increased robustness and is also very useful in sensorless drives. Extensive experimental results are provided.

- In chapter six, a new speed observer, based on the mechanical model of the drive and on PLL theory, is proposed. Two very similar schemes have been analyzed, simulated and tested. Extensive experimental results are provided.
- A modified scheme for Model Reference Adaptive speed estimators has been proposed in chapter six. It was experimentally tested, also.
- In chapter seven, a new generic DTC scheme is proposed. Four variants of this basic scheme are developed. The fist one, called Linear-DTC is a linear torque and flux controller. The other three schemes are based on Variable Structure Systems theory and implement the same torque and flux controller in as variable structure controllers. All proposed schemes achieve the same dynamic performance as DTC and better steady state performance.
- All proposed observers and controllers have been integrated into several sensorless drives that have been extensively experimentally tested. Some of these drives are entirely based on variable structure control, since both, the state observer and the controller are variable structure systems. Others use linear observers and controllers and are linear systems.
- Experimental results at very low speed, including zero speed and 3 rpm, in sensorless operation, have been carried out. Very low speed motoring and regenerative operation has been demonstrated. As far as it is known, the 3 rpm is the lowest speed ever obtained in sensorless operation.

The future work on this fascinating subject will be devoted to:

- Induction machine sensorless position control based on sliding mode estimation and variable structure control.
- Direct torque control based on nonlinear decoupling, feedback linearization and variable structure control.
- Improvements of the proposed solutions and development of very high-speed sensorless induction machine drives.

APPENDIX A

FUNDAMENTALS OF NONLINEAR SYSTEMS STABILITY THEORY

Nonlinear systems

A nonlinear dynamic system can, usually, be represented by a set of nonlinear differential equations in the form

$$dx/dt = f(x,u,t), \tag{A.1}$$

where f is a $n\times 1$ nonlinear vector function, x is the $n\times 1$ state vector and u is the $m\times 1$ input vector. A solution $x(t)$ of (A.1) usually corresponds to a curve in state space, as $t\to\infty$ and is referred as a *state trajectory* or a *system trajectory*.

Definition A.1 (Autonomous Systems) The nonlinear system (A.1) is said to be *autonomous* if f does not depend explicitly on time, i.e., if the state equation can be written

$$dx/dt = f(x), \tag{A.2}$$

Otherwise, the system is called *non-autonomous*.

The fundamental difference between autonomous and non-autonomous systems is that the state trajectory of an autonomous system is independent of the initial time, while that of a non-autonomous system generally is not. Autonomous linear systems are called time-invariant, while non-autonomous linear systems are called time-varying systems.

It is possible for a system trajectory to correspond to only a single point in state space. Such a point is called an equilibrium point.

Definition A.2 (Equilibrium Points) A state x^* is an *equilibrium state*, or *equilibrium point* of the system (A.1) if, once $x(t)$ is equal to x^*, it remains equal to x^* for all future time. Mathematically, this means that x^* satisfies $0=f(x^*)$.

Stability and instability

Nonlinear systems behavior is complex and their analysis involves a number of refined stability concepts, such as asymptotic stability, local and global stability, etc.

Definition A.3 (Stability) The equilibrium state x^* is said to be *stable* if for

$\forall R > 0,\ \exists r > 0,$ such that, if $\|x(0)-x^*\| < r \Rightarrow \|x(t)-x^*\| < R,$ for $\forall t \geq 0.$

Otherwise, the equilibrium point is *unstable*.

Essentially, stability (also called *Lyapunov stability*) means that the system trajectory can be kept arbitrarily close to x^* by starting sufficiently close to it.

Definition A.4 (Asymptotic Stability) The equilibrium point x^* is said to be *asymptotically stable* if it is stable and if, in addition, states started close to x^* actually converge to x^* as time goes to infinity, i.e.

$\forall R > 0,\ \exists r > 0,$ such that, if $\|x(0)-x^*\| < r \Rightarrow \|x(t)-x^*\| \to 0,$ as $t \to \infty.$

An equilibrium point that is Lyapunov stable, but not asymptotically stable is called *marginally stable*.

Definition A.5 (Global Stability) If asymptotic stability holds for any initial state, the equilibrium point is said to be *globally asymptotically stable* (or *stable in the large*). Otherwise, the stability is *local*.

Linear time-invariant systems are either asymptotically stable, or marginally stable, or unstable. Linear asymptotic stability is always global and linear instability always implies exponential blow-up. The following theorem is a cornerstone of nonlinear systems stability analysis.

Lyapunov theorem for global stability

Theorem T1 (Global Stability) Consider a nonlinear autonomous system

$$dx / dt = f(x), \tag{A.3}$$

Assume that there exists a scalar function V of the state x, with continuous first and second derivatives, such that, for the whole state space

1. $V(x)$ is positive definite, i.e., $V(0)=0$ and $V(x)>0$ for any $x \neq 0$,
2. $dV(x)/dt$ is negative definite, i.e., $-V(x)$ is positive definite,
3. $V(x)$ is radially unbounded, i.e., $V(x) \to \infty$ as $\|x\| \to \infty$.

Then the equilibrium point at the origin is *globally asymptotically stable*.

The basic philosophy of Lyapunov theorem is the mathematical extension of a fundamental physical observation: if the total energy of a system is continuously dissipated, then the system, whether linear or nonlinear, must eventually settle down to an equilibrium point. Thus, the system's stability may be examined by means of a single, energy like scalar function.

Although many *Lyapunov functions* V may exist for the same system, there is no general way of finding such functions for nonlinear systems; the specialized literature gives mathematical formal approaches to constructing Lyapunov function candidates [1]. However this is of little use for complex systems.

On the other hand, if engineering insight and physical properties of the system are properly exploited, then an elegant and powerful Lyapunov analysis may be possible for very complex systems. It is the case of electric drives, where properly selected Lyapunov function may be helpful in designing certain system parameters, or may suggest the structure of an entire subsystem (speed estimators, for example).

Lyapunov theorem for nonautonomous systems

Theorem T2 (Global Stability) If, for a non-autonomous dynamic system $dx/dt = f(x,t)$, there exist a scalar function $V(x,t)$ with continuous partial derivatives, such that, conditions 1, 2, 3 from Theorem T1, and condition

4. $V(x,t)$ is descrescent, i.e., $V(0,t)=0$ and, $V(x,t)<V'(x)$ for $\forall t\geq 0$, where $V'(x)$ is a time-invariant positive definite function,

are all satisfied, than the equilibrium point at origin is globally uniformly asymptotically stable.

Global stability for linear time-invariant systems

Theorem T3 (Asymptotical Stability) A necessary and sufficient condition for a linear time-invariant system $dx/dt = Ax + Bu$ to be strictly stable is that, for any symmetric positive definite matrix $\boldsymbol{Q}$, the unique matrix solution $\boldsymbol{P}$ of equation

$$A^T P + PA = -Q, \tag{A.4}$$

to be symmetric positive definite. Equation (A.4) is the *Lyapunov equation*.

Definition A.6 (Positive definite matrices) A square $n \times n$ matrix $\boldsymbol{M}$ is positive definite if the quadratic function $f=x^T\boldsymbol{M}x$ is a positive definite function, where x is an arbitrary nonzero $n \times 1$ vector.

Alternatively, a linear time-invariant system is asymptotically stable if and only if the system's matrix is Hurwitz, i.e. all its eigenvalues are located strictly in the left-half plane. Unfortunately, this *does not apply* to linear time-varying systems [1]. For such systems a Lyapunov type analysis must be performed. A simple result, however, can be derived in this way.

Global stability for linear time-varying systems

Theorem T4 (Asymptotical Stability) The time variable dynamic system $dx/dt = A(t)x + Bu$ is asymptotically stable if the eigenvalues of the symmetric matrix $A(t)+A(t)^{\mathrm{T}}$ (all of each are real) remain strictly in the left half complex plane.

Lyapunov stability theorems T1, T2 and T4 are sufficient stability conditions for dynamic systems stability. Lyapunov theorem is also known as *Lyapunov's direct method*. A large number of specialized theorems and other valuable results are available for stability and dynamic behavior analysis of nonlinear systems. These include Lyapunov's linearization method that serves as the fundamental justification of using linear control techniques in practice, Popov's criterion, Barbalat's lemma, Kalman-Yakubovich lemma, invariant set theorems and others [1].

References

[1] Jean-Jacques E. Slotine, Weiping Li, *Applied Nonlinear Control.*, Prentice Hall, Englewood Cliffs, New Jersey, 1991

APPENDIX B
INDUCTION MACHINES

All experiments and simulations presented herewith have been carried out utilizing two industrial standard induction machines. Specifications, nameplate data and parameters of these machines are presented next.

Machine 1

Producer: ABB

Type: M2AA112M IP55, isolation class F.

Nameplate data: $P_N = 4.0$ kW

$U_N = 380\text{-}420$ V, Y $I_N = 8.9$ A

$U_N = 220\text{-}240$ V, Δ $I_N = 15.4$ A

$f_N = 50$ Hz

$n_N = 1430$ rpm

$T_N = 27$ Nm

$\cos\varphi = 0.8$

Parameters: $R_s = 1.55\ \Omega$ $R_r = 1.35\ \Omega$

$L_s = L_r = 0.172$ H $L_m = 0.168$ H

$J = 0.015$ kgm^2

Rotor: squirrel cage

Machine 1 was used for all simulations and for experiments with Classical Direct Torque Control (DTC), Linear Direct Torque Control (Linear-DTC) together with Luenberger Observers and Jansen-Lorenz observers.

Machine 2

Producer: Electromotor Timisoara, Romania

Type: B3-90S×1.1×1500S IP44, isolation class F.

Nameplate data: $P_N = 1.1$ kW

$U_N = 380$ V, Y $I_N = 2.77$ A

$U_N = 220$ V, Δ $I_N = 4.82$ A

$f_N = 50$ Hz

$n_N = 1410$ rpm

$T_N = 7{,}45$ Nm

$\cos\varphi = 0.79$

Parameters: $R_s = 5.46\ \Omega$ $R_r = 4.45\ \Omega$

$L_s = L_r = 0.492$ H $L_m = 0.475$ H

$J = 0.008$ kgm^2

Rotor: squirrel cage

Measured data for magnetizing inductance L_m versus main flux magnitude ψ_m and shortcircuit inductance $L_{sc}=L_{1\sigma}+L_{2\sigma}$ versus phase current are presented in Figure B.1. The magnetizing inductance is approximated as

$$L_m = c_0 + \sum_{k=1}^{5} c_k e^{-2k\psi_m^2} \tag{B.1}$$

where c_0=0.002093 H, c_1=3.3311 H, c_2=-10.6093 H, c_3=17.1183 H, c_4=-13.2716 H, c_5=2.93556 H.

The shortcircuit inductance is approximated as

$$L_{sc} = c_0 + c_1\sqrt{I_s} + c_2 I_s + c_3\sqrt{I_s^3} \tag{B.1}$$

where c_0=0.068835 H, c_1=-0.03088 HA$^{-0.5}$, c_2=0.012381 HA^{-1}, c_3=0.001773 HA$^{-1.5}$.

In both cases, coefficients c_k have been determined by the least square method.

Experimental torque versus slip and current versus slip characteristics, for Machine 2, are presented in Figure B.2.

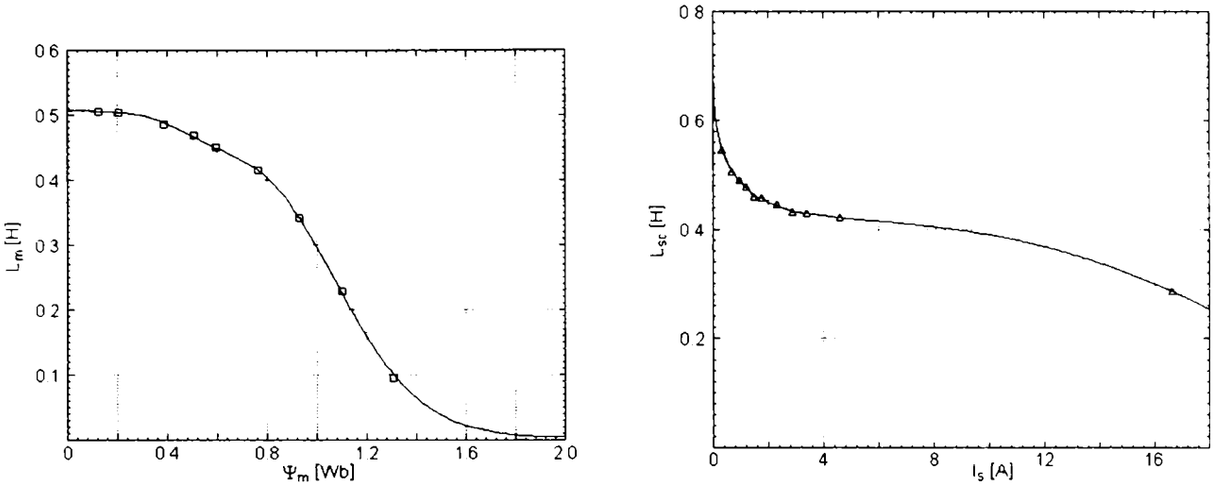

a. Magnetizing inductance versus main flux b. Shortcircuit inductance versus current

Figure B.1 Magetizing inductance and shortcircuit inductance of Motor 2

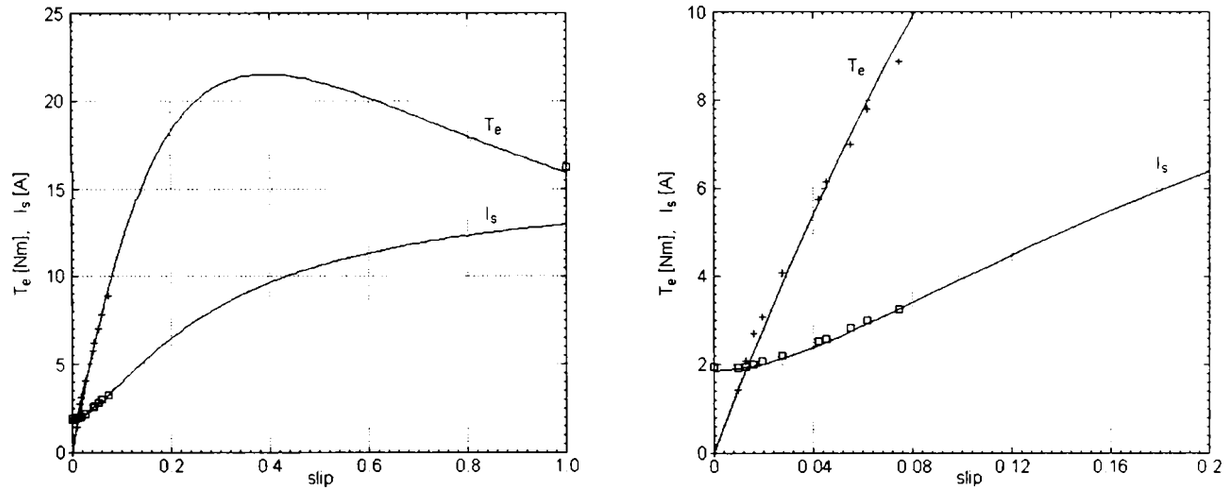

Figure B.2 Torque versus slip and current versus slip characteristics of Motor 2

DC Generator

Type: Permanent magnet DC servomotor P1COL20

Nameplate data: $T_N = 20.3$ Nm $T_{max} = 180$ Nm

$I_N = 36.2$ A, $I_{max} = 321$ A

$V_{max} = 118$ V

$n_{max} = 2000$ rpm

J = 0.07 kgm^2 (measured)

APPENDIX C
EXPERIMENTAL SETUP

The experimental setup of the sensorless DTC drive is presented in Figure C.1. The hardware setup contains a multiprocessor system with two Digital Signal Processors (DSP) and other hardware. Its components are:

1. The personal computer (PC) accomplishes two functions: software development for the DTC sensorless drive and monitoring and data acquisition. For software development, firmware software tools (compilers and debuggers) have been used. For monitoring and data acquisition, dedicated software, called *Spectrum*, has been developed.
2. The ADSP-21062 EZ-LAB board contains the ADSP-21062 SHARC Digital Signal Processor (DSP) from Analog Devices. It is a powerful, floating-point, 32-bit processor with Super Harvard architecture, powered at 33 MHz clock frequency. This subsystem is responsible for the realization of estimation and control algorithms. All algorithms described herewith were developed in C language for the ADSP-21062 EZ-LAB platform.
3. The TMS320F243 EVM board contains the TMS320F243 DSP from Texas Instruments. It is a fixed-point, 16-bit DSP with Harvard architecture, powered at 20 MHz clock frequency. This subsystem contains the VSI interface and is responsible for master sampling period generation, and for PWM generation. Programs for this platform were developed in C language and in assembler.
4. The Voltage Source Inverter is an industrial, open architecture inverter, VLT5004, from Danfoss, Denmark. Its nameplate data are: rated power S_N=4.3 kVA, motor shaft rated power P_N=2.2 kW (3 HP), rated voltage U_N=380 V, rated current I_N=5.6 A. It is operated at 10 kHz switching frequency, with 2 μs dead time.

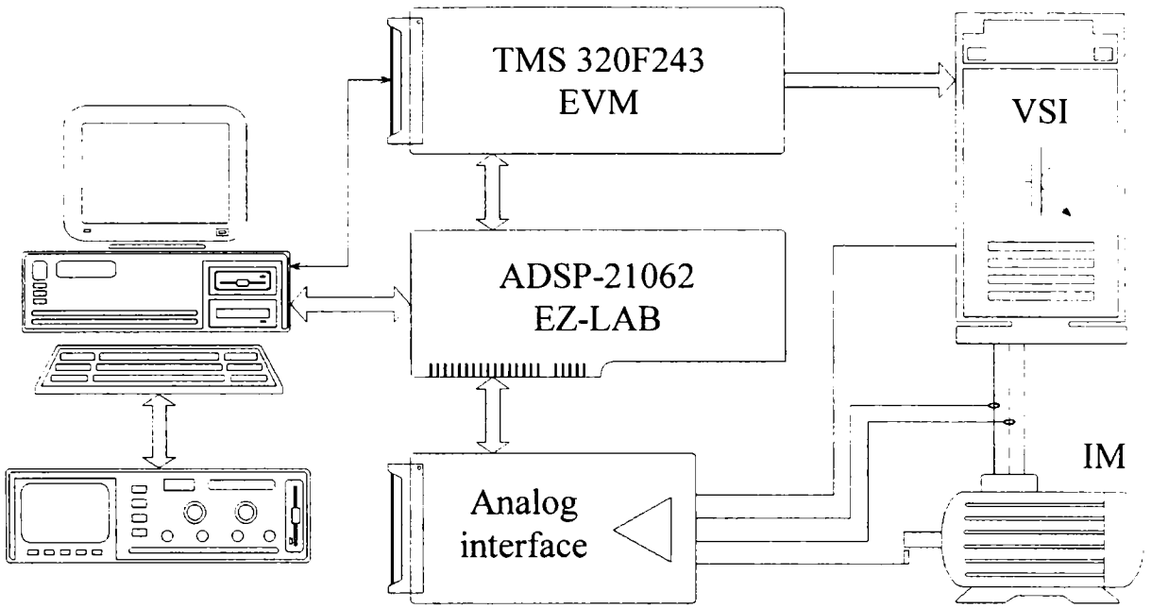

Figure B.2 Experimental setup of the sensorless DTC drive

5. The analog interface contains two boards: the current and voltage sensors board and the analog to digital conversion (ADC) board. The ADC is a simultaneous sampling, four-channel device, with 4 μs conversion time.
6. The induction machine is either Machine 1, or Machine 2. When Machine 1 was used, a more powerful inverter, VLT5008, also from Danfoss, was employed. The DC generator was connected to induction machines.
7. For speed monitoring only, an encoder with 5000 lines was employed.

This architecture is powerful and flexible and allows fast software development. The interface between the two DSP boards is realized by a fast dual-port memory. Another dual-port memory (ADSP internal memory) connects the ADSP to PC. The communication between PC and TMS is realized on the standard parallel interface using firmware software. In normal operation, three programs run simultaneously: one on each DSP platform and one on PC.

Nevertheless that the dual processor system operates stand-alone. The PC is only a supervisor and user interface. The VSI receives the switching signals from the EVM module trough a fiber optics interface. The current and voltage information is measured by the ADSP with 10 kHz sampling frequency. The ADSP executes the estimation and control algorithms and sends the modulation signals to TMS that implements the SVM.

The software package developed for the induction machine sensorless DTC drive contains the following major software projects:

1. The simulation project. It is developed in C++ language for PC and ADSP21062 and contains 21 files and a total of about 17000 lines of code. The program is based on object-oriented technology and it is able to perform real time simulation (hardware on the loop simulation) in connection with the powerful EZ-LAB platform. In this case, the estimation and control algorithms run on the ADSP processor and the PC simulates the motor.
2. The DTC project. It is developed in C language and assembler for the EZ-LAB and EVM platforms and implements the proposed estimation and control algorithms for the real drive. This project contains 27 files with about 1000 lines of code. The code is developed for real time execution.
3. The Spectrum project. It implements a user-friendly interface developed in C++ language that realizes the data acquisition from the EZ-LAB platform. It implements the sensorless DTC drive user interface that allows the user to control the drive operation from the computer's keyboard. This project contains 7 files with about 2000 lines of code.

References

[1] Brian W. Kernigham, Dennis M. Ritchie, *The C Programming Language, second edition.*, Prentice Hall International, Englewood Cliffs, New Jersey, 1988.

[2] Bjarne Stroustrup, *The C++ Programming Language, third edition.*, Addison-Wesley Publishing Company, Inc., Reading, Massachusetts, 1997.

[3] Allan V. Oppenheim, Ronald W. Schafer, *Digital Signal Processing.*, Prentice-Hall International Inc., Englewood Cliffs, New Jersey, 1975.

[4] John G. Proakis, Dimitris G. Manolakis, *Digital Signal Processing. Principles, Algorithms and Applications. Third Edition.*, Prentice-Hall Inc., Englewood Cliffs, New Jersey, 1996.

REFERENCES

Induction machine drives control and generalities

[1] R.D. Lorenz, T.A. Lipo, D.W. Novotny, *Motion control with induction motors.*, Proceedings of IEEE, vol. 82, no. 8, July-Aug. 1994, pp. 1215-1240.

[2] R.W. Doncker, D.W. Novotny, *The Universal Field Oriented Controller.*, IEEE Transactions on Industry Applications, vol. 30, no. 1, Jan./Feb. 1994, pp. 92-100.

[3] R.B. Sepe, J.H. Lang, *Implementation of Discrete-Time Field-Oriented Current Control.*, IEEE Transactions on Industry Applications, vol. 30, no. 3, May/June 1994, pp. 723-728.

[4] K. Kaga, R. Ueda, T. Sonoda, *Constitution of V/f control for reducing the steady state error to zero in induction motor drive system.*, IEEE Transactions on Industry Applications, vol. 28, no 2, Mar./Apr. 1992, pp. 455-462.

[5] I. Boldea, S.A. Nasar, *Unified treatment of core losses and saturation in the orthogonal-axis model of electric machines.*, IEE Proc., vol. 134, Pt. B, No.6, November 1987, pp. 355-363.

[6] G.R. Slemon, *Modeling of Induction Machines for Electric Drives.*, IEEE Transactions on Industry Applications, vol. 25, no. 6, Nov./Dec. 1989, pp. 1126-1131.

[7] E. Levi, V. Vuckovic, *Field-Oriented Control of Induction Machines in the Presence of Magnetic Saturation.* EM & PS, vol. 16, no. 2, March/April 1989, pp. 133-147.

[8] E. Levi, V. Vuckovic, *Rotor Flux Computation in Saturated Field-Oriented Induction Machines.* Electric Machines & Power Systems, vol. 21, no. 6, Nov./Dec. 1993, pp. 741-754.

[9] Emil Levi, *Rotor Flux Oriented Control of Induction Machines Considering the Core Loss.* Electric Machines & Power Systems, vol. 24, no. 1, Jan./Feb. 1996, pp. 37-50.

[10]S.-D. Wee, M.-H. Shin, D.-S. Hyun, *Stator-Flux-Oriented Control of Induction Motor Considering Iron Loss.*, IEEE Trans. Ind. Electronics, vol. 48, no. 3, June 2001, pp. 602-608.

[11]J. Holtz, *Methods for Speed Sensorless Control of AC Drives.*, in K. Rajashekara (Editor) "Sensorless Control of AC Motors", IEEE Press, 1996.

[12]J. Holtz, *Sensorless Position Control of Induction Motors – An Emerging Technology.* IEEE Transactions on Industrial Electronics, vol. 45, no. 6, Dec. 1998, pp. 840-852.

[13]J. Holtz, *The Representation of AC Machine Dynamics by Complex Signal Flow Graphics.*, IEEE Transactions on Industrial Electronics, vol. 42, no. 3, June 1995, pp. 263-271.

[14]J.-K. Seok, S.-K. Sul, *Optimal Flux Selection of an Induction Machine for Maximum Torque Operation in Flux-Weakening Region.*, IEEE Transactions on Power Electronics, vol. 14, no. 4, July 1999, pp. 700-708.

[15]S.-H. Kim, S.-K. Sul, *Voltage Control Strategy for Maximum Torque Operation of an Induction Machine in the Field-Weakening Region.*, IEEE Transactions on Industrial Electronics, vol. 44, no. 4, August 1997, pp. 512-518.

[16]M.-H. Shin, D.-S. Hyun, S.-B. Cho, *Maximum Torque Control of Stator-Flux-Oriented Induction Machine Drive in the Field-Weakening Region.*, IEEE Transactions on Industry Applications, vol. 38, no. 1, Jan./Feb. 2002, pp. 117-122.

[17]B.K. Bose, *Energy, Environment and Advances in Power Electronics.*, IEEE Transactions on Power Electronics, vol. 15, no. 4, July 2000, pp. 688-701.

[18]D. Divan, *Powering the Next Millennium with Power electronics.*, IEEE 1999 Conf. On Power Electronics and Drive Systems, PEDS'99, July 1999, Hong-Kong, pp. 7-10.

[19]R.J. Kerkman, G.L. Skibinski, D.W. Schlegel, *AC Drives: Year 2000 (Y2K) and Beyond.*, APEC'99, The 14th Applied Power Electronics Conf., 1999, Dallas, vol. 1, pp. 28-39.

[20]T.M. Jahns, E.L. Owen, *AC Adjustable-Speed Drives at the Millennium: How Did We Get Here.*, IEEE Transactions on Power Electronics, vol. 16, no. 1, Jan. 2001, pp. 17-25.

PWM and SVM

[21]J. Holtz, *Pulsewidth Modulation for Electronic Power Conversion.*, Proceedings of IEEE, vol. 82, no. 8, August 1994, pp. 1194-1214.

[22]J. Holtz, *Pulsewidth Modulation - A Survey.*, IEEE Transactions on Industrial Electronics, vol. 39, no. 5, Dec. 1992, pp. 410-420.

[23]H.W. van der Broeck, H.-C. Skudelny, G.V. Stanke, *Analysis and Realization of a Pulsewidth Modulator Based on Voltage Space Vectors.*, IEEE Transactions on Industry Applications, vol. 24, no. 1, Jan./Feb. 1988, pp. 142-150.

[24]J. Holtz, P. Lammert, W. Lotzkat, *High-Speed Drive System with Ultrasonic MOSFET PWM Inverter and Single-Chip Microprocessor Control.*, IEEE Trans. on Industry Applications, vol. IA-23, no. 6, Nov./Dec. 1987, pp. 1010-1015.

[25]J. Holtz, B. Bayer, *The Trajectory Tracking Approach – A New Method for Minimum Distortion PWM in Dynamic High-Power Drives.*, IEEE Transactions on Industry Applications, vol. 30, no. 4, July/Aug. 1994, pp. 1048-1057.

[26]J. Holtz, B. Bayer, *Optimal Pulse-width Modulation for AC Servos and Low-Cost Industrial Drives*, IEEE Trans. on Industry Applications, vol. 30, no. 4, July/Aug. 1994, pp. 1039-1047.

[27]J. Holtz, E. Bube, *Field-Oriented Asynchronous Pulse-Width Modulation for High-Performance ac Machine Operating at Low Switching Frequency.*, IEEE Transactions on Industry Applications, vol. 27, no. 3, May/June 1991, pp. 574-581.

[28]J. Holtz, W. Lotzkat, A.M. Khambadkone, *On Continuous Control of PWM Inverters in the Overmodulation Range Including the Six-Step Mode.*, IEEE Transactions on Power Electronics, vol. 8, no. 4, Oct. 1993, pp. 546-553.

[29]J. Holtz, B. Bayer, *Optimal Synchronous Pulsewidth Modulation with a Trajectory-Tracking Scheme for High-Dynamic Performance.* IEEE Transactions on Industry Applications, vol. 29, no. 6, Nov./Dec. 1993, pp. 1098-1105.

[30]J. Holtz, B. Bayer, *Fast Current Trajectory Tracking Control Based on Synchronous Optimal Pulsewidth Modulation.*, IEEE Transactions on Industry Applications, vol. 31, no. 5, Sept./Oct. 1995, pp. 1110-1120.

[31]J.-O. Krah, J. Holtz, *High Performance Current Regulation and Efficient PWM Implementation for Low-Inductance Servo Motors.*, IEEE Transactions on Industry Applications, vol. 35, no. 5, Sept./Oct. 1999, pp. 1039-1049.

[32]A.M. Trzynadlowski, S. Legowski, *Minimum-Loss Vector PWM Strategy for Three Phase Inverters.*, IEEE Transactions on Power Electronics, vol. 9, no. 1, January 1994, pp. 26-34.

[33]A.M. Trzynadlowski, R.L. Kirlin, S.F. Legowski, *Space Vector PWM Technique with Minimum Switching Losses and a Variable Pulse Rate.*, IEEE Transactions on Industrial Electronics, vol. 44, no. 2, April 1997, pp. 173-181.

[34]P. Thoegersen, J.K. Pedersen, *Stator Flux Oriented Asynchronous Vector Modulation for AC-Drives.*, Proceedings of PESC'90, 1990, pp. 641-648.

[35]F. Blaabjerg, J.K. Pedersen, P. Thoegersen, *Improved Modulation Techniques for PWM - VSI Drives.*, IEEE Trans. on Industrial Electronics, vol. 44, no. 1, Feb. 1997, pp. 87-95.

[36]F. Blaabjerg, J.K. Pedersen, *A New Low-Cost, Fully Fault-Protected PWM-VSI Inverter with True Phase-Current Information.*, IEEE Transactions on Power Electronics, vol. 12, no. 1, Jan. 1997, pp. 187-197.

[37]G. Pfaff, A. Weschta, A. Wick, *Design and Experimental Results of a Brushless AC Servo-Drive.*, The IEEE IAS Annual Meeting, 1982, vol. 1, pp. 692-697

[38]T.R. Rowan, R.L. Kerkman, *A New Synchronous Current Regulator and an Analysis of Current-Regulated PWM Inverters.*, IEEE Transactions on Industry Applications, vol. 22, no. 4, July/Aug. 1986, pp. 678-690.

[39]F. Briz, M.W. Degner, R.D. Lorenz, *Analysis and Design of Current Regulators Using Complex Vectors.*, IEEE Trans. on Ind. App., vol. 36, no. 3, May/June 2000, pp. 817-825.

[40]D. Zmood, D.G. Holmes, *Practical Performance Limitations for PWM Strategies.* The 33rd IEEE IAS Annual Meeting, 1998, St. Louis, CD-ROM paper 27.6.

[41]J. Holtz, W. Lotzkat, A.M. Khambadkone, *On Continuous Control of PWM Inverters in the Overmodulation Range Including the Six-Step Mode.*, IEEE Transactions on Power Electronics, vol. 8, no. 4, Oct. 1993, pp. 546-553.

[42]A.M. Hava, S.-K. Sul, R.J. Kerkman, T.A. Lipo, *Dynamic Overmodulation Characteristics of Triangle Intersection PWM Methods.*, IEEE Transactions on Industry Applications, vol. 35, no. 4, July/Aug. 1999, pp. 896-907.

[43]J.-K. Seok, J.-S. Kim, S.-K. Sul, *Overmodulation Strategy for High-Performance Torque Control.*, IEEE Transactions on Power Electronics, vol. 13, no. 4, July 1998, pp. 786-792.

[44]D. Leggate, R.J. Kerkman, *Pulse-Based Dead-Time Compensator for PWM Voltage Inverters.*, IEEE Trans. on Industrial Electronics, vol. 44, no. 2, April 1997, pp. 191-197.

[45]A.R. Muñoz, T.A. Lipo, *On-Line Dead-Time Compensation Technique for Open Loop PWM-VSI Drives.*, IEEE Trans. on Power Electronics, vol. 14, no. 4, July 1999, pp. 683-689.

[46]J.-W. Choi, S.-K. Sul, *Inverter Output Voltage Synthesis Using Novel Dead Time Compensation.*, IEEE Trans. on Power Electronics, vol. 11, no. 2, March 1996, pp. 221-227.

[47]K. Zhou, D. Wang, *Relationship Between Space-Vector Modulation and Three-Phase Carrier-Based PWM: A Comprehensive Analysis.*, IEEE Transactions on Industrial Electronics, vol. 49, no. 1, Feb. 2002, pp. 186-196.

Induction machine state estimation

[48]D.G. Luenberger, *An Introduction to Observers.*, IEEE Transactions on Automatic Control, vol. AC-16, no. 6, Dec. 1971, pp. 596-602.

[49]K.D. Hurst, T.G. Habetler, G. Griva, F. Profumo, *Zero-Speed Tacholess IM Torque Control: Simply a Matter of Stator Voltage Integration.*, IEEE Transactions on Industry Applications, vol. 34, no. 4, July/Aug. 1998, pp. 790-795.

[50]B.K. Bose, N.R. Patel, *A Programmable Cascaded Low-Pass Filter-Based Flux Synthesis for a Stator Flux-Oriented Vector-Controlled Induction Motor.*, IEEE Transactions on Industrial Electronics, vol. 44, no. 1, Feb. 1997, pp. 140-143.

[51]J. Hu, B. Wu, *New Integration Algorithms for Estimating Motor Flux Over a Wide Speed range.*, IEEE Transactions on Power Electronics, vol. 13, no. 5, Sept. 1998, pp. 969-977.

[52]J. Holtz, J. Quan, *Sensorless Vector Control of Induction Motors at Very Low Speed Using a Nonlinear Inverter Model and Parameter Identification.*, The 36th IEEE Industry Applications Society Annual Meeting, 2001, CD-ROM paper 62.3.

[53]P.L. Jansen, R.D. Lorenz, *A Physically Insightful Approach to the Design and Accuracy Assessment of Flux Observers for Field Oriented I.M. Drives.*, IEEE Transactions on Industry Applications, vol. 30, no. 1, Jan./Feb. 1994, pp 101-110.

[54]P.L. Jansen, R.D. Lorenz, D.W. Novotny, *Observer-Based Direct Field Orientation: Analysis and Comparison of Alternative Methods.*, IEEE Transactions on Industry Applications, vol. 30, no. 4, July/Aug. 1994, pp. 945-953.

[55]R.J. Kerkman, B.J. Seibel, T.M. Rowan, D.W. Schlegel, *A New Flux and Stator Resistance Identifier for AC Drive Systems.*, IEEE Transactions on Industry Applications, vol. 32, no. 3, May/June 1996, pp. 585-593.

[56]G. Verghese, S.R. Sanders, *Observers for Flux Estimation in Induction Machines.*, IEEE Transactions on Industrial Electronics, vol. 35, no. 1, Feb. 1988, pp. 85-94.

[57]H. Kubota, K. Matsuse, T. Nakano, *DSP Based Speed Adaptive Flux Observer for Induction Motor Applications.*, IEEE Transactions on Industry Applications, vol. 29, no. 2, Mar./Apr. 1993, pp. 344-348.

[58]H. Kubota, K. Matsuse, *Speed Sensorless Field-Oriented Control of Induction Motor with Rotor Resistance Adaptation.*, IEEE Transactions on Industry Applications, vol. 30, no. 5, Sept./Oct. 1994, pp. 1219-1224.

[59]H. Kubota, Y. Kataoka, H. Ohta, K. Matsuse, *Sensorless Vector Controlled Induction Machine Drives with Fast Stator Voltage Offset Compensation.*, The 34th IEEE Industry Applications Society Annual Meeting, 1999, Phoenix, AZ, CD-ROM paper 52.7.

[60]H. Kubota, I. Sato, Y. Tamura, K. Matsuse, H. Ohta, Y. Hori, *Regenerating-Mode Low-Speed Operation of Sensorless Induction Motor Drive with Adaptive Observer.*, IEEE Transactions on Industry Applications, vol. 38, no. 4, July/August 2002, pp. 1081-1086.

[61]J. Maes, J. Melkebeek, *Speed Sensorless Direct Torque Control of Induction Motors using an Adaptive Flux Observer.*, IEEE Transactions on Industry Applications, vol. 36, no. 3, May/June 2000, pp. 778-785.

[62]J. Maes, J. Melkebeek, *Improved Adaptive Flux Observer for Wide Speed Range Sensorless Induction Motor Drives.*, Elrctromotion '99, International Symposium on Advanced Electromechanical Motion Systems, 1999, pp. 379-384.

[63]M. Abrate, G. Griva, F. Profumo, A. Tenconi, *High Speed Sensorless Fuzzy-Like Luenberger Observer.*, The 30th IEEE PESC99 Record, 1999, vol. 1, pp. 477-481.

[64]K.D. Hurst, T.G. Habetler, G. Griva, F. Profumo, P.L. Jansen, *A Self-Tuning Closed Loop Flux Observer for Sensorless Torque Control of Standard Induction Machines.*, IEEE Transactions on Power Electronics, vol. 12, no. 5, Sept. 1997, pp. 807-815.

[65]M.-H. Shin, D.-S. Hyun, S.-B. Cho, S.-Y. Choe, *An Improved Stator Flux Estimation for Speed Sensorless Stator Flux Orientation Control of Induction Motors.*, IEEE Transactions on Power Electronics, vol. 15, no. 2, Sept. 2000, pp. 312-318.

[66]R.J. Kerkman, B.J. Seibel, T.M. Rowan, D.W. Schlegel, *A New Flux and Stator Resistance Identifier for AC Drive Systems.*, IEEE Transactions on Industry Applications, vol. 32, no. 3, May/June 1996, pp. 585-593.

[67]J. Song, K.-B. Lee, J.-H. Song, I. Choy, K.-B. Kim, *Sensorless Vector Control of Induction Motor Using a Novel Reduced-Order Extended Luenberger Observer.*, The 35th IEEE Industry Applications Society Annual Meeting, 2000, Rome, CD-ROM paper 42.2.

[68]G.D. Andreescu, *Flux Estimator with Offset Correction Loop for Low Speed Sensorless Control of AC Drives.*, Proc. of OPTIM 2002, Brasov Romania, 2002, vol. 2, pp. 531-538.

[69]G.D. Andreescu, R. Rabinovici, *Observer based torque control with inertia identification using only position transducer for electric drives.*, Record of ICEM 2000, Espoo, August 2000, pp. 1428-1432.

[70]G.D. Andreescu, *Flux Observers Based on Combined Voltage-Current Models for Control of PMSM Drives.*, The 9th International Conference on Power Electronics and Motion Control – EPE-PEMC 2000, pp. 6-64 – 6-69.

[71]J.-S. Choi, W.-M. Kim, Y.-S. Kim, *Speed Sensorless Control of Induction motor Considering the Flux Saturation*, Proc. of IEEE APEC 2000, 2000, CD-ROM paper 4.5.

[72]Z. Krzeminski, A. Jaderko, *A Speed Observer System of Induction Motor with Magnetizing Curve Identification.*, The 9th International Conference on Power Electronics and Motion Control – EPE-PEMC 2000, pp. 6-109 – 6-113.

[73]J.-H. Kim, J.-W. Choi, S.-K. Sul, *New Strategy to Estimate the Rotor Flux of Induction Motor by Analyzing Observer Characteristic Function.*, KIEE Trans. on Electrical Machinery and Energy Conversion Systems, vol. 11B, no. 2, June 2001, pp. 51-58.

[74]R.D. Lorenz, *Observers and State Filters in Drives and Power Electronics.*, Proceedings of OPTIM 2002, Brasov, Romania, 2002, CD-ROM paper PKA01.

[75]R.D. Lorenz, K.W. Van Patten, *High-Resolution Estimation for All-Digital, ac Servo Drives.*, IEEE Trans. Industry Applications, vol. 27, no. 4, July/Aug. 1991, pp. 701-705.

[76]H. Tajima,Y. Hori, *Speed Sensorless Field-Oriented Control of the Induction Machine.*, IEEE Transactions on Industry Applications, vol. 29, no.1, Jan./Feb. 1993, pp. 175-180.

[77]K. Ohnishi, N. Matsui, Y. Hori, *Estimation, Identification and Sensorless Control in Motion Control Systems.*, Proc. of IEEE, vol. 82, no. 8, August 1994, pp. 1253-1265.

[78]T. Pana, Y. Hori, *Simultaneous speed estimation and rotor resistance identification for sensorless induction motor drives.*, Proceedings of Japan Industry Applications Society Conference, Ehime, Japan, 1994, pp. 135-140.

[79]C. Schauder, *Adaptive Speed Identification for Vector Control of Induction Motors without Rotational Transducers.*, IEEE Transactions on Industry Applications, vol. 28, no. 5, Sept./Oct. 1992, pp. 1054-1061.

[80]L. Harnefors, H.-P. Nee, *A General Algorithm for Speed and Position Estimation of AC Motors.*, IEEE Transactions on Industrial Electronics, vol. 47, no. 1, Feb. 2000, pp. 77-83.

[81]L. Harnefors, *Speed Estimation from Noisy Resolver Signals.*, IEE Power Electronics and Variable Speed Drives, Conference Publication No. 429, 1996, pp. 279-282.

[82]F.Z. Peng, T. Fukao, J.-S. Lai, *Low-Speed Performance of Robust Speed Identification Using Instantaneous Reactive Power for Tacholess Vector Control of Induction Motors.*, The IEEE Industry Applications Society Annual Meeting 1994, pp. 509-514.

[83]A. Consoli, G. Scarcella, A. Testa, *A New Zero-Frequency Flux-Position Detection Approach for Direct-Field-Oriented-Control Drives.*, IEEE Transactions on Industry Applications, vol. 36, no. 3, May/June 2000, pp. 797-804.

[84]M.W. Degner, R.D. Lorenz, *Position Estimation in Induction Machines Utilizing Rotor Bar Slot Harmonics and Carrier-Frequency Signal Injection.*, IEEE Transactions on Industry Applications, vol. 36, no. 3, May/June 2000, pp. 736-742.

[85]S.V. Drakunov, V.I. Utkin, *Sliding Mode Observers. Tutorial.*, CDC 1995, The 34th Conference on Decision and Control, New Orleans, LA, 1995, pp. 3376-3378.

[86]S.V. Drakunov, V.I. Utkin, *Discrete Event Sliding Mode Observers for Continuous-Time Systems.*, CDC 1995, The 34th Conference on Decision and Control, 1995, pp. 3403-3405.

[87]I. Haskara, U. Ozguner, V.I. Utkin, *On Sliding Mode Observers via Equivalent Control Approach.*, International Journal of Control, vol. 71, no. 6, 1998, pp. 1051-1067.

[88]B.L. Walcott, M.J. Corless, S.H. Żak, *Comparative study of non-linear state-observation techniques.*, International Journal of Control, vol. 45, no. 6, 1987, pp. 2109-2132.

[89]F. Chen, M.W. Dunnigan, *Comparative Study of a Sliding-Mode Observer and Kalman Filters for Full State Estimation in an Induction Machine.*, IEE Proceedings on Electric Power Applications, vol. 149, no. 1, January 2002, pp. 53-64.

[90]E.A. Misawa, J.K. Hedrick, *Nonlinear Observers – A State-of-the-Art Survey.*, Trans. ASME Journal of Dynamic Systems, Measurement and Control, vol. 111, Sept. 1989, pp. 344-352.

[91]J.-J.E. Slotine, J.K. Hedrick, E.A. Misawa, *On Sliding Observers for Nonlinear Systems.*, Trans. ASME Journal of DSM&C, vol. 109, Sept. 1987, pp. 245-252.

[92].C. Aitken, H.M. Schwartz, *Towards Robust Discrete-Time Sliding Mode Observers.*, 1995 American Control Conference, Seattle, WA, 1995, pp. 3730-3734.

[93]Z. Yan, C. Jin, V.I. Utkin, *Sensorless Sliding-Mode Control of Induction Motors.*, IEEE Transactions on Industrial Electronics, vol. 47, no. 6, Dec. 2000, pp. 1286-1297.

[94]A. Benchaib, A. Rachid, E. Audrezet, M. Tadjine, *Real-Time Sliding-Mode Observer and Control of an Induction Motor.*, IEEE Transactions on Industrial Electronics, vol. 46, no. 1, Feb. 1999, pp. 128-137.

[95]M. Tursini, R. Petrella, F. Parasiliti, *Adaptive Sliding Mode Observer for Speed Sensorless Control of Induction Motors.*, IEEE Transactions on Industry Applications, vol. 36, no. 5, Sept./Oct. 2000, pp 1380-1387.

[96]S. Doki, S. Sangwongwanich, S. Okuma, *Implementation of Speed-Sensor-Less Field-Oriented Vector Control using Adaptive Sliding Observer.*, IEEE IECON'92, The 1992 International Conference on Industrial Electronics, 1992, vol. 1, pp. 453-458.

[97]S. Sangwongwanich, S. Doki, T. Yonemoto, S. Okuma, *Adaptive Sliding Observers for Direct Field-Oriented Control of Induction Motor.*, IEEE IECON'90, The 16th Annual Conference of Industrial Electronics Society, 1990, vol. 2, pp. 915-920.

[98]A. Kheloui, K. Aliouane, M. Medjaoui, B. Davat, *Design of a Stator Flux Sliding Mode Observer for Direct Torque Control of Sensorless Induction Machine.*, The 35th IEEE Industry Applications Society Annual Meeting, 2000, Rome, CD-ROM paper 33.7.

[99]G.D. Andreescu, *Robust Sliding Mode Based Observer for Sensorless Control of Permanent Magnet Synchronous Motor Drives.*, Proc. of PEMC'98, vol. 6, pp. 172 – 177.

[100]L. Salvatore, S. Stasi, L. Tarchioni, *A New EKF-Based Algorithm for Flux Estimation in Induction Machines.*, IEEE Trans. Ind. Electronics, vol. 40, no. 5, Oct. 1993, pp. 496-504.

DTC

[101]I. Takahashi, T. Noguchi, *A New Quick Response and High Efficiency Strategy of an Induction Motor.*, Record of IEEE IAS, 1985 Annual Meeting, 1985, pp. 495-502.

[102]M. Depenbrock, *Direct Self Control for High Dynamics Performance of Inverter Feed a.c. Machines.*, ETZ Archive, vol. 7, no. 7, 1985, pp. 211-218.

[103]D. Casadei, F. Profumo, G. Serra, A. Tani, *FOC and DTC: Two Viable Schemes for Induction Motors Torque Control.*, Proc. of EPE-PEMC 2000, 2000, pp. 1-128 - 1-135.

[104]I. Boldea, S.A. Nasar, *Torque Vector Control (TVC) - A Class of Fast and Robust Torque, Speed and Position Digital Controllers for Electric Drives.*, Proceedings of EMPS, vol. 15, 1988, pp. 135-148.

[105]D.Telford M.W.Dunnigan B.W.Williams, *A Comparison of Vector Control and Direct Torque Control of an Induction Machine.*, IEEE PESC 2000 Conf., CD-ROM paper 14.1.

[106]Hoang Le-Huy, *Comparison of Field-Oriented Control and Direct Torque control for Induction Motor Drives.*, The 34th IEEE IAS Annual Meeting, 1999, CD-ROM paper 28.1.

[107]P. Pohjalainen, P. Tiitinen, J. Lalu, *The Next-Generation Motor Control Method – Direct Torque Control, DTC.*, EPE Chapter Symp., Lausanne, 1994, pp. 115-120.

[108]R. Nilsen, T. Kasteenpohja, *Direct Torque Controlled Motor Drive Utilized in an Electrical Vehicle.*, Record of EPE'95, 1995, pp. 2.877-2.882.

[109]J.-K. Kang, S.-K. Sul, *Analysis and Prediction of Inverter Switching Frequency in Direct Torque Control of Induction Machine Based on Hysteresis Bands and Machine Parameters.*, IEEE Trans. Industrial Electronics, vol. 48, no. 3, June 2001, pp. 545-553.

[110]D. Casadei, G. Serra, A. Tani, *Implementation of a Direct Torque Control Algorithm for Induction Motors Based on Discrete Space Vector Modulation.*, IEEE Transactions on Power Electronics, vol. 15, no. 4, July 2000, pp. 769-777.

[111]D. Casadei, G. Serra, A. Tani, *Improvement of Direct Torque Control Performance by Using a Discrete SVM Technique.*, The 29th IEEE PESC98, 1998, vol. 2, pp. 997-1003.

[112]D. Casadei, G. Serra, A. Tani, *Direct Flux and Torque Control of Induction Machine for Electric Vehicle Applications.*, IEE Electrical Machines and Drives, Conference Publication No. 412, Sept. 1995, pp. 349-353.

[113]D. Casadei, G. Serra, A. Tani, *Steady-State and Transient Performance Evaluation of a DTC Scheme in the Low Speed Range.*, IEEE Transactions on Power Electronics, vol. 16, no. 6, Nov. 2001, pp. 846-851.

[114]D. Casadei, C. Rossi, G. Serra, A. Tani, *A New Voltage-Vector Selection Algorithm in Direct Torque Control of Induction Motor Drives.*, Proceedings of Electromotion 2001 Conference, Bologna, June 2001, pp. 119-124.

[115]D. Casadei, G. Serra, A. Tani, *Stator Flux Vector Control for High Performance Induction Motor Drives using Space Vector Modulation.*, Proceedings of OPTIM'96, Brasov, Romania, 1996, pp. 1413-1422.

[116]D. Casadei, G. Serra, A. Tani, L. Zarri, F. Profumo, *Performance Analysis of a Speed Sensorless Induction Motor Drive Based on a Constant Switching Frequency DTC Scheme.*, The 35th IEEE IAS Annual Meeting, 2000, Rome, CD-ROM paper 33.3.

[117]T.G. Habetler, F. Profumo, M. Pastorelli, L.M. Tolbert, *Direct Torque Control of Induction Machines Using Space Vector Modulation.*, IEEE Transactions on Industry Applications, vol. 28, no. 5, Sept./Oct. 1992, pp. 1045-1053.

[118]G. Griva, T.G. Habetler, F. Profumo, M. Pastorelli, *Performance Evaluation of a Direct Torque Controlled Drive in the Continuous PWM-Square Wave Transition Region.*, IEEE Transactions on Power Electronics, vol. 10, no. 4, July 1995, pp. 464-471.

[119]G. Griva, F. Profumo, M. Abrate, A. Tenconi, D. Berruti, *Wide Speed Range DTC Drive Performance with New Flux Weakening Control.*, The 29th IEEE PESC98 Record, 1998, vol. 2, pp. 1599-1604.

[120]B.H. Kenny, R.D. Lorenz, *Stator and Rotor Flux Based Deadbeat Direct Torque Control of Induction Machines.*, The 36th IEEE IAS Conf., 2001, CD-ROM paper 3.5.

[121]M.P. Kazmierkowski, A.B. Kasprowicz, *Improved Direct Torque and Flux Vector Control of PWM Inverter-Fed Induction Motor Drives.*, IEEE Transactions on Industrial Electronics, vol. 42, no. 4, August 1995, pp. 344-350.

[122]P.Z. Grabowski, M.P. Kazmierkowski, B.K. Bose, F. Blaabjerg, *A Simple Direct-Torque Neuro-Fuzzy Control of PWM-Inverter-Fed Induction Motor Drive.*, IEEE Transactions on Industrial Electronics, vol. 47, no. 4, August 2000, pp. 863-870.

[123]A. Mir, M.E. Elbuluk, D.S. Zinger, *Fuzzy Implementation of Direct Self Control of Induction Motors.*, IEEE Trans. Ind. App., vol. 30, no. 3, May/June 1994, pp. 729-735.

[124]A. Mir, M.E. Elbuluk, D.S. Zinger, *Fuzzy Controller for Inverter Feed Induction Machine.*, IEEE Trans. on Industry Applications, vol. 30, no. 1, Jan./Feb. 1994, pp. 78-84.

[125]J.-K. Kang, S.-K. Sul, *New Direct Torque Control of Induction Motor for Minimum Torque Ripple and Constant Switching Frequency.*, IEEE Transactions on Industry Applications, vol. 35, no. 5, Sept./Oct. 1999, pp. 1076-1082.

[126]J.-K. Kang, S.-K. Sul, *Analysis and Prediction of Inverter Switching Frequency in Direct Torque Control of Induction Machine Based on Hysteresis Bands and Machine Parameters.*, IEEE Trans. on Ind. Electronics, vol. 48, no. 3, June 2001, pp. 545-553.

[127]K.L. Shi, T.F. Chan, Y.K. Wong, S.L. Ho, *Direct Self Control of Induction Motor Based on Neural Network.*, Trans. Ind. App., vol. 37, no. 5, Sept./Oct. 2001, pp. 1290-1298.

[128]C. Attaianese, V. Nardi, G. Tomasso, A. Perfetto, *Vectorial Torque Control (VTC): A Novel Approach to Torque and Flux Control of Induction Motor Drives.*, IEEE Transactions on Industry Applications, vol. 35, no. 6, Nov./Dec. 1999, pp. 1399-1405.

[129]P. Vas, M. Rashed, M. Zordan, A.F. Stronach, C.H. Ng, *DTC PMSM Drives with Torque Ripple Minimization*, PCIM 2000 Europe, 2000, CD-ROM paper imd11.

VSC

[130]R.A. DeCarlo, S.H. Zak, G.P.Matthews, *Variable Structure Control of Nonlinear Multivariable Systems: A Tutorial.*, Proc. of IEEE, vol. 76, no. 3, March 1988, pp. 212-232.

[131]J.Y. Hung, W. Gao, J.C. Hung, *Variable Structure Control. A Survey.*, IEEE Transactions on Industrial Electronics, vol. 40, no. 1, Feb. 1993, pp. 2-22.

[132]W. Gao, J.C. Hung, *Variable Structure Control of Nonlinear Systems: A New Approach.*, IEEE Transactions on Industrial Electronics, vol. 40, no. 1, Feb. 1993, pp. 45-55.

[133]K.D. Young, V.I. Utkin, U. Ozguner, *A Control Engineer's Guide to Sliding Mode Control.*, IEEE Trans. on Control Systems Technology, vol. 7, no. 3, May 1999, pp. 328-342.

[134]V.I. Utkin, *Sliding Mode Control Design Principles and Applications to Electric Drives.*, IEEE Transactions on Industrial Electronics, vol. 40, no. 1, Feb. 1993, pp. 23-36.

[135]S.V. Drakunov, V.I. Utkin, *Sliding Mode Control in Dynamic Systems.*, International Journal of Control, vol. 55, no. 4, 1992, pp. 1029-1037.

[136]G. Bartolini, A. Ferrara, V.I. Utkin, *Adaptive Sliding Mode Control in Discrete-Time Systems.*, Automatica, vol. 31, no. 5, 1995, pp. 769-773.

[137]A. Bartoszewicz, *Discrete-Time Quasi-Sliding-Mode Control Strategies.*, IEEE Transactions on Industrial Electronics, vol. 45, no. 4, August 1998, pp. 633-637.

[138]Z. Yan, C. Jin, V.I. Utkin, *Sensorless Sliding-Mode Control of Induction Motors.*, IEEE Transactions on Industrial Electronics, vol. 47, no. 6, Dec. 2000, pp. 1286-1297.

[139]O. Kaynak, K. Erbatur, M. Ertugrul, *The Fusion of Computationally Intelligent Methodologies and Sliding-Mode Control – A Survey.*, IEEE Transactions on Industrial Electronics, vol. 48, no. 1, Feb. 2001, pp. 4-17.

[140]A. Benchaib, A. Rachid, E. Audrezet, M. Tadjine, *Real-Time Sliding-Mode Observer and Control of an Induction Motor.*, Trans. Ind. Elec., vol. 46, no. 1, Feb. 1999, pp. 128-137.

[141]H.-J. Shieh, K.-K. Shyu, *Nonlinear Sliding-Mode Torque Control with Adaptive Backstepping Approach for Induction Motor Drive.*, IEEE Transactions on Industrial Electronics, vol. 46, no. 2, April 1999, pp. 380-389.

[142]M. Rodič, K. Jezernik, *Speed-Sensorless Sliding-Mode Torque Control of an Induction Motor.*, IEEE Transactions on Industrial Electronics, vol. 49, no. 1, Feb. 2002, pp. 87-95.

[143]F. Moldoveanu, V. Comnac, M. Cernat, I. Draghici, L. Cazac, R. Ungar, *Torque and Stator Flux Control of PWM Inverter-Feed Asynchronous Machine: A Sliding Mode Approach*, Proceedings of PCIM 2000 Europe, 2000, CD-ROM paper imd10.

[144]I. Boldea, A. Trica, *Torque vector control (TVC) voltage fed induction motor drives-very low performance via sliding mode.*, Proceedings of ICEM-1990, vol. 3, pp. 1212-1217.

[145]F.S. Neves, T.G. Habetler, B.R. Menezes, R.P. Landim, S.R. Silva, *Induction Motor DTC Strategy Using Discrete-Time Sliding Mode Control.*, The 34th IEEE Industry Applications Society Annual Meeting, 1999, Phoenix, AZ, CD-ROM paper 2.6.

[146]M. Rodič, K. Jezernik, A. Šabanović, *Speed Sensorless Sliding Mode Torque Control of Induction Motor.*, IEEE IAS Annual Meeting, 2000, Rome, CD-ROM paper 42.1.

[147]M. Rodič, K. Jezernik, *Speed-Sensorless Sliding-Mode Torque Control of an Induction Motor.*, IEEE Transactions on Industrial Electronics, vol. 49, no. 1, Feb. 2002, pp. 87-95.

[148]M. Rodič, K. Jezernik, *An Analysis of Speed Sensorless Torque and Flux Controller for Induction Motor.*, IEEE, PESC 2000 Conference, 2000, CD-ROM paper 24.1.

[149]K. Erbatur, M.O. Kaynak, A. Šabanović, *A Study on Robustness Property of Sliding-Mode Controllers: A Novel Design and Experimental Investigations.*, IEEE Transactions on Industrial Electronics, vol. 46, no. 5, Oct. 1999, pp. 1012-1018.

[150]C. Rossi, A. Tonielli, *A Unifying Approach to Robust Control of Electrical Motor Drives.*, IEEE IECON'92, The Int. Conf. on Industrial Electronics, vol. 1, 1992, pp. 95-100.

Monographies

[151]Werner Leonhard, *Control of Electrical Drives.*, Springer-Verlag, Berlin, Heidelberg, New-York, Tokyo, 1985.

[152]I. Boldea, S.A. Nasar, *Vector control of a.c. drives.*, C.R.C. Press Florida, Boca Raton, Ann Arbor, London, Tokyo, 1992.

[153]I. Boldea, S.A. Nasar, *Electric machines: dynamics and control.*, CRC Press Florida, Boca Raton, Ann Arbor, London, Tokyo, 1992.

[154]I. Boldea, S.A. Nasar, *Electric Drives.*, CRC Press Boca Raton, London, New York, Washington, D.C., 1999.

[155]D.W. Novotny, T.A. Lipo, *Vector Control and Dynamics of AC Drives.*, Clarendon Press - Oxford, Oxford University Press, New York, 1996.

[156]A.M. Trzynadlowski, *The field orientation principle in control of induction motors.*, Kluwer Academic Press, Boston, 1994.

[157]Karl J. Astrom, Bjorn Wittenmark, *Computer Controlled Systems: Theory and Design.*, Prentice Hall International, Englewood Cliffs, New Jersey, 1984.

[158]Yasuhiko Dote, *Servo Motor and Motion Control Using Digital Signal Processors.*, Prentice Hall, Englewood Cliffs, New Jersey & Texas Instruments, 1990.

[159]Robert Grover Brown, Patrick Y. C. Hwang, *Introduction to Random Signals and Applied Kalman Filtering, third edition.*, John Wiley & Sons, USA, 1997.

[160]Jean-Jacques E. Slotine, Weiping Li, *Applied Nonlinear Control.*, Prentice Hall, Englewood Cliffs, New Jersey, 1991

[161]Vadim I. Utkin, *Sliding Modes in Control Optimization.*, Springer-Verlag Berlin, Heidelberg, 1992.

[162]Vadim Utkin, Jurgen Guldner, Jingxin Shi, *Sliding Mode Control in Electromechanical Systems.*, Taylor & Francis, 1999.

[163]Yasuhiko Dote, Richard G. Hoft, *Intelligent Control. Power Electronic Systems.*, Oxford University Press, Oxford, New-York, Tokyo, 1998.

[164]K. Rajashekara (Editor), *Sensorless Control of AC Motors.*, IEEE Press, 1996.

[165]Bimal K. Bose (Editor) et al., *Power Electronics and Variable Frequency Drives Technology and Applications.*, IEEE Press, 1997.

[166]N. Mohan, T.M. Undeland, W.P. Robbins, *Power Electronics: Converters, Applications and Design.*, Second Edition, John Wiley & Sons, New York, 1995.

[167]Allan V. Oppenheim, Ronald W. Schafer, *Digital Signal Processing.*, Prentice-Hall International Inc., Englewood Cliffs, New Jersey, 1975.

[168]John G. Proakis, Dimitris G. Manolakis, *Digital Signal Processing. Principles, Algorithms and Applications. Third Edition.*, Prentice-Hall Inc., Englewood Cliffs, New Jersey, 1996.

[169]Brian W. Kernigham, Dennis M. Ritchie, *The C Programming Language, second edition.*, Prentice Hall International, Englewood Cliffs, New Jersey, 1988.

[170]Bjarne Stroustrup, *The C++ Programming Language, third edition.*, Addison-Wesley Publishing Company, Inc., Reading, Massachusetts, 1997.

[171]Arpad Kelemen, Maria Imecs, *Sisteme de reglare cu orientare după cîmp ale maşinilor de current alternativ.*, Ed. Academiei Române, Bucureşti, 1989.

[172]Dan Larionescu, *Metode numerice.*, Ed. Tehnică, Bucureşti, 1989.

[173]Dan Sângeorzan, *Echipamente de reglare numerică.*, Ed. Militară, Bucureşti, 1990.

[174]Octavian Catrina, Iuliana Cojocaru, *Turbo C++.*, Ed. Teora, Bucureşti, 1993.

[175]Dan Somnea, Doru Turturea, *Iniţiere în C++. Programarea orientată pe obiecte.*, Ed. Tehnică, Bucureşti 1993.

[176]I. Dumitrache, S. Dumitru, I. Mihu, F. Munteanu, G. Muscă, C. Calcev, *Automatizări Electronice.*, Ed. Didactică şi Pedagogică, Bucureşti, 1993.

[177]Gheorghe Daniel Andreescu, *Estimatoare în sisteme de conducere a acționărilor electrice.*, Ed. Orizonturi Universitare, Timişoara, 1999.

[178]Teodor Pană, *Matlab în sisteme de acționare electrică.*, Ed. Mediamira, Cluj-Napoca, 1996.

[179]Pal K. Kovacs, *Analiza regimurilor tranzitorii ale maşinilor electrice.*, Ed. Tehnică, Bucureşti 1980.

[180]Vasile N. Nedelcu, *Regimurile de funcționare ale maşinilor de curent alternativ.*, Ed. Tehnică, Bucureşti 1968.

Personal papers

[181]Ion Boldea, Cristian Lascu, *The Torque Vector Controlled Universal AC Drive - The Theory.*, Proceedings of the International Conference on Optimization of Electrical and Electronic Equipments - OPTIM'96, Brasov 1996, pp. 1423-1440.

[182]C. Lascu, I. Boldea, F. Blaabjerg, *The Torque Vector Controlled (TVC) Universal AC Drive. Implementation Aspects.*, Proc. of the International Conference on Optimization of Electrical and Electronic Equipments - OPTIM'98, Brasov 1998, vol. 2, pp. 369-374.

[183]N. Patriciu, C. Lascu, A. Patriciu, *PWM Strategies for Controlling the Tandem Inverter.*, Proceedings of the International Conference on Automation and Quality Control - A&Q'98, Cluj-Napoca 1998, vol. Q, pp. Q444-Q449.

[184]N. Patriciu, C. Lascu, L. Tutelea, A. Patriciu, *The Improvement of the Output Current Waveform Using Three-Phase Current Source Inverter and Three-Phase Voltage Source Inverter - Comparative Analysis and Solutions.*, Proceedings of the National Conference on Electrical Drives - CNAE'98, Craiova 1998, pp. 215-220.

[185]N. Patriciu, C. Lascu, L. Tutelea, A. Patriciu, *The Tandem Inverter, a Solution for High-Power Adjustable Speed A.C. Drives.*, Buletinul Stiintific al Universitatii "Politehnica" din Timisoara, Transactions on Electrical Engineering, Electronics and Communications, Tom. 43 (57), Fasc. 2, Timisoara 1998, pp. 87-94.

[186]C. Lascu, I. Boldea, F. Blaabjerg, *A Modified Direct Torque Control (DTC) for Induction Motor Sensorless Drive.*, The 33rd IEEE Industry Applications Society Annual Meeting 1998, St. Louis, MO, USA, vol. 1, pp. 415-422.

[187]C. Lascu, I. Boldea, F. Blaabjerg, *A Modified Direct Torque Control for Induction Motor Sensorless Drive.*, IEEE Transactions on Industry Applications, vol. 36, no. 1, Jan./Feb. 2000, pp. 122-130.

[188]Cristian Lascu, Andrzej M. Trzynadlowski, *A DSP-Based Performance Monitor for Induction Motors.*, Texas Instruments DSPs Fest, Houston, TX, August 1999.

[189]Cristian Lascu, Andrzej M. Trzynadlowski, *A DSP-Based Torque Monitor for Induction Motors.*, Texas Instruments DSPs Fest, Houston, TX, August 2000.

[190]I. Boldea, S. Scridon, L. Tutelea, C. Lascu, N. Muntean, *The Flux Reversal Machine (FRM) as an Automotive Alternator With 42/14 V D.C. Dual Output.*, Proceedings of the International Conference on Optimization of Electrical and Electronic Equipments – OPTIM 2000, Brasov 2000, vol. 2, pp. 337-344.

[191]Cristian Lascu, Andrzej M. Trzynadlowski, *A TMS320C243-Based Torque Estimator for Induction Motor Drives.*, IEEE International Electric Machines and Drives Conference - IEMDC 2001, Cambridge, MA, 2001, pp. 733-735.

[192]Cristian Lascu, Andrzej M. Trzynadlowski, *A Sensorless Hybrid DTC Drive for High-Volume Applications Using the TMS320F243 DSP Controller.*, The 36th IEEE Industry Applications Society Annual Meeting 2001, Chicago, IL, USA, vol. 1, pp. 482-489.

[193]Cristian Lascu, Ion Boldea, *Direct Torque Control of Sensorless Induction Motor Drives. A Sliding Mode Approach.*, Proceedings of the International Conference on Optimization of Electrical and Electronic Equipments – OPTIM 2002, Brasov 2002, vol. 2, pp. 481-488.